Dissertation
submitted to the
Combined Faculty of Mathematics, Engineering and Natural Sciences
of Heidelberg University, Germany
for the degree of
Doctor of Natural Sciences

Put forward by
Stefan Robert Erlewein
born in: Stuttgart, Germany
Oral examination: 2024-07-23

Implementation of a superconducting shimming and shielding system in the BASE experiment

1st referee: Klaus Blaum
2nd referee: Belina von Krosigk

Zusammenfassung:
Das BASE (Baryon Antibaryon Symmetry Experiment) Experiment, welches sich am Antiproton Entschleuniger Komplex des CERN befindet, testet die Gültigkeit der CPT-Invarianz mit Baryonen durch Vergleiche der Ladungs-zu-Masse Verhältnisse und der g-Faktoren von Protonen und Antiprotonen. Beide Messungen basieren auf dem Vergleich der freien Zyklotronfrequenz bzw. der Larmorfrequenz der in einer Penningfalle gefangenen Teilchen. Diese Arbeit beschreibt das Design, die Implementierung sowie die Charakterisierung eines supraleitenden magnetischen Shim- und Abschirmungssystems welches das gefangene Teilchen von externen Änderungen des Magnetfelds abschirmt und die Möglichekeit bietet, das Magnetfeld sowie seine ersten beiden Ableitungen zu verändern. Mit Hilfe dieses Systems kann die quadratische Inhomogenität $B_2 \approx 100\ \frac{\mathrm{mT}}{\mathrm{m}^2}$ des magnetischen Feldes, welche in der letzten g-Faktor Messung die dominante Unsicherheit darstellte, eliminiert werden, was eine Messung des Antiproton g-Faktors auf 100 p.p.t. Level ermöglicht. Des Weiteren können systematische Effekte direkt untersucht werden indem absichtlich eine Inhomogenität des Magnetfelds herbeigeführt wird. Die erhöhte Homogenität des Magnetfelds erlaubt erstmals die Möglichkeit der Verwendung von kohärenten Anregungsmethoden bei der Messung der Larmorfrequenz des gefangenen Teilchens wodurch die Sättigungsverbreiterung im Profil der g-Faktor Resonanz verringert und die beobachtete Inversion erhöht werden können.

Abstract:
The BASE (Baryon Antibaryon Symmetry Experiment) experiment, located at CERN's Antiproton decelerator, tests CPT-invariance by comparing the charge-to-mass ratios and g-factors of protons and antiprotons at high precision. Both measurements rely on the comparison of the particle's free cyclotron and Larmor frequencies in a high-precision Penning trap. This thesis describes the successful design, implementation and characterization of a superconducting magnetic shimming and shielding system which shields the trapped particle from magnetic field fluctuations induced by the noisy environment of the experiment hall and provides the possibility to tune the magnetic field as well as its first two derivatives. With the help of this system the quadratic inhomogeneity $B_2 \approx 100\ \frac{\mathrm{mT}}{\mathrm{m}^2}$ of the magnetic field, which was the dominant uncertainty in the last g-factor measurement was eliminated, which paves the wave for a measurement of the antiproton g-factor at the 100 p.p.t. level. In addition, the shimming system provides the possibility to directly study systematic shifts by introducing magnetic field inhomogeneities on purpose. Finally, the increased homogeneity of the magnetic field creates the novel possibility to use coherent excitation techniques for the measurement of the trapped particle's Larmor frequency which reduces the power broadening in the g-factor resonance.

Contents

1 Introduction

1.1 Theoretical Motivation

The Standard Model of particle physics (SM) [1] can considered to be one of the greatest successes of modern physics. It predicted the existence and properties of the W and Z bosons [2, 3], the top quark [4, 5], the gluon [6–9] as well as the unification of the electromagnetic and weak force [10]. With the discovery of the Higgs boson [11, 12] 50 years after its prediction [13, 14] all particles predicted by the Standard Model have been found. Despite this overwhelming success, the Standard Model has it's limitations. First of all, the Standard Model does not describe gravity and no indication of the graviton, which is the hypothetical force carrying boson of gravity in quantum gravity theories, has been found. In addition, the Standard Model can not explain how the mass of neutrinos arises. The observation of neutrino oscillations [15] indicates, that at least two out of the three neutrino flavors need to have mass [16]. The interaction with the Higgs field, which gives mass to the fermions, requires left- and right-handed versions of said fermion to exist, however, no right-handed neutrinos have ever been observed. Alternatively, neutrinos could be Majorana perticles, however, in that case neutrinoless $\beta\beta$-decay, which so far has not been observed, should be possible [17].
Given that the Standard Model is a local and Lorentz-invariant quantum field theory with a positive-definite hermitian Hamiltonian that preserves micro-causality, the combined conjugation of charge, parity and time (CPT-symmetry) [1] should conserve the laws of physics and matter and antimatter should be perfect mirror images of each other [18, 19]. Thus, the Standard Model predicts that matter and antimatter should have been created in equal amounts during baryogenesis, however, the observable universe is dominated by matter and no hints of the missing antimatter can be observed [20]. The observed asymmetry between matter and antimatter can be characterized using the asymmetry parameter η which is defined as the ratio between baryon number N_B, antibaryon number $N_{\bar{B}}$ and photon number N_γ [21]:

$$\eta = \frac{N_B - N_{\bar{B}}}{N_\gamma} = 6.14(25) \times 10^{-10}. \tag{1.1}$$

Furthermore the ΛCDM-model requires the existence of dark matter, which interacts only

gravitationally with ordinary matter, to describe the formation and large-scale structure of galaxies [22] in addition to dark energy which is required to describe the accelerated expansion of the universe [23]. Measurements of the Planck collaboration [24] indicate the energy content of the universe to be made up of approximately $69\,\%$ dark energy, $26\,\%$ and only $5\,\%$ baryonic matter.
In order to tackle this observed baryon asymmetry, Andrei Sakharov proposed three condition that are required to produce matter and antimatter at different rates [25]. These conditions – called Sakharov conditions – are:

1. Baryon number violation:
   In order for matter and antimatter to be produced at different rates, a process that violates baryon number conservation has to exist. In general, interactions within the Standard Model conserve that baryon number and while hypothetical exceptions exist [26], no such process has ever been observed.

2. CP-symmetry violation:
   Even in case that a process that favored the creation of baryons over antibaryons existed, CP-symmetry would predict an equivalent process favoring the creation of antimatter over matter at the same rate to exist. While the Standard Model allows for CP-violation and indirect [27] and direct [28, 29] CP-violation has been discovered, the amount of CP-violation is not sufficient to explain the observed imbalance of matter and antimatter, given the limits on baryon number violation.

3. Interaction out of thermal equilibrium:
   The matter producing processes have to happen outside of thermal equilibrium, as a system in thermal equilibrium with baryon number $B = 0$ would stay at $B = 0$ and no baryon asymmetry could be created. Given the expansion of the universe, this condition is fulfilled as well.

Note that in case CPT violation is allowed the second and third conditions are no longer required [30, 31].
Motivated by interactions in string theories that lead to spontaneous breaking of Lorentz invariance [32], Alan Kostelecký and Don Colladay developed an extension of the Standard Model which allows for Lorentz-violation and CPT-violation [33, 34]. This effective field theory – called Standard Model extension (SME) – introduces Lorentz-violating terms and corresponding coupling coefficients into the Standard Model and studies the effects these new interactions would have on experimental observations. The SME therefore does not introduce new particles and does not explain the origin of these interactions but rather provides the framework to

constrain the effects new theories containing spontaneous Lorentz-symmetry breaking would have on the interactions of the existing Standard Model particles. By comparing experimental results to the effects introduced in the SME framework, limits on the magnitude of the coupling coefficients can be given [35]. To date, no coefficient with a significant deviation from zero has been observed.

1.2 CPT tests with antimatter

1.2.1 Prediction and discovery of antimatter

In 1928, Paul Dirac published the Dirac equation which combined special relativity with the Schrödinger equation and succesfully predicted the magnetic moment of the electron [36]. While Dirac initially could not explain the arising negative energy solutions, he later published a follow-up paper predicting the existence of the positron [37], the antimatter conjugate of the electron with the same mass and opposite charge. In 1932, the positron was observed in cosmic radiation for the first time [38]. Initially, it was believed that matter and antimatter had to behave exactly the same under charge conjugation (C), parity inversion (P) or time reversal (T) [18, 19]. In 1957, the Wu experiment demonstrated however, that P-symmetry was violated in the β-decay of Co-60 [39]. Later in was shown that the combination of charge conjugation and parity reversal (CP-symmetry) was not conserved in the decay of neutral kaons [27–29]. By comparing the fundamental properties of matter particles with their antimatter conjugates, CPT-symmetry can be experimentally tested to high precision.

1.2.2 Creation of antimatter in the laboratory

Given the high energy required for the production of baryonic antimatter, research is limited by the availability of particle accelerators with high enough energy to create antiprotons. The first antiproton [40] was created at the Bevatron in 1955 and in 1956 discovery of the antineutron followed [41]. The mass of both particles matched the mass of their respective matter counterparts while the charge and magnetic moment had the same magnitude but opposite sign. The next big milestone in antimatter research was the creation of antimatter nuclei [42] at CERN's Proton Synchrotron. In 1982 the low energy antiproton ring (LEAR) [43], a dedicated storage ring for antimatter research, started operation at CERN.

1.2.3 First low-energy measurements at LEAR

At LEAR, the TRAP collaboration managed to demonstrate the feasibility to study antimatter at low energies by demonstrating the ability to slow [44], trap [45] and cool [46] antiprotons in a

Penning trap for the first time, thus establishing many techniques that are still used in high-precision antimatter Penning trap measurements today. In 1990, TRAP managed to measure to compare the charge-to-mass ratio of the proton and antiproton using clouds of 100 particles at a fractional uncertainty of 40 p.p.b. [47], which corresponded to an improvement of more than a factor 1000 compared to earlier measurements. Additionally, this measurement set new limits for the antiproton's lifetime. In 1996, the uncertainty was improved by a further factor of 40 by comparing the cyclotron frequencies of a single proton and a single antiproton in the same magnetic field [48]. Given the opposite charge of the particles, this measurement requires a change of polarity of the trapping fields which introduces systematic shifts in case the magnetic field at the location of the proton and antiproton differ due to slight differences in trapping voltage. In order to overcome this limitation, a final charge-to-mass comparison was conducted at a fractional precision of 90 p.p.t. [49] by comparing the charge-to-mass ratio between an antiproton and an H^--ion which can be trapped in the same potential.
Another milestone was the creation of nine antihydrogen atoms by passing the antiprotons cycling in LEAR through Xe gas, which allowed the creation of electron-positron pairs in collisions between the antiprotons and the Xe atoms [50]. In addition, scientists at KEK observed that antiprotons survived in liquid helium for extended periods of time [51], which lead to increased interest in the study of antiprotonic helium systems which consist of a helium atom in which one of the electrons is replaced with an antiproton. In conjunction with the history of successful experiments with antimatter at low energies as well as the new possibility of antihydrogen spectroscopy experiments, the Antiproton decelerator (AD) [52] was built at CERN.

1.2.4 Measurements at the Antiproton decelerator

The first milestone achieved at the AD was the production of cold antihydrogen by the ATHENA and ATRAP collaborations [53, 54]. These experiments created cold antihydrogen by trapping antiprotons and positrons in a nested Penning trap. After mixing the clouds, the dominant binding mechanism occurs in three-body collisions between an antiproton and two positrons which can lead to a final state in which one positron ends up bound to the antiproton while the other positron carries away the excess energy [55]. In 2021, the AEgIS collaboration [56] managed to demonstrate the formation of a pulsed beam of cold antihydrogen via a charge-exchange reaction between Rydberg positronium and trapped antiprotons [57]. Given the successful creation of antihydrogen, the ALPHA collaboration subsequently demonstrated the confinement [58], spectroscopy [59, 60] and laser-cooling [61] of neutral antihydrogen. Using the location of antihydrogen annihilation after the magnetic trap was ramped down, ALPHA

was able confine the ratio of the gravitational mass to the inertial mass of antihydrogen to values below 75 [62]. In 2023, a more precise measurement [63] measured the gravitational acceleration of antimatter $a_{\bar{g}} = (0.75 \pm 0.13(\text{statistical} + \text{systematic}) \pm 0.16(\text{simulation}))g$, where $g = 9.81\ \frac{\text{m}}{\text{s}^2}$. In addition, two more collaborations plan to probe the gravitational behavior of antimatter. The GBAR experiment [64] attempts to trap positively charged antihydrogen ions which can be sympathetically cooled to low temperatures by coulomb interaction with laser-cooled beryllium ions. By ionizing the trapped antihydrogen ion, a cold and neutral antihydrogen atom is created. Due to its lack of charge, this particle is no longer confined by the electrostatic fields of the trap and its behavior in the gravitational field of the earth can be studied. In contrast, AEgIS plans to study the effect of gravity using a Moire deflectometer.

In addition to the research conducted on antihydrogen, multiple experiments were conducted on other antimatter systems. Following up on the observations at KEK [51] the ASACUSA collaboration managed to conduct two-photon laser spectroscopy on antiprotonic helium and determined the antiproton-to-electron mass ratio in 2016 [65]. Given the successful measurements of the TRAP collaboration at LEAR, a follow-up experiment – ATRAP – was established at the Antiproton decelerator. After the successful resolution of single spin flips of a trapped proton [66], the ATRAP collaboration published a new measurement of the antiproton's magnetic moment [67], which improved earlier uncertainties by a factor of 680. Later, the BASE collaboration improved this value by a further factor of 3000 [68]. In addition BASE compared the charge-to-mass ratio of the proton and antiproton at a fractional precision of 16 parts-per-trillion [69] in 2022. Currently two experiments, PUMA [70] and BASE-STEP [71], are working on the implementation of a transportable antiproton trap. The PUMA experiment plans to transport trapped antiprotons to CERN's ISOLDE facility [72] where exotic nuclei are injected into the trap and neutron halos [73] are studied. In contrast, BASE-STEP is designed in a way that not only allows loading of antiprotons into the trap but rather provides the possibility to transfer the trapped antiprotons from the transportable trap to different experiments. This would open the way for non-destructive antimatter research independent of access to the Antiproton decelerator.

In addition to the laboratory test on baryonic antimatter outlined above, the Alpha Magnetic Spectrometer (AMS) [74, 75] which is located on the International Space Station (ISS) is looking for antimatter in cosmic rays. Given the comparably easy access to positrons via the β^+ decay of NA-22, comparisons between the properties of electrons and positrons have been conducted in the past [76]. Furthermore, comparison between the anomalous frequency of muons and antimuons [77] expand the tests of CPT symmetry in the leptonic sector.

This thesis describes the design, successful implementation and characterization of a superconducting magnetic shimming and shielding system. Following the theoretical motivation and introduction of CPT-test with antimatter given above, the first chapter introduces the physics of the Penning trap and gives an overview over the main systematic shifts. Next, an overview over the BASE experiment and the techniques for the comparison of the charge-to-mass ratio and g-factor of the proton and antiproton are given. The 4th chapter introduces the principle and design of the magnetic shimming and shielding system that was implemented in the BASE experiment. Chapter 5 introduces the measurement techniques in the precision trap which serve as the basis for an antiproton g-factor measurement and are necessary for the characterization of the magnetic shimming and shielding system in chapter 6. Chapter 7 describes the characterization of the Analysis trap which is required in a g-factor campaign to resolve the spin state of the trapped particle. Chapter 8 discusses the impact of the magnetic shimming and shielding system in the context of future charge-to-mass ratio and g-factor measurement campaigns and gives an outlook on novel measurement techniques enabled by the shimming and shielding system.

2 Penning trap theory

Measurements of the fundamental properties of charged particles at the highest precision rely on non-destructive observation at extended measurement times. It is therefore necessary to confine the studied particle to a small highly homogenous region. In case of charged particles electric fields can be used to interact with the ions and trap them. As a consequence of Maxwell's equations, the divergence of any electrostatic potential $\Phi(x, y, z)$ vanishes in charge-free space:

$$\Delta\Phi = \frac{\partial^2\Phi}{\partial x^2} + \frac{\partial^2\Phi}{\partial y^2} + \frac{\partial^2\Phi}{\partial z^2} = 0. \tag{2.1}$$

Thus, the static potential has no local minima and no point at which a charged particle would be confined in all directions exists (Earnshaw's theorem [78]). To overcome this fundamental limitation, two approaches exist:

- Radio frequency ion traps combine electrostatic potentials with time-dependent potentials to create a ponderomotive force that confines particle in a harmonic potential in all spacial directions. These traps, first proposed by Paul in 1953 [79], have widespread applications in trapped ion quantum computing [80] and laser spectroscopy in the absence of magnetic fields [81]. Radio frequency ion traps have high selectivity with respect to the charge-to-mass-ratio of particles that can be trapped and provide the possibility to trap positive and negative particles in the same field.
- Penning traps combine a static magnetic field that provides radial confinement with an electrostatic potential that confines particles along the symmetry axis of the trap [82]. Penning traps provide the possibility to trap charged particles of vastly different charge-to-mass ratios, however, positive and negative charged particles can not be trapped at the same time.

2.1 The ideal Penning trap

Ideal Penning traps use a rotationally symmetric electrostatic quadrupole potential $\Phi(z, \rho)$ to confine particles of charge q and mass m along the trap axis. The potential is created by

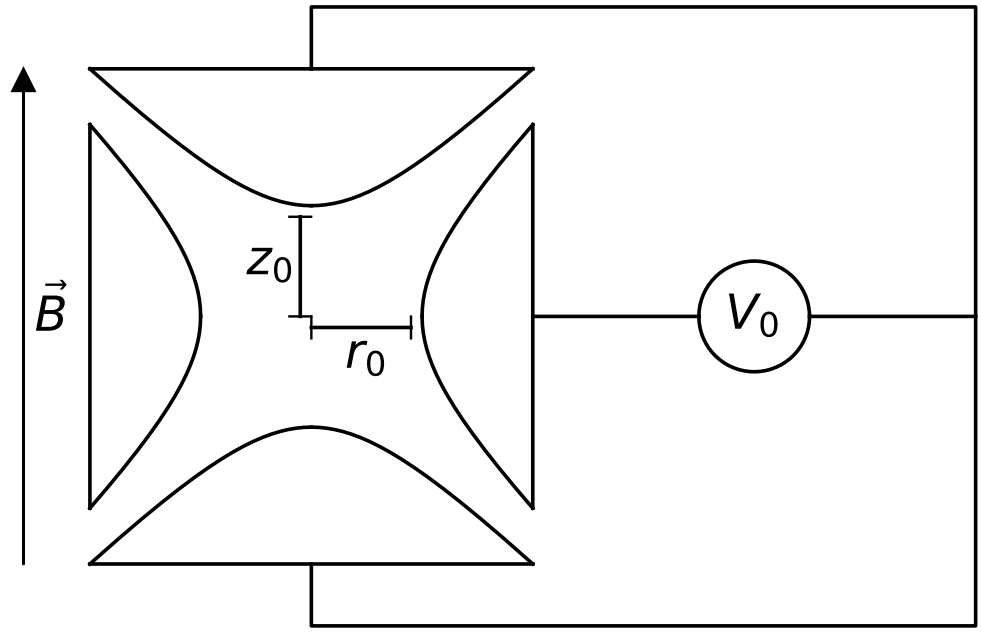

Figure 2.1: Cross-section through the electrodes of a hyperbolic Penning trap. By applying a voltage V_0 between the ring electrode and the endcap electrodes, charged particles are trapped along the axial direction. The magnetic field $\mathbf{B}$ along the trap axis provides confinement in the radial direction.

two rotated hyperbolic endcap electrodes and a hyperboloid ring electrode which follow the equipotential lines. Figure 2.1 shows a cross-section through the electrodes of a hyperbolic Penning trap. The derivation of the eigenfrequencies of a charged particle in a hyperbolic Penning trap follows [83].

In case the trap axis is aligned with the z axis of the coordinate system, the potential is given by:

$$\Phi(z,\rho) = \frac{V_0}{2d^2}\left(z^2 - \frac{\rho^2}{2}\right) \tag{2.2}$$

$$\text{with } \rho = \sqrt{x^2+y^2}, C_2 = \frac{1}{2d^2} \text{ and } d = z_0^2 + \frac{r_0^2}{2}.$$

ρ describes the radial distance from the trap's symmetry axis, d is a characteristic distance

depending on the trap geometry and C_2 characterizes the scaling of the potential for a given voltage V_0. This potential causes particles with opposite charge of V_0 to be repelled from the endcaps, which leads to trapping in the axial direction. In order to overcome the repelling component in the radial direction, a homogeneous magnetic field is superimposed in parallel to the trap's symmetry axis. The total force $\mathbf{F}(\mathbf{x})$ experienced by a particle of charge q and mass m is given by the Lorentz force:

$$\mathbf{F}(\mathbf{x}) = q\left(\mathbf{E}(\mathbf{x}) + \dot{\mathbf{x}} \times \mathbf{B}\right) = q\left(-\nabla\Phi(\mathbf{x}) + \dot{\mathbf{x}} \times \mathbf{B}\right). \tag{2.3}$$

By introducing the axial frequency

$$\omega_z = \sqrt{\frac{2qV_0}{m}C_2} \tag{2.4}$$

and the free cyclotron frequency

$$\omega_c = \frac{qB}{m}, \tag{2.5}$$

the equations of motion can be written as:

$$\ddot{x} - \omega_c\dot{y} - \frac{1}{2}\omega_z^2 x = 0, \tag{2.6}$$

$$\ddot{y} + \omega_c\dot{x} - \frac{1}{2}\omega_z^2 y = 0, \tag{2.7}$$

$$\ddot{z} + \omega_z^2 z = 0. \tag{2.8}$$

The axial motion is solved by a harmonic oscillation with frequency ω_z. The motion in the radial direction can be solved by introducing the variable $u = x + iy$ and combining Eqs. (2.6) and (2.7) into a single equation:

$$\ddot{u} + i\omega_c\dot{u} - \frac{1}{2}\omega_z^2 u = 0. \tag{2.9}$$

Inserting the Ansatz $u(t) = e^{(-i\omega t+\varphi)}$ yields the frequencies

$$\omega_+ = \frac{1}{2}\left(\omega_c + \sqrt{\omega_c^2 - 2\omega_z^2}\right) \tag{2.10}$$

called modified cyclotron frequency, and

$$\omega_- = \frac{1}{2}\left(\omega_c - \sqrt{\omega_c^2 - 2\omega_z^2}\right) \approx \frac{\omega_z^2}{2\omega_c} \tag{2.11}$$

called magnetron frequency. Note that the sign of ω_c determines the signs of ω_+ and ω_- and thus defines the direction of the rotation. Due to its experimental importance the terms modified cyclotron frequency and cyclotron frequency are used interchangeably and refer both to the modified cyclotron frequency. The frequency $\omega_c = \frac{qB}{m}$ is denoted as the free cyclotron frequency.

The general solution to Eq. (2.9) is thus given by

$$u(t) = R_+ e^{(-i\omega_+ t + \varphi_+)} + R_- e^{(-i\omega_- t + \varphi_-)} \tag{2.12}$$

$$= R_+ \cos(\omega_+ t + \varphi_+) + R_- \cos(\omega_- t + \varphi_-) - i\left[R_+ \sin(\omega_+ t + \varphi_+) + R_- \sin(\omega_- t + \varphi_-)\right]. \tag{2.13}$$

Separating the real and imaginary parts finally yields the solutions of the equations of motion:

$$x(t) = R_+ \cos(\omega_+ t + \varphi_+) + R_- \cos(\omega_- t + \varphi_-), \tag{2.14}$$

$$y(t) = -\left[R_+ \sin(\omega_+ t + \varphi_+) + R_- \sin(\omega_- t + \varphi_-)\right], \tag{2.15}$$

$$z(t) = R_z \cos(\omega_z t + \varphi_z). \tag{2.16}$$

Figure 2.2 shows the trajectory of a charged particle in a Penning trap. Note that the frequency ratios were chosen in a way that makes the individual eigenmotions visible.
In case the magnetic field is not strong enough to overcome the radial repulsion introduced by the quadrupole potential, the radicands in Eqs. (2.10) and (2.11) are imaginary and the radial eigenfrequencies ω_+ and ω_- become complex valued. In this case, $x(t)$ and $y(t)$ contain components that grow exponentially over time and a trapped particle would be lost by hitting the walls of the trap. The maximum ring voltage V_{max} that still provides stable trajectories is thus given by:

$$V_{max} = \frac{1}{4C_2}\frac{q}{m}B^2. \tag{2.17}$$

V_{max} depends on the charge-to-mass ratio $\frac{q}{m}$ and thus can be used to remove contaminants with smaller charge to mass ratio than the desired species.

There are several relations between the eigenfrequencies of a trapped particle:

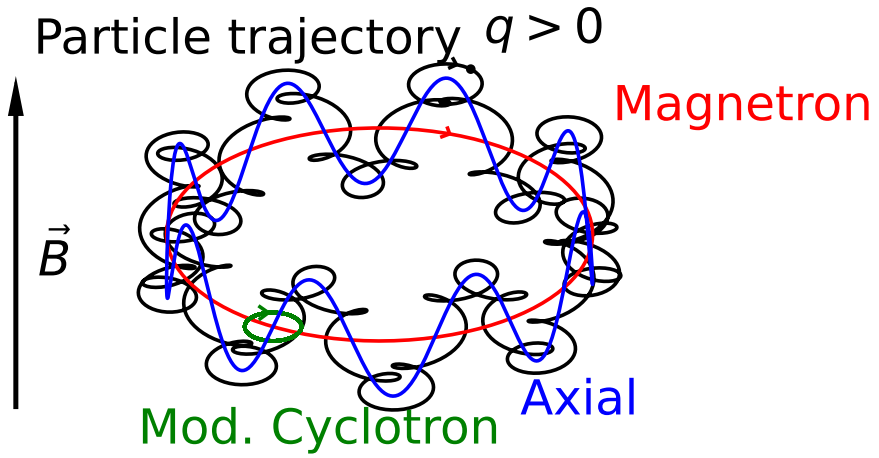

Figure 2.2: Trajectory of a charged particle in a Penning trap. The frequency ratio $\omega_- = \frac{1}{8}\omega_z = \frac{1}{40}\omega_+$ was chosen in a way to clearly show the individual eigenmotions. The axial motion is superimposed on the magnetron orbit to show the oscillation along the trap axis.

$$\omega_+ + \omega_- = \omega_c, \tag{2.18}$$

$$2\omega_+\omega_- = \omega_z^2, \tag{2.19}$$

$$\omega_+^2 + \omega_z^2 + \omega_-^2 = \omega_c^2. \tag{2.20}$$

Of these, the Brown-Gabrielse invariance theorem [82], given by Eq. (2.20), is of highest importance as it is insensitive to an elliptically deformed potential and misalignment of the trap with respect to the magnetic field.

The amplitudes R_-, R_+ and R_z of the individual eigenmotions depend on the respective energies E_-, E_+ and E_z:

$$E_- = \frac{1}{2}m\omega_-^2 R_-^2 - \frac{1}{4}m\omega_z^2 R_-^2 \approx -\frac{1}{4}m\omega_z^2 R_-^2, \tag{2.21}$$

$$E_z = \frac{1}{2}m\omega_z^2 R_z^2, \tag{2.22}$$

$$E_+ = \frac{1}{2}m\omega_+^2 R_+^2 - \frac{1}{4}m\omega_z^2 R_+^2 \approx \frac{1}{2}m\omega_+^2 R_+^2. \tag{2.23}$$

Note that in case of the magnetron motion an increase in radius leads to a decrease of the total energy as the magnetron frequency is small compared to the axial frequency and the increase in kinetic energy is not enough to compensate the loss of potential energy. Rewriting the system of harmonic oscillators by the Hamiltonian

$$H = \hbar\omega_+\left(n_+ + \frac{1}{2}\right) + \hbar\omega_z\left(n_z + \frac{1}{2}\right) - \hbar\omega_-\left(n_- + \frac{1}{2}\right) \tag{2.24}$$

provides the possibility to express the total energy in terms of the principal quantum numbers n_+, n_z and n_-. Figure 2.3 shows the energy levels as a function of the principal quantum numbers for the BASE precision trap.

2.2 The real Penning trap

Hyperbolic Penning traps provide highly harmonic electrical potentials but are difficult to manufacture and provide no easy axial access to the trap center. Therefore many experiments [84, 85] that require the adiabatic transport of trapped ions use cylindrical Penning traps consisting of multiple stacked cylindrical electrodes. These electrodes are easy to machine and

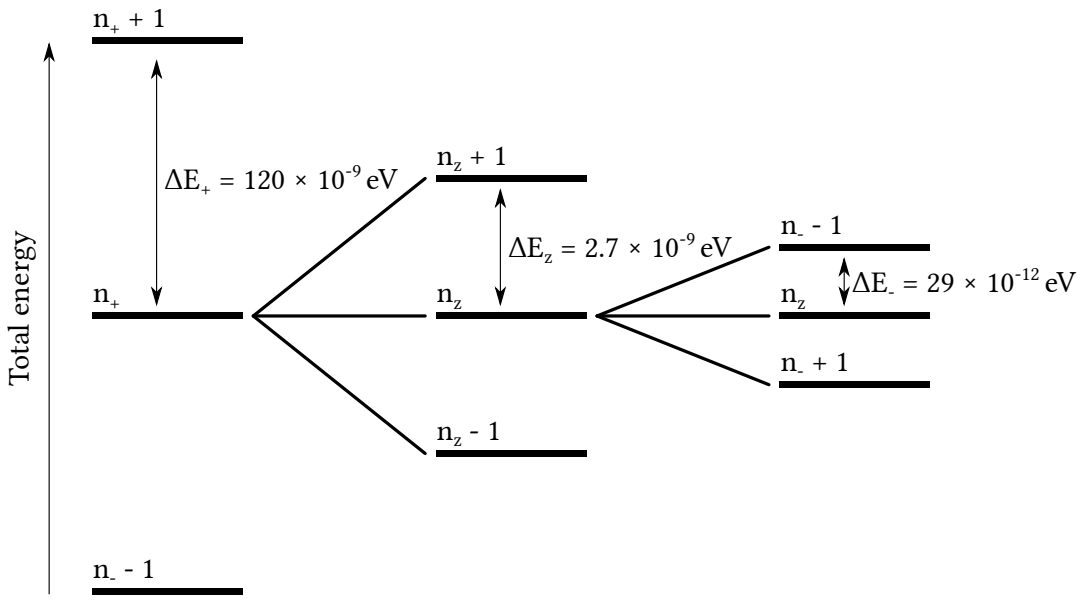

Figure 2.3: Energy levels of a particle trapped in a Penning trap. The relative levels are not drawn to scale. As the magnetron motion has negative energy, increasing n_- leads to a decrease in total energy.

the open endcaps provide easy access for particle loading, interaction with lasers and transport between traps in a multi-trap setup. Given the azimuthal symmetry of the system, determination of the potential $\Phi(z, \rho)$ is easiest by solving the Laplace equation in cylindrical coordinates:

$$\Delta\Phi(z,\rho) = \frac{1}{\rho}\frac{\partial}{\partial\rho}\left(\rho\frac{\partial\Phi(z,\rho)}{\partial\rho}\right) + \frac{\partial^2\Phi(z,\rho)}{\partial z^2} = 0. \tag{2.25}$$

Using the ansatz $\Phi(z, \rho) = Z(z) \cdot R(\rho)$ yields the two differential equations

$$\rho^2\frac{\partial^2 R(\rho)}{\partial\rho^2} + \rho\frac{\partial R(\rho)}{\partial\rho} - \rho^2 k^2 R(\rho) = 0 \tag{2.26}$$

$$\frac{\partial^2 Z(z)}{\partial z^2} + k^2 Z(z) = 0 \tag{2.27}$$

which are linked by the separation parameter k. Equation 2.26 is a modified Bessel equation and the radial components of the potential are thus described by the modified Bessel functions $R(\rho) = I_0(k\rho)$. The axial component given by eq. 2.27 is solved by $Z(z) = A(k)\sin(kz) + B(k)\cos(kz)$. If the origin is placed at one end of the trap and it is assumed that the potential at both ends of the trap stack vanishes, all $B(k)$ have to vanish. Additionally, $A(k)$ vanishes at

the ends of the endcaps only if $k\pi$ is an integer multiple of the total trap length Λ. The general solution to eq. 2.25 is thus given by

$$\Phi(z,\rho) = \sum_{n=1}^{\infty} A_n \sin(k_n z) I_0(k_n \rho) \quad \text{with } k_n = n\frac{\pi}{\Lambda}. \tag{2.28}$$

The coefficients A_n are determined by the boundary conditions, i.e. the potential on the trap electrodes. In order to calculate A_n, the potential at the trap radius R is expanded in terms of orthogonal functions. Using the orthogonality relation

$$\frac{2}{\Lambda}\int_0^{\Lambda} \sin\Big(n\frac{\pi}{\Lambda}z\Big)\sin\Big(m\frac{\pi}{\Lambda}z\Big)\mathrm{d}z = \delta_{n,m} \quad \text{with } n,m \in \mathbb{N} \tag{2.29}$$

A_n can be determined by multiplying both sides of eq. 2.28 with $\sin\big(n\frac{\pi}{\Lambda}z\big)$ and integrating over the length of the trap stack:

$$\int_0^{\Lambda} \Phi(z,R)\sin(k_n z)\mathrm{d}z = \frac{\Lambda}{2} I_0(k_n R) A_n. \tag{2.30}$$

Figure 2.4 shows a cross-section through the electrodes of the BASE precision trap as well as the electrical potential on the trap axis close to the typical working point.
The potential $\Phi(z,R)$ on the trap radius is given by the voltages V_i applied to the N individual electrodes and interpolated linearly in the gaps between electrodes. If $z_{i,s}$ and $z_{i,e}$ denote the start and end coordinates of the i-th electrode respectively, the integral over the boundary can be split it into multiple integrals over the N electrodes and $N-1$ gaps:

$$\int_0^{\Lambda} \Phi(z,R)\sin(k_n z)\mathrm{d}z = \underbrace{\sum_{i=1}^{N} V_i \int_{z_{i,s}}^{z_{i,e}} \sin(k_n z)\mathrm{d}z}_{\text{Electrodes}} + \underbrace{\sum_{i=1}^{N-1}\int_{z_{i,e}}^{z_{i+1,s}} \left[V_i + \frac{V_{i+1}-V_i}{z_{i+1,s}-z_{i,e}}(z-z_{i,e})\right]\sin(k_n z)\mathrm{d}z}_{\text{Gaps}}. \tag{2.31}$$

By shifting $z \to z + \frac{\Lambda}{2}$ the trap center is located at $z = 0$ and the potential is given by:

$$\begin{aligned}\Phi(z,\rho) =& \frac{2}{\Lambda}\sum_{n=1}^{\infty}\left[\left(\frac{V_1\cos(k_n z_{1,s}) - V_N\cos(k_n\Lambda)}{k_n} + \sum_{i=1}^{N-1}\frac{V_{i+1}-V_i}{z_{i+1,s}-z_{i,e}}\frac{\sin(k_n z_{i+1,s}) - \sin(k_n z_{i,e})}{k_n^2}\right)\right. \\ &\left.\times\frac{I_0(k_n\rho)}{I_0(k_n R)}\sin\left(k_n(z+\frac{\Lambda}{2})\right)\right].\end{aligned} \tag{2.32}$$

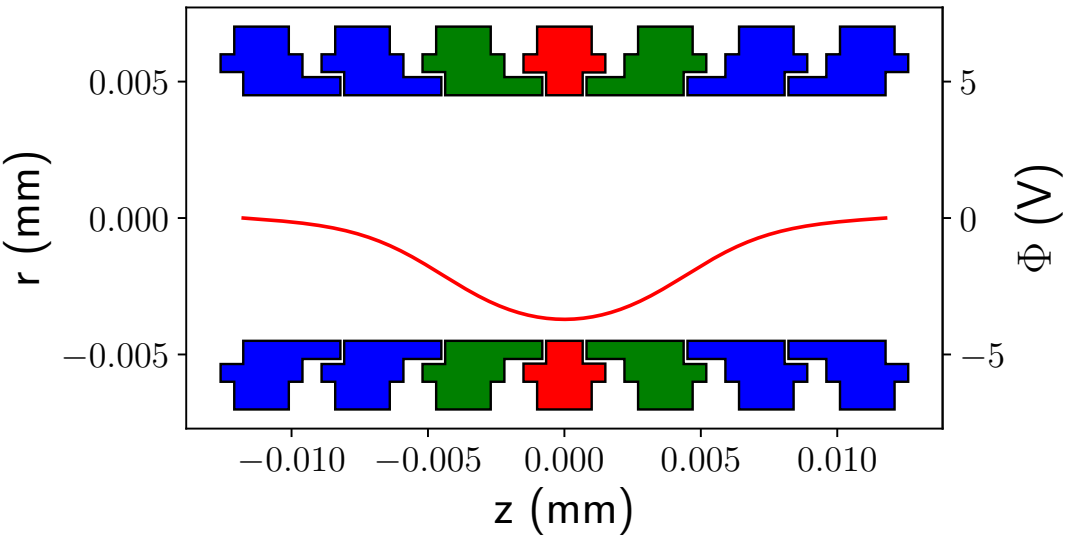

Figure 2.4: Schematic cross-section of the BASE precision trap. The trap consists of multiple cylindrical electrodes. During precision measurements the endcaps (blue) are grounded. Applying a negative voltage V_{R} to the ring electrode (red) traps positively charged particles in the trap center. The voltage $V_{\mathrm{C}} = \mathrm{TR} \cdot V_{\mathrm{R}}$ applied to the correction electrodes (green) causes higher order components in the expansion of the electrical potential around the trap center to vanish. The red line shows the axial potential for parameters close to the typical operating point ($V_{\mathrm{R}} = -4.76\,\mathrm{V}$ and $\mathrm{TR} = 0.883$).

All traps in the BASE experiment are 5-electrode traps ($N = 5$) with constant distance d between electrodes and are typically operated with grounded endcaps ($V_1 = V_5 = 0$). In order to determine the influence of the voltage $V_3 = V_\mathrm{R}$ applied to the ring electrode and $V_2 = V_4 = V_\mathrm{C}$ applied to the correction electrodes, eq. 2.32 is expanded in of powers of z^p around the trap center. By introducing the dimensionless tuning ratio (TR)

$$\mathrm{TR} = \frac{V_C}{V_R} \tag{2.33}$$

the potential can be expressed in terms of the ring voltage V_R and the coefficients $C_j = E_j + \mathrm{TR}D_j$:

$$\begin{array}{rrcccccccl} & \Phi_\mathrm{R}(z) & = & (E_2 z^2 & + & E_4 z^4 & + & E_6 z^6 & + & O(z^8)) \quad V_R \\ + & \Phi_\mathrm{C}(z) & = & (D_2 z^2 & + & D_4 z^4 & + & D_6 z^6 & + & O(z^8)) \quad V_R \cdot \mathrm{TR} \\ \hline = & \Phi(z) & = & (C_2 z^2 & + & C_4 z^4 & + & C_6 z^6 & + & O(z^8)) \quad V_R \end{array} \tag{2.34}$$

In the case of constant distance d between electrodes and grounded endcaps ($V_1 = V_5 = 0$) the coefficients on the trap axis ($\rho = 0$) are given by

$$\begin{aligned} E_j =& \frac{2}{\Lambda} \sum_{n=1}^{\infty} \left[\frac{\sin(k_n z_{3,s}) - \sin(k_n z_{2,e})}{k_n^2 d} \right. \\ & \left. \times \frac{1}{I_0(k_n R)} \frac{k_n^j}{j!} \sin\left(\frac{\pi}{2}(n+j)\right) \right] \end{aligned} \tag{2.35}$$

$$\begin{aligned} D_j =& \frac{2}{\Lambda} \sum_{n=1}^{\infty} \left[\frac{\sin(k_n z_{2,s}) - \sin(k_n z_{1,e}) + \sin(k_n z_{4,s}) - \sin(k_n z_{3,e})}{k_n^2 d} \right. \\ & \left. \times \frac{1}{I_0(k_n R)} \frac{k_n^j}{j!} \sin\left(\frac{\pi}{2}(n+j)\right) \right] \end{aligned} \tag{2.36}$$

$$\begin{aligned} C_j =& \frac{2}{\Lambda} \sum_{n=1}^{\infty} \left[\frac{\sin(k_n z_{3,s}) - \sin(k_n z_{2,e}) + \mathrm{TR}\left[\sin(k_n z_{2,s}) - \sin(k_n z_{1,e}) + \sin(k_n z_{4,s}) - \sin(k_n z_{3,e})\right]}{k_n^2 d} \right. \\ & \left. \times \frac{1}{I_0(k_n R)} \frac{k_n^j}{j!} \sin\left(\frac{\pi}{2}(n+j)\right) \right]. \end{aligned} \tag{2.37}$$

The coefficients E_j and D_j depend solely on the trap geometry and describe how the axial potential changes with the voltages applied to the ring and correction electrodes. The coefficients C_j depend on the trap geometry as well as the tuning ratio and determine the axial frequency as well as the magnitude of systematic shifts. To first order the axial frequency depends only

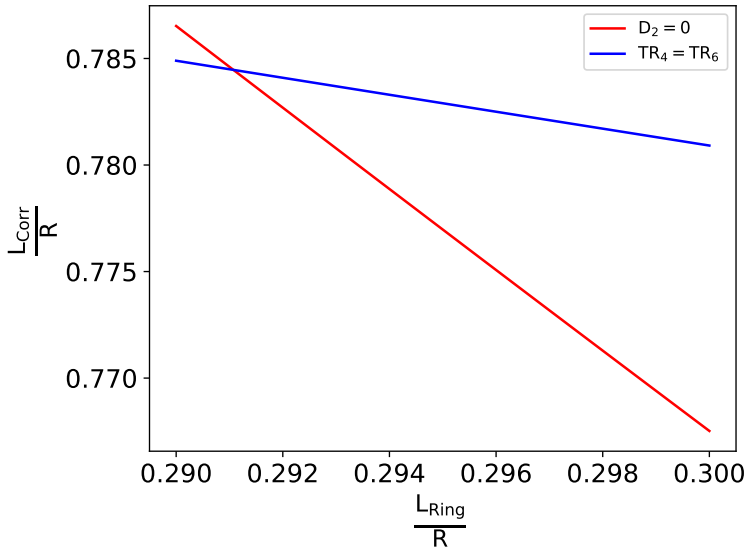

Figure 2.5: Red: Electrode length to trap radius ratios that produce an orthogonal trap ($D_2 = 0$). Blue: Electrode length to trap radius ratios that produce an orthogonal trap ($\mathrm{TR}_4 = \mathrm{TR}_6$). In case the ratio between the electrode distance d and the trap radius R is $\frac{d}{R} = \frac{140\,\mu\mathrm{m}}{4.5\,\mathrm{mm}} \approx 0.031$, the trap is orthogonal and compensated if $\frac{L_R}{R} = 0.291$ and $\frac{L_C}{R} = 0.784$ are chosen. In this case, the tuning ratio is approximately $\mathrm{TR} = 0.881$

.

on $C_2 = E_2 + \mathrm{TR} \cdot D_2$. For experimental purposes, it is desirable that the axial frequency is independent of the tuning ratio. This property is called orthogonality and corresponds to $D_2 = 0$. In order to suppress systematic shifts due to the axial energy of the trapped particle, higher order coefficients ($C_2, C_6, \dots$) should be as close to zero as possible. By choosing a tuning ratio $TR_j = -\frac{E_j}{D_j}$, the coefficient C_j can be tuned to 0. A trap is called compensated if $TR_4 = TR_6$ and thus C_4 and C_6 can be tuned to 0 for one simultaneous tuning ratio.
In order to design a trap that is both orthogonal and compensated, the length of the ring electrode L_R and the length of the correction electrodes L_C have to be chosen accordingly. Figure 2.5 shows the ratios $\frac{L_R}{R}$ and $\frac{L_C}{R}$ at which a 5-pole trap with grounded endcaps is orthogonal or compensated for $\frac{d}{R} = \frac{140\,\mu\mathrm{m}}{4.5\,\mathrm{mm}}$. Note that these ratios change with the ratio $\frac{d}{R}$ between the inter-electrode distance d and the trap radius R. In the case of $R = 4.5\,\mathrm{mm}$ and $d = 140\,\mu\mathrm{m}$ the trap is orthogonal and compensated for $L_R = 1.31\,\mathrm{mm}$ and $L_C = 3.53\,\mathrm{mm}$. The optimal tuning ratio in this case is $\mathrm{TR} \approx 0.881$.

2.3 Systematic shifts

Even though great care is taken in the design of the BASE Penning traps, patch potentials and manufacturing tolerances can cause higher power coefficients to appear in the expansion of the axial electric potential described by Eq. (2.34). Under normal experimental conditions, uneven coefficients $C_{2n-1}, n \in \mathbb{N}$ are strongly suppressed due to the symmetry of the trap. Presence of higher order contributions to the axial potential or the magnetic field cause the particle's eigenfrequencies to shift with the energies of the individual eigenmodes. Calculations of these systematic shifts are for example given by [82] and [86] and the relevant results are presented here. Note that [82] and [86] use dimensionless coefficients $\mathcal{C}_j$ in the expansion of the axial potential

$$\Phi(z) = \sum_{j=0}^{\infty} \frac{\mathcal{C}_j}{2d^j} z^j = \sum_{j=0}^{\infty} C_j z^j \tag{2.38}$$

and thus the results need to be translated to the C_j coefficients according to

$$C_j = \frac{\mathcal{C}_j}{2d^j}. \tag{2.39}$$

Additionally, it is convenient to treat the systematic shifts as a function of the energies in the different eigenmodes rather than the radii. The relative shifts of the eigenfrequencies caused by higher order contributions of the electrostatic potential are given by:

$$\begin{pmatrix} \frac{\Delta\omega_+}{\omega_+} \\ \frac{\Delta\omega_z}{\omega_z} \\ \frac{\Delta\omega_-}{\omega_-} \\ \frac{\Delta\omega_L}{\omega_L} \end{pmatrix} = M_{C_4} \begin{pmatrix} E_+ \\ E_z \\ E_- \end{pmatrix} + M_{C_6} \begin{pmatrix} E_+^2 \\ E_z^2 \\ E_-^2 \\ E_+E_z \\ E_+E_- \\ E_zE_- \end{pmatrix} + O(C_8). \tag{2.40}$$

Introducing $\Omega = \frac{\omega_z}{\omega_+}$, approximating $\omega_c = \omega_+ + \omega_- \approx \omega_+$ and using Eqs. (2.18 - 2.20), the corresponding matrices are given by:

$$M_{C_4} = \frac{1}{qV_0}\frac{C_4}{C_2^2}\begin{pmatrix} \frac{3}{4}\Omega^4 & -\frac{3}{2}\Omega^2 & -3\Omega^2 \\ -\frac{3}{2}\Omega^2 & \frac{3}{4} & 3 \\ -3\Omega^2 & 3 & 3 \\ 0 & 0 & 0 \end{pmatrix}, \tag{2.41}$$

$$M_{C_6} = \frac{1}{q^2V_0^2}\frac{C_6}{C_2^3}\begin{pmatrix} -\frac{15}{16}\Omega^6 & -\frac{45}{16}\Omega^2 & -\frac{45}{4}\Omega^2 & \frac{45}{8}\Omega^4 & -\frac{45}{4}\Omega^4 & -\frac{45}{2}\Omega^2 \\ \frac{45}{16}\Omega^4 & \frac{15}{16} & \frac{45}{4} & -\frac{45}{8}\Omega^2 & -\frac{45}{2}\Omega^2 & \frac{45}{4} \\ \frac{45}{8}\Omega^4 & \frac{45}{8} & \frac{15}{2} & -\frac{45}{2}\Omega^2 & -\frac{45}{2}\Omega^2 & \frac{45}{2} \\ 0 & 0 & 0 & 0 & 0 & 0 \end{pmatrix}. \tag{2.42}$$

Note that the Larmor frequency is not shifted by electrostatic inhomogeneities.

Magnetic inhomogeneities can be treated equivalently to the electrostatic imperfections by expanding the axial magnetic field as

$$B(z) = \sum\nolimits_{j=0}^{\infty} B_j z^j. \tag{2.43}$$

The magnetic inhomogeneities cause the strength of the magnetic field to change in the radial direction and thus the magnetic field experienced by the particle depends on its radial energies. In addition, the interaction of the magnetic moment associated with the trajectory of the trapped particle and the magnetic field inhomogeneities creates an additional force in the axial direction which changes the axial frequency. The shifts of the individual eigenfrequencies are given by

$$\begin{pmatrix} \frac{\Delta\omega_+}{\omega_+} \\ \frac{\Delta\omega_z}{\omega_z} \\ \frac{\Delta\omega_-}{\omega_-} \\ \frac{\Delta\omega_L}{\omega_L} \end{pmatrix} = M_{B_2}\begin{pmatrix} E_+ \\ E_z \\ E_- \end{pmatrix} + M_{B_4}\begin{pmatrix} E_+^2 \\ E_z^2 \\ E_-^2 \\ E_+E_z \\ E_+E_- \\ E_zE_- \end{pmatrix} + O(B_6) \tag{2.44}$$

with the matrices

$$M_{B_2} = \frac{1}{m\omega_z^2}\frac{B_2}{B_0}\begin{pmatrix} -\Omega^2 & 1 & 2 \\ 1 & 0 & -1 \\ 2 & -1 & -2 \\ -\Omega^2 & 1 & 2 \end{pmatrix} \tag{2.45}$$

$$\text{and } M_{B_4} = \frac{3}{2}\frac{B_4}{B_0}\frac{1}{m^2\omega_z^4}\begin{pmatrix} \Omega^4 & \Omega^4 & 4\Omega^4 & -4\Omega^2 & -8\Omega^2 & 8\Omega^4 \\ -2\Omega^2 & 0 & -8 & 2 & 8 & -8 \\ 4\Omega^2 & 1 & 4 & -8 & -8 & 8 \\ \Omega^4 & \Omega^4 & 4\Omega^4 & -4\Omega^2 & -8\Omega^2 & 8\Omega^4 \end{pmatrix}. \tag{2.46}$$

Note that the relative shift of the Larmor frequency is equal to the relative shift of the modified cyclotron frequency.
In case the gradient B_1 of the magnetic field does not vanish at the position of the particle, the magnetic moments associated with the magnetron and cyclotron motions create an additional force that shifts the particle along the trap axis. These shifts are calculated in [87] and can be written as

$$\begin{pmatrix} \frac{\Delta\omega_+}{\omega_+} \\ \frac{\Delta\omega_z}{\omega_z} \\ \frac{\Delta\omega_-}{\omega_-} \\ \frac{\Delta\omega_L}{\omega_L} \end{pmatrix} = M_{B_1}\begin{pmatrix} E_+ \\ E_z \\ E_- \end{pmatrix} \tag{2.47}$$

with

$$M_{B_1} = \frac{1}{m\omega_z^2}\frac{B_1^2}{B_0^2}\begin{pmatrix} -1 & 0 & 1 \\ 0 & 0 & 0 \\ 0 & 0 & 0 \\ -1 & 0 & 1 \end{pmatrix}. \tag{2.48}$$

Even in case no electrostatic or magnetic inhomogeneities are present at all, relativistic corrections lead to shifts of the characteristic frequencies which are once again given by

$$\begin{pmatrix} \frac{\Delta\omega_+}{\omega_+} \\ \frac{\Delta\omega_z}{\omega_z} \\ \frac{\Delta\omega_-}{\omega_-} \\ \frac{\Delta\omega_L}{\omega_L} \end{pmatrix} = M_R\begin{pmatrix} E_+ \\ E_z \\ E_- \end{pmatrix} \tag{2.49}$$

with

$$M_R = -\frac{1}{mc^2}\begin{pmatrix} 1 & \frac{1}{2} & -\Omega^2 \\ \frac{1}{2} & \frac{3}{8} & -\frac{1}{4}\Omega^2 \\ -\Omega^2 & -\frac{1}{4}\Omega^2 & \frac{1}{4}\Omega^2 \\ \frac{2}{9} & \frac{1}{2} & -\Omega^2 \end{pmatrix}. \tag{2.50}$$

Under typical conditions, C_4 and C_6 can be tuned close to 0, such that the related shifts are small. Therefore, the main concerns regarding systematic shifts are caused by inhomogeneities of the magnetic field. In order to overcome the limitations these shifts impose on the precision with which the frequencies can be measured, one of the following measures needs to be taken:

- All measurements need to be carried out with particles that have similar energies in their eigenmodes.
- The energies of the individual eigenmodes have to be determined for each measurement and the related shifts have to be corrected.
- The size of the systematic shifts has to be decreased by decreasing the inhomogeneous components of the magnetic field.

Chapters 3.4 and 3.5 give a more detailed overview of the main systematic uncertainties in past measurements of the antiproton charge-to-mass ratio [69] and the antiproton g-factor [88]. This work covers the implementation of a magnetic shimming and shielding system that provides the possibility to tune B_2 in the precision trap close to 0 which eliminates the main systematic uncertainty in the measurement of the g-factor.

2.4 Asymmetric potential contributions

While the influence of higher order coefficients C_j in the expansion of the electrostatic potential $\Phi(z) = \sum_{j=0}^{\infty} C_j z^j$ has been studied in detail [82, 86] for even coefficients, the odd coefficients are often neglected as they are close to 0 if the particle is located in the center of the trap. The process of determining the electrostatic center of the trap is called asymmetry compensation and is described in sections 5.5 and 7.2 of this thesis work. In this chapter, the systematic shifts that arise in case the particle is not tuned to the center of the trap are discussed. Under the assumption, that the trap has perfect axial symmetry, changing the ring voltage V_0 or tuning ratio TR will not move the particle along the axial direction. In order to shift the location of the potential minimum, an asymmetric voltage has to be applied to the correction electrodes.

Similarly to the tuning ratio TR, which describes the fraction of the ring voltage which is applied to the correction electrodes, the offset ratio OR describing the difference between the voltages $V_{Corr,left}$ and $V_{Corr,right}$ on the correction electrodes. Instead of describing the potential using the voltages V_0, $V_{Corr,left}$ and $V_{Corr,right}$, the potential is characterized by the following parameters:

$$\text{Ring voltage} : V_0 \tag{2.51}$$

$$\text{Tuning ratio} : \text{TR} = \frac{\frac{V_{Corr,right}+V_{Corr,left}}{2}}{V_0} \tag{2.52}$$

$$\text{Offset ratio} : \text{OR} = \frac{V_{Corr,right} - V_{Corr,left}}{V_0}. \tag{2.53}$$

Thus, the TR is given by the mean voltage on the correction electrodes, while the OR depends on the difference between the correction electrode voltages. The overall potential is fully described by V_0, TR and OR and is given by:

$$\begin{array}{rrcccccccl} & \Phi_{\mathrm{R}}(z) & = & (E_0 + E_1 z^1 & + & E_2 z^2 & + & E_3 z^3 & + & O(z^4)) \quad V_0 \\ + & \Phi_{\mathrm{C}}(z) & = & (D_0 + D_1 z^1 & + & D_2 z^2 & + & D_3 z^3 & + & O(z^4)) \quad V_0 \cdot \mathrm{TR} \\ + & \Phi_{\mathrm{F}}(z) & = & (F_0 + F_1 z^1 & + & F_2 z^2 & + & F_3 z^3 & + & O(z^4)) \quad V_0 \cdot \mathrm{OR} \\ \hline = & \Phi(z) & = & (C_0 + C_1 z^1 & + & C_2 z^2 & + & C_3 z^3 & + & O(z^4)) \quad V_0 \end{array}. \tag{2.54}$$

Due to the symmetry of the trap electrodes, all odd coefficients E_j and D_j as well as the even coefficients F_j vanish in the trap center, however, once the particle is shifted out of the center this is no longer the case.

In order to determine the tuning ratio TR and offset ratio OR which are required to shift the particle by a distance z_{min} out of the trap center, the coefficients $E_j(z_{min})$, $D_j(z_{min})$ and $F_j(z_{min})$ are determined by expanding Eq. (2.32) around z_{min}. Figures 2.6a - 2.6d show $E_j(z_{min})$, $D_j(z_{min})$ and $F_j(z_{min})$ up to 4th order.

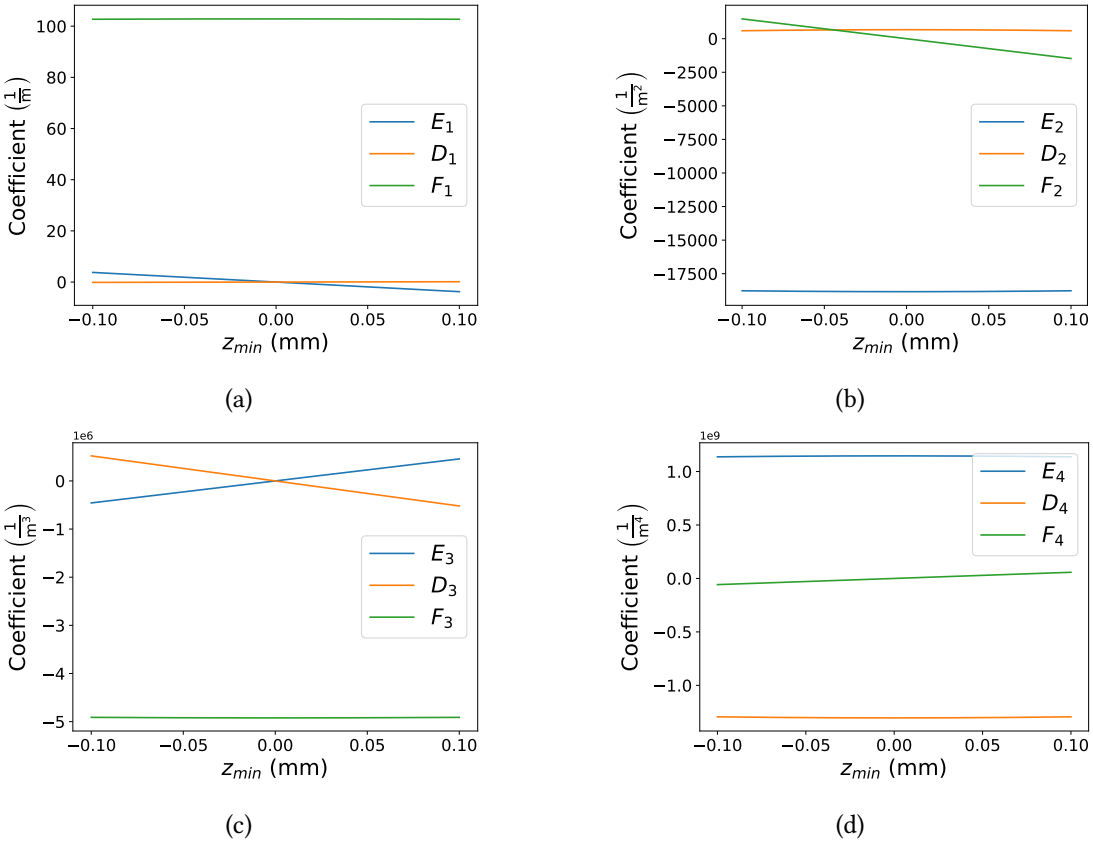

Figure 2.6: Potential coefficients $E_j(z_{min})$, $D_j(z_{min})$ and $F_j(z_{min})$ up to fourth order. In the trap center ($z_{min} = 0$) the odd coefficients E_j, D_j as well as the even coefficients F_j vanish.

Given the symmetry of the trap electrodes, the odd E_j, D_j coefficients as well as the even F_j coefficients are suppressed. As the coefficients change slowly with z_{min}, a first approximation for the location z_{min} of the potential minimum can be given by using the coefficients in the trap center. Given that the orthogonal design of the BASE traps, D_2 is small compared to E_2 and C_2 is approximately independent of the tuning ratio:

$$z_{min} \approx -\frac{C_1}{2C_2} \approx -\frac{F_1}{2E_2} \times \mathrm{OR} = 2.73\,\mathrm{mm} \times \mathrm{OR}. \tag{2.55}$$

In order to determine the exact TR and OR that shift the particle by z_{min}, the first derivative of the potential needs to vanish at z_{min} which corresponds to $C_1(z_{min}) = 0$. We thus require:

$$C_1(z_{min}) = E_1(z_{min}) + D_1(z_{min}) \times \mathrm{TR} + F_1(z_{min}) \times \mathrm{OR} = 0. \tag{2.56}$$

Given that we have two free parameters in TR and OR, we can additionally force C_4 to vanish:

$$C_4(z_{min}) = E_4(z_{min}) + D_4(z_{min}) \times \mathrm{TR} + F_4(z_{min}) \times \mathrm{OR} = 0. \tag{2.57}$$

We denote the combination of TR and OR which causes C_4 to vanish as TR_4 and OR_4. Solving the system of linear equations results in:

$$\mathrm{TR}_4(z_{min}) = -\frac{F_1(z_{min})E_4(z_{min}) - E_1(z_{min})F_4(z_{min})}{F_1(z_{min})D_4(z_{min}) - D_1(z_{min})F_4(z_{min})} \tag{2.58}$$

$$\mathrm{OR}_4(z_{min}) = -\frac{E_1(z_{min}) + D_1(z_{min}) \times \mathrm{TR}_4(z_{min})}{F_1(z_{min})}. \tag{2.59}$$

Figures 2.7a and 2.7b show the required TR_4 and OR_4 as a function of the desired offset z_{min}.

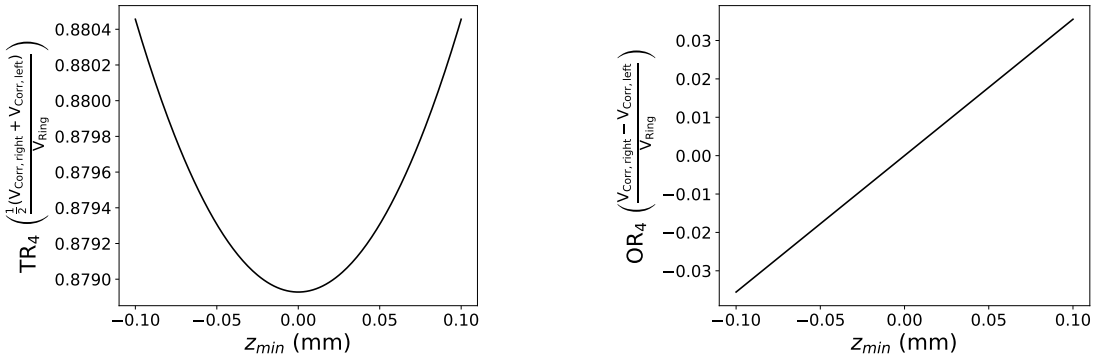

(a) (b)

Figure 2.7: Tuning ratio (left) and offset ratio (right) required to shift the particle by z_{min} out of the trap center if C_4 is tuned to 0 at the location of the potential minimum. The required offset ratio scales approximately linearly with the desired offset z_{min}.

The asymmetric voltage required to move the particle out of the trap center causes odd coefficients $C_3, C_5, ...$ to appear in the expansion of the potential around the location of the new minimum z_{min}, which cause additional shifts of the eigenfrequencies with the trapped particle's eigenenergies. Due to the axial anharmonicity C_3 of the axial potential, the axial frequency ω_z shifts with the axial energy E_z. This shift is for example given in [89] and [90] and, translated to the C_j parameters used in the BASE experiment, yields:

$$\frac{\Delta\omega_z}{\omega_z} = -\frac{1}{qV_0}\frac{15}{16}\frac{C_3^2}{C_2^3}E_z = -\frac{1}{m\omega_z^2}\frac{15}{8}\frac{C_3^2}{C_2^2}E_z. \tag{2.60}$$

Note that the systematic shift related to C_3 always leads to a reduction in axial frequency with

increasing axial energy E_z and does not depend on the sign of C_3 which is to be expected as the asymmetric potential always pulls the particle into the direction of less curvature.
Additionally, given that the potential is asymmetric, the particle's oscillation is no longer symmetric around the potential minimum z_{min}, but the mean position $\bar{z}$ depends on C_3 as well as the axial energy. The shift $\Delta z = \bar{z} - z_{min}$ is given in [90] and translated into the BASE parameter convention results in:

$$\Delta z = \bar{z} - z_{min} = -\frac{1}{m\omega_z^2}\frac{3}{2}\frac{C_3}{C_2}E_z. \tag{2.61}$$

This shift leads to a change in the modified cyclotron frequency ω_+ as a function of the axial energy E_z which is given by:

$$\frac{\Delta\omega_+}{\omega_+} = \frac{B_1\Delta z}{B_0} = -\frac{1}{m\omega_z^2}\frac{3}{2}\frac{C_3}{C_2}\frac{B_1}{B_0}E_z. \tag{2.62}$$

In order to verify the magnitude of these shifts, numerical simulation were conducted in Python. The potential was extended by a C_3 term, the equation of motion was transformed into of a proton in the potential was solved by numerical integration. Figures 2.8a - 2.8d show the simulated scaling of the axial frequency and mean location shift for different parameters C_3 and axial temperatures T_z. The frequency and position shifts determined from numerical simulations agree well with theory.

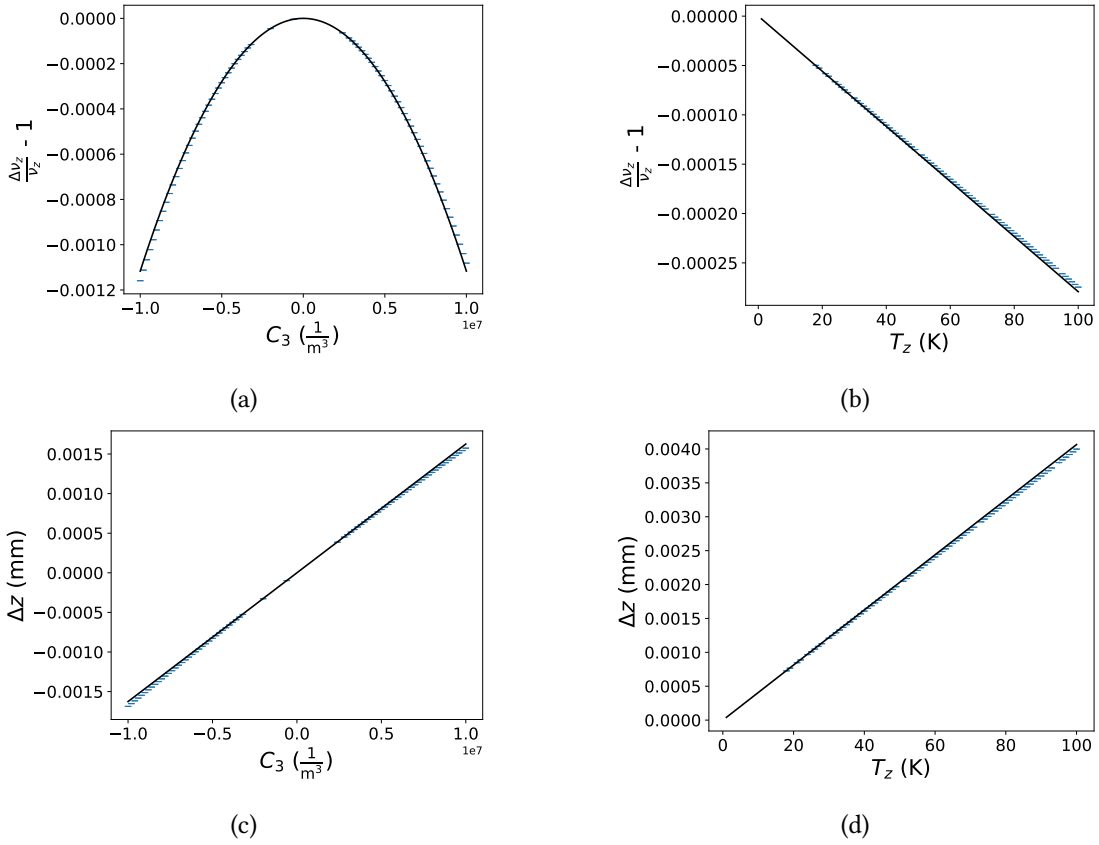

Figure 2.8: Relative shift $\frac{\Delta\nu_z}{\nu_z}$ of the axial frequency and mean position Δz for different anharmonicities C_3 and axial temperatures T_z. The blue points show the result of numerical simulations whereas the black lines show the theoretic predictions according to Eqs. (2.60) and (2.61).

In addition to the axial component, C_3 also changes the radial component of the potential. Given that the potential hast to satisfy Laplace's equation, the redial component of the anharmonicity $\Phi_3(z, \rho)$ created by C_3 is fully determined by C_3 and is given by:

$$\Phi_3(z, \rho) = V_0 C_3 \left(z^3 - \frac{3}{2}\rho^2 z \right). \tag{2.63}$$

The potential also depends on the radial position ρ of the particle, which changes with the radial energies E_+ and E_-. The radial term creates an additional force in the axial direction which depends in the radius ρ. Thus, a change in radius shifts the position of the particle in the magnetic field gradient B_1, until the additional force is balanced by the force μB_1 due to the magnetic moment associated with the radial motion. Given that the radial magnetic moment is dominated by the cyclotron motion, this shift is dominated by the cyclotron energy E_+ and

leads to a shift of the axial frequency ω_z given by:

$$\frac{\Delta\omega_z}{\omega_z} = \frac{3}{2}\frac{1}{m\omega_z^2}\frac{C_3}{C_2}\frac{B_1}{B_0}E_+. \tag{2.64}$$

Under typical experimental conditions, the particle is tuned to the center of the trap and C_3 vanishes. In this case the tuning ratio which maximizes the signal-to-noise ratio approximately corresponds to the conditions under which C_4 is tuned to 0. However, in the presence of the additional C_3 shift outlined in Eq. (2.60), the dependence of ω_z on the axial energy E_z is no longer minimized if $C_4 = 0$ but rather if the combined term vanishes:

$$\frac{3}{2}C_4C_2 - \frac{15}{8}C_3^2C_2^2 = 0. \tag{2.65}$$

In order to maximize the signal-to-noise ratio, the tuning ratio has to be chosen such, that

$$12C_4C_2 - 15C_3^2 = 0. \tag{2.66}$$

We denote the tuning- and offset ratios that maximize the signal-to-noise ratio as TR_3 and OR_3. For each shift z_{min}, the required combination of TR_3 and OR_3 can be determined by solving the following system of equations:

$$C_1(\mathrm{TR}_3, \mathrm{OR}_3) = 0 \tag{2.67}$$

$$12C_4(\mathrm{TR}_3, \mathrm{OR}_3)C_2(\mathrm{TR}_3, \mathrm{OR}_3) - 15C_3^2(\mathrm{TR}_3, \mathrm{OR}_3) = 0. \tag{2.68}$$

Inserting $\mathrm{OR}_3(z_{min}) = -\frac{E_1(z_{min})+D_1(z_{min})\mathrm{TR}_3}{F_1(z_{min})}$ leads to a quadratic equation in TR_3 which can be solved analytically. One of the solutions has to be rejected since it corresponds to conditions under which C_2 is strongly suppressed near the trap center. Figures 2.9a and 2.9b show the tuning and offset ratios TR_4 and OR_4, which correspond to $C_4 = 0$ as well as TR_3 and OR_3, which result in $12C_4C_2 - 15C_3^2 = 0$.

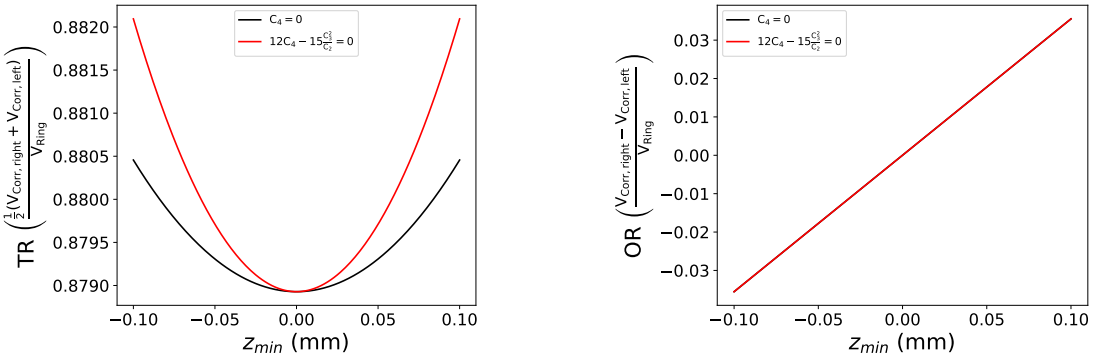

(a) (b)

Figure 2.9: Comparison between the tuning and offset ratios TR_4 and OR_4 which correspond to $C_4 = 0$ (black) as well as TR_3 and OR_3 which result in $12C_4C_2 - 15C_3^2 = 0$ (red). In both cases, the offset ratios are practically identical and change linearly with the desired offset z_{min}. The tuning ratio TR_3 which maximizes the signal-to-noise ratio shows stronger scaling with the offset compared to TR_3, which corresponds to $C_4 = 0$.

After a tuning ratio scan, the signal-to-noise ratio is maximized, which results in a residual C_4 term:

$$C_4(\mathrm{TR}_3) = \frac{5}{4}\frac{C_3^2}{C_2}. \tag{2.69}$$

Figures 2.10a - 2.10d show the scaling of C_2, C_3, C_4 and C_6 as a function of the particle position z_{min} in the trap. Given that C_2 shows no strong scaling with z_{min} and C_3 scales linearly, the residual C_4 scales approximately quadratically with z_{min}. It is therefore crucial to correct measurements conducted outside of the trap center for the residual C_4 and C_6 in addition to the C_3 shift outlined above.

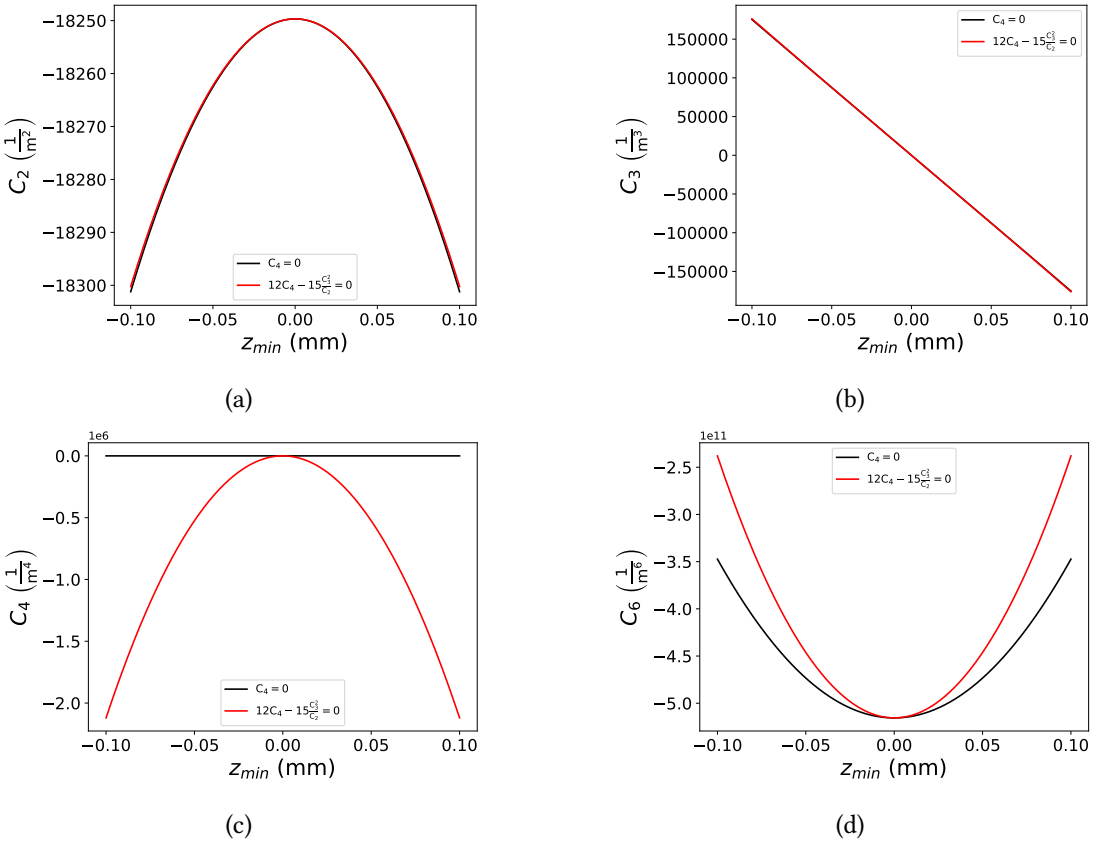

Figure 2.10: Scaling of the parameters C_2, C_3, C_4 and C_6 as a function of the particle position z_{min}. The black line shows the parameters if the tuning ration and offset ratio are chosen such that $C_4 = 0$, whereas the red line shows the conditions corresponding to maximum signal-to-noise ratio ($12C_4C_2 - 15C_3^2 = 0$). After the signal-to-noise ratio is maximized in a tuning ratio scan, the residual C_4 and C_6 terms lead to systematic shifts which have to be considered if measurements are conducted outside the trap center.

In order to determine the significance of the shifts outlined above in the context of charge-to-mass ratio and g-factor measurements, the shift of the free cyclotron frequency ν_c and Larmor frequency ν_L in the presence of a C_3 have to be studied. Given that the odd coefficients E_3 and D_3 are small, the strength of C_3 depends mainly on F_3 and the applied offset ratio OR. If the offset ratio OR is applied and the signal-to-noise ratio is maximized in a tuning ratio scan, C_4 and the residual C_4 are given by:

$$C_3 = F_3 \times \mathrm{OR} \tag{2.70}$$

$$C_4 = \frac{5}{4}\frac{C_3^2}{C_2} = \frac{5}{4}\frac{F_3^2}{C_2} \times \mathrm{OR}^2. \tag{2.71}$$

These parameters lead to a dependence of the cyclotron frequency ν_c and Larmor frequency ν_L on the particles eigenenergies. Given that the ratio R of charge-to-mass ratios is measured by measuring the ratio of free cyclotron frequencies in the same potential, R is only shifted if the individual cyclotron frequency measurements are conducted at different temperatures. Thus the shifts are strongly suppressed under experimental conditions. In contrast, given that the g-factor is determined by measuring the ratio of Larmor- and cyclotron frequencies, shifts of the cyclotron frequency do not cancel. Given that the Larmor frequency depends on the average magnetic field the particle experiences during the measurement, shifts due to the shift of the average position z_{min} cancel in case both particles are measured at the same eigenenergies. However, shifts of the free cyclotron frequency due to C_3 and the residual C_4 term cause the observed cyclotron frequency to deviate from the true cyclotron frequency which causes a systematic shift that has to be accounted for.

3 The BASE Experiment

3.1 The Antiproton decelerator

The Antiproton decelerator (AD) [52] is a particle decelerator located at CERN, that delivers low energy antiprotons to the connected experiments. It was built as a successor to the Antiproton Accumulator (AA) and the Antiproton Collector (AC) who formed the Antiproton Accumulator Complex (AAC) and provided particles to the Proton–Antiproton Collider ($\mathrm{Sp\bar{p}S}$) and the Low Energy Antiproton Ring (LEAR). In 1983, the UA1 and UA2 experiments located at the $\mathrm{Sp\bar{p}S}$ discovered the W and Z bosons [2, 3]. In contrast to the AA and the AC, the AD is able to decelerate antiprotons and distributes low-energy antiprotons to multiple experiments [56, 64, 70, 91–93]. Figure 3.1 provides an overview over the Antiproton decelerator facility.

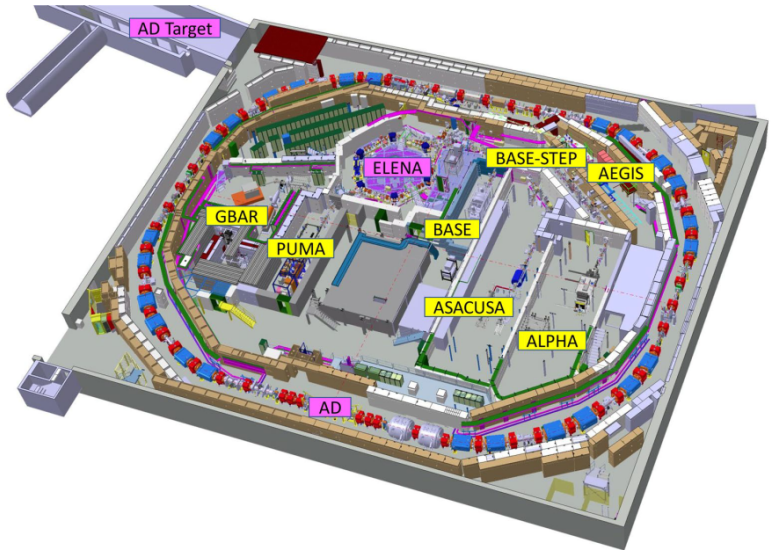

Figure 3.1: Overview of the Antiproton decelerator (AD) facility located at CERN. The AD (outer ring) provides initial deceleration from 3.5 GeV to 5.3 MeV. The smaller ELENA ring splits the beam received from the AD into 4 bunches, further decelerates the antiprotons to an energy of 100 keV and distributes the individual bunches to the experiments.

In order to create antiprotons, a bunch of approximately 10^{13} protons is accelerated to an energy of $26\,\mathrm{GeV}$ in CERN's Proton Synchrotron (PS). This bunch is focused on a water-cooled iridium rod and antiprotons are created by pair production. A magnetic horn focuses and injects the bunch of $3.5\,\mathrm{GeV}$ antiprotons into the AD. During the deceleration to an energy of $5.3\,\mathrm{MeV}$, the particles are cooled using stochastic cooling and electron cooling. After the deceleration cycle of around $120\,\mathrm{s}$ has finished, the bunch of approximately 3×10^7 antiprotons is ejected from the AD using fast kicker magnets.
Since 2021, the Extra Low Energy Antiproton (ELENA) ring provides a 2nd stage of deceleration [94]. Each bunch received from the AD is split into 4 smaller bunches of approximately 5×10^6 antiprotons which are decelerated further to an energy of $100\,\mathrm{keV}$. After the $13\,\mathrm{s}$ deceleration cycle, each bunch can be ejected to a different experiment which allows operation in parallel. Thanks to the reduced energy of the individual bunches, the more efficient degrader foils [95] can be used which results in a net increase of available protons due to higher trapping efficiency.

3.2 The BASE apparatus

3.2.1 Vacuum and superconducting magnet

The BASE zone is located in the center of the Antiproton decelerator hall. A superconducting magnet system consisting of one main solenoid and twelve shimming coils houses the cryogenic stage consisting of the Penning traps, detection circuits [96] and filters [93]. Two cryostats, each consisting of a combination of a liquid nitrogen ($\mathrm{LN_2}$) and liquid helium (LHe) vessel, are located on either side of the superconducting magnet and cool the cryogenic stage to temperatures close to $4\,\mathrm{K}$. This reduces noise on the electronic components, increases the vacuum inside the trap can as residual gas freezes out on the walls and enables the application of superconducting detection systems as well as the realization of the magnetic shimming and shielding system described in the thesis. Multiple beam monitors are located in the upstream side of the cryogenic stage and provide the possibility to steer the antiproton beam onto the degrader window [95]. Figure 3.2 shows a schematic of the experimental apparatus.

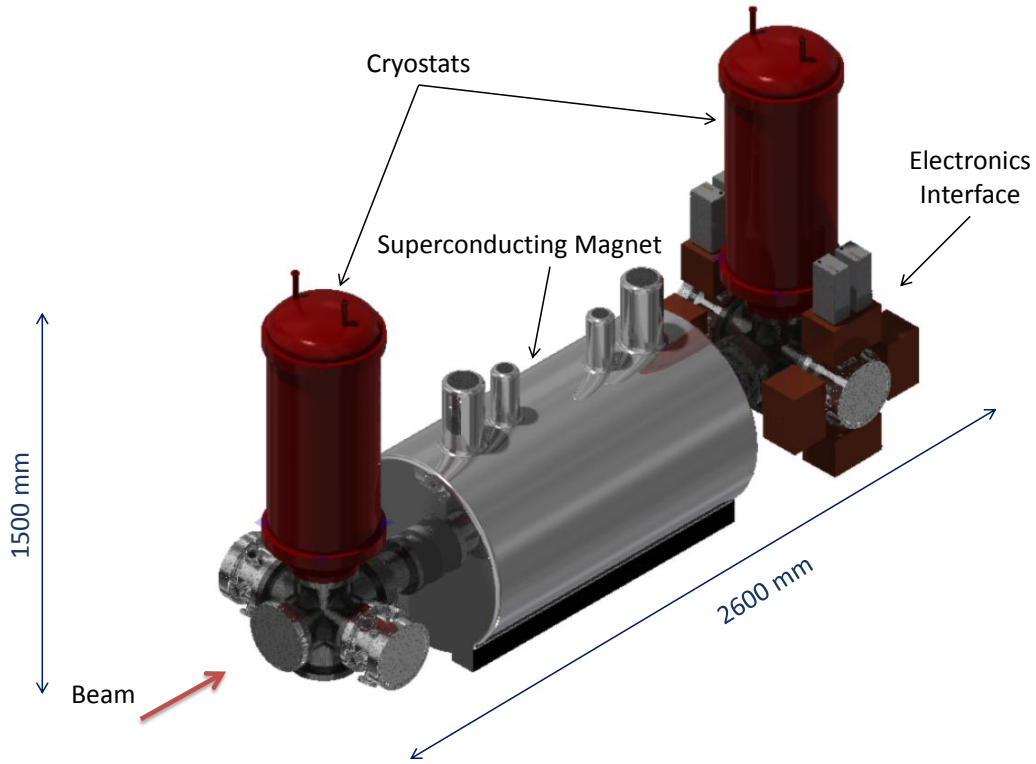

Figure 3.2: Drawing of the BASE apparatus. The Penning traps are located in the center of the superconducting magnet and connected to two cryostats, cooling the experiment to temperatures close to $4\,\mathrm{K}$. The experimental assembly is mounted in the magnet using Kevlar strings to decouple the trap stack vibrationally from the boiling cryoliquids.

The Penning traps as well as the most sensitive electronic components, including the precision trap cyclotron resonator, are located in a metal cylinder machined out of high purity oxygen free copper (OFHC). A thin degrader foil provides a vacuum-tight window that allows antiprotons to enter the trap can. After assembly of the trap stack, the trap can is pumped to a vacuum of typically around $5 \times 10^{-7}\,\mathrm{mbar}$ and the evacuated trap can is placed in the superconducting magnet. After cooling the experiment to cryogenic temperatures, the residual gas in the trap can freezes out on the walls which provides the excellent vacuum conditions on the order of $1 \times 10^{-18}\,\mathrm{mbar}$ [97] necessary to trap antiprotons for years [98]. In addition to the trap stack, the trap can contains an electron gun which provides the possibility to load electrons which, thanks to their high cyclotron frequency, lose energy via synchrotron radiation and provide sympathetic cooling during antiproton catching. Additionally, the electron gun is used to trap protons during commissioning measurement runs by ionizing hydrogen atoms frozen out on

the degrader window.

3.2.2 Trap stack

The BASE trap stack consists of four cylindrical Penning traps which each serve a dedicated purpose. Unless otherwise stated, all electrodes are manufactured out of high-purity oxygen-free copper (OFHC) and are coated with an inner layer of $7\,\mu\mathrm{m}$ of silver and an outer layer of $8\,\mu\mathrm{m}$ gold. In the course of this work, the trap stack was redesigned to provide larger spacial separation between the precision trap and the analysis trap which are described below. This reduces the influence of the strong magnetic bottle created by the ferromagnetic ring electrode of the analysis trap on the field gradients in the precision trap and reduces systematic shifts of the frequencies measured in the precision trap. Figures 3.3a and 3.3b show the old trap stack used in the 2017 g-factor campaign as well as the redesigned version currently in use. Compared to the 2017 version, the high-voltage electrodes were shrunk in order to provide the possibility to add additional electrodes between the precision trap and the analysis trap without increasing the total length of the trap stack. Overall, the redesign of the trap stack increased the distance between the precision trap and the analysis trap by $2.5\,\mathrm{cm}$, which reduces the effect of the analysis traps ferromagnetic ring electrode on the magnetic field in the center of the precision trap.

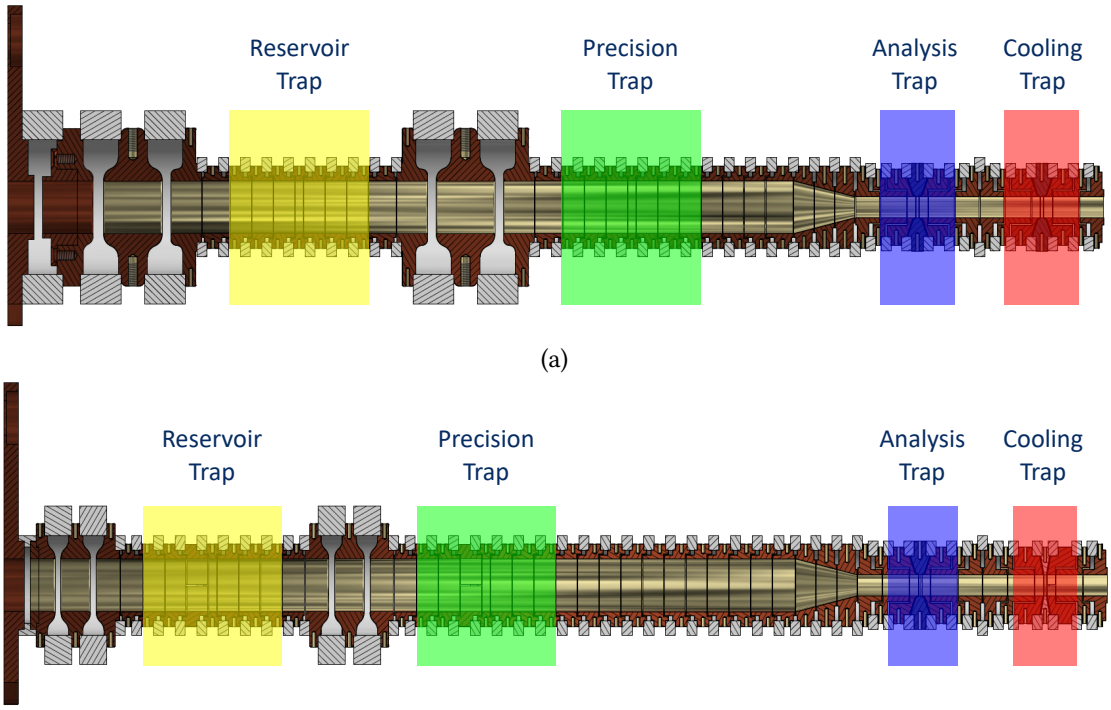

Figure 3.3: Comparison between the BASE Penning trap stack used in the 2017 g-factor run (top) and the modified trap stack currently in use (bottom). Compared to the 2017 configuration, the high-voltage electrodes were shrunk in order to add additional electrodes between the precision trap and the analysis trap. This decreases the influence of the ferromagnetic ring electrode of the analysis trap on the field gradients in the precision trap without increasing the total length of the trap stack.

In addition to the four Penning traps described below, the trap stack contains two sets of "high-voltage electrodes" called HV-Static (HVS) and HV-Pulse (HVP). In order to load antiprotons, electrons are trapped in the reservoir trap where they rapidly cool via synchrotron radiation. HV-Static, located downstream of the reservoir trap is charged to a high negative potential. Next, the antiproton bunch delivered by the AD in injected and HV-Pulse located upstream of the reservoir trap is switched to a high negative voltage. This traps the antiprotons between the high voltage electrodes where they cooled sympathetically via interaction with the trapped electrons.

Reservoir trap

The reservoir trap [98] is located between the two sets of high-voltage electrodes and is identical in design to the precision trap. It is used for catching and storing of antiprotons, protons and H^--ions for extended periods of time. In case the particle used to conduct experiments is lost,

a new particle can rapidly be extracted from the reservoir trap. Additionally, the reservoir of trapped antiprotons provides the possibility to conduct high-precision measurements outside the beamtime of the antiproton decelerator, which decreases magnetic field noise created by operation of the AD as well as the other experiments and makes high-precision measurements possible in the first place. During antiproton operation, a mixed cloud of antiprotons and H^--ions is trapped. The voltage supplies of the reservoir trap are backed up by batteries, which protect the system against power cuts. BASE has demonstrated the ability to trap antiprotons for more than $400\,\mathrm{d}$ in the past. The reservoir trap is equipped with an axial detector which provides the possibility to monitor and cool the cloud of antiprotons. Cooling of the radial modes is achieved via sideband coupling (see chapter 5.2.1).
Given the excellent vacuum conditions in the trap can, no loss of trapped antiprotons and protons due to collisions with rest gas have been observed so far. By continuously monitoring the reservoir of trapped antiprotons, a direct experimental lower limit on the lifetime $\tau_{\bar{p}}$ of the free antiproton can be given [97]. Using additional data acquired during the 2017 charge-to-mass-ratio campaign, the lower limit on the directly constrained antiproton lifetime was improved to $\tau_{\bar{p}} > 26.15$ years [99].

Precision trap

The precision trap is located downstream of the static high-voltage electrode and is used for the measurement of the particle's free cyclotron frequencies. The precision trap has an inner diameter of $9\,\mathrm{mm}$ and consists of a $1.34\,\mathrm{mm}$ long ring electrode and $3.56\,\mathrm{mm}$ long correction electrodes on either side. The lengths are chosen such that the trap is orthogonal and compensated in order to suppress systematics (see chapter 2.2).
In order to detect the axial frequency of a trapped particle, the precision trap is equipped with a tunable superconducting axial detector [96] with a resonance frequency of typically $650\,\mathrm{kHz}$ and quality factor on the order of $Q = 30\,000$. A varactor diode provides the possibility to change the parallel capacitance of the detector and thus detector can be tuned to match its frequency to the axial frequencies of antiprotons as well as H^--ions oscillating in the same electrostatic potential which suppresses systematic shifts during the measurement of the proton-to-antiproton charge-to-mass ratio (see chapter 3.4). In order to further suppress shifts created by inhomogeneities of the magnetic field, a superconducting shimming and shielding system was implemented in the course of this work (see chapters 4 and 6).
In addition to the axial detector, the precision trap is equipped with a tunable cyclotron detector which provides the possibility to observe a trapped particle's modified cyclotron frequency directly via resonant excitation [100]. The cyclotron detector is used to resistively cool the cyclotron temperature of trapped particles below the sideband-limit $T_{+,SB} = \frac{\nu_+}{\nu_z} T_z \approx 300\,\mathrm{K}$ (see section 3.3.2). Under typical conditions, the cyclotron detector has a cooling time constant

of approximately $90\,\mathrm{s}$, thus requiring cooling cycles of several minutes. Both detectors are equipped with a feedback loop as described in section 3.3.3 to further reduce their temperatures. Lastly, a spin flip coil provides the possibility to irradiate trapped particles with radio-frequencies close to the Larmor frequency in order to drive spin flips as described in chapter 3.5.

Analysis trap

The analysis trap is located downstream of the precision trap and is used to detect the spin state of trapped particles [101, 102]. It is a five-pole trap with an inner diameter of $3.6\,\mathrm{mm}$ and ring and correction electrodes of $0.4\,\mathrm{mm}$ and $1.4\,\mathrm{mm}$ length, respectively. In order to create the strong magnetic bottle necessary to couple the trapped particles spin state to it's axial frequency (see chapter 3.5), the ring electrode is manufactured out of VACOFLUX 50 [103] which deforms the magnetic field close to the center of the analysis trap and creates a magnetic bottle of approximately $B_{2,AT}272(22)\,\frac{\mathrm{kT}}{\mathrm{m}^2}$.

A feedback-cooled axial detector is used to determine the trapped particle's axial frequency. Due to the strong dependency of the axial frequency on the particle's cyclotron temperature, observation of the axial frequency is only possible, if the particle's cyclotron temperature does not change [104]. Therefore, the analysis trap is not equipped with a cyclotron detector as the particle's movement through the thermal Boltzmann distribution would cause the axial dip to vanish. For the same reason, measurement of the radial frequencies via sideband coupling is impossible.

In order to detect the radial frequencies, the analysis trap is equipped with a radial excitation coil that can be used to irradiate the particle until a change in axial frequency can be observed. In order to reduce noise driving cyclotron transitions, the radial excitation coil is bandpass filtered and grounded using cryogenic switches as long as no excitation is applied. An additional spin flip coil witch is filtered but not switched [105] is used to provide the high power necessary to drive spin state transitions in the analysis trap.

Cooling trap

In order to reduce cooling times and increase the sampling statistics, a dedicated cooling trap was implemented in the experiment. With an inner diameter of $3.6\,\mathrm{mm}$ a $0.42\,\mathrm{mm}$ long ring electrode and $1.38\,\mathrm{mm}$ long correction electrodes, the design of the cooling trap is nearly identical to the analysis trap. However, the cooling trap features only a slightly ferromagnetic ring electrode creating a weak magnetic bottle of $B_{2,CT} = 42\,\frac{\mathrm{kT}}{\mathrm{m}^2}$.

In addition to an axial detector, the cooling trap features a tunable cyclotron detector which can be used to resistively cool the trapped particles cyclotron motion. The cyclotron temperature couples to the axial frequency via the weak magnetic bottle and can be observed in real time. Once the particle is cold, the cyclotron detector is detuned and the particle's random walk through the thermal distribution stops. By cooling and observing the particle's cyclotron

temperature in the same trap, it is no longer necessary to shuttle the particle between the precision trap and the analysis trap which leads to faster cooling cycles. Additionally, the cyclotron detector in the cooling trap has a lower temperature, higher Q-factor and – given the smaller trap radius – couples stronger to the particle. Considering all these improvements, it is estimated that the thermalization time is on the order to seconds instead of minutes and a particle with a cyclotron temperature cold enough for single spin flip detection can be prepared within minutes compared to multiple hours which are required when the particle is thermalized on the PT cyclotron resonator.

3.3 Frequency measurements

High-precision frequency measurements build the basis for charge-to-mass-ratio and g-factor measurements in Penning traps. Given the effort that is necessary to prepare a single particle in the trap stack and the number of measurement cycles required to accumulate enough statistics, it is absolutely crucial to measure the particle's eigenfrequencies non-destructively.

3.3.1 Axial frequency measurements

A particle of mass m and charge q, oscillating with axial frequency $\nu_p = \frac{1}{2\pi^2}\sqrt{2\frac{q}{m}C_2V_0}$, can be modeled as a series LC-circuit oscillating at $\nu_p = \frac{1}{2\pi\sqrt{l_p c_p}}$ using the particle's equivalent capacitance $c_p = \frac{1}{\omega_p^2}\frac{q^2}{D^2}$ and its equivalent inductance $l_p = \frac{mD^2}{q^2}$ [106]. The effective electrode distance D depends on the design of the trap electrodes and the signal pickup [107]. The impedance $Z_p(\nu)$ of the particle's equivalent series LC-circuit vanishes at the particle's resonance frequency. By connecting a high-Q parallel RCL-detector [96] with impedance $Z_d(\nu)$ in parallel, the particle's axial frequency can be determined by measuring the Nyquist-Johnson noise over the combined system's impedance $Z(\nu)$. Figure 3.4a shows the particle trap with the connected detection system. Using the Boltzman constant k_B and the temperature T of the detection circuit, the thermal voltage noise density e_p produced by the impedance $Z(\nu)$ can be calculated as

$$e_p(\nu) = \sqrt{4k_B T\,\mathrm{Re}(Z(\nu))}. \tag{3.1}$$

The shape of the noise density spectrum is fully determined by the real part $\mathrm{Re}(Z(\nu))$ of the impedance [108], which provides a way to measure the trapped particle's axial frequency non-destructively and in thermal equilibrium with the detection circuit.

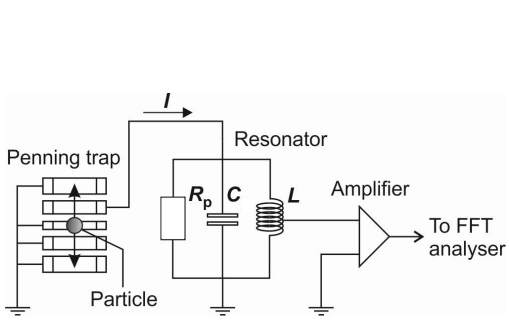

(a)

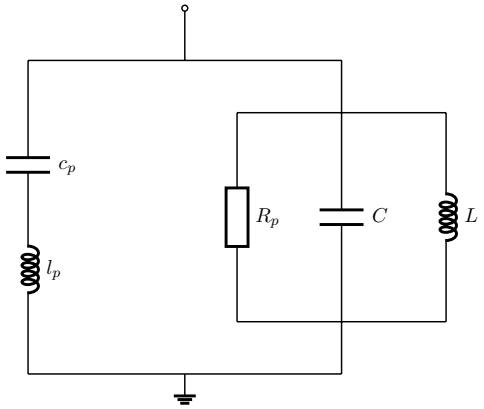

(b)

Figure 3.4: (a): A particle oscillating in the trap induces image currents in the trap electrodes. The voltage drop over the RCL detection circuit is amplified by a cryogenic low-noise amplifier and processed by a fast Fourier Transform spectrum analyser [96]. (b): Equivalent circuit of the particle-detector system in thermal equilibrium. The particle properties are represented by a series LC-circuit which is in parallel with the parallel RLC-circuit representing the detector.

Given the detector's effective parallel resistance R_p, its inductance L and its capacitance C, the frequency-dependent impedance $Z(\nu)$ of the particle-detector-system, as shown in Fig. 3.4b, can be calculated using Kirchhoff's circuit laws:

$$\frac{1}{Z} = \frac{1}{Z_d} + \frac{1}{Z_p} = \frac{1}{R_p} + \frac{1}{\mathrm{i}\omega L} + \mathrm{i}\omega C + \frac{1}{\mathrm{i}\omega l_p + \frac{1}{\mathrm{i}\omega c_p}}. \tag{3.2}$$

By introducing the detection circuit's resonance frequency $\omega_0 = \frac{1}{\sqrt{LC}}$, its quality factor $Q = \frac{R_p}{\omega_0 L}$ and the damping constant $\gamma = \frac{R_p q^2}{mD^2}$, the total impedance can be written as

$$\begin{aligned} Z =& \frac{R_p(\nu_p^2 - \nu^2)^2}{(\nu_p^2 - \nu^2)^2 + [\frac{Q}{\nu\nu_0}(\nu_0^2 - \nu^2)(\nu^2 - \nu_p^2) + \frac{\gamma}{2\pi}\nu]^2} \\ &+\mathrm{i}\frac{[\frac{R_p Q}{\nu\nu_0}(\nu_0^2 - \nu^2)(\nu^2 - \nu_p^2)^2 + \frac{\gamma}{2\pi}R_p\nu(\nu^2 - \nu_p^2)]}{(\nu_p^2 - \nu^2)^2 + [\frac{Q}{\nu\nu_0}(\nu_0^2 - \nu^2)(\nu^2 - \nu_p^2) + \frac{\gamma}{2\pi}\nu]^2}. \end{aligned} \tag{3.3}$$

Dropping the imaginary part and further simplification finally yields:

$$\mathrm{Re}(Z) = \frac{R_p}{1 + \left[\frac{\frac{Q}{\nu_0}(\nu_0^2 - \nu^2)(\nu^2 - \nu_p^2) + \frac{\gamma}{2\pi}\nu^2}{\nu(\nu^2 - \nu_p^2)}\right]^2}. \tag{3.4}$$

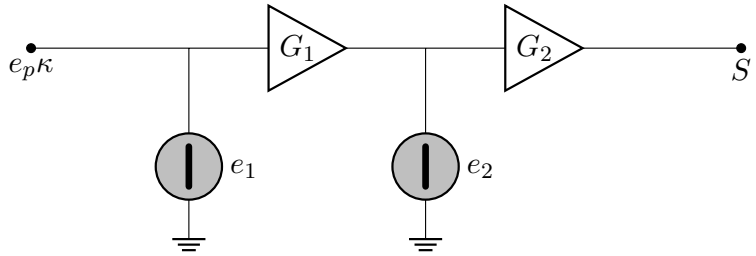

Figure 3.5: Simplified amplifier chain. For sufficiently large amplification G_1 the signal-to-noise ratio is independent of the noise components e_2 created by the later amplifiers, the single-sideband converter and the spectrum analyser.

In order to determine the parameters of the lineshape, knowledge of the noise density close to the resonator and particle frequency is sufficient. Therefore, the noise signal over the detection circuit is fed into a single sideband down-converter (SSB), which shifts the noise spectrum by a known frequency ν_{SSB} towards lower frequencies. This shift cuts off frequency components containing no information about the particle-resonator-system and reduces the necessary sampling rate ν_S to resolve the noise spectrum with a fast Fourier Transform spectrum analyser (FFT). The SSB, FFT and further amplifiers in the detection chain add white noise components e_2 to the spectrum which introduce a background noise level to the signal given by eq. (3.4). The signal-to-noise ratio (SNR) is defined as the ratio between the noise density on top of the resonator and the background noise density. In order to decouple the SNR from the noise created by the components of the detection chain, a cryogenic low-noise amplifier with gain G_1 and input noise density e_1 is used as a first stage. Figure 3.5 shows a simplified model of the detection chain in which the components of the detection chain are modeled as an amplifier with input noise density e_2 and gain G_2. Assuming a coupling factor κ between the voltage noise density e_p of the particle-detector circuit and the amplifier chain, the measured voltage noise density S is given by

$$S = \sqrt{((e_p^2\kappa^2 + e_1^2)G_1^2 + e_2^2)G_2}. \tag{3.5}$$

For sufficiently high gain G_1, the noise density e_2 can be neglected and the SNR is, to first order, determined by the thermal noise $e_p(\nu)$ of the particle-detector circuit and the input noise e_1 of the first amplifier stage.
Introducing the resonator noise level $n_1 \approx \sqrt{4k_BTR_p\kappa^2G_1^2G_2^2}$ and the background noise level $n_0 = \sqrt{(e_1^2G_1^2 + e_2^2)G_2^2}$, the observed noise spectrum S can parametrized in terms of experimentally observable quantities:

$$S(\nu) = \sqrt{\frac{n_1^2}{1 + \left[\frac{\frac{Q}{\nu_0}(\nu_0^2-\nu^2)(\nu^2-\nu_p^2)+\frac{\gamma}{2\pi}\nu^2}{\nu(\nu^2-\nu_p^2)}\right]^2} + n_0^2} \tag{3.6}$$

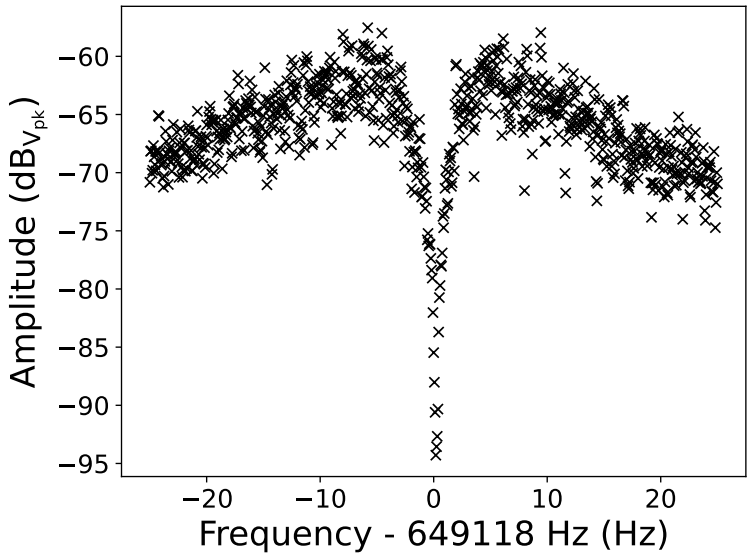

Figure 3.6: Noise spectrum of a particle tuned to the resonator frequency for typical parameters used in the BASE precision trap. At the particle frequency ν_p, the noise is shorted to the background noise floor.

Figure 3.6 shows the observable lineshape for typical parameters used in the BASE precision trap. At $\nu = \nu_p$ the denominator in Eq. (3.6) diverges and $S(\nu)$ has a minimum. The width of the dip feature is defined as the difference between the frequencies at which $S(\nu)$ has dropped to $\frac{n_1}{\sqrt{2}}$ and can be calculated by solving

$$\left|\frac{\frac{Q}{\nu_0}(\nu_0^2-\nu^2)(\nu^2-\nu_p^2)+\frac{\gamma}{2\pi}\nu^2}{\nu(\nu^2-\nu_p^2)}\right| = 1. \tag{3.7}$$

While fourth-order polynomials have analytic solutions, Eq. (3.7) can be simplified using the fact that $\frac{Q}{\nu_0}(\nu_0^2-\nu^2)(\nu^2-\nu_p^2)$ is small compared to $\frac{\gamma}{2\pi}{}_0\nu^2$ if the particle is tuned to resonance with the resonator ($\nu_0 = \nu_p$). Solving

$$0 = \frac{\gamma}{2\pi}\nu^2 \pm \nu(\nu^2-\nu_p^2) \tag{3.8}$$

yields four solutions. Two of the solutions appear at negative frequencies and carry no physical

information, which leaves the solutions

$$\nu_{1/2} = \sqrt{\frac{\gamma^2}{16\pi^2} + \nu_p^2} \pm \frac{\gamma}{4\pi}. \tag{3.9}$$

The dip-width $\Delta\nu = \nu_2 - \nu_1 = \frac{\gamma}{2\pi}$ of a particle centered on the resonator is therefore determined by the damping constant $\gamma = \frac{R_p q^2}{mD^2}$ and depends on the particle's properties m and q, the geometry of the trap and the pickup line D, and the resonator parameters $R_p = 2\pi\nu QL$.

3.3.2 Radial frequency measurements

In order to measure the radial eigenfrequencies of a trapped particle, sideband coupling between the radial mode and the axial oscillation can be utilized [109]. In order to couple a radial motion to the axial motion, a quadrupole drive close to the radial-axial sideband frequency is irradiated. By choosing the negative cyclotron sideband frequency $\nu_{SB,+} = \nu_+ - \nu_z$ or the positive magnetron sideband frequency $\nu_{SB,-} = \nu_z + \nu_-$, energy is continuously transported back and forth between the radial mode and the axial mode which is in thermal contact with the axial resonator. This leads to an equalization of the radial and axial quantum numbers $n_\pm$ and n_z. The transport of energy corresponds to a modulation of the respective oscillation amplitudes with the Rabi frequency

$$\Omega = \frac{qE_0}{2m\sqrt{\omega_z\omega_\pm}}, \tag{3.10}$$

which depends on the amplitude E_0 of the coupling-field gradients. During experimental operation, the precise sideband frequency is not known a priory and the irradiated frequency $\nu_{rf} = \nu_{SB,\pm} + \delta$ is detuned by a small amount δ from the true sideband frequency. In this case, the modulation frequency of the amplitudes is given by the modified Rabi frequency

$$\Omega' = \sqrt{\Omega^2 + \delta^2}, \tag{3.11}$$

which depends on the amplitude of the drive as well as the detuning from the true sideband frequency.
For small detunings, the modulation of the axial amplitude in the time domain leads to the appearance of two dips in the axial Fourier spectrum. In case of the modified cyclotron motion, these dips appear at the frequencies

$$\nu_{l,+} = \nu_z - \left(\frac{\Omega' + \delta}{2}\right) \text{ and } \nu_{r,+} = \nu_z + \left(\frac{\Omega' - \delta}{2}\right), \tag{3.12}$$

whereas in case of magnetron-axial sideband coupling the position of the two dips is given by

$$\nu_{l,-} = \nu_z - \left(\frac{\Omega' - \delta}{2}\right) \text{ and } \nu_{r,-} = \nu_z + \left(\frac{\Omega' + \delta}{2}\right). \tag{3.13}$$

By measuring the positions ν_l and ν_r of the sidebands during radial excitation at a drive frequencies $\nu_{rf,\pm}$ and known axial frequency ν_z, the modified cyclotron frequency ν_+ is given by

$$\nu_+ = \nu_{rf,+} + \nu_l + \nu_r - \nu_z \tag{3.14}$$

and the magnetron frequency can be determined as

$$\nu_- = \nu_{rf,-} + \nu_z - \nu_l - \nu_r. \tag{3.15}$$

Figure 3.7 shows the axial spectrum with and without application of the cyclotron-axial sideband drive.

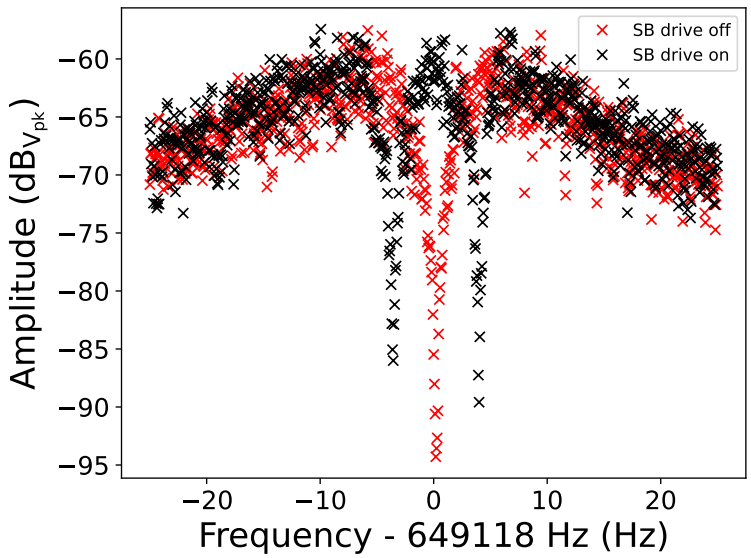

Figure 3.7: Red: Axial frequency spectrum if no drive is applied. The particle shorts the noise of the resonator at the axial frequency ν_z. Black: Once the resonant sideband drive is switched on, the axial dip vanishes and two dips separated by the Rabi frequency Ω appear at $\nu_z \pm \frac{\Omega}{2}$

The uncertainty with which ν_z, ν_l and ν_r can be determined depends on the signal-to-noise ratio (SNR) and the width $\Delta\nu$ of the dip, which are parameters of the axial detection system. Feedback cooling provides the possibility to reduce the width of the dips in the axial spectrum at the cost of reduced signal-to-noise ratio (see section 3.3.3).

Given the hierarchy $\nu_+ > \nu_z \gg \nu_-$ of the eigenfrequencies, the magnetron frequency typically does not need to be measured and can be approximated using Eq. (2.19) during calculation of the free cyclotron frequency ν_c via the invariance theorem $\nu_c^2 = \nu_+^2 + \nu_z^2 + \nu_-^2$. Additionally, given that the modified cyclotron frequency is approximately 50 times larger than the axial frequency, the uncertainty of ν_c is dominated by the uncertainty in the determination of ν_+. In order to overcome the resolution limit imposed by the dip width in the spectrum of the axial detector, direct observation of the modified cyclotron frequency on the cyclotron detector can be used.

By irradiating the particle directly on the modified cyclotron frequency, it's modified cyclotron radius is increased and the particle induces strong image currents in the cyclotron detector which result in a peak at the modified cyclotron frequency. The width of the peak feature is determined by the utilized window function and the spectrum acquisition time and typically on the order of 200-300 mHz. Figure 3.8 shows a peak spectrum acquired during the characterization of the superconducting coil system.

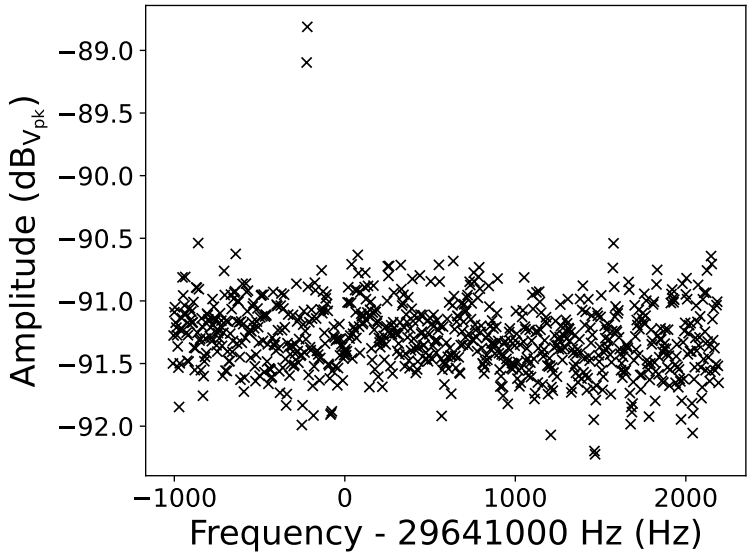

Figure 3.8: Peak spectrum created by an excited particle on the cyclotron resonator. The width of the peak feature is determined by the window function. After excitation to high cyclotron energies, the position of the peak is shifted by relativistic effects and coupling to the magnetic bottle which leads to drifts as the particle cools.

Note that the excitation necessary to create the peak feature significantly heats the particle's cyclotron temperature and thus leads to shifts of the modified cyclotron frequency due to relativistic effects and coupling to the residual magnetic bottle present in the precision trap.

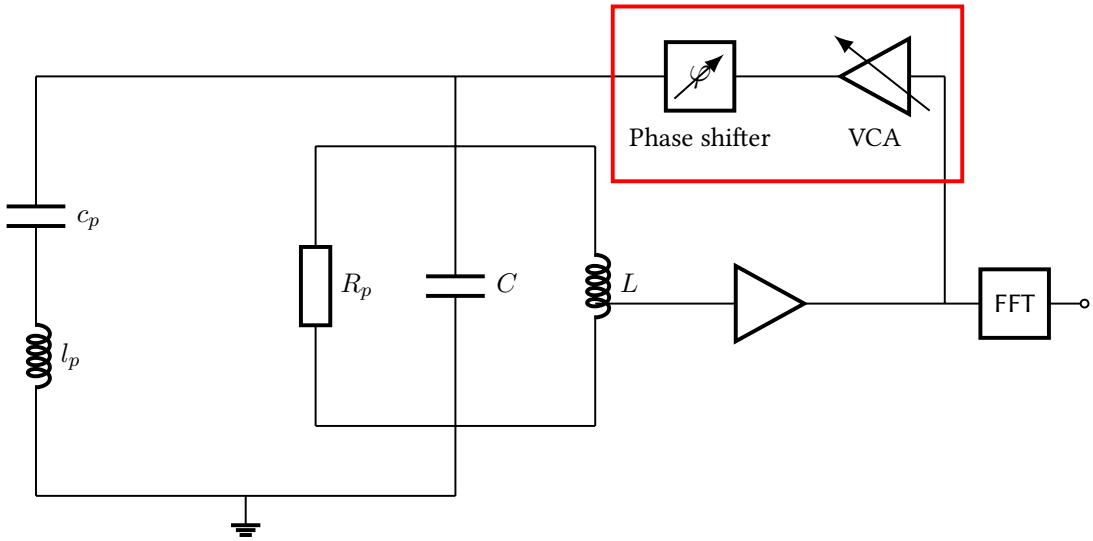

Figure 3.9: Schematic of the feedback loop (red). The signal from the detector is amplified, phase shifted and fed back to the detector.

In order to correct for these shifts, the cyclotron energy E_+ after excitation has to be known. By simultaneously acquiring an axial spectrum, E_+ can be determined using Eq. (2.45) and the modified cyclotron frequency $\nu_{+,0}$ at vanishing cyclotron energy can be calculated. By improving the quality of the cyclotron detector [100], the energy required to resolve a clean peak feature can be reduced. Additionally, interaction with the cyclotron resonator causes the ion to oscillate at a frequency different than it's natural frequency which pulls the position of the peak towards the frequency of the cyclotron resonator [110]. A detailed description of the relevant systematic shifts in the peak method is given in [104].

3.3.3 Feedback loops

In order to study systematic effects and reduce the preparation time of cold particles for single spin flip detection, the temperature of the superconducting axial and cyclotron resonator systems can be modified via application of electronic feedback [111, 112]. Part of the signal is picked up, phase shifted and attenuated and fed back to the detector. Figure 3.9 shows a schematic of a feedback loop.
In case the resonator has a temperature T_0 before feedback is applied, the temperature T_{FB} after application of feedback depends on the total gain G_{FB} of the feedback loop and is given by

$$T_{FB} = T_0(1 + G_{FB}). \tag{3.16}$$

Depending on the chosen phase, the feedback can either be positive ($G > 0$), which increases the effective temperature T_{FB} or negative ($G < 0$), which reduces the temperature. Changing the temperature of the resonator changes its effective resistance as well. Thus, changing the resonator temperature via feedback leads to change in the cooling time constant $\tau \propto \frac{1}{\gamma}$ given by

$$\tau_{FB} = \tau(1 - G_{FB}). \tag{3.17}$$

This change of cooling time constant leads to a change in the width $\frac{\gamma}{2\pi}$ of the dip on the axial resonator given by Eq. (3.9). Figure 3.10 shows the axial spectrum with and without negative feedback being applied.

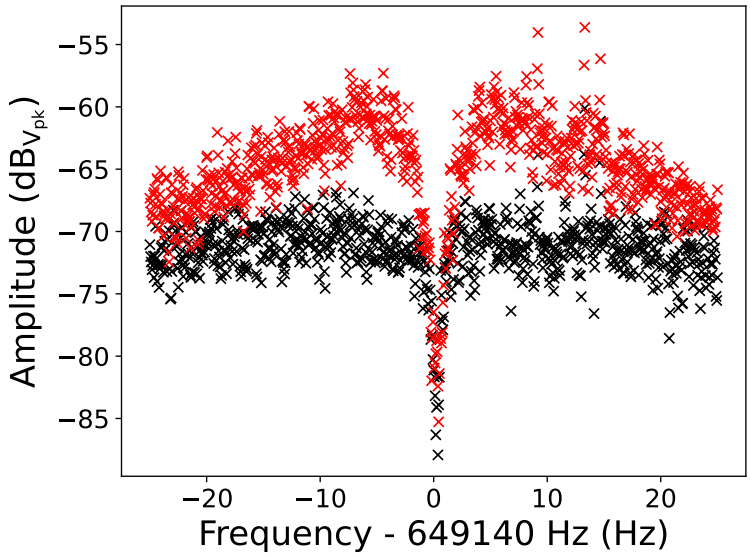

Figure 3.10: Axial spectrum of a particle in case no feedback is applied (black) and with negative feedback (red). Application of positive feedback increases the noise level as well as the width of the dip feature.

Typically, the temperature of the axial detectors can be reduced by a factor of six before noise introduced in the feedback loop starts to dominate.

3.3.4 Electronics and FFT chain

Detection of the trapped particle's eigenfrequencies relies on the precise measurement of small image currents induced by the oscillating particle in the trap electrodes. As the eigenfrequencies depend on the applied axial potential, all traps electrodes are biased using high-precision power

supplies by Stahl-electronics which provide voltages between $\pm 14\,\mathrm{V}$ and show fluctuations below the 10^{-7} level [113]. Low-pass filter stages at room temperature and in the cryogenic section further suppress noise coupling to the trap electrodes. The radiofrequency required for particle manipulation is provided by frequency generators which are locked to a common $10\,\mathrm{MHz}$ rubidium clock. A switch matrix grounds the radiofrequency lines in case no drive is applied and routes the signal through different filters depending on the applied frequency. These filters prevent the undesired excitation by parasitic frequency components close to the trapped particle's eigen- and sideband frequencies. In addition, cryogenic switches decouple the radial excitation coil in the analysis trap in case no drive is applied. This suppresses noise driving cyclotron transitions in the analysis trap.
In order to detect the particle's eigenmotions, cryogenic detection circuits are used (see chapter 3.3.1). The image currents induced by the particle in the trap electrodes result in a voltage drop over a high-impedance resonant circuit and are amplified by a cryogenic amplifier stage. Room temperature amplifiers further increase the signal which is then down-converted to frequencies in the order of 50-$100\,\mathrm{kHz}$ using a single-sideband down converter from Stahl-electronics. The resulting signal is then analyzed using a Stanford Research Systems SR780 FFT analyzer [114] which is locked to the rubidium clock. Figure 3.11 shows a schematic overview over the components in the signal chain.

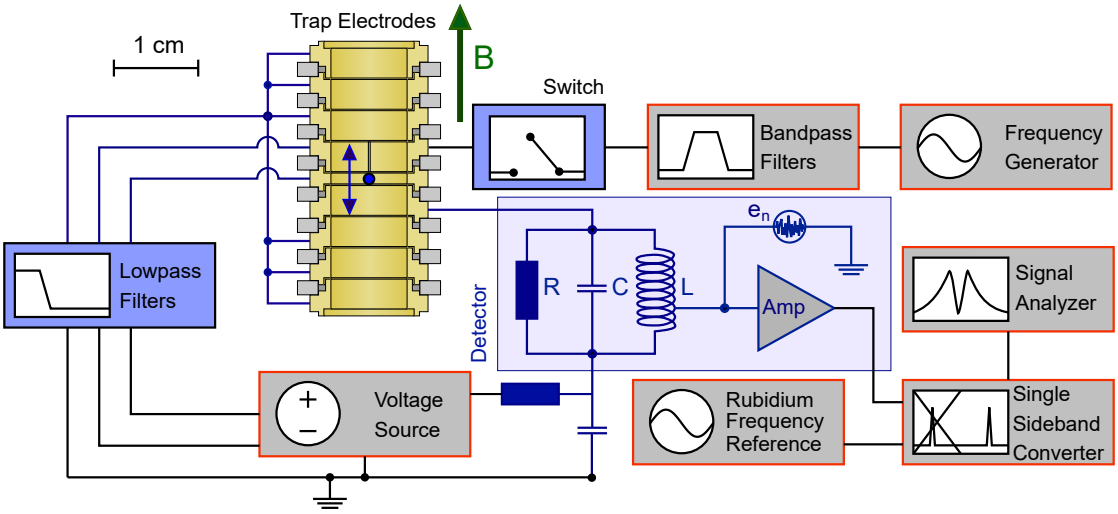

Figure 3.11: Overview over the main components in the signal chain for one axial detector. The trapping voltages are provided by high-precision voltage supplies and filtered to suppress fluctuations. Radiofrequency drives are created by function generators locked to a 10 MHz rubidium clock. A switch matrix connects the drive signals to bandpass filters suppressing frequency components outside of the desired excitation frequency. The image currents created by the particle in the trap electrodes are picked up by a superconducting detection circuit, amplified and down-converted to frequencies between 50-100 kHz. A SR780 Signal Analyzer is used to create the Fourier spectrum of the signal.

3.4 Measurement of the proton-to-antiproton charge-to-mass ratio

Comparison between the charge-to-mass ratio $\frac{q}{m}$ of the proton and antiproton relies on the measurement of the respective particle's free cyclotron frequency

$$\nu_c = \frac{1}{2\pi}\frac{q}{m}B \tag{3.18}$$

in a common magnetic field B. Assuming CPT symmetry holds, the ratio $R = \frac{\left(\frac{q}{m}\right)_p}{\left(\frac{q}{m}\right)_{\bar{p}}} = -\frac{\nu_{c,p}}{\nu_{c,\bar{p}}}$ between the charge-to-mass ratios of the proton and antiproton is expected to be -1.
In order to ensure that systematic shifts caused by voltage offsets and drifts are suppressed as far as possible, it is desirable to measure the free cyclotron frequencies of both particles in the same potential. As Penning traps do not provide the possibility to simultaneously trap particles of opposite charge, the free cyclotron frequencies of an antiproton and a H^- ion are compared

and the resulting ratio is corrected using the mass-ratio $\frac{m_{\mathrm{H}^-}}{m_{\mathrm{p}}}$ of a H^- and a proton:

$$\frac{m_{\mathrm{H}^-}}{m_{\mathrm{p}}} = 1 + 2\frac{m_e}{m_p} - \frac{E_1}{m_p c^2} - \frac{E_2}{m_p c^2} + \alpha_{\mathrm{H}^-}\frac{B_0^2}{m_p c^2} = 1.001\,089\,218\,753\,80(3). \tag{3.19}$$

The mass of an H^- ion is dominated by the mass of the proton with small corrections due to the rest mass m_e of the bound electrons [115–118], the electron affinity E_1 [119] and binding energy E_2 [120] of the electrons and a correction due to the ion's polarizibility in the strong magnetic field of the BASE magnet. Table 3.1 summarizes the magnitude of the individual corrections as well as their contribution to the relative uncertainty of the H^--to-proton mass ratio R_{theo}.

Correction	Abs. value	Rel. uncertainty
$2\frac{m_e}{m_p}$	0.00108923404299(2)	0.02 p.p.t.
$-\frac{E_1}{m_p c^2}$	-0.00000000080381(2)	0.02 p.p.t.
$-\frac{E_2}{m_p c^2}$	-0.00000001449306	$< 1 \times 10^{-18}$
$\alpha_{\mathrm{H}^-}\frac{B_0^2}{m_p}$	0.00000000000769(2)	0.02 p.p.t.

Table 3.1: Magnitude of the corrections to the H^--to-proton mass ratio and their respective contributions to the relative uncertainty. The relative uncertainty of the H^--to-proton mass ratio is at the level of 0.03 p.p.t. and therefore about a factor 500 below the statistical uncertainty of the charge-to-mass ratio measurement campaign carried out in 2017.

The resulting relative uncertainty of the ratio R is 0.03 p.p.t. and thus around a factor 500 below the statistical uncertainty of the 16 p.p.t. charge-to-mass ratio measurement campaign carried out in 2017 [69].

Due to the slight mass difference between the antiproton and the H^- ion, their axial frequencies differ by approximately $350\,\mathrm{Hz}$. In order to measure their free cyclotron frequencies, the particles' respective axial frequencies have to match the frequency of the axial detection circuit. In past measurements [121], this was achieved by adjusting the trapping potential to tune the respective axial frequency to the frequency of the axial detection system. However, changing the axial potential could result in a slight difference Δz of the particles' equilibrium positions which leads to a change $\Delta B = \Delta z B_1$ in the average magnetic field due to the residual B_1 term. In order to eliminate this source of systematic errors, the trap was equipped with a tunable axial detector which provides the possibility to match the detectors resonance frequency to the axial frequencies of the respective particles without change of the axial potential. In addition, a multilayer magnetic shielding system [122] was implemented, providing protection against external fluctuations of the magnetic field caused by activity in the Antiproton decelerator

hall. Lastly, the stiff connections mounting the cryogenic stage in the superconducting magnet were replaced by Kevlar strings. This decouples the trap stack mechanically from the boiling cryoliquids which cause vibrations tilting the symmetry axis of the trapping potential with respect to the magnetic field.

The ratio R is measured by extracting an antiproton and an H^- ion from the reservoir trap into electrodes further downstream. The upstream particle is moved into the precision trap and its free cyclotron frequency is determined using either sideband coupling or direct detection of the modified cyclotron frequency via resonant excitation (see chapter 5.2). Once the free cyclotron frequency of the upstream particle has been determined, the particle is parked in an electrode located between the precision trap and the reservoir trap and the downstream particle is moved into the precision trap. Once again, the free cyclotron frequency is measured and the particles are moved back into the initial configuration. This sequence is repeated and yields two datasets $\nu_{c,\bar{p}}$ and ν_{c,H^-} which each consist of multiple Gaussian sub-distributions depending on the environmental conditions during the measurement [69]. Figure 3.12 shows the measurement scheme outlined above.

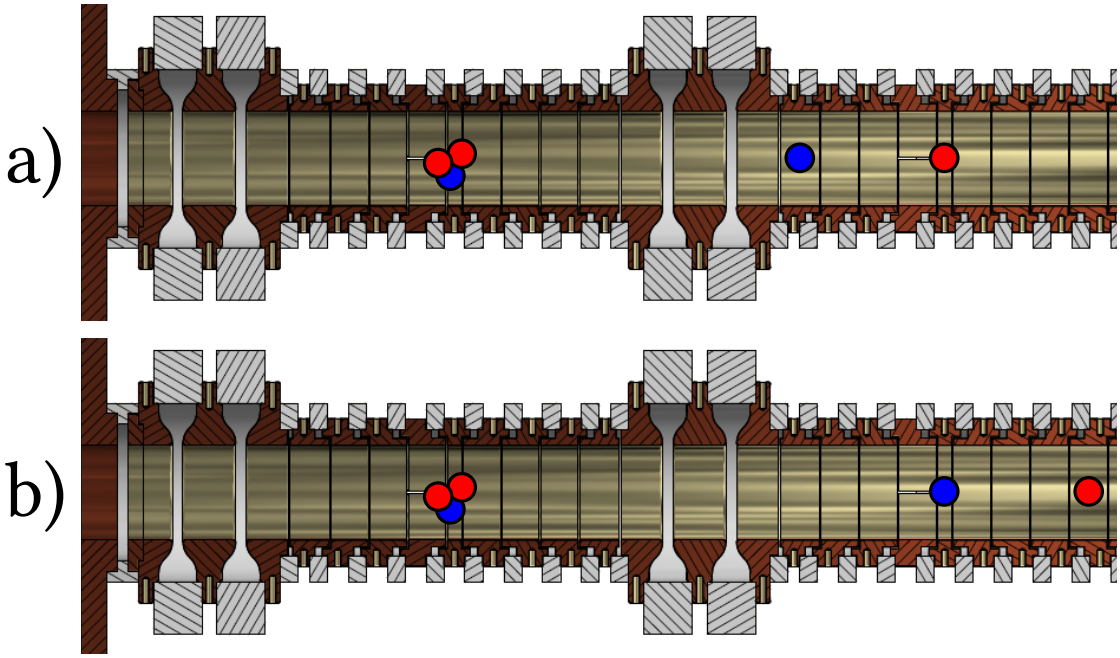

Figure 3.12: a) An antiproton (downstream, red) and an H^- ion (upstream, blue) are extracted from the mixed cloud stored in the reservoir trap. The upstream particle is stored in an electrode between the precision trap and the reservoir trap while the cyclotron frequency $\nu_{c,\bar{p}}$ of the antiproton is measured. b) The antiproton is moved towards the analysis trap and stored in one of the transport electrodes while the cyclotron frequency ν_{c,H^-} of the H^- ion is measured in the precision trap. In order to test for systematic shifts introduced due to the transport, the measurement sequence is repeated with two particles of the same kind.

Given that the environmental conditions in the antiproton decelerator hall change depending on operation of the AD and other experiments, outliers caused for example by movement of the ferromagnetic crane are removed using robust block stability and median absolute deviation filters. In order to account for drifts of the magnetic field between the measurements of $\nu_{c,\bar{p},k}$ and $\nu_{c,H^-,k}$, both datasets are combined into a common cyclotron frequency dataset ν_c using the ratio R as a free multiplicative parameter. Next this combined dataset is split into sub-groups $\nu_{c,k}$ representing windows of constant experimental parameters typically covering a time span between $1.5\,\mathrm{h}$ and $4\,\mathrm{h}$. A polynomial $p(t)$ of order q is fit to the sub-group $\nu_{c,k}$ and R_k is determined by maximizing the log-likelihood function. The uncertainty σR_k of each sub-group is estimated using Cramer-Rao bounds and the final result R is given as the weighted arithmetic mean of the entire acquired data set. The influence of polynomial order q, sub-group length and filter criteria was studied and the robustness of this data evaluation approach was verified using Monte-Carlo simulations.

Even in case both the antiproton and the H^- ion are measured in the same potential, changes in the temperatures of the particles' eigenmotions can lead to systematic shifts that are not identical between both particles. The main contributions to this shift are given by the residual magnetic bottle B_2 present in the precision trap and relativistic shifts. The associated shifts are given by Eq. (2.45) and Eq. (2.50) and the experimentally measured ratio R_{Exp} between the free cyclotron frequencies scales with the temperature difference ΔT_z between the particles:

$$R_{Exp} = R_{theo}\left(1 + \left(\frac{1}{4\pi^2 m\nu_z^2}\frac{B_2}{B_0} - \frac{1}{2mc^2}\right)k_B\Delta T_z\right). \tag{3.20}$$

Under the conditions present in the BASE experiment, the relative shift of the ratio due to the residual magnetic bottle is on the order of

$$\frac{\Delta R_{Exp}}{R_{Exp}} = \frac{k_B}{4\pi^2 m\nu_z^2 B_0}B_2\Delta T_z = \frac{262.48\text{p.p.t.}}{\frac{\text{T}}{\text{m}^2}\text{K}}B_2\Delta T_z. \tag{3.21}$$

Given the residual magnetic bottles of $267(2)\ \frac{\text{mT}}{\text{m}^2}$ and $-89.4(6)\ \frac{\text{mT}}{\text{m}^2}$ present in the 2017 and 2018/2019 data acquisition campaigns, these shifts are on the order of $\frac{70\text{p.p.t.}}{\text{K}}$ and $\frac{-23.5\text{p.p.t.}}{\text{K}}$ respectively.

Relativistic effects are present even in case of a perfectly harmonic trapping potential and homogenous magnetic field and result in a shift on the level of

$$\frac{\Delta R_{Exp}}{R_{Exp}} = -\frac{k_B}{mc^2}\frac{\nu_+}{\nu_z}\Delta T_z = \frac{4.25\text{p.p.t.}}{\text{K}}\Delta T_z. \tag{3.22}$$

In order to minimize the influence these shifts have on the final result, great care has to be taken to ensure that both particles are measured at the same axial temperature. Therefore, the axial temperature is measured multiple times during each charge-to-mass ratio campaign and identical particles are compared to ensure that no systematic shifts are introduced by the measurement sequence. Using the superconducting shimming system implemented in the course of this thesis, the main systematic caused by the uncertainty in the axial temperature similarity can be eliminated by tuning B_2 close to zero.

3.5 Measurement of the magnetic moment

The g-factor describes the proportionality between a particle's spin $\mathbf{S}$ and it's magnetic moment $\mu_{\mathbf{S}}$. Using the nuclear magneton $\mu_N = \frac{e\hbar}{2m_p}$, the magnetic moment is given by

$$\mu_{\mathbf{S}} = g\mu_N\frac{\mathbf{S}}{\hbar}. \tag{3.23}$$

In case of point-like spin $\frac{1}{2}$ particles, the Dirac equation predicts g to be exactly 2, however, additional effects explained by hadronic and weak interaction contributions result in an anomalous magnetic moment that deviates from the predicted value. In case of the electron g-factor, analytic calculation of the anomalous magnetic moment is possible using Feynman diagrams up to 8th order in the fine structure constant α [123] and numerical calculations up to 10th order exist [124]. In contrast, due to the internal substructure of the proton no convincing theory predicting its spin exists [125] and theoretical calculations are not possible.
In order to measure the g-factor of the antiproton, a single particle is placed in the strong magnetic field B of a Penning trap which leads to a splitting $\Delta E = 2\mu_{\mathbf{S}}\mathbf{B}$ of energy levels depending on the orientation of the magnetic moment with respect to the magnetic field:

$$\Delta E = 2\mu_{\mathbf{S}}\mathbf{B} = 2g\mu_N \frac{|\mathbf{S}|}{\hbar} B = g\mu_N B. \tag{3.24}$$

The Larmor frequency $\nu_L = \frac{\Delta E}{2\pi\hbar}$ describes the associated frequency that drives transitions between the two possible spin states. Thus, g can be determined by measuring ν_L in a known magnetic field B. By measuring the free cyclotron frequency $\nu_c = \frac{1}{2\pi}\frac{e}{m_p}B$ in the same magnetic field, g can be expressed as the ratio of the Larmor frequency ν_L and the free cyclotron frequency ν_c:

$$g = \frac{\Delta E}{\mu_N B} = \frac{2\pi\hbar\nu_L}{\mu_N B} = 2\frac{\nu_L}{\nu_c}. \tag{3.25}$$

The non-distructive measurement of the free cyclotron frequency ν_c is a routine in state-of-the-art Penning-trap experiments and described in chapter 5.2. In contrast, the determination of the Larmor frequency ν_L is challenging as the ν_L precession is not associated with any of the eigenmotions of the trapped particle and can thus not be detected using image currents. By superimposing a strong axial magnetic bottle $B_2\left(z^2 - \frac{\rho^2}{2}\right)$ onto the magnetic background field, the continuous Stern-Gerlach effect creates an additional axial potential component $\Phi_{Bottle}(z) = \mu_{\mathbf{S}}\mathbf{B_2}(z)$ acting on the particle. Depending on the orientation of the particle's spin with respect to the magnetic field, this potential can either be confining or deconfining. The effective potential experienced by the particle is therefore given by the sum of the electrostatic potential and the potential $\Phi_{Bottle}(z) = \mu_S(B_0 \pm B_2 z^2)$ due to the magnetic bottle. Solving the axial equation of motion yields the modified axial frequency $\nu_{z,SF}$ which depends on the spin state and is slightly shifted from the axial frequency ν_z of a particle without spin:

$$\nu_{z,SF} = \frac{1}{2\pi}\sqrt{\frac{2qV_0}{m_p}C_2 \pm \frac{g}{2}\frac{2\mu_N}{m_p}B_2} = \nu_z\sqrt{1 \pm g\frac{\mu_N}{4\pi^2 m_p \nu_z^2}B_2} \tag{3.26}$$

$$\approx \nu_z\left(1 \pm \frac{g}{2}\frac{\mu_N}{4\pi^2 m_p \nu_z^2}B_2\right) = \nu_z \pm \frac{\Delta\nu_z'}{2} \tag{3.27}$$

with

$$\Delta\nu_{z,SF} = g\frac{\mu_N}{4\pi^2 m_p \nu_z}B_2 \approx \frac{g}{2}\frac{h\nu_+}{4\pi^2 m_p \nu_z}\frac{B_2}{B_0} = 172(8)\,\mathrm{mHz}. \tag{3.28}$$

In addition to spin flips, the strong magnetic bottle couples the energy of the radial modes to the axial frequency. Expressing the radial energies $E_+ = h\nu_+\left(n_+ + \frac{1}{2}\right)$ and $E_- = -h\nu_-\left(n_- + \frac{1}{2}\right)$ in terms of the radial quantum numbers n_+ and n_-, the overall shift $\Delta\nu_z$ of the axial frequency can be given in terms of the radial quantum numbers n_+ and n_- and the spin state quantum number $m_S = \pm\frac{1}{2}$:

$$\Delta\nu_z = \frac{h\nu_+}{4\pi^2 m\nu_z}\frac{B_2}{B_0}\left(\left(n_+ + \frac{1}{2}\right) + \frac{\nu_-}{\nu_+}\left(n_- + \frac{1}{2}\right) + \frac{g}{2}m_S\right). \tag{3.29}$$

Under typical conditions, the axial frequency in the analysis trap is around $\nu_z = 675\,\mathrm{kHz}$ and thus a jump of the axial frequency associated with a spin flip ($\Delta m_S = 1$) in the magnetic bottle $B_2 = 272(12)\,\frac{\mathrm{kT}}{\mathrm{m}^2}$ is around $\Delta\nu_{z,SF} = 172(8)\,\mathrm{mHz}$. Note that this shift is more than a factor 650 lower than the shift for an electron oscillating at the same axial frequency in the same magnetic bottle. Shifts of the axial frequency due to a change $\Delta n_- = \pm 1$ are suppressed by a factor $\frac{\nu_-}{\nu_+} \approx \frac{1}{1500}$ and are thus negligibly small with $\Delta\nu_{z,n_-} = 0.040(2)\,\mathrm{mHz}$. In contrast, a change of the cyclotron quantum number $\Delta n_+ = \pm 1$ leads to a change in axial frequency of $\Delta\nu_{z,n_+} = 62(3)\,\mathrm{mHz}$. It is therefore crucial to ensure that the cyclotron quantum number n_+ does not change significantly during the determination of the Larmor frequency, as a change in axial frequency due to a spin flip can not be distinguished from changes induced by fluctuation in the cyclotron quantum number.

The cyclotron transition rate χ_+ of a particle itself scales linearly with the cyclotron quantum number n_+ and can be calculated using first-order transitions in a quantum mechanical oscillator driven by radial electric field noise with spectral power density S_E [104]:

$$\zeta_+ = \frac{q^2 n_+}{4\pi m\nu_+}S_E(\nu_+). \tag{3.30}$$

The cyclotron transition rate scales linearly with the cyclotron quantum number $n_+ \propto E_+$. In order to achieve the high axial frequency stability necessary to resolve spin flips it is therefore

important to prepare a particle with low cyclotron energy E_+. In order to increase the cyclotron temperature acceptance it is crucial to reduce the spectral power density $S_E(\nu_+)$ coupling to the cyclotron motion as much as possible. In addition, increasing the cyclotron frequency by increasing the strength of the magnetic field in the center of the trap has the potential to reduce the cyclotron transition rate and leads to higher axial frequency stability. One possible approach to maximize the magnetic field at the particle's position is the development of an analysis trap containing two ferromagnetic correction electrodes which create an inverted magnetic bottle in the center of the trap [126]. In this configuration, the magnetic field has a maximum at the position of the particle and thus the cyclotron transition rate is decreased compared to the conventional setup using a ferromagnetic ring electrode.
The following sections outline different measurement techniques that have been applied for the measurement of the (anti)proton g-factor.

3.5.1 Single-trap method

In order to measure the free cyclotron frequency ν_c as well as the Larmor frequency ν_L in a single trap, a strong magnetic bottle needs to be superimposed on the axial magnetic field. The large B_2 coefficient leads to a significant energy dependence of the particle's eigenfrequencies in the trap. As the particle is in thermal contact with the axial detection circuit and its axial energy constantly samples the Boltzmann distribution, the techniques that were used for the determination of the free cyclotron frequency in the homogenous magnetic field of the precision trap can not be used in the strong magnetic bottle of the analysis trap. Under typical conditions, the strong magnetic bottle causes the Larmor frequency to shift by $5.9\,\frac{\mathrm{kHz}}{\mathrm{K}}$. Sideband coupling of the axial and cyclotron motions causes the cyclotron energy to move through a Boltzmann distribution of $300\,\mathrm{K}$ and thus corresponds to a linewidth of multiple $100\,\mathrm{kHz}$.
Since that particle exchanges energy with the axial resonator on timescales given by the resonator's cooling time constant $\tau \approx 50\,\mathrm{ms}$, its axial energy follows a Boltzmann distribution and the probability that the likelihood has axial energy E_z is given by:

$$p(E_z) = \frac{1}{k_B T_z} e^{-\frac{E_z}{k_B T_z}}. \tag{3.31}$$

The width of this distribution is determined by the temperature T_z of the axial detection circuit. Given the strong magnetic bottle B_2, any change in the axial energy E_z leads to a shift of the modified cyclotron frequency according to Eq. (2.44). The observed modified cyclotron frequency ν'_+ is thus not constant but shifted by an exponential distribution from the cyclotron frequency ν_+ at vanishing axial energy. The probability density distribution of ν'_+ is given by

$$p(\nu'_+) = \Theta(\nu'_+ - \nu_+)\frac{1}{\Delta\nu_+}e^{-\frac{(\nu'_+ - \nu_+)}{\Delta\nu_+}} \tag{3.32}$$

with the Heaviside function Θ and the characteristic width

$$\Delta\nu_+ = \frac{\nu_+}{4\pi^2 m\nu_z^2}\frac{B_2}{B_0}k_B T_z. \tag{3.33}$$

For positive B_2, the probability to observe a cyclotron frequency below ν_+ is zero. For frequencies above ν_+, the probability follows an exponential distribution with a width $\Delta\nu_+$ given by the temperature T_z of the axial resonator and the strength $B_2 = 272(12)\,\frac{\mathrm{kT}}{\mathrm{m}^2}$ of the magnetic bottle. Under typical conditions, $\Delta\nu_+$ is around 9300 Hz, thus it is not possible to observe the free cyclotron frequency ν_+ directly via sideband coupling or resonant excitation. Instead, ν_+ is measured by irradiating the particle with different radiofrequencies ν_{rf} close to ν_+. As long as ν_{rf} is below ν_+, the random walk of the particle's modified cyclotron frequency ν'_+ is never resonant with the drive frequency ν_{rf} and thus the cyclotron quantum number will not change. As soon as ν_{rf} is above ν_+, the particle's motion through the thermal Boltzmann distribution will cause its cyclotron frequency ν'_+ to momentarily be in resonance with the drive and thus the cyclotron quantum number n_+ will change. As the particle is in the strong magnetic bottle of the analysis trap, the change in cyclotron energy leads to a change in axial frequency according to Eq. (3.29). As a change of the cyclotron quantum number n_+ is only possible when the particle's modified cyclotron frequency ν'_+ momentarily coincides with the drive frequency, the axial frequency scatter is proportional to the distribution of modified cyclotron frequencies given by Eq. (3.32). By changing the drive frequency until the scatter of the axial frequency is maximized, the modified cyclotron frequency ν_+ at vanishing axial energy can be determined. The measurement of the Larmor frequency follows the same principle as the measurement of the modified cyclotron frequency given that the average magnetic field the particle experiences depends on the strength of the magnetic bottle B_2 and the axial energy E_+. Therefore, spinflips can not only be driven by irradiating directly at the Larmor frequency ν_L, but also at higher frequencies. The axial frequency scatter Ξ_z depends on the background stability Ξ_{BG} of the axial frequency as well as the additional scatter Ξ_{SF} induced by spinflips [101]:

$$\Xi_z = \sqrt{\Xi_{BG}^2 + \Xi_{SF}^2} = \sqrt{\Xi_{BG}^2 + p_{SF}\Delta\nu_{z,SF}^2}. \tag{3.34}$$

By measuring the axial frequency stability Ξ_z at a known background stability Ξ_{BG}, the spin flip probability p_{SF} can be determined for different drive frequencies. As long as the drive frequency ν_{rf} is below the Larmor frequency ν_L, the particle's random motion through the thermal Boltzmann distribution never brings its momentary Larmor frequency ν'_L into resonance

with the drive. Once the drive frequency is above the Larmor frequency, spin flips become possible and the axial frequency scatter rises. In contrast to measurements of the cyclotron frequency, the spin state can only change between two states whereas the change of cyclotron quantum number is not bound. Compared to excitation of the modified cyclotron frequency, the added axial frequency scatter due to spin flips is therefore bounded and measurement of the Larmor frequency takes significantly more time. Note that due to the incoherent drive, the maximum theoretically achievable spin flip probability is $50\,\%$. Under experimental conditions, the maximum observed spin flip probability depends on the strength and duration of the drive as well as the coupling of particle to the axial detection circuit and needs to be carefully optimized to provide sufficiently high contrast without broadening the Larmor resonance too far. A more detailed description of the lineshapes is given by Brown [127]. Figures 3.13a and 3.13b show the antiproton cyclotron and Larmor resonances measured in the BASE analysis trap [88].

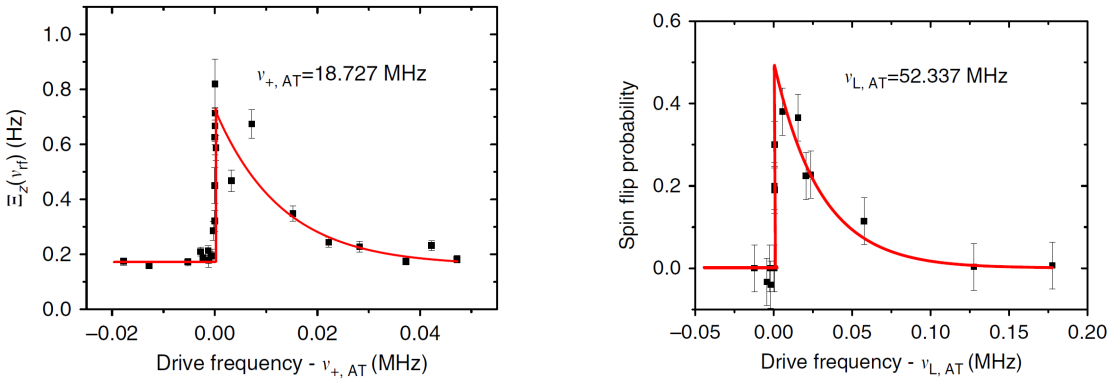

(a) (b)

Figure 3.13: The strong magnetic bottle present in the BASE analysis trap convolves the axial temperature distribution into the cyclotron and Larmor resonance curves. The width of the distributions is determined by the axial temperature and the strength of the magnetic bottle. (a) The axial frequency scatter increases rapidly once the drive frequency is above the modified cyclotron frequency $\nu_{+,AT}$ of a particle with negligible axial energy. (b) Once the drive frequency is above the Larmor frequency $\nu_{L,AT}$ of a particle with negligible axial energy, the spin flip probability increases up to a maximum of $50\,\%$.

In order to measure the g-factor using the single trap technique, a particle with low cyclotron energy is prepared in the precision trap by bringing it into contact with a detection circuit resonating at the modified cyclotron frequency. By shuttling the particle into the analysis trap and observing the axial frequency, the cyclotron temperature of the particle can be determined. The cooling process is repeated until a particle with sufficiently low cyclotron temperature is

extracted into the analysis trap and thus background scatter of the axial frequency is sufficiently low. As a first step, the magnetron mode of the particle is cooled in the analysis trap. Next, the cyclotron frequency $\nu_{c,1}$ is measured by scanning the cyclotron resonance curve until the axial frequency scatter increases and the steep onset located at ν_+ is clearly resolved. In order to measure the Larmor frequency, first the axial background frequency stability Ξ_{BG} for a drive frequency below ν_L is measured. Next, the drive frequency is scanned over the Larmor resonance and the spin flip probability p_{SF} for different drive frequencies is determined using Eq. (3.34). As in the case of the modified cyclotron frequency, the Larmor frequency is determined from the position of the center of the steep onset. Finally, the cyclotron frequency $\nu_{c,2}$ is measured a second time and the g-factor is calculated according to Eq. (3.25) using the arithmetic mean $\nu_c = \frac{\nu_{c,1}+\nu_{c,2}}{2}$ of the individual cyclotron measurements to account for linear drifts in the magnetic field during the measurement of the Larmor frequency. Since both the cyclotron frequency ν_c as well as the Larmor frequency ν_L are determined from the steep increase of the axial frequency scatter once the irradiated radio-frequency is above ν_c or ν_L respectively, the final uncertainty is determined by the ability to resolve the onset of the respective spectra. Due to the strong magnetic bottle present in the analysis trap, the noise driven random walk of the particle's magnetron radius leads to a change of the average magnetic field the particle experiences and thus washes out the steep onset of the resonance lines. In order to quantify the effect of the random walk on the final uncertainty of the g-factor, Monte-Carlo simulations of the magnetron random walk were run and the mean frequency during the simulated walk was compared to the frequency extracted from the measurements. Using the single trap scheme outlined above, six individual measurements of the antiproton g-factor were carried out during weekend- or night-shifts between 20th February 2016 and 5th March 2016 the antiproton g-factor was determined to a fractional precision of 800 p.p.b. [88].

3.5.2 Double-trap method

Measurements of the g-factor in a single trap are limited by the strong magnetic bottle required to detect spin flips of the trapped particle. In order to overcome these systematic limitations it is desirable to measure the free cyclotron frequency ν_c and the Larmor frequency ν_L in a homogenous magnetic field where shifts of the frequencies due to the energies E_+, E_z and E_- of the eigenmotions are strongly suppressed. A rather intuitive approach is the separation of the measurement procedure into two distinct traps [128]. The precision trap, which has a very homogenous magnetic field and was used for the preparation of a cold particle in the single trap scheme is now used to measure the cyclotron and Larmor frequencies whereas the analysis trap is used for spin state detection only. Given the residual magnetic bottle of typically less

than $3\,\frac{\mathrm{T}}{\mathrm{m}^2}$ present in the precision trap, the width of the cyclotron and Larmor resonances due to the Boltzmann distribution of the axial temperature is reduced by a factor of approximately $100\,000$ and becomes negligible. On the other hand, separation of the spin flip excitation and detection means that the axial frequency scatter in the analysis trap can no longer be monitored while the spin flip drive is applied. Instead, the spin state is determined by resolving single spin flips in the analysis trap.

In order to determine the spin state of a particle in the analysis trap, an initial measurement of the particle's axial frequency $\nu_{z,AT,1}$ is taken. Next, a strong radio-frequency drive at the particle's Larmor frequency $\nu_{L,AT}$ is applied, the spin is flipped with probability $p_{SF} \approx 50\,\%$ and the axial frequency $\nu_{z,AT,2}$ after Larmor excitation is measured. If the spin did not flip, the axial frequency difference $\Delta\nu_{z,AT} = \nu_{z,AT,2} - \nu_{z,AT,1}$ will be close to zero. In case a spin flip occurred, however, the axial frequency will be shifted by $\pm\Delta\nu_{z,SF} = \pm 172(8)\,\mathrm{mHz}$. Assuming that the axial background frequency scatter is described by a normal distribution $\mathcal{N}(\mu, \sigma)$ with mean $\mu = 0$ and standard deviation $\sigma = \Xi_{BG}$, the probability to observe a frequency shift of $\Delta\nu_{z,AT}$ is given by the probability density

$$\begin{aligned} p(\Delta\nu_{z,AT}) =& (1 - p_{SF})\,\mathcal{N}(0, \Xi_{BG}) \\ &+ p_{SF}\,p_{\uparrow}\,\mathcal{N}(-\Delta\nu_{z,SF}, \Xi_{BG}) \\ &+ p_{SF}\,(1 - p_{\uparrow})\,\mathcal{N}(\Delta\nu_{z,SF}, \Xi_{BG}). \end{aligned} \tag{3.35}$$

The first line in Eq. (3.35) corresponds to the case that no spin flip occurs whereas the second and third line correspond to a spin flip from $\uparrow\Rightarrow\downarrow$ and $\downarrow\Rightarrow\uparrow$ respectively. The black line in Fig. 3.14 shows a plot of the probability density for $p_{SF} = 0.5$, $p_{\uparrow} = 0.5$ and a background frequency scatter of $\Xi_{BG} = 50\,\mathrm{mHz}$ whereas the colored lines indicate the individual subdistributions. This choice of p_{SF} and $p_{\uparrow}$ corresponds to the typical case where spin flips are driven incoherently in the analysis trap without any information of the initial spin state. In order to determine the initial spin state from a measurement of $\Delta\nu_{z,AT}$, the observed frequency shift $\Delta\nu_{z,AT}$ needs to be assigned to one of the three subdistributions contributiong to Eq. (3.14). By choosing a threshold value $\Delta\nu_{Th}$ observations of $\Delta\nu_{z,AT}$ are categorized as follows:

- $|\Delta\nu_{z,AT}| < \Delta\nu_{Th}$: In case the absolute change in axial frequency is below the threshold value, it is assumed that no spin flip occurred and the Larmor drive did not change the spin. In this case, no information over the spin state before application of the Larmor drive can be gained.
- $\Delta\nu_{z,AT} \leq -\Delta\nu_{Th}$: In case the axial frequency jumps by more than $\Delta\nu_{Th}$ towards lower

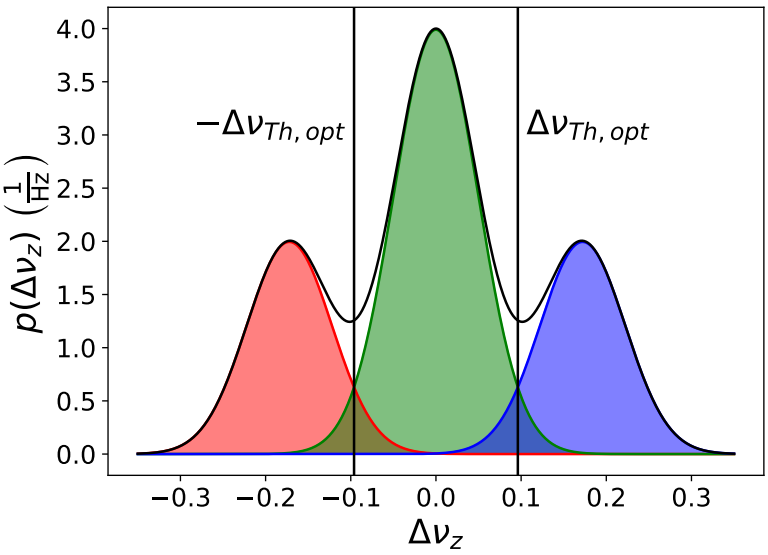

Figure 3.14: Probability density to observe an axial frequency jump $\Delta\nu_z$ in case spin flips are driven at $50\,\%$ spin flip probability and the initial spin state is undetermined. Once a change $|\Delta\nu_{z,AT}| \geq \Delta\nu_{Th}$ is observed, it is assumed that a spin flip occurred and thus the initial spin state can be reconstructed. The optimal threshold $\Delta\nu_{Th,opt}$ minimizes the probability to misidentify the observed frequency jump and lies at the frequency at which the values of the central and shifted distributions are equal.

frequencies, it is assumed that a spin transition $\uparrow\Rightarrow\downarrow$ was driven by the Larmor excitations. Thus the particle initially had to be in the spin $\uparrow$ state.

- $\Delta\nu_{z,AT} \geq \Delta\nu_{Th}$: If a jump of more than $\Delta\nu_{Th}$ towards higher frequencies is observed, the associated spin transition is assumed to be $\downarrow\Rightarrow\uparrow$ and thus the particle initially was in the $\downarrow$ spin state.

The error rate E_{Th} to assign the wrong spin state transition from a single observation of $\Delta\nu_{z,AT}$ can be calculated by integrating the individual sub distributions over the range of observations $\Delta\nu_{z,AT}$ for which the wrong spin state would be applied. By minimizing E_{Th} with respect to the chosen threshold value, the optimal threshold value $\Delta\nu_{Th,opt}$ in case that no prior knowledge of the spin state is available ($p_\uparrow = p_\downarrow = 0.5$) can be determined:

$$\Delta\nu_{Th,opt} = \frac{\Delta\nu_{z,SF}}{2}\left(1 + 2\left(\frac{\Xi_{BG}}{\Delta\nu_{z,SF}}\right)\right)\ln\left(\frac{2}{p_{SF}} - 2\right). \tag{3.36}$$

This choice coincides with the intuitive approach to choose the threshold such that the central density and the shifted densities have the same value at $\Delta\nu_{Th}$. Under typical conditions of $\Xi_{BG} \approx 65\,\mathrm{mHz}$ the ideal threshold value is $\Delta\nu_{Th,opt} = 103\,\mathrm{mHz}$ which corresponds to a probability $P(|\Delta\nu_z| \geq \Delta\nu_{Th,opt}) = 48.4\,\%$ to observe a spin flip and an error rate E_{Th} in determining the initial spin state from a single observation of $E_{Th} = 12.8\,\%$. Multiple spin flips can be driven in the analysis trap and a Bayesian model can be applied to determine the initial spin state with increased accuracy [102].
In order to measure the (anti)proton g-factor using two traps, a particle with low cyclotron energy is prepared by bringing it into thermal contact with the cyclotron detector in the precision trap. After letting the particle interact with the cyclotron detector for multiple cooling time constants τ, it is moved to the analysis trap and the cyclotron temperature is determined by measuring the axial frequency. Once a particle with sufficiently low cyclotron temperature is found, the Larmor drive is applied in the analysis trap until a jump $|\Delta\nu_{z,AT}|$ in axial frequency above a chosen initialization threshold $\Delta\nu_{z,i}$ is observed. By increasing $\Delta\nu_{z,i}$, the probability $P(|\Delta\nu_z| \geq \Delta\nu_{z,i})$ to observe a spin flip is reduced, however, the initialization error rate E_i decreases as well. Under typical axial frequency stability of $\Xi_{BG} \approx 65\,\mathrm{mHz}$ choosing an initialization threshold of $190\,\mathrm{mHz}$ leads to an initialization error rate of less than $0.1\,\%$. Once a particle with known spin state is prepared, it is moved into the precision trap and its free cyclotron frequency $\nu_{c,PT,1}$ is measured using sideband coupling of the axial and modified cyclotron mode. Note that this heats the cyclotron temperature to $T_+ = \frac{\nu_+}{\nu_z}T_z \approx 300\,\mathrm{K}$. Next, the particle is irradiated with a radiofrequency $\nu_{rf,PT}$ close to the Larmor frequency $\nu_{L,PT}$ in the precision trap and the free cyclotron frequency $\nu_{c,PT,2}$ is measured a second time. In order

to determine if the applied radiofrequency lead to a spin flip, the spin state after application of the drive has to be determined in the analysis trap as described above. Since the determination of the spin state with high fidelity requires low cyclotron temperature, the particle has to be cooled again. Depending on the noise conditions in the analysis trap and the associated cyclotron temperature suitable for single spin flip detection, the preparation of a cold particle takes between $90\,\mathrm{min}$ (BASE-Mainz) and $48\,\mathrm{h}$ (BASE-CERN). Once a cold particle is detected in the analysis trap, its spin state is analyzed using the scheme outlined above. Figure 3.15 shows the individual steps of the measurement scheme outlined above.

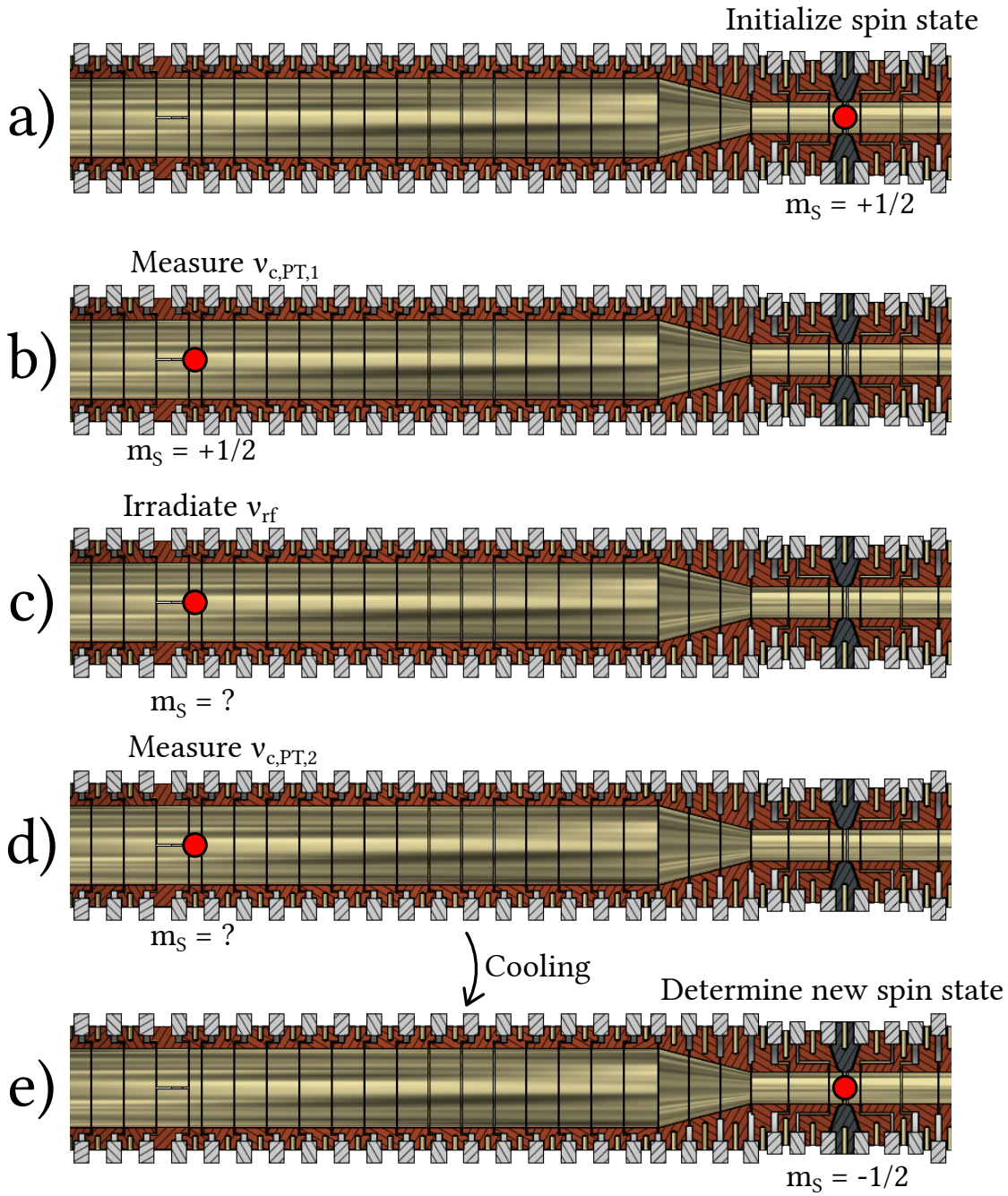

Figure 3.15: Double-trap measurement scheme of the (anti)proton g-factor: a) A cold particle is prepared in the precision trap and its spin state is initialized in the analysis trap. b) The particle is moved to the precision trap and its free cyclotron frequency $\nu_{c,PT,1}$ is measured. c) The particle is irradiated with a radiofrequency $\nu_{rf,PT}$ close to the Larmor frequency in the precision trap. d) The free cyclotron frequency $\nu_{c,PT,2}$ is measured a second time to account for linear drifts. e) The particle is moved to the analysis trap and the spin state after irradiation in the precision trap is determined.

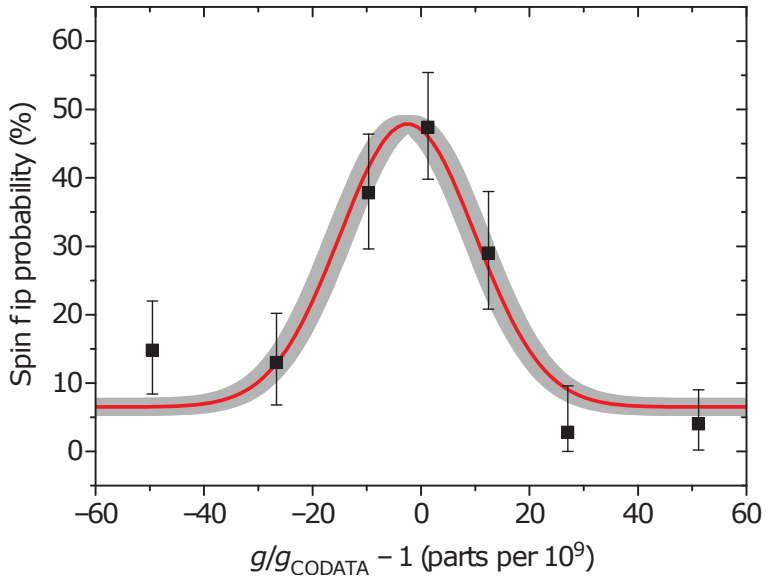

Figure 3.16: Proton g-factor resonance consisting of 450 measurements in the double trap of the BASE-Mainz experiment [129]. The spin flip probability is maximized if the ratio $\frac{\nu_{rf,PT}}{\nu_{c,PT}}$ between the irradiated radiofrequency $\nu_{rf,PT}$ and the free cyclotron frequency $\nu_{c,PT}$ is equal to $\frac{g}{2}$.

The probability to flip the spin is maximized if the irradiated radiofrequency $\nu_{rf,PT}$ is equal to the Larmor frequency $\nu_{L,PT} = \frac{g}{2}\nu_{c,PT}$ in the precision trap. Thus, the value of $\frac{g}{2} = \frac{\nu_{L,PT}}{\nu_{c,PT}}$ can be determined by measuring the spin flip probability p_{SF} as a function of the ratio $\frac{\nu_{rf,PT}}{\nu_{c,PT}}$. The free cyclotron frequency $\nu_{c,PT}$ is determined by averaging the measurements $\nu_{c,PT,1}$ and $\nu_{c,PT,2}$ before and after application of the radiofrequency. Figure 3.16 shows the g-factor resonance for a proton consisting of 450 data points measured in the double-trap setup located in Mainz [129]. Using this novel approach, the proton g-factor was determined by the BASE-Mainz experiment with a fractional uncertainty of 3.3 p.p.b. [129]. In a later measurement campaign [130], this result was improved to a fractional uncertainty of 300 p.p.t. In this modified scheme, systematic shifts due to temporal fluctuations of the magnetic field and the particle temperature are suppressed as ν_L and ν_c are measured at the same time. Additionally, the g-factor resonance was measured at a lower drive power which no longer saturates the spin flip probability and a new cyclotron detector was implemented leading to faster cooling times and a higher sampling rate. Nevertheless, the final uncertainty of the updated measurement is dominated by the statistical uncertainty caused by the long cooling times required to prepare particles at temperatures low enough for single spin flip detection.

3.5.3 Two-particle method

Given the long cooling times of typically $48\,\mathrm{h}$ necessary to prepare an antiproton with a cyclotron temperature suitable for single spin flip detection in the BASE-CERN experiment, a novel technique utilizing two particles was implemented in the 2017 antiproton g-factor run. The general measurement scheme is equivalent to double-trap method described in chapter 3.5.2, however, instead of using the same particle to measure the free cyclotron frequency $\nu_{c,PT}$ and the Larmor frequency $\nu_{L,PT}$, two particles are used. This approach exploits the fact that the measurement of the spin flip probability after irradiation with the radiofrequency $\nu_{rf,PT}$ does not heat the cyclotron temperature T_+ of the particle. Thus, as long as the cyclotron detector in the precision trap is detuned during the irradiation with $\nu_{rf,PT}$, the particle's cyclotron mode is not heated and no cooling is required. In the two particle scheme, one particle – called Larmor particle – is used to probe spin flips and thus needs to be cooled to low cyclotron temperatures T_+ providing single spin flip resolution. A second particle – called cyclotron particle – is used to measure the cyclotron frequency. Measurement of $\nu_{c,PT}$ heats the cyclotron temperature T_+ of the particle, however, since the cyclotron particle is not used for spin state detection no subthermal cooling of the cyclotron particle is required.
In order to measure the antiproton g-factor, two particles are extracted from the reservoir trap and stored in the precision and analysis trap respectively. As a first step, the cyclotron particle located in the precision trap is stored in a transport electrode upstream and the Larmor particle is moved from the analysis trap to the precision trap. As in the single particle double-trap method, the Larmor particle is thermalized by interaction with the cyclotron detector until a cold particle with axial frequency stability suitable for single spin flip detection is found in the analysis trap. Next, the Larmor particle's spin state is initialized by driving spin flips in the analysis trap until a large jump is observed. Once the spin state is initialized, the cyclotron particle is moved into the precision trap and the free cyclotron frequency $\nu_{c,PT,1}$ is measured using sideband coupling of the axial and modified cyclotron modes. Next the cyclotron detector in the precision trap is detuned and the cyclotron particle is parked in the upstate transport electrode. The Larmor particle is moved into the precision trap and the radio-frequency $\nu_{rf,PT}$ is irradiated. Note that this does not heat the cyclotron temperature of the Larmor particle and thus – in contrast to the single particle double-trap method – no cooling is required and the Larmor particle is directly moved into the analysis trap. Next, the cyclotron particle is moved back into the precision trap and the free cyclotron frequency $\nu_{c,PT,2}$ is measured a second time. In order to determine if the irradiation with $\nu_{rf,PT}$ lead to a change of the Larmor particle's spin state, spin flips are driven in the analysis trap and the spin state after irradiation in the precision trap is recovered as described in chapter 3.5.2. Given the observed mean heating rate

of less than $17\,\mathrm{mK}$ per cycle, up to 75 measurements can be conducted before the particle has to be cooled again. Figure 3.17 shows the individual steps of the measurement scheme outlined above.

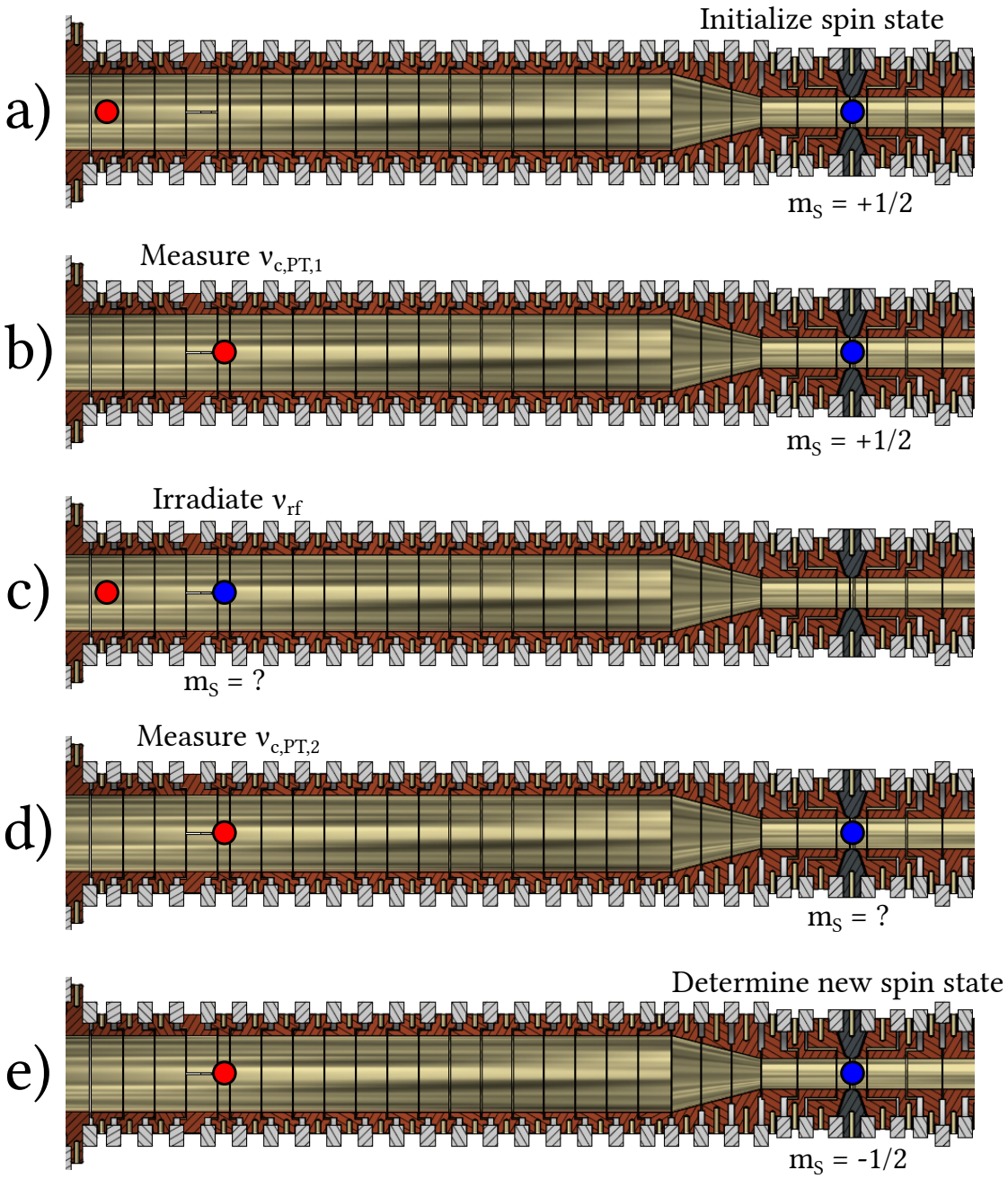

Figure 3.17: Two particle measurement scheme of the antiproton g-factor: a) The Larmor particle (blue) is thermalized in the precision trap and its spin state is initialized in the analysis trap. b) The cyclotron particle (red) is moved into the precision trap and its free cyclotron frequency $\nu_{c,PT,1}$ is measured. c) The Larmor particle is moved into the precision trap and a radio-frequency $\nu_{rf,PT}$ close to the Larmor frequency in the precision trap is irradiated. d) The Larmor particle is moved to the analysis trap and the free cyclotron frequency $\nu_{c,PT,2}$ is measured a second time using the cyclotron particle. e) The spin state of the Larmor particle after irradiation with $\nu_{rf,PT}$ in the precision trap is determined.

As in the two trap measurement scheme, the g-factor is determined by measuring the spin flip probability p_{SF} as a function of the ratio $\frac{\nu_{rf,PT}}{\nu_{c,PT}}$. However, given that different particles are used for the determination of $\nu_{L,PT}$ and $\nu_{c,PT}$, the free cyclotron frequency can not be measured while the radio-frequency drive is applied. Given the residual magnetic gradients in the precision trap of $B_{1,PT} = 71.2(4)\,\frac{\mathrm{mT}}{\mathrm{m}}$ and $B_{2,PT} = 2.74(22)\,\frac{\mathrm{T}}{\mathrm{m}^2}$ present in the 2017 antiproton g-factor run, differences in the axial and cyclotron temperatures of the Larmor and cylotron particle lead to systematic shifts of the measured ratios $\frac{\nu_{rf,PT}}{\nu_{c,PT}}$ which translates into a shift of the final g-factor. Given that the free cyclotron frequency is measured while the particle is sideband coupled to the axial detector, the cyclotron temperature $T_{+,c}$ of the cyclotron particle is significantly higher than the cyclotron temperature $T_{+,L}$ of the cold Larmor particle. The resulting temperature difference $\Delta T_+ = T_{+,c} - T_{+,L} = 356(27)\,\mathrm{K}$ leads to a relative shift of the final g-factor of +$0.22(2)$ p.p.b. due to a change in axial equilibrium position caused by $B_{1,PT}$ and +$0.12(2)$ p.p.b. due to a change in radial position in the magnetic bottle $B_{2,PT}$. In order to characterize a possible difference in axial temperature T_z caused by additional noise added during irradiation of the radio-frequency $\nu_{rf,PT}$, the detector noise level was observed during measurements with and without application of the Larmor drive. In case the spin flip drive was applied, the observed noise level was increased by $0.355(36)\,\mathrm{dB}$. To give a conservative estimate it is assumed that the increased noise level couples to the input stage of the resonator and thus increases the axial temperature of the Larmor particle by $\Delta T_z = 0.68\,\mathrm{K}$ which causes the Larmor particle to experience a different average magnetic field. The resulting uncertainty in Larmor frequency is given by Eq. (2.45) and leads to the dominant systematic uncertainty of $0.97(7)$ p.p.b. A detailed description including all systematic shifts is given in [68].

Figure 3.18 shows the g-factor resonance measured in the BASE-CERN double trap in 2017. In order to ensure a good contrast in the spin flip probability between resonant and off-resonant drive, the Larmor frequency was driven at high amplitude which leads to significant saturation in the g-factor resonance.

Using the novel two particle method, the antiproton g-factor was determined with a fractional precision of 1.5 p.p.b in 2017. The main contribution of 0.97 p.p.b to the uncertainty is given by the possible difference of the axial temperatures of the two particles. The residual magnetic bottle $B_{2,PT}$ present in the precision trap causes the free cyclotron frequency ν_c and the Larmor frequency ν_L to be measured in different mean magnetic fields in case the particles mean squared amplitudes differ. In the course of this work, a magnetic shimming system was implemented which provides the possibility to tune $B_{2,PT}$ close to zero, thus eliminating the dependency of the free cyclotron frequency ν_c and the Larmor frequency ν_L on the particles' respective axial energies.

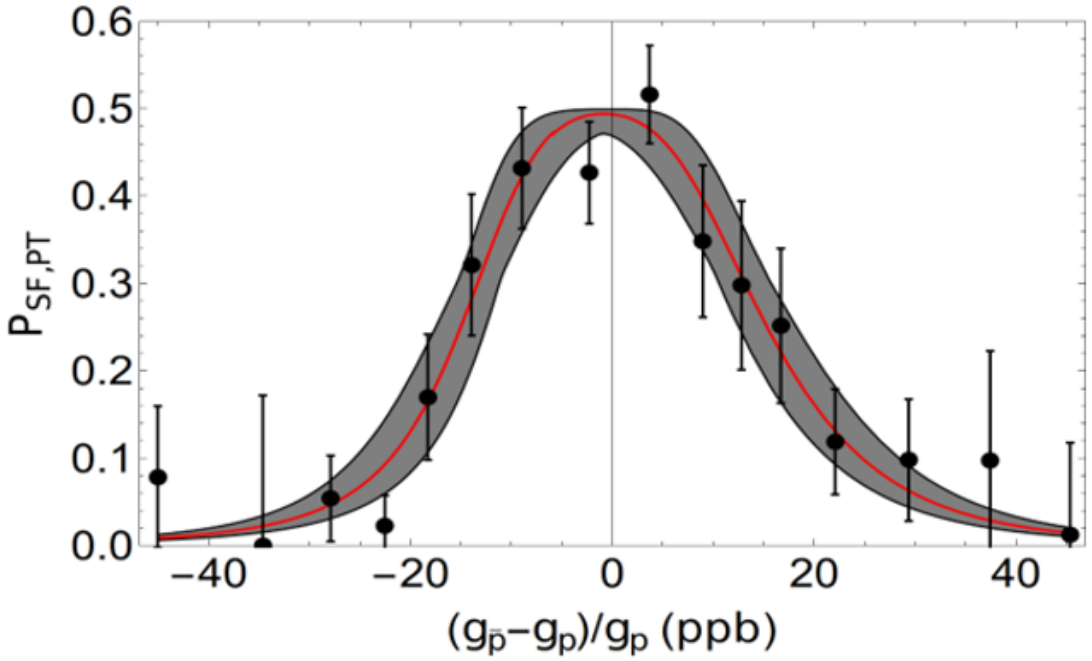

Figure 3.18: Antiproton g-factor resonance measured using two particles in the BASE-CERN double trap [68]. In order to ensure good contrast between resonant and off-resonant drive, spin flips were driven at high power in the precision trap and the resonance was saturated on purpose.

4 Magnetic shimming and shielding system

4.1 Motivation

In order to gain control over the main systematic uncertainties of frequency measurements in Penning traps, a superconducting shimming and shielding system was implemented in the experiment. This system consists of four coils which are wrapped around the trap can. Three shimming coils provide tunability of the coefficients B_2, B_1 and B_0 in the expansion of the magnetic field $B(z) = B_0 + B_1 z + B_2 z^2 + \dots$ around the center of the precision trap at $z = 0$ while the 4th coil is wound in a length to diameter ratio that provides good shielding against homogeneous fluctuations of the magnetic background field [131]. The three shimming coils are wound in a way that each of the coils has a large transfer function for one of the parameters B_2, B_1 or B_0 while the transfer function for the other two parameters is small. Figure 4.1 shows the shimming coil system and the self-shielding coil (SSC) on the trap can.
All coils are equipped with a quench resistor R_Q which provides the possibility to locally heat part of the superconducting wire above it's critical temperature causing any current flowing in the coil to decay. Additionally, the three shimming coils can be loaded via loading joints located on both sides between the quench heater and the coil. Figure 4.2 shows the schematic setup of the coils. A detailed explanation of the loading procedure is given in section 4.6.

4.2 Calculation of the coil transfer functions

All coils of the shimming and shielding system are made up of one or more tightly wound solenoids of constant radius. For this reason, the transfer functions of each coil can be calculated by adding the transfer functions of the individual solenoids, taking account of the direction of winding. The magnetic flux density $B(z, \rho)$ at an axial distance z and radial distance ρ from the coil center can be expressed with the help of the complete elliptic integrals $K(k)$, $E(k)$ and $\Pi(n, k)$ of the first, second and third kind:

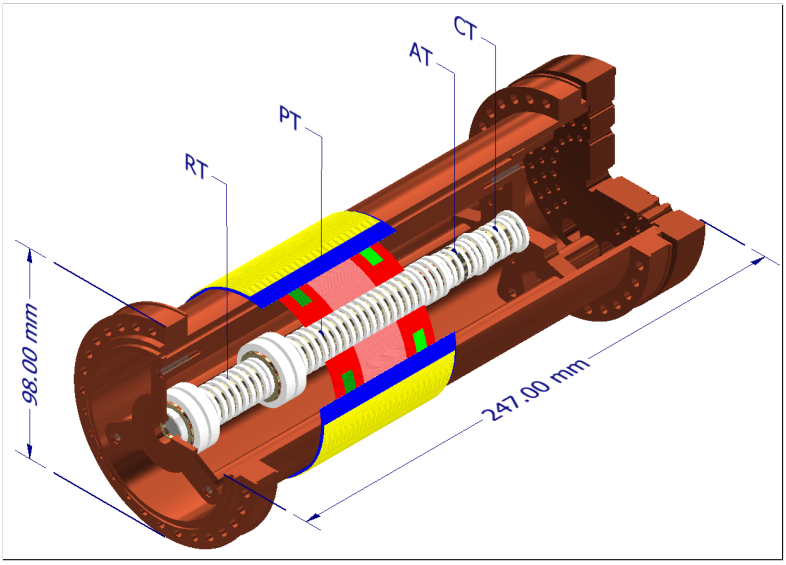

Figure 4.1: Position of the B2 coil (red), B1 coil (green), B0 coil (blue) and the SSC (yellow) on the trap can. Different shades of the same color indicate a reversal of winding direction. The center positions of the Reservoir trap (RT), Precision trap (PT), Analysis trap (AT) and Cooling trap (CT) are indicated. The shimming and shielding system is centered around the Precision trap.

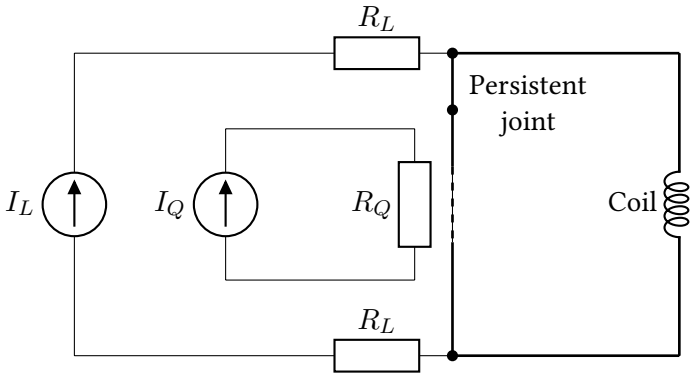

Figure 4.2: Schematic setup of the shimming coils. Thick lines indicate superconducting wires. By running the quench current I_Q through the quench resistor R_Q, which is in thermal contact with the superconducting wire, part of the coil is heated above the critical temperature, and becomes non-persistent (dashed line). The shimming coils are equipped with loading joints which can be used to apply an external loading current I_L to charge the coils. The heat dissipation in the parasitic loading resistances R_L limits the maximum current that can be loaded without quenching part of the coil.

$$K(m) = \int_0^{\frac{\pi}{2}} \frac{1}{\sqrt{1 - m^2 \sin^2(\theta)}} \mathrm{d}\theta, \tag{4.1}$$

$$E(m) = \int_0^{\frac{\pi}{2}} \sqrt{1 - m^2 \sin^2(\theta)} \mathrm{d}\theta, \tag{4.2}$$

$$\Pi(n, m) = \int_0^{\frac{\pi}{2}} \frac{1}{(1 + n \sin^2 \theta)\sqrt{1 - m^2 \sin^2(\theta)}} \mathrm{d}\theta. \tag{4.3}$$

The axial and radial magnetic flux density components $B_z(z, \rho)$ and $B_\rho(z, \rho)$ created by a current I running through a tightly wound solenoid with n windings, radius R and length L are given by [132]:

$$B_\rho(z, \rho) = \frac{\mu_0 n I}{\pi L} \sqrt{\frac{R}{\rho}} \left[\frac{g^2 - 2}{2k} K(g^2) + \frac{E(g^2)}{g} \right]_{\zeta_-}^{\zeta_+}, \tag{4.4}$$

$$B_z(z, \rho) = \frac{\mu_0 n I}{4\pi L} \sqrt{\frac{1}{\sqrt{R\rho}}} \left[\zeta g \left(K(g^2) + \frac{R - \rho}{R + \rho} \Pi(h^2, g^2) \right) \right]_{\zeta_-}^{\zeta_+}. \tag{4.5}$$

The permeability of free space is given by μ_0, $\zeta_\pm = z \pm \frac{L}{2}$, $h^2 = \frac{4R\rho}{(R+\rho)^2}$ and $g^2 = \frac{4R\rho}{(R+\rho)^2 + \zeta^2}$ are geometry dependent parameters and $[f(x)]_b^a = f(a) - f(b)$.
On the symmetry axis $B_\rho(z)$ vanishes and $B_z(z)$ becomes

$$B_z(z) = \frac{\mu_0 n I}{2L} \left(\frac{z + \frac{L}{2}}{\sqrt{R^2 + (z + \frac{L}{2})^2}} - \frac{z - \frac{L}{2}}{\sqrt{R^2 + (z - \frac{L}{2})^2}} \right). \tag{4.6}$$

The transfer functions at position z_0 can be determined by comparing the Taylor expansion coefficients $B_z(z) = \sum_{n=0}^{\infty} \frac{1}{n!} \frac{\partial^n B_z(z)}{\partial z^n}^n$ of Eq. (4.6) with their respective terms in the field expansion $B_z(z) = \sum_{n=0}^{\infty} B_n (z - z_0)^n$. Figure 4.3 shows a cross section through the coil system. Table 4.1 gives an overview over the design parameters (Radius r, Offsets z_{Off} from the trap center, Lengths L and Number of windings n of the subcoils) and transfer functions at the trap center $\frac{B_0}{I}, \frac{B_1}{I}, \frac{B_2}{I}, \ldots$ of the 3 shimming coils and the SSC.
Figures 4.4a - 4.4c show the transfer functions of the shimming coils at different positions along

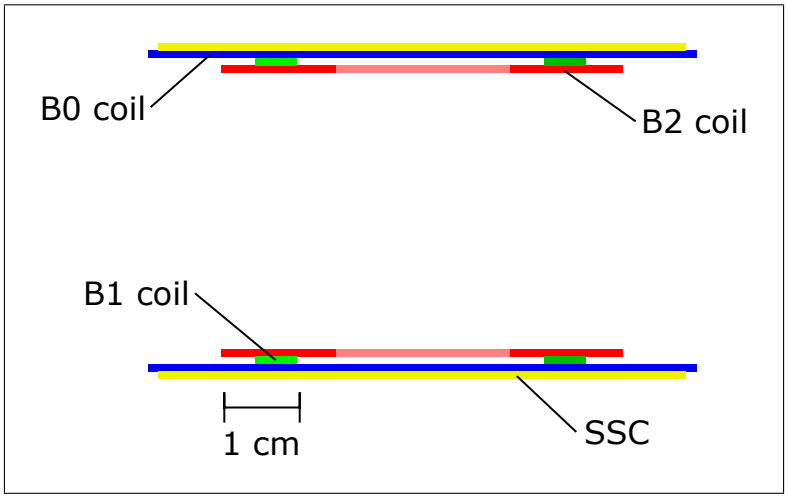

Figure 4.3: Cross section through the B2 coil (red), B1 coil (green), B0 coil (blue) and the SSC (yellow). Different shades of the same color indicate a reversal of winding direction.

Coil	r [mm]	z_{Off} [mm]	L [mm]	n	$\frac{B_0}{I}$ $[\frac{\text{T}}{\text{A}}]$	$\frac{B_1}{I}$ $[\frac{\text{T}}{\text{m A}}]$	$\frac{B_2}{I}$ $[\frac{\text{T}}{\text{m}^2\text{A}}]$
B2 coil	38.575	$-19.125, 0, 19.125$	$15.3, 22.95, 15.3$	$102, -153, 102$	-359×10^{-9}	0	1.87
B1 coil	39.075	$-19.5, 19.5$	$5.55, 5.55$	$37, 37$	0	26×10^{-3}	0
B0 coil	39.575	0	72.75	485	5.67×10^{-3}	0	-1.6
SSC	40.075	0	70.2	468	5.52×10^{-3}	0	-1.65

Table 4.1: Design parameters of the shimming and shielding coil system. Negative windings indicate a reversal of the winding direction. The parameters were given to the full precision used in the calculations of the transfer function and inductances, however, given that the coils were wound by hand and on top of each other, it is expected that the physical system deviates from the design values.

the trap axis. Both the B_2 and the B_1 coil show a large transfer function for the parameter they are designed to change, while in the chosen design the transfer function for the other two parameters vanishes. The number of windings was chosen based on finite-element simulations of the residual field inhomogeneities in the PT caused by the ferromagnetic ring electrode of the AT. An estimate for the achievable loading current was determined in an earlier work [133]. The B_0 coil is wound as a single solenoid and thus has a large transfer function for both B_2 and B_0. This design was chosen over a setup with two solenoids in Helmholtz configuration to have a second solenoid which provides partial self-shielding. Using multiple self-shielding solenoids with different length-to-diameter ratios provides the possibility to run different combinations of coils with slightly different self-shielding characteristic and increases robustness against misalignment and uncertainties in the winding process as well as effects of mutual inductance with the main coil of the BASE magnet.

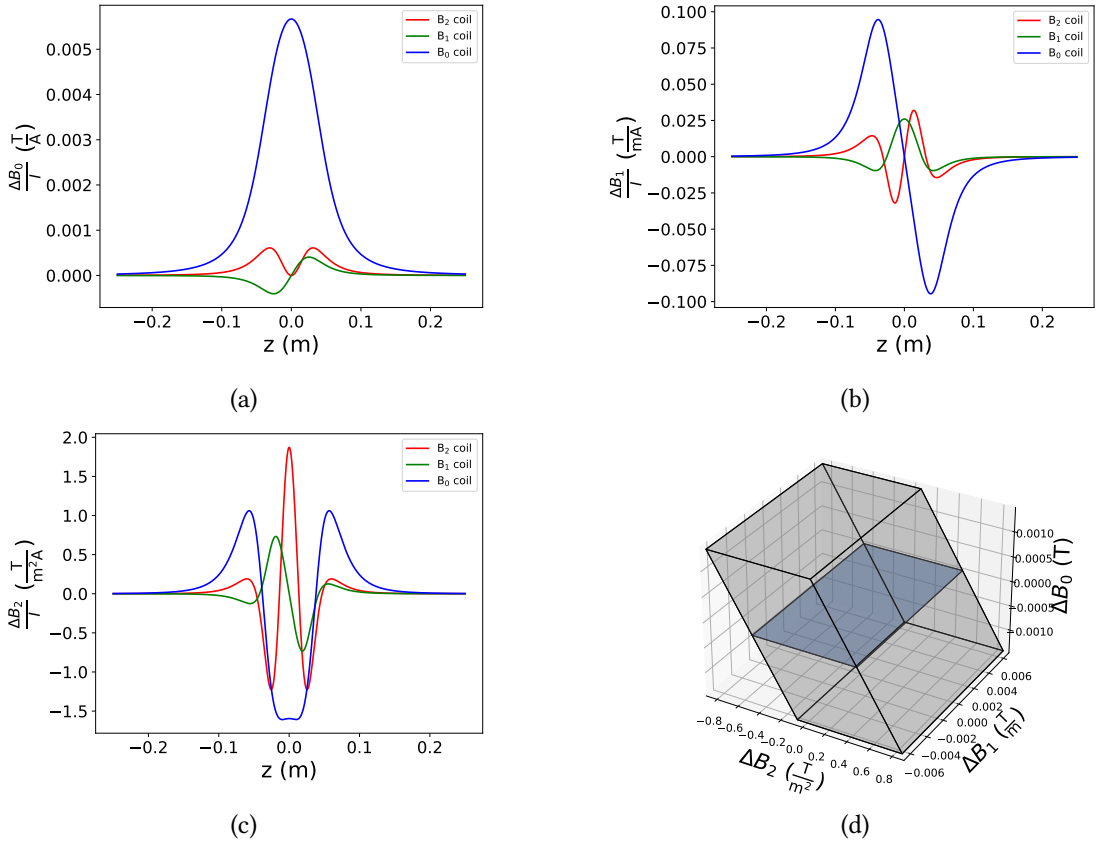

Figure 4.4: (a) B_0 transfer function as a function of axial position. (b) B_1 transfer function as a function of axial position. (c) B_2 transfer function as a function of axial position. (d) Combination of field expansion parameters that can be compensated with currents less than 250 mA. The colored plane at $\Delta B_0 = 0$ indicates the region in which ΔB_2 and ΔB_1 can be tuned without changing B_0.

4.3 Calculation of inductances

In order to calculate the shielding provided by different coil geometries, the coils self- and mutual inductances must be known. The self-inductance L of a coil relates the change ΔI of current running in the coil to the change $\Delta\Phi$ of the magnetic flux through the coil:

$$L = \frac{\Delta\Phi}{\Delta I}. \tag{4.7}$$

This relation is symmetric, meaning that a change in current I causes a change in magnetic flux Φ through the coil and any change in magnetic flux through a coil induces a corresponding current in the coil. In case the system consists of multiple coils $\mathrm{C}_1, \ldots, \mathrm{C}_\mathrm{n}$, the flux Φ_j through

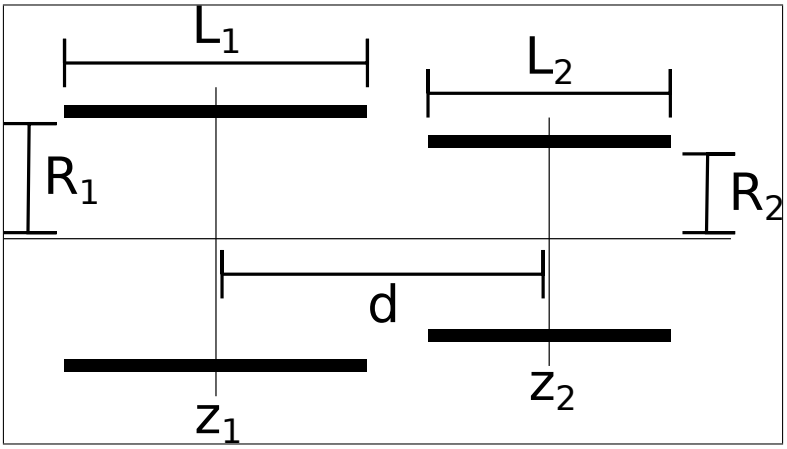

Figure 4.5: The mutual inductance between two coils only depends on their lengths L, radii R, their relative distance d and number of windings n.

coil $\mathrm{C_j}$ can change not only when the current I_j through $\mathrm{C_j}$ changes, but also when any of the other coils $\mathrm{C_k}$ experiences a change in current $\mathrm{I_k}$. The mutual inductance M_{jk} describes the change $\Delta\Phi_i$ in flux through coil $\mathrm{C_j}$ caused by a change in current I_j through coil $\mathrm{C_j}$. The total change in flux $\Delta\Phi_1, \ldots, \Delta\Phi_n$ through each coil can thus be written as the product of the mutual inductance matrix M and the change in current $\Delta I_1, \ldots, \Delta I_n$ through each coil:

$$\begin{pmatrix} \Delta\Phi_1 \\ \Delta\Phi_2 \\ \vdots \\ \Delta\Phi_N \end{pmatrix} = \begin{pmatrix} M_{11} & M_{12} & \ldots & M_{1N} \\ M_{21} & \ddots & & M_{2n} \\ \vdots & & \ddots & \vdots \\ M_{N1} & \ldots & \ldots & M_{NN} \end{pmatrix} \begin{pmatrix} \Delta I_1 \\ \Delta I_2 \\ \vdots \\ \Delta I_N \end{pmatrix}. \tag{4.8}$$

Note that M is symmetric ($M_{jk} = M_{kj}$) and that the diagonal elements of M contain the self-inductances of the coils ($M_{jj} = L_j$). The individual elements M_{jk} of M depend only the physical parameters of the coils $\mathrm{C_j}$ and $\mathrm{C_k}$ and their alignment towards each other. Figure 4.5 shows the geometrical parameters relevant for the calculation of the mutual inductance between two coils.

The derivation of the mutual inductance between two coaxial coils with lengths L_1 and L_2, radii R_1 and R_2, windings n_1 and n_2 and relative distance d is given by Cohen [134] and only the main steps are outlined here.

The mutual inductance M_{Loop} between two coaxial current loops with radii R_1 and R_2 separated by a distance d is given by the integrals over the two current loops:

$$M_{Loop} = \mu_0 \int_0^{2\pi} \int_0^{2\pi} \frac{R_1 R_2 \cos(\phi_1 - \phi_2)}{r(\phi_1, \phi_2)} \mathrm{d}\phi_1 \mathrm{d}\phi_2. \tag{4.9}$$

The distance $r(\phi_1, \phi_2)$ between the infinitesimal elements along the loop is given by

$$r(\phi_1, \phi_2) = \sqrt{R_1^2 + R_2^2 + d^2 - 2R_1 R_2 \cos(\phi_1 - \phi_2)}. \tag{4.10}$$

Replacing the integral over both angles with an integral over the difference of the angles ψ and using symmetry of the cosine, Eq. (4.9) can be rewritten as:

$$M_{Loop} = 4\pi\mu_0 \int_0^{\pi} \frac{R_1 R_2 \cos(\psi)}{\sqrt{R_1^2 + R_2^2 + d^2 - 2R_1 R_2 \cos(\psi)}} \mathrm{d}\psi. \tag{4.11}$$

In order to calculate the mutual inductance $M_{j,k}$ between the coils, M_{Loop} is integrated over the windings of both coils:

$$M = 4\pi\mu_0 \frac{n_1}{L_1} \frac{n_2}{L_2} \int_{z_1 - \frac{L_1}{2}}^{z_1 + \frac{L_1}{2}} \int_{z_2 - \frac{L_2}{2}}^{z_2 + \frac{L_2}{2}} M_{Loop} \mathrm{d}z_1 \mathrm{d}z_2. \tag{4.12}$$

Integration over z_1 and z_2 is straight forward and – as expected – the resulting mutual inductance M depends only on the distance d between the coil centers and not on the absolute positions z_1 and z_2 of the coil centers:

$$\begin{aligned} M = 4\pi\mu_0 \frac{n_1}{L_1} \frac{n_2}{L_2} \int_0^{\pi} \frac{(R_1 R_2)^2 \sin^2(\psi)}{R_1^2 + R_2^2 - 2R_1 R_2 \cos(\psi)} \Bigg[& \sqrt{R_1^2 + R_2^2 + \left(d + \frac{L_1}{2} + \frac{L_2}{2}\right)^2 - 2R_1 R_2 \cos(\psi)} \\ & + \sqrt{R_1^2 + R_2^2 + \left(d - \frac{L_1}{2} - \frac{L_2}{2}\right)^2 - 2R_1 R_2 \cos(\psi)} \\ & - \sqrt{R_1^2 + R_2^2 + \left(d + \frac{L_1}{2} - \frac{L_2}{2}\right)^2 - 2R_1 R_2 \cos(\psi)} \\ & - \sqrt{R_1^2 + R_2^2 + \left(d - \frac{L_1}{2} + \frac{L_2}{2}\right)^2 - 2R_1 R_2 \cos(\psi)} \Bigg] \mathrm{d}\psi. \end{aligned} \tag{4.13}$$

By defining $c_1 = d + \frac{L_1}{2} + \frac{L_2}{2}$, $c_2 = d - \frac{L_1}{2} - \frac{L_2}{2}$, $c_3 = d + \frac{L_1}{2} - \frac{L_2}{2}$ and $c_4 = d - \frac{L_1}{2} + \frac{L_2}{2}$

the integrals in Eq. (4.13) can be brought to a common form

$$V_n = \int_0^{\pi} \frac{(R_1 R_2)^2 \sin^2(\psi)}{R_1^2 + R_2^2 - 2R_1 R_2 \cos(\psi)} \sqrt{R_1^2 + R_2^2 + c_n^2 - 2R_1 R_2 \cos(\psi)} \mathrm{d}\psi \tag{4.14}$$

and the mutual inductance can be written as

$$M = 4\pi\mu_0 \frac{n_1}{L_1} \frac{n_2}{L_2} \left(V_1 + V_2 - V_3 - V_4\right). \tag{4.15}$$

The full derivation of the solution of Eq. (4.14) is given in [134] and only the final form will be given here. By introducing the parameters

$$k_n^2 = \frac{4R_1 R_2}{(R_1 + R_2)^2 + c_n^2}, \tag{4.16}$$

$$k_n'^2 = 1 - k_n^2, \tag{4.17}$$

$$\text{and } \sin^2(\theta_n) = \frac{(R_1^2 - R_2^2) + c_n^2 (R_1 - R_2)^2}{(R_1^2 - R_2^2) + c_n^2 (R_1 + R_2)^2} \tag{4.18}$$

as well as the incomplete elliptic integrals $K'(\theta, m)$ and $E'(\theta, m)$ of first and second kind

$$K'(\varphi, m) = \int_0^{\varphi} \frac{1}{\sqrt{1 - m^2 \sin^2(\alpha)}} \mathrm{d}\alpha, \tag{4.19}$$

$$E'(\varphi, m) = \int_0^{\varphi} \sqrt{1 - m^2 \sin^2(\alpha)} \mathrm{d}\alpha. \tag{4.20}$$

V_n can be expressed as

$$\begin{aligned} V_n = &- (R_1^2 - R_2^2) c_n \left[K(k_n) \left(K'(\theta_n, k_n') - E'(\theta_n, k_n') - E(k_n) K'(\theta_n, k_n')\right)\right] \\ &+ \frac{c_n^4 - (R_1^2 - 6R_1 R_2 + R_2^2) c_n^2 - 2(R_1^2 - R_2^2)^2}{3\sqrt{(R_1 + R_2)^2 + c_n^2}} K(k_n) \\ &+ \frac{2(R_1^2 + R_2^2) - c_n^2}{3} \sqrt{(R_1 + R_2)^2 + c_n^2} E(k_n) - \frac{\pi}{2} \sqrt{(R_1^2 - R_2^2)^2 c_n^2}. \end{aligned} \tag{4.21}$$

In case the radii of the coils are equal ($R_1 = R_2$) or two ends of the coils coincide ($c_n = 0$),

some of the expressions in Eq. (4.21) vanish or diverge:

1. $R_1 = R_2 = R$ and $c \neq 0$
   In case the radii of the coils are equal but the ends do not coincide, the parameters in Eqs. (4.16 - 4.18) become $k_n^2 = 0, k_n'^2 = 1,$ and $\sin^2(\theta_n) = 0$. In this case V_n is given by:

$$\begin{aligned} V_n =& \frac{c_n^4 + 4R^2 c_n^2}{3\sqrt{4R^2 + c_n^2}} K(k_n) \\ &+ \frac{16R^4 - c_n^4}{3\sqrt{4R^2 + c_n^2}} E(k_n). \end{aligned} \tag{4.22}$$

2. $R_1 \neq R_2$ and $c = 0$
   In case the radii of the coils are different but the ends coincide, the parameters are $0 < k_n^2 < 1,\ 0 < k_n'^2 < 1,$ and $\sin^2(\theta_n) = 1$. Therefore the terms containing the incomplete elliptic integrals vanish and V_n becomes:

$$\begin{aligned} V_n =& \frac{-2(R_1^2 - R_2^2)^2}{3(R_1 + R_2)} K(k_n) \\ &+ \frac{2(R_1^2 + R_2^2)}{3} (R_1 + R_2) E(k_n). \end{aligned} \tag{4.23}$$

3. $R_1 = R_2 = R$ and $c = 0$
   If the radii of the coils are equal and the ends coincide, the parameters become $k_n^2 = 1,\ k_n'^2 = 0,$ and $\sin^2(\theta_n)$ becomes undefined. However, the terms containing the (incomplete) elliptic integrals $K'(k_n, \theta_n), E'(k_n, \theta_n)$ and $K(k_n)$ vanish and V_n simplifies to:

$$V_n = \frac{8R^3}{3}. \tag{4.24}$$

The total mutual inductance between two shimming coils can be calculated by summing the mutual inductances between the individual subcoils taking account of the winding directions. Table 4.2 shows the mutual inductances between the three subcoils of the B_2-coil and the two coils of the B_1-coil.
The matrix element corresponding to the total mutual induction between two shimming coils in Eq. (4.8) is the sum of mutual inductances between the subcoils. Given the design parameters listed in Tab. 4.1, the mutual inductance matrix M of the shielding and shimming coil system is given by:

	B2 coil left	B2 coil center	B2 coil right
B1 coil left	$0.47\,\mathrm{mH}$	$-0.26\,\mathrm{mH}$	$0.07\,\mathrm{mH}$
B1 coil right	$-0.07\,\mathrm{mH}$	$0.26\,\mathrm{mH}$	$-0.47\,\mathrm{mH}$

Table 4.2: Mutual inductance between the subcoils of the B_2 and B_1 shimming coils. The total mutual inductance between the two coils is given by the sum of all values in the table.

$$\mathrm{M} = \begin{pmatrix} 2.30 & 0 & 1.04 & 0.97 \\ 0 & 0.42 & 0 & 0 \\ 1.04 & 0 & 13.39 & 12.95 \\ 0.97 & 0 & 12.95 & 13.03 \end{pmatrix} \mathrm{mH}. \tag{4.25}$$

4.4 Calculation of shielding factors

The Antiproton Decelerator (AD), which is used to supply the experiments with low energy antiprotons, uses dipole and quadrupole magnets to define the trajectory of the antiprotons during deceleration. The magnetic field which is required to prevent the antiprotons from hitting the wall of the AD's vacuum chambers changes with the energy of the antiprotons. Therefore, the current in the AD's bending magnets changes with a period of roughly $120\,\mathrm{s}$. This change in current also changes the magnets' far fields which causes the cyclotron frequency in the precision trap to fluctuate by up to $10\,\mathrm{Hz}$ peak-to-peak per deceleration cycle [122]. The influence of the AD can be partially mitigated by synchronizing the measurement sequence to the deceleration cycle of the AD, however, high-precision measurements require these external fluctuations to be shielded. Gabrielse and Tan suggested placing a superconducting coil which counteracts external fluctuations of the magnetic field around the trap can [131]. The following derivation of shielding factors is outlined in [131].

In case a superconducting coil with self-inductance L is wound around the trap can, a homogeneous change of the external magnetic field B_{ext} along the symmetry axis of the coil will change the magnetic flux $\Phi = \int_A \mathbf{B}_{\mathrm{ext}} \mathrm{d}\mathbf{A}$ through the coil. Note that the flux surface A is given by the product of the cross-section πr^2 and the number of windings of the individual subcoils, taking the direction of winding into account. Using Eq. (4.7) we can calculate the induced current I that counteracts the change in magnetic flux:

$$I = \frac{\Phi}{L} = \frac{\int_A B_{\mathrm{ext}} \mathrm{d}\mathbf{A}}{L} = \frac{A}{L} B_{ext}. \tag{4.26}$$

Given that the shielding coil is superconducting, the induced current I will continue to flow

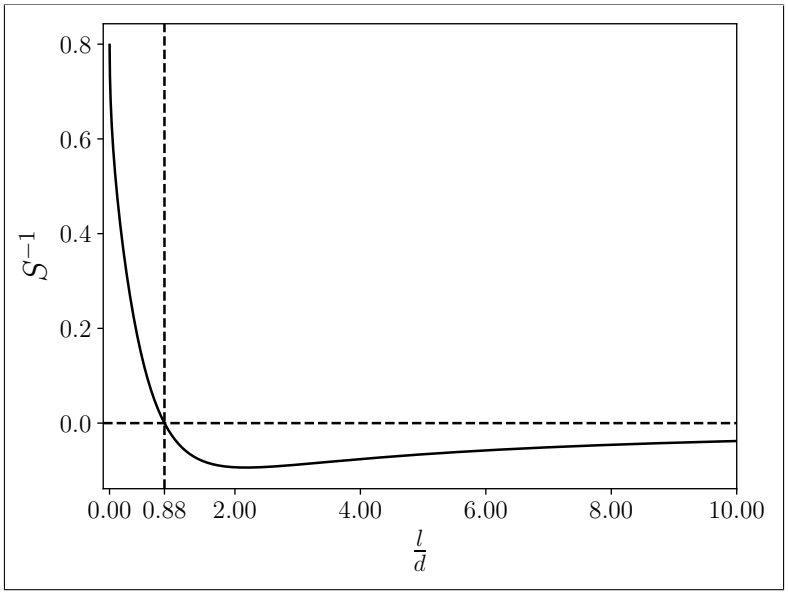

Figure 4.6: Inverse shielding factor at the center of a single air-core solenoid for different length to diameter ratios $\frac{l}{d}$. At $\frac{l}{d} \approx 0.876$ homogeneous external fluctuations are shielded completely.

indefinitely. This current produces a magnetic flux density B_{Coil} at the position of the particle that depends on the transfer function $g = \frac{\Delta B_{Coil}}{I}$ of the coil. The total change of the magnetic flux density ΔB at the location of the particle is given by

$$\Delta B = B_{ext} - B_{Coil} = B_{ext} - gI_{Coil} = B_{ext} - gB_{ext}\frac{A}{L} = B_{ext}\left(1 - \frac{gA}{L}\right) \tag{4.27}$$

and thus external fluctuations are reduced by the inverse shielding factor $S^{-1} = 1 - \frac{gA}{L}$. Figure 4.6 shows the inverse shielding factor at the center of a solenoid for different length to diameter ratios $\frac{l}{d}$. At a ratio $\frac{l}{d} \approx 0.876$ the solenoid shields external homogeneous fluctuations of the magnetic field completely.

In case there are multiple coils involved, calculation of the shielding factor is more complicated. When the external magnetic field changes, currents are induced in all coils and the mutual inductances M_{jk} between the coils start to play a role. The currents $I_1, \ldots, I_N$ in the individual coils can be determined by solving:

$$\begin{pmatrix} M_{11} & M_{12} & \dots & M_{1n} \\ M_{21} & \ddots & & M_{2n} \\ \vdots & & \ddots & \vdots \\ M_{n1} & \dots & \dots & M_{NN} \end{pmatrix} \begin{pmatrix} I_1 \\ I_2 \\ \vdots \\ I_N \end{pmatrix} = \begin{pmatrix} A_1 \\ A_2 \\ \vdots \\ A_N \end{pmatrix} B_{ext}. \tag{4.28}$$

Once the currents are known, the magnetic flux density created by the coil system can be calculated by adding the contributions of the individual coils. If the transfer functions $g_1, \dots, g_N$ of the individual coils are written as a vector $\mathbf{g}$, the change in flux density ΔB experienced by the particle is given by:

$$\Delta B = B_{ext} - \mathbf{g}^\intercal \mathbf{I} = B_{ext} - \mathbf{g}^\intercal \mathbf{M}^{-1} \mathbf{A} B_{ext} = B_{ext}(1 - \mathbf{g}^\intercal \mathbf{M}^{-1} \mathbf{A}). \tag{4.29}$$

In this case, the inverse shielding factor S^{-1} is given by:

$$S^{-1} = (1 - \mathbf{g}^\intercal \mathbf{M}^{-1} \mathbf{A}). \tag{4.30}$$

Table 4.3 shows the inverse shielding factor S^{-1} as well as the shielding factor S of all possible coil configurations. The highlighted rows indicate the configurations in which all coils are active (shimming and shielding) or only the SSC is active (shielding only). The system was designed to provide good shielding in both of these cases. Note that the high shielding factors given in Tab. 4.3 will not be achieved in the physical realization of the system since multiple assumptions which were necessary for the calculation of the mutual inductances and shielding factors are not valid in the experiment:

1. The wire used to wind the coils has a finite diameter ($150\,\mu\mathrm{m}$ which causes the mutual- and self-inductances to be different from the ones that were calculated using the approximation of a continuous current sheet.

2. Fitting the coil system with quench heaters and placing the persistent joints outside of the high field region requires additional wire which is not accounted for in the calculations.

3. The coils are wound on top of each other using PTFE tape to fixate the coils and Kapton sheets to separate them and provide a flat surface to wind the next layer on. For the purpose of designing the system, it was estimated that this increases the diameter by $1\,\mathrm{mm}$ per layer.

4. Given the distance between the BASE coil system and other sources of magnetic field in the AD hall it can be assumed that the external fluctuations of the magnetic field are

B2 coil	B1 coil	B0 coil	SSC	S^{-1}	S
inactive	inactive	inactive	inactive	1	1
active	inactive	inactive	inactive	1.0004	0.999 963
inactive	active	inactive	inactive	1	1
inactive	inactive	active	inactive	−0.010 351 1	−96.6082
inactive	inactive	inactive	active	$4.722\,77 \times 10^{-5}$	21 174
active	active	inactive	inactive	1.000 04	0.999 963
active	inactive	active	inactive	0.000 229 08	4365.29
active	inactive	inactive	active	0.011 536 4	86.6822
inactive	active	active	inactive	−0.010 351 1	−96.6082
inactive	active	inactive	active	$4.722\,77 \times 10^{-5}$	21 174
inactive	inactive	active	active	−0.014 034 8	−71.2514
active	active	active	inactive	0.000 229 08	4365.29
active	active	inactive	active	0.011 536 4	86.6822
active	inactive	active	active	−0.002 866 13	−348.902
inactive	active	active	active	−0.014 034 8	−71.2514
active	active	active	active	−0.002 866 13	−348.902

Table 4.3: Shielding factors of all possible coil configurations. The highlighted configurations correspond to the two main modes of operation the system was designed for.

homogeneous over the length of the coil system, however, they are not necessarily aligned along the axis of the coil system. Given that the shielding system only compensates the component along the trap axis, external fluctuations in the radial direction can change the misalignment between the electric and magnetic field of the trap which leads to higher order shifts.

4.5 Monte-Carlo simulations of the coil system

The coil system in wound by hand of the outside of the trap coil and thus it is expected that the lengths and positions of the individual subcoils deviate from the design values. In order to estimate the expected deviations of the transfer functions and shielding factors of the implemented system from the values calculated in sections 4.2 - 4.4, Monte-Carlo simulations of the system were carried out. For each subcoil, the position, length, radius and number of windings were varied by drawing from independent Gaussian distributions and the transfer functions, mutual inductances, shielding factors and coupling constants were calculated. Given the accuracy with which the position on the outside of the trapcan could be determined, the standard deviation of the position was set to $1\,\mathrm{mm}$, whereas length and radius were chosen

to have a standard deviation of $0.5\,\mathrm{mm}$ given the estimated flatness of the Kapton sheets on which the coils were wound. The number of windings was simulated with a standard deviation of 1 winding to account for counting errors. The whole system was simulated 1000 times and the distributions of the calculated parameters were plotted. The distributions of the transfer functions as well as the mutual inductances and inverse shielding factors of the B_2 coil the B_0 coil and the SSC roughly follow Gaussian distributions as the relative errors on the design parameters are low. However, the shielding factors as well as the coupling constants depend on the relative distances and differences in the inductances of the coils. Therefore small deviations in the characteristics of one coil can have a large influence on the shielding factor and coupling constant. Figures 4.7a and 4.7b show the distributions of the B_2 transfer function of the B_2 coil as well as the coupling factor between the B_0 coil and the SSC.

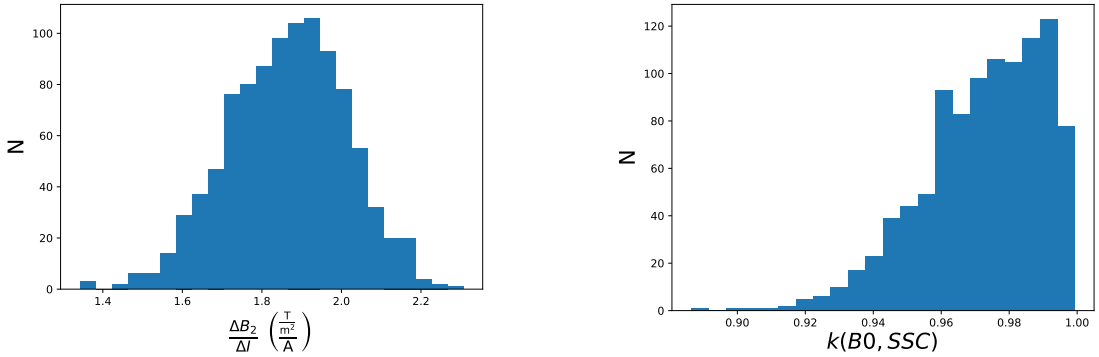

(a) (b)

Figure 4.7: (a) The distribution of the simulated B_2 transfer function of the B_2 coil roughly follows a Gaussian distribution as small deviations from the design value result in small deviations of the transfer function. (b) The coupling factor $k(B_0, SSC)$ between the B_0 coil and the SSC has to be below 1 and can not be approximated by a Gaussian distribution.

In order to quantify how much deviation between the measured parameters and the design values is to be expected given the uncertainties in manufacturing, the mean and standard deviation of the simulated parameters was determined. Table 4.4 summarizes the results of the Monte-Carlo simulations for the transfer functions and inverse shielding factors. The relative deviation between the design value μ_{Design} and simulation result is given by dividing the mean μ_{MC} of the simulated parameter by the design value. The relative uncertainty is given by as the ratio of simulated standard deviation σ_{MC} and simulated mean μ_{MC}. Matrices 4.31 and 4.32 give the mean and standard deviation of the mutual inductance matrix $\mathrm{M_{MC}}$ and coupling matrix $\mathrm{k_{MC}}$ respectively.

Parameter	μ_{Design}	μ_{MC}	σ_{MC}	$\frac{\mu_{MC}}{\mu_{Design}}$	$\left\lvert\frac{\sigma_{MC}}{\mu_{MC}}\right\rvert$
$B_2(B_2$ coil) $[\frac{\mathrm{T}}{\mathrm{m^2\,A}}]$	1.87	1.86	0.14	0.994	0.08
$B_1(B_2$ coil) $[\frac{\mathrm{mT}}{\mathrm{m\,A}}]$	0	0.32	4.18	-	13
$B_0(B_2$ coil) $[\frac{\mathrm{mT}}{\mathrm{A}}]$	-3.6×10^{-4}	-0.001	0.058	3.37	48
$B_2(B_1$ coil) $[\frac{\mathrm{T}}{\mathrm{m^2\,A}}]$	0	-7×10^{-4}	0.041	-	62
$B_1(B_1$ coil) $[\frac{\mathrm{mT}}{\mathrm{m\,A}}]$	-26.00	-25.97	0.68	0.998	0.03
$B_0(B_1$ coil) $[\frac{\mathrm{mT}}{\mathrm{A}}]$	0	3×10^{-4}	0.02	-	84
$B_2(B_0$ coil) $[\frac{\mathrm{T}}{\mathrm{m^2\,A}}]$	-1.60	-1.60	0.03	1.0001	0.018
$B_1(B_0$ coil) $[\frac{\mathrm{mT}}{\mathrm{m\,A}}]$	0	-0.08	3.16	-	79
$B_0(B_0$ coil) $[\frac{\mathrm{mT}}{\mathrm{A}}]$	0	0	0	0	0
B_2(SSC) $[\frac{\mathrm{T}}{\mathrm{m^2\,A}}]$	0	0	0	0	0
B_1(SSC) $[\frac{\mathrm{T}}{\mathrm{m\,A}}]$	0	0	0	0	0
B_0(SSC) $[\frac{\mathrm{mT}}{\mathrm{A}}]$	0	0	0	0	0

Table 4.4: Comparison between the design parameters and the results of the Monte-Carlo simulations.

$$\mathrm{M_{MC}} = \begin{pmatrix} 2.3(1) & 0.0(4) & 1.03(7) & 0.97(7) \\ 0.00(4) & 0.42(2) & 0.00(5) & 0.00(6) \\ 1.03(7) & 0.00(5) & 13.4(3) & 12.8(3) \\ 0.97(7) & 0.00(6) & 12.9(3) & 13.04(3) \end{pmatrix} \mathrm{mH}. \tag{4.31}$$

$$\mathrm{k_{MC}} = \begin{pmatrix} 1(0) & 0.00(4) & 0.19(2) & 0.18(2) \\ -0.00(4) & 1(0) & -0.00(2) & 0.00(2) \\ 0.19(2) & 0.00(2) & 1(0) & 0.97(2) \\ 0.18(2) & 0.0(2) & 0.97(2) & 1(0) \end{pmatrix}. \tag{4.32}$$

4.6 Loading scheme

In order to compensate the residual inhomogeneities B_2 and B_1 in the precision trap, it is necessary to load current into the B2 and B1 coil. Once loaded, the current in the superconducting coils keeps flowing and only changes if the magnetic flux through the coil changes (inductive change) or the coil is quenched (external change). Note that all external changes of current require the coil to be quenched. If a loading current I_L is applied to the loading joints while the coil is persistent, the current can either bypass the coil (I_B) or flow through the field-creating part of the coil (I_C). However, any fraction of the loading current I_C flowing through the field-creating part causes a change in magnetic flux through the coil and thus results in an induced current $I_I = I_C$ of the same magnitude flowing in the opposite direction. The net

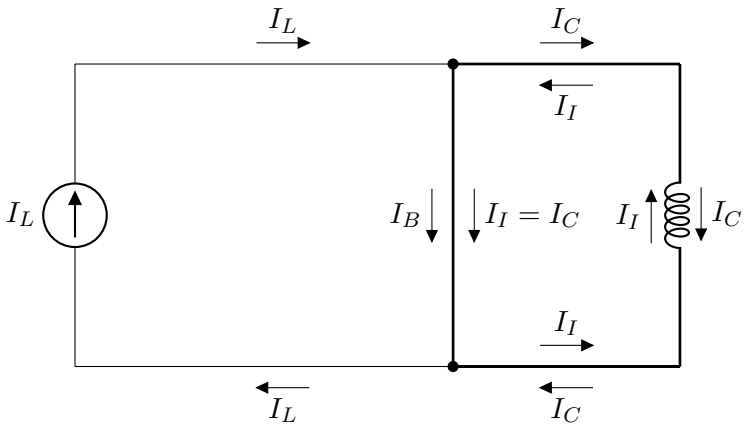

Figure 4.8: Applying a loading current I_L to a persistent coil does not change the current through the coil as any current I_C flowing through the field-creating part induces a current I_I of same magnitude in the opposite direction. Therefore, the net current in the field-creating part of the coil is $I_C - I_I = 0$ and the current in the quench branch $I_B + I_C = I_L$ is equal to the full loading current.

current flowing in the field-creating part of the coil is therefore $I_C - I_I = 0$ and the whole loading current $I_L = I_B + I_C$ bypasses the field-creating part of the coil. Figure 4.8 shows the currents in case the coil is persistent. Thick lines indicate superconducting wires. For the sake of clarity, components present in Fig. 4.2 that are irrelevant to the process are not shown.
Loading a coil with a persistent current requires multiple steps which are outlined below and shown in Fig. 4.9a - 4.9d:

1. The quench current $I_Q \approx 5\,\mathrm{mA}$ is applied and power is dissipated in the quench resistor $R_Q = 120\,\Omega$. Part of the quench branch of the superconducting coil is raised above the critical temperature and becomes resistive adding the small resistance R_W in the coil branch bypassing the field-creating part.

2. Immediately after applying the loading current I_L, an opposite current that counteracts the change in magnetic flux through is induced in the coil. This current decays over the resistive part of the wire with time constant $\tau = \frac{L}{R}$. After a short time, the whole loading current flows through the coil and the magnetic flux through the coil has changed.

3. After current flows through the coil, the quench current I_Q is removed and the coil becomes persistent again. The loading current keeps running through the coil in order to conserve the magnetic flux.

4. Once the coil is persistent, the flux in the coil is conserved. If the external loading current

is removed, flux conservation keeps the current through the coil constant and the circuit is closed through the superconducting bypass.

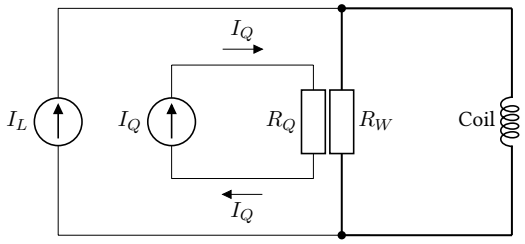

(a) The quench current I_Q dissipates power in the quench heater R_Q and warms up part of the superconducting wire above its critical temperature. This creates a small resistance R_W in the superconducting coil.

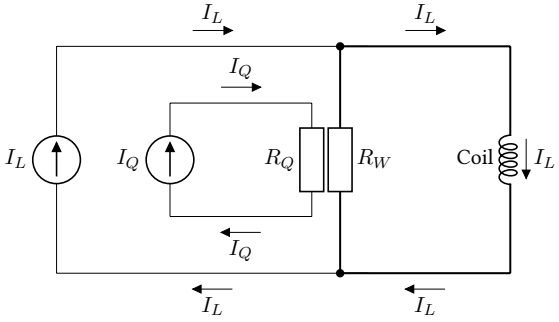

(b) Applying a loading current to the coil initially creates an induced current of same magnitude in the opposite direction, however, this current decays over R_W with a time constant $\tau = \frac{L}{R}$ and after a short time the full loading current flows through the coil.

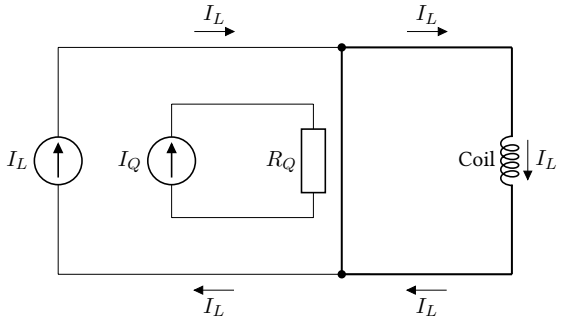

(c) After removing the quench current and making the coil persistent, flux conservation keeps the current flowing through the field-creating part of the coil.

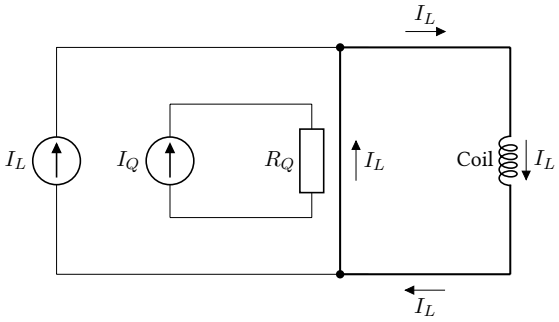

(d) After the external loading current is removed, the current flowing in the coil is conserved and the system can be decoupled from the outside to reduce noise.

Figure 4.9: Coil loading scheme: (a) Apply quench current. (b) Apply loading current. (c) Remove quench current. (d) Remove loading current.

In case that multiple persistent coils are present, loading is not as simple as outlined above as the mutual inductance between the coils causes an inductive change of the current in coil C_j when coil C_k is loaded externally. The straight forward approach to circumvent this problem is quenching all coils simultaneously, applying the loading currents and unquenching all coils

together. However, when this loading scheme is applied in the experiment, the combined power dissipation of all quench currents running simultaneously heats part of the field-producing branch of the coil above its critical temperature. As a result, no persistent path exists between the two loading joints and the loading current dissipates further power in the superconducting coil. Even if the quench currents are removed, any current flowing through the coil decays over the resistive wires in the field-creating path and no current is loaded in the coil. In order to reliably load the desired currents into the system the coils are loaded and quenched in series. The change in current in each coil is therefore described by a series of inductive changes according to Eq. (4.8) and external changes which set the current in a coil to the external current. The loading sequence typically used to load the B2 coil is outlined below:

1. All coils are quenched to start the loading sequence from a defined state.
2. The quench currents are removed from the B1 coil, the B0 coil and the SSC to reduce the thermal load in the system.
3. The B2 loading current is applied and the flux through the coils changes. This causes current to be induced in the B0 coil and the SSC.
4. The B2 quench current is removed and the B2 coil becomes persistent.
5. The B2 loading current is removed and loading of the B2 coil is finished.
6. The B1 coil is quenched and any current that was inductively loaded in the B1 coil decays.
7. The B1 quench current is removed and the B0 coil and the SSC are quenched simultaneously. After this step, no current flows in either the B0 coil or the SSC.

Table 4.5 summarizes the timings and currents of the sequence outlined above. The B0 coil and SSC are quenched after the B1 coil since residual currents in the B1 coil have practically no influence on the loaded B2 and B0 values.
The real currents loaded into the coils after the sequence has finished can be calculated using a series of flux-conserving and flux-changing steps. When a subset $\mathrm{C}_{\mathrm{quenched}}$ of the coils is quenched, the currents through these coils are given by the externally applied loading currents or 0 in case of the SSC). If this process causes a change $\mathbf{\Delta I_{quenched}}$ in the currents through the quenched coils $\mathrm{C}_{\mathrm{quenched}}$, the magnetic flux through the persistent coils $\mathrm{C}_{\mathrm{persistent}}$ would change according to Eq. (4.8):

$$\Delta\Phi_{persistent} = M_{Load}\mathbf{\Delta I_{quenched}}. \tag{4.33}$$

t[s]	$I_{B2,Q}$[mA]	$I_{B1,Q}$[mA]	$I_{B0,Q}$[mA]	$I_{SSC,Q}$[mA]	$I_{B2,L}$[mA]	$I_{B2,L}$[mA]	$I_{B2,L}$[mA]
0	5	5	4	5	0	0	0
30	5	0	0	0	0	0	0
60	5	0	0	0	100	0	0
70	0	0	0	0	100	0	0
100	0	0	0	0	0	0	0
150	0	5	0	0	0	0	0
170	0	0	4	5	0	0	0
190	0	0	0	0	0	0	0

Table 4.5: Loading sequence used to load the B2 coil with $100\,\mathrm{mA}$. Initially, the B2 coil is loaded and the B0 coil and SSC are charged up inductively. Afterward the other coils are quenched sequentially in order to keep the thermal load small. Given their large mutual inductance, the B0 coil and the SSC have to be quenched simultaneously.

M_{Load} is the mutual inductance matrix containing only the rows corresponding to the persistent coils and only the columns corresponding to the quenched coils. M_{Load} therefore describes the change of flux through the persistent coils changes by a change in current through the quenched coils. Given that the flux through persistent coils can not change (see Fig. 4.8), currents $\mathbf{\Delta I_{persistent}}$ are induced in the persistent coils such that the overall change in flux through the persistent coils is conserved:

$$M_{persistent}\mathbf{\Delta I_{persistent}} + M_{Load}\mathbf{\Delta I_{quenched}} = \mathbf{0}. \tag{4.34}$$

$M_{persistent}$ is the mutual inductance matrix containing only the rows and columns of the persistent coils as any induced change of current in a quenched coil decays rapidly. The induced current changes $\mathbf{\Delta I_{persistent}}$ are therefore given by

$$\mathbf{\Delta I_{persistent}} = -M^{-1}_{persistent} M_{Load}\mathbf{\Delta I_{quenched}}. \tag{4.35}$$

Figure 4.10 shows the normalized currents flowing in the individual coils as a function of time for the sequence that was typically used to load the B2 coil. When the loading current is applied to the B2 coil, mutual inductance causes currents to be induced in the B0 coil and the SSC. In order to ensure that only the B2 coil carries current, the B0 coil and the SSC are quenched simultaneously once B2 is loaded. Quenching the B0 coil and the SSC changes the flux through the B2 coil and thus, some of the loaded current is lost and once the scheme is finished only approximately $96\,\%$ of the applied current is expected to be loaded into the B2 coil.

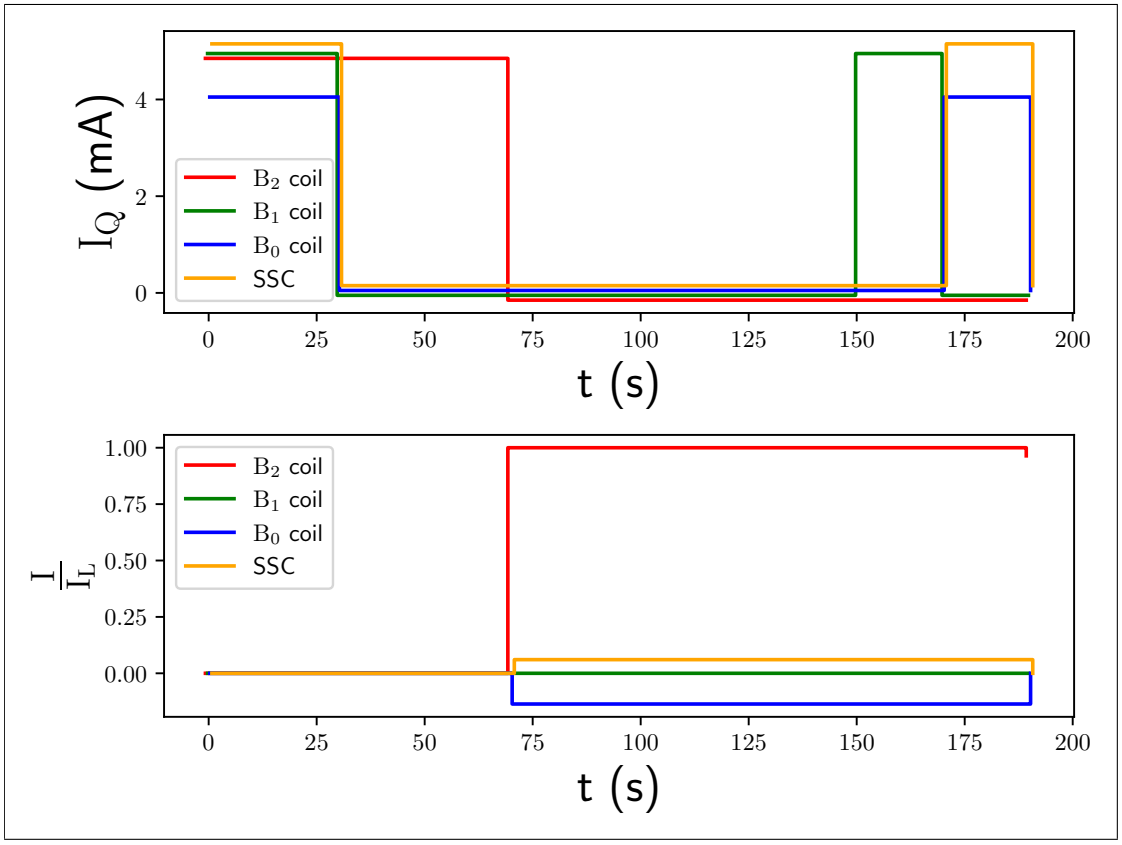

Figure 4.10: B2 coil loading sequence: (a) Applied quench currents as a function of time. For the sake of clarity, the plots have bees shifted slightly to avoid overlapping. (b) Currents flowing in the individual coils as a function of time. When loading current is applied to the B2 coil, currents are induced in the B0 coil and the SSC. After the B2 coil is loaded, the other coils are quenched sequentially in order for the inductive currents to decay.

4.7 Experimental realization of the coil system

The shimming coils are wound out of $150\,\mu\mathrm{m}$ diameter superconducting niobium-titanium (Nb-Ti) wire. To prevent shorts and to provide a flat surface for winding, an insulating Kapton layer was placed between the different layers of the shielding system. Once wound, each coil was fixed in place with PTFE tape. In order to provide enough space to fit the coils with loading joints and to close the coils with a persistent joint, multiple meters of spare wire were left on either side of each coil.
Once a shimming coil was wound, it was equipped with loading joints. These joints are necessary to change the current through the shimming coils. The loading joints are realized by winding the bare Nb-Ti wire around a $1\,\mathrm{mm}$ thick low-resistance OFHC copper wire. The general design is outlined in [133] and the main manufacturing steps are described below:

1. The insulating varnish is removed along an approximately $3\,\mathrm{cm}$ long stretch of the spare wire on either side of the coil.
2. The bare wire is cleaned using Acetone and Isopropyl alcohol.
3. An approximately $5\,\mathrm{cm}$ long piece of $1\,\mathrm{mm}$ thick high-purity OFHC copper wire is prepared and cleaned using Acetone and Isopropyl alcohol.
4. The bare Nb-Ti wire is wound in a helix around the OFHC wire.
5. A thin ($250\,\mu\mathrm{m}/500\,\mu\mathrm{m}$) copper wire is cleaned and tightly wound around the OFHC wire. This presses the Nb-Ti wire against the thick OFHC wire.
6. The joint is fixed by covering the assembly in solder. Figures 4.11a and 4.11b show the loading joint before and after fixation by soldering.
7. A long piece of OFHC wire is soldered to the loading joint.
8. The loading joint is wrapped in PTFE tape to prevent shorts and protect the joint
9. The joint is fixed on the trap can with PTFE tape.
10. The long piece of OFHC wire is inserted in a PTFE sleeve and wrapped around the trapcan to provide good thermal contact. This prevents power dissipated by the loading current in the low-resistance wires connecting the $4\,\mathrm{K}$ stage to the $77\,\mathrm{K}$ stage from heating up the loading joint.

11. One loading joint is grounded on the trap can while the other is fitted with long $250\,\mu m$ thick Manganin wire to connect the loading joint to the $77\,K$ stage in the experimental apparatus.

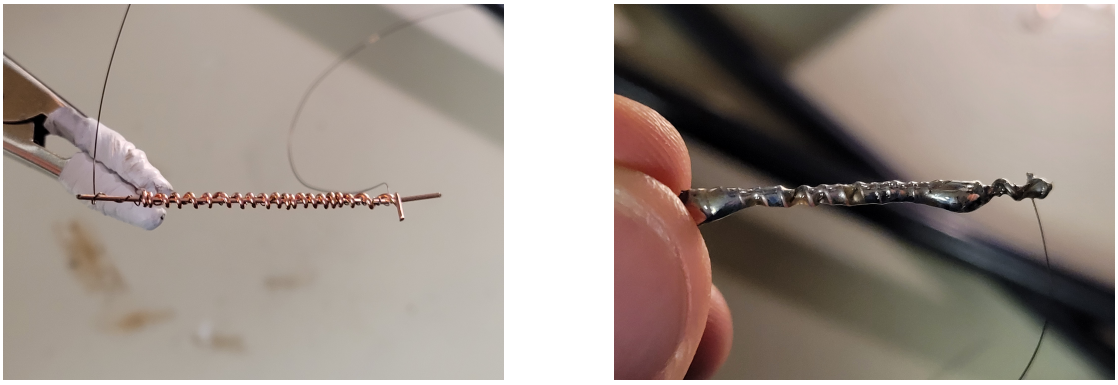

(a) (b)

Figure 4.11: (a) Loading joint before fixation by soldering. A tightly wrapped copper helix presses the Nb-Ti wire against the OFHC wire. (b) The joint is fixed by covering the assembly in solder.

In order to allow current to flow persistently once loaded, the coil has to be closed with a persistent joint. The persistent joints were manufactured using the technique developed in [133]. A summary of the individual steps is given below:

1. The last $3\,cm$ of each wire are cleaned using sandpaper to remove the insulating varnish.
2. The ends are cleaned using acetone and isopropyl alcohol to remove grease.
3. The ends are pulled through a metal ferrule until about $2\,cm$ of wire are visible.
4. The wires are fixed in the ferrule by filling it with solder.
5. The protruding ends are cleaned with Acetone and isopropyl alcohol again.
6. The wires are twisted tightly around each other and the last $5\,mm$ of this twisted pair is cut to provide a clean spot for welding.
7. The wires are spot welded under inert atmosphere using a PUK U5 spot welder ($2\,\%$ power at $1\,ms$ welding time).
8. The resulting weld is cleaned using acetone and isopropyl alcohol.

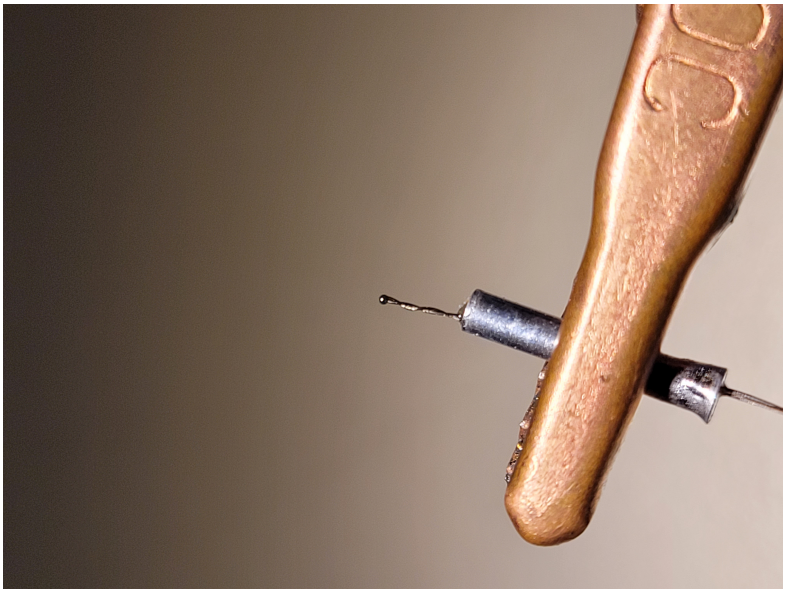

Figure 4.12: Image of a persistent joint after spot welding. The shiny ball forms a superconducting connection between the twisted pair of NbTi wire. In order to protect the joint, the joint is retracted into the ferrule filled with solder and wrapped in PTFE tape.

9. The joint is examined under a microscope. Figure 4.12 shows an image of a persistent joint. If the welding spot looks stained or breaks easily under mechanical stress the joint is assumed to be resistive, the wire is cut behind the ferrule and the process is started again from 1.

10. If the joint looks good, the solder in the ferrule is reheated and the twisted wire is pulled back into the ferrule to protect the welding spot.

11. In the final assembly, the persistent joints were guided out of the region of high magnetic field and fixed to the mechanical support of the trap can. Figure 4.15 shows the location of the persistent joints in the experimental assembly. The coil system and quench heaters are covered by tightly wound copper braid to ensure good thermalization.

All coils were equipped with quench heaters providing the possibility to locally quench part of the superconducting coil. The quench heaters are realized by wrapping part of the superconducting NbTi coil wire around a $120\,\Omega$ resistor. The resistor is then wrapped in PTFE tape, fitted with $250\,\mu\mathrm{m}$ Manganin wires and fixed to the trap can with multiple layers of Kapton sheets providing thermal insulation between the quench heater and the trap can. Figure 4.13 shows a quench heater before it is wrapped in PTFE tape and fixed to the trap can.

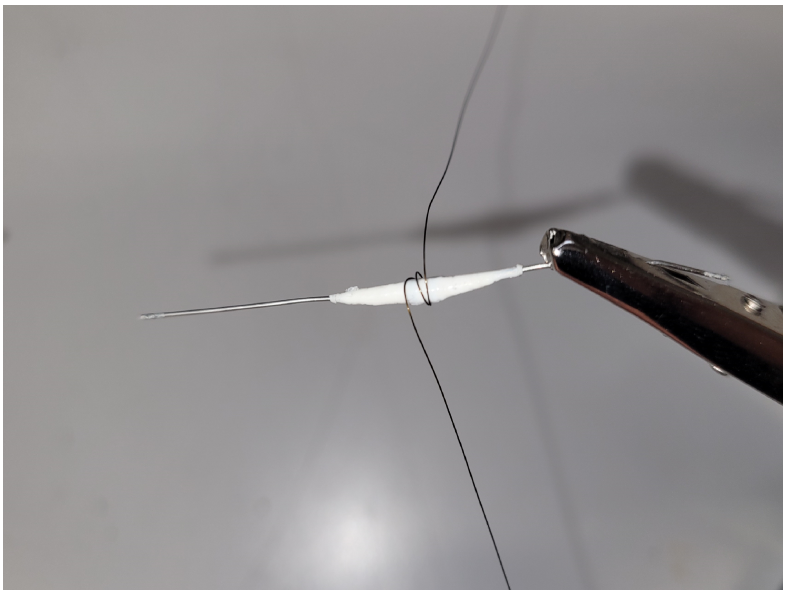

Figure 4.13: Part of the superconduction wire of the coil is wrapped around a $120\,\mathrm{Ohm}$ resistor. By running current through the resistor, the superconducting wire is heated above its critical temperature and the coil is locally quenched.

The quality of the manufactured joints was tested in a cryogenic assembly driven by a Gifford-McMahon cryocooler (Sumitomo SRDK-408D2). Figure 4.14 shows a schematic cross section through the test setup. The coil under test (green) is attached to the cryocooler, pumped to a pressure of and cooled down to approximately 5 K. A NVE AA002 GMR sensor (yellow) is placed close to the center on the axis of the test coil and connected to a voltmeter. The loading joints (blue) and quench heater (red) are connected to independent current supplies. An excitation coil (orange), wound on the 77 K heat shield of the assembly, provides the opportunity to change the magnetic flux through the test coil.

In order to test if the persistent joint is superconducting, the test coil is quenched an excitation current I_{Exc} is applied to the excitation coil. Next, the quench current is taken away, the quench heater is given time to cool down and the excitation current is removed. Removing the field created by the excitation coil changes the flux through the test coil and thus induces a current in the test coil. In case the superconducting joint works, the induced current keeps flowing and creates a magnetic field at the position of the GMR sensor which results in an output voltage $V_{\text{GMR, Loaded}}$. Next, the test coil is quenched and the output voltage $V_{\text{GMR, Quenched}}$ of the GMR sensor is compared to $V_{\text{GMR, Loaded}}$. In case the output voltages changes significantly after quenching, current was flowing in the coil and thus the joint is superconducting.

The loading joints are tested in a very similar manner by applying the scheme outlined in chapter 4.6. As a first step, the coil is quenched by running current through the quench heater. Once part of the test coil has lost superconductivity, an external loading current I_{Load} is applied and creates a magnetic field at the position of the GMR sensor. The output voltage $V_{\text{GMR, Quenched}}$ is measured and the quench current is taken away. Once the coil has been given sufficient time to cool down and become superconducting, the loading current can be taken away without changing the current through the coil. By measuring the output voltage $V_{\text{GMR, Persistent}}$ of the GMR sensor and comparing it with $V_{\text{GMR, Quenched}}$, the fraction of the current that has been persistently loaded into the coil can be determined.

The maximum current that can be loaded into the coil is limited by the performance of the loading joints as well as the persistent joint. Given that spot welding NbTi significantly reduces the critical current density in the join region [135], the maximum current that can flow through the persistent joint without quenching it varies from joint to joint. Additionally, the maximum loading current is limited by the resistance R_{L} and the thermal anchoring of the loading joints. As long as the external loading current I_{Load} is applied, it dissipates the power $P = I_{\mathrm{Load}} R_{\mathrm{L}}$ in the loading joints. If the thermal connection between the loading joints and the trap can is bad, the loading joints are heated above the critical temperature of the NbTi wire and the coil stays locally quenched even if no quench current is applied. In this case, the current running through the test coil decays over these resistive parts of the coil as soon as the external loading current

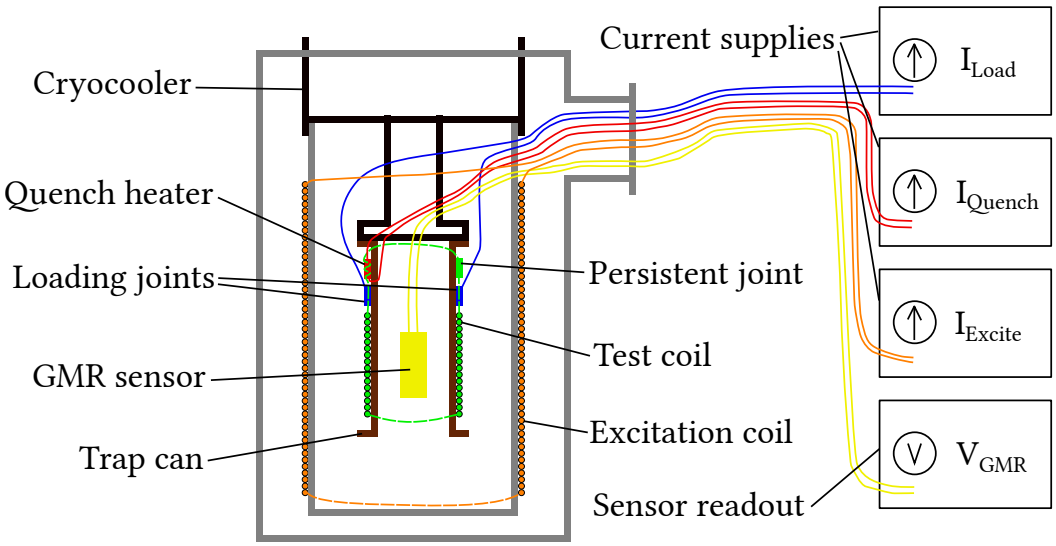

Figure 4.14: Schematic cross-section through the cryogenic setup used to test the manufacturing process. Joints can be tested by loading the superconducting coil inductively with an external solenoid or by direct loading via the loading joints. A GMR sensor located in the center of the test coil measures the magnetic field and can be used to determine if the test coil is persistent.

is taken away.

One way to overcome the limitations introduced by the residual resistance of the loading joints is to reduce the amount of energy $E = Pt_{\text{Load}}$ that is deposited in the loading joints by decreasing the time t_{Load} during which the loading current is applied. Typical maximum loading currents that could be applied to the loading joints for extended periods of time were of the order of 3 A, however, due to saturation of the GMR sensor it was not possible to determine if the full current was loaded persistently. These values are comparable to the maximum loaded current of 2.5 A quoted in [133] that was used to design the coils.

First test of the system in the superconducting magnet of the experiment showed that the performance that was observed in the cryogenic test setup could not be reproduced. Quenching the coils and applying an external loading current caused a significant change in the magnetic field, however, no current could be loaded into the coils. Given that applying the loading current did not change the resistance over the loading joints, we conclude that the joints were not heated above the critical temperature and the maximum current was limited by the persistent joint. Since the critical current density depends on the temperature as well as the magnetic field a second system was wound and fitted with enough wire on both ends of the coil to move the

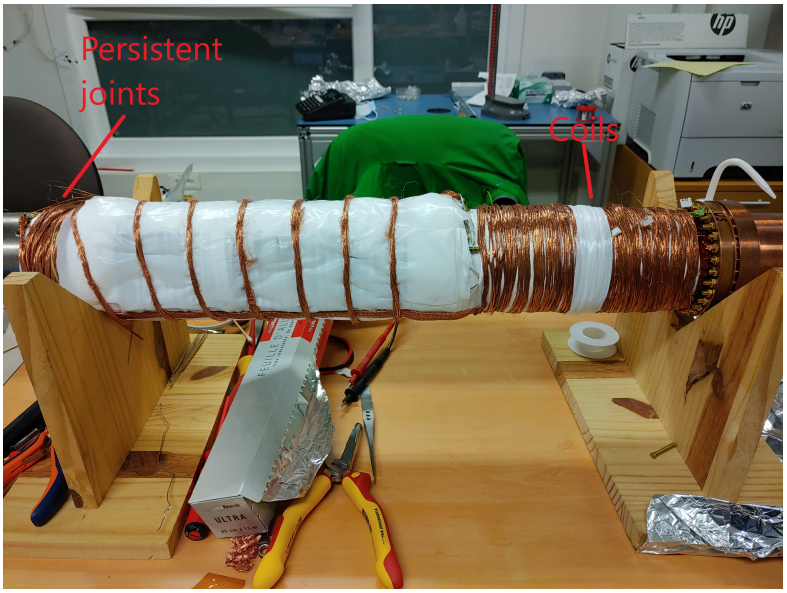

Figure 4.15: Position of the shielding system and the persistent joints in the final assembly. The persistent joints are moved out of the region of high magnetic field.

persistent joint out of the region of high field. Figure 4.15 shows the location of the persistent joints in the experimental assembly. The NbTi wires connecting the joints with the coils are guided on the surface of the experimental assembly and are covered by tightly wound copper braid to ensure good thermalization.

5 Precision trap measurements

The precision trap provides an environment in which frequencies can be measured at low uncertainty as the homogeneous fields strongly suppress systematic shifts. In order to compare the charge-to-mass ratios of two particles, their free cyclotron frequencies $\nu_{c,1} = \frac{1}{2\pi}\frac{q_1}{m_1}B_0$ and $\nu_{c,2} = \frac{1}{2\pi}\frac{q_2}{m_2}B_0$ are measured in the common magnetic background field B_0 present in the precision trap. In case the particles have similar eigenenergies their radii are identical and the particles probe a common magnetic field. In this case, the ratio

$$R = \frac{\frac{q_1}{m_1}}{\frac{q_2}{m_2}} = \frac{\nu_{c,1}}{\nu_{c,2}} \tag{5.1}$$

does not depend on the magnetic background field. Charge-to-mass ratio measurements thus require a good understanding of the particles' temperatures and higher order coefficients in the expansion of the magnetic and electric fields which lead to systematic shifts.
In case the g-factor of the proton or antiproton are measured, the Larmor frequency ν_L and the free cyclotron frequency ν_c have to be determined in a common magnetic field and $\frac{g}{2}$ is given by

$$\frac{g}{2} = \frac{\nu_L}{\nu_c}. \tag{5.2}$$

By determining both ν_c and ν_L in the highly homogenous precision trap, systematic effects that lead to broadening of the respective lineshapes are suppressed [127]. However, given the high harmonicity of the fields in the precision trap, the spin state of a particle can not be determined in the precision trap and thus the determination of the Larmor frequency ν_L requires a second trap, called Analysis trap (see chapters 3.5 and 7). Compared to measurements in a single trap [88], application of this multi-trap scheme [68] lead to a reduction in the uncertainty of the antiproton magnetic moment by more than a factor 500.
The final uncertainty for charge-to-mass ratio measurements thus depends on the ability to resolve the free cyclotron frequency ν_c at high precision. For g-factor measurements, the free cyclotron frequency ν_c as well as the Larmor frequency ν_L need to be determined. Therefore, it is crucial to understand and minimize the influence of systematic shifts caused by imperfections of the electrostatic and magnetic fields in the precision trap.

5.1 Axial frequency determination

As outlined in chapter 3.3.1, the axial frequency ν_z is measured using a superconducting cryogenic detection circuit [96]. All traps in the BASE experiment are equipped with an axial detector which cools the axial motion of the particle. Typically, the axial frequency of the particle is tuned to be in resonance with the frequency of the detection circuit, however, a novel detection scheme using a detuned particle was theorized and experimentally tested in the course of this thesis.

5.1.1 Dip-based detection

In order to detect the axial frequency of a trapped particle, the ring voltage is changed such that the particle's axial frequency ν_z matches the resonance frequency ν_0 of the detection circuit. In this case, the particle shorts the thermal noise spectrum of the resonator and the resulting spectal noise density $S(\nu)$ is given by Eq. (3.6). By introducing the resonator width $\Delta\nu_0 = \frac{\nu_0}{Q}$ and the dip width $\Delta\nu_z = \frac{\gamma}{2\pi}$, the equation can be rewritten as

$$S(\nu) = \sqrt{\frac{n_1^2}{1 + \left[\frac{\frac{1}{\Delta\nu_0}(\nu_0^2-\nu^2)(\nu^2-\nu_p^2)+\Delta\nu_z\nu^2}{\nu(\nu^2-\nu_p^2)}\right]^2} + n_0^2}. \tag{5.3}$$

In order to determine the particle's axial frequency, Eq. (5.3) is fitted to the log. axial spectrum acquired with the spectrum analyzer. The signal in each frequency bin follows a log. chi-distribution with the number of the degrees of freedom depending on the averaging time and span of the spectrum. Nevertheless, the spectra are fit using robust least-squares fitting algorithms which yield a fit scatter well below the uncertainty introduced by systematic shifts. Figure 5.1 shows a typical axial spectrum.

In the presence of magnetic inhomogeneities and anharmonicities of the electrostatic field created by the trap electrodes, the axial frequency depends on the energy of the trapped particle's eigenmodes. The anharmonicity of the magnetic field is characterized by the higher order terms $C_3, C_4, ...$ in the expansion of the electrostatic potential around the minimum

$$\Phi(z) = (C_0 + C_2 z^2 + C_3 z^3 + C_4 z^4 + ...) \times V_0. \tag{5.4}$$

Given the symmetric design of the trap, odd coefficients are strongly suppressed and the main contributions to the energy dependency of the particle's frequency are given by C_4 and C_6. Under ideal conditions the tuning ratio applied to the correction electrodes can be chosen such, that C_4 and C_6 vanish simultaneously. However, in case the tuning ratio deviates from the

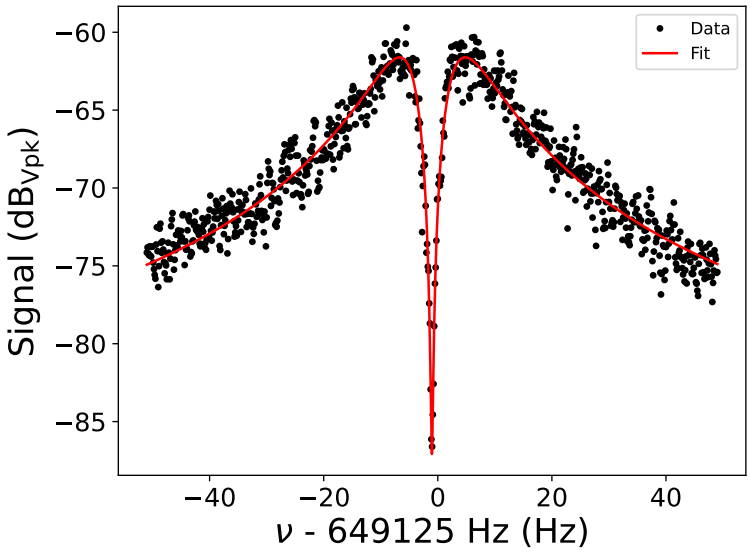

Figure 5.1: Typical dip spectrum of a particle in the precision trap. At its axial frequency ν_z, the particle shorts the noise of the resonant detection circuit to the background noise level. The width $\Delta\nu = \frac{\gamma}{2\pi} = \frac{R_p q^2}{2\pi m D^2}$ of the dip is determined by the cooling time constant γ and depends on charge q and mass m of the particle, the parallel resistance R_p of the detection circuit and the effective electrode distance D which depends on the trap geometry and the coupling of the electronic readout to the trap.

ideal value, C_4 and C_6 no longer vanish. The change of C_4 and C_6 with the tuning ratio is characterized by the geometry dependent parameters D_4 and D_6 as described in chapter 2.2. Combining the calculated values of $D_4 = -1.3 \times 10^9 \frac{1}{\mathrm{m^2 U}}$ and $D_6 = 6.76 \times 10^{13} \frac{1}{\mathrm{m^4 U}}$ with Eq. (2.40) provides the possibility to calculate the systematic shift $\Delta\nu_z$ of the axial frequency with the energies E_z and E_+ in case the tuning ratio deviates by $\Delta\mathrm{TR}$ from the ideal tuning ratio. Given that $\Delta\mathrm{TR}$ is typically optimized to less than 1×10^{-5} and the axial temperature is on the order of 10 K, the related shifts are on the order of:

$$\left(\frac{\Delta\nu_z}{\nu_z}\right)_{D_4} = \frac{3}{2}\frac{1}{4\pi^2 m\nu_z^2}\frac{D_4}{C_2}E_z\Delta\mathrm{TR} = 0.62\frac{1}{\mathrm{eV\,U}}E_z\Delta\mathrm{TR} \approx 5 \times 10^{-9}. \tag{5.5}$$

In addition, the frequency detection chain consisting of the single-sideband down-converter and the FFT can introduce a systematic shift that has to be characterized directly by measuring the output on the FFT for a known input signal.

Beside the systematic shifts outlined above, fitting the line shape to the noise spectrum introduces a statistical uncertainty. The uncertainty of the fitted axial frequency depends on the width of the dip feature, the bin width, the signal-to-noise ratio, which describes the difference between the resonator noise level and the dip noise level, and the noise on the line shape which is a function of the averaging time. In case the FFT span and averaging time are kept constant, the statistical fit uncertainty is determined by the physical parameters of the trap and resonator system which are hard to modify and place a lower bound on the statistical uncertainty.

5.1.2 Dispersive peak based detection

Detection of spinflips in the Analysis trap require the resolution of small changes in the trapped particle's axial frequency. In the following section, a novel approach for the detection of changes in the axial frequency of a trapped particle is presented, which circumvents the limits imposed by the dip width and SNR and provides the possibility to determine a particles spin-state at low averaging times, thus increasing the cyclotron temperature acceptance for high-fidelity spin-state detection [102], which drastically reduces the particle preparation time by sub-thermal resistive-cooling [88].

Equation (5.3) describes the lineshape for a particle centered on the resonator. However, Eq. (5.3) also applies in the case of a cold particle which is detuned from the resonator. Figure (5.2) shows the lineshape for different particle frequencies at constant resonator frequency. At $\nu = \nu_p$ the noise spectrum is shorted to the background noise level n_0, however, the interaction between the impedance of the particle and the impedance of the detector results in a noise peak close to the particle frequency. Just considering the impedance aspects of this system, the noise level on top of this peak is independent of the detuning and is given by the top noise level n_1.

The noise-floor level is defined by the resonator background noise level at the peak frequency.

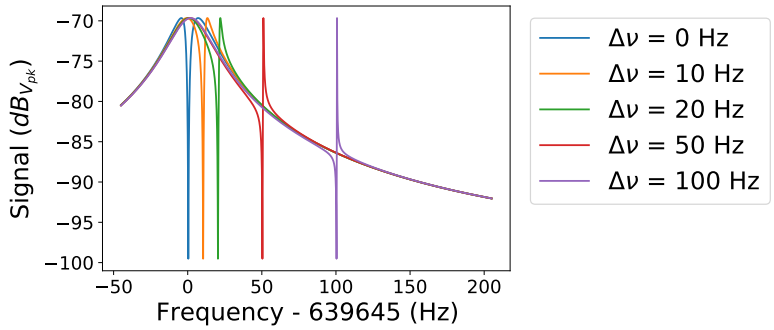

Figure 5.2: Lineshape for different resonator-particle-detunings Δf at a constant resonator frequency. Maximum and minimum of the dispersive feature are independent of detuning.

For large enough detunings $\Delta\nu$, the lineshape can be described as the undisturbed resonator and a narrow dispersive feature created by the particle. Figure 5.3 shows this dispersive feature for a constant particle frequency and varying resonator-particle-detuning.

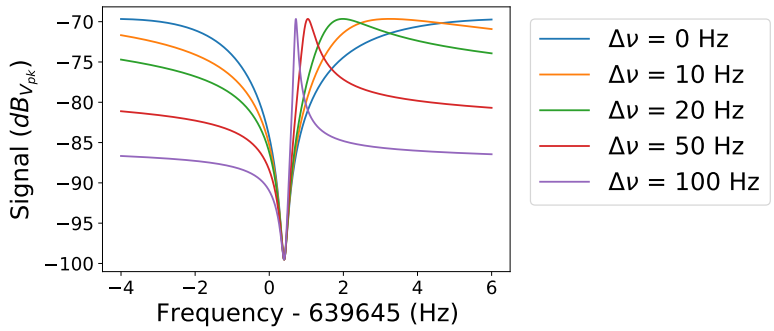

Figure 5.3: Lineshape for different resonator-particle-detunings $\Delta\nu$ at a constant particle frequency. Increasing the detuning decreases the peak's width and causes it to move closer to the dip at the particle frequency.

The position of the maxima can be calculated by minimizing the denominator in Eq. (3.6) which is equivalent to solving:

$$\frac{Q}{\nu_0}(\nu_0^2 - \nu^2)(\nu^2 - \nu_p^2) + \frac{\gamma}{2\pi}\nu^2 = 0. \tag{5.6}$$

Since ν appears only in even powers this equation can be solved and yields the following peak positions:

$$\nu_{1/2} = \sqrt{\frac{1}{2}\left(\nu_0^2 + \nu_p^2 + \frac{\gamma\nu_0}{2\pi Q}\right) \pm \sqrt{\frac{1}{4}\left(\nu_0^2 + \nu_p^2 + \frac{\gamma\nu_0}{2\pi Q}\right)^2 - \nu_0^2\nu_p^2}}. \tag{5.7}$$

Given that $\frac{\gamma_0\nu_0}{2\pi Q}$ is small compared to ν_0^2 and ν_p^2, approximate solutions can be obtained:

$$\nu_{1/2} \approx \sqrt{\frac{1}{2}(\nu_0^2 + \nu_p^2) \pm \sqrt{\frac{1}{4}(\nu_0^2 + \nu_p^2)^2 - \nu_0^2\nu_p^2}} \tag{5.8}$$

$$\approx \sqrt{\frac{1}{2}((\nu_0^2 + \nu_p^2) \pm (\nu_0^2 - \nu_p^2))} \tag{5.9}$$

$$\approx \frac{1}{2}((\nu_0 + \nu_p) \pm (\nu_0 - \nu_p)). \tag{5.10}$$

As expected, $\nu_1 \approx \nu_0$ corresponds to the resonator peak while $\nu_2 \approx \nu_p$ corresponds to the dispersive feature close to the particle's axial frequency. Figure 5.4 shows the difference between the peak frequency ν_{Peak} and the true particle frequency ν_p as a function of the detuning $\Delta\nu$ for typical conditions. The peak frequency approaches the particle frequency with increasing detuning asymptotically. For large detunings, changes in the particle's axial frequency are therefore transferred directly to the peak frequency $\Delta\nu_{Peak}$. Therefore, changes in the peak frequency be used to detect changes in the particle's axial frequency $\Delta\nu_z$.

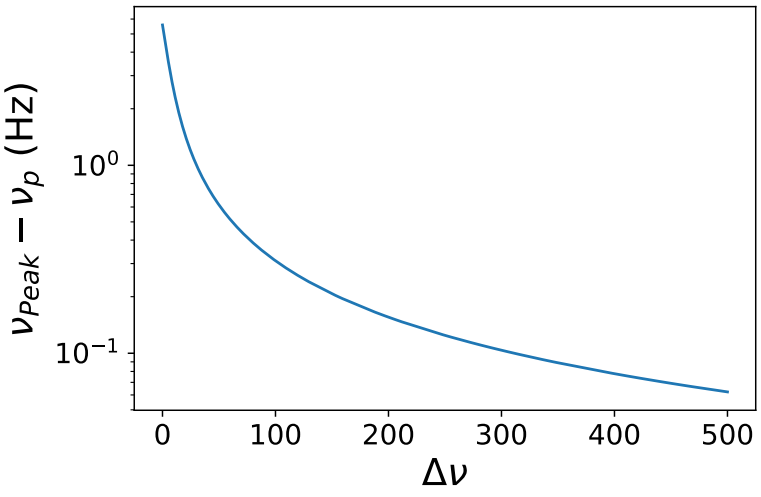

Figure 5.4: Difference between the peak frequency f_{Peak} and the true particle frequency f_p as a function of the detuning Δf for typical conditions.

Calculating the -3 dB width of the peak analytically is possible since 4th order polynomials

have analytic solutions, however, calculation of the analytic solution is limited by the machine precision and a numerical calculation is more efficient. Since spectra are usually fit in log-units, the FWHM of the log-peak feature is used to characterize the peak width. Figure 5.5 shows the log-FWHM of the dispersive feature as a function of the detuning $\Delta\nu$ for typical conditions. As the detuning increases, the damping the resonator imposes on the particle vanishes and the width of the dispersive feature decreases.

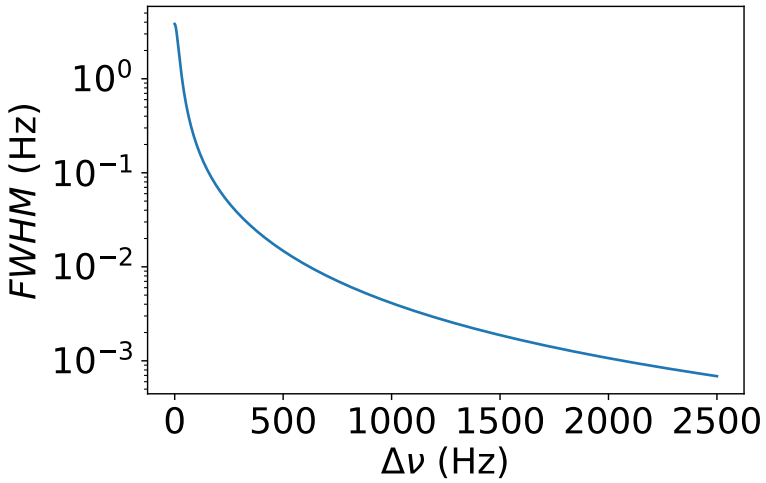

Figure 5.5: FWHM of the dispersive peak as a function of the detuning Δf for typical conditions. Note that since fitting is done in log. units, this width does not correspond to the -3 dB width.

Due to the finite acquisition time, the experimentally observed lineshape $S_{exp}(\nu)$ is however influenced by the window function $w(t)$ applied to the measured time series. Using the convolution theorem, the experimentally observed noise spectrum $S_{exp}(\nu)$ can be calculated as the convolution of the theoretical power spectral density $S^2(\nu)$ and the squared Fourier transform $W^2(\nu)$of the window function:

$$S_{exp}(\nu) = \sqrt{\int_{-\infty}^{\infty} S^2(\nu) W^2(\nu - \nu') \mathrm{d}\nu'}. \tag{5.11}$$

Depending on the choice of $w(t)$, the shape of the observed noise spectrum changes. Typically, a Hann window is used, which provides good frequency selectivity as well as a suppression of more than $30\,\mathrm{dB}$ of the first sidelobes compared to the central maximum. Figure 5.6 shows a Hann window in both time and frequency domain, normalized such that the equivalent noise bandwidth of the window is 1. Thus this window is scaled to conserve noise power rather than

on-bin amplitude. The full-width-at-half-maximum (FWHM) of the window in the frequency domain depends on the acquisition time $t_{Spectrum}$ and is given by FWHM $= \frac{1.4382}{t_{Spectrum}}$ [136].

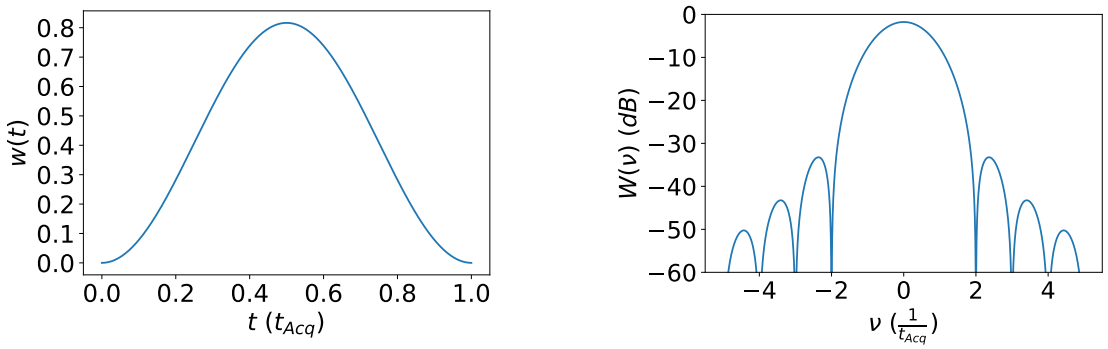

(a) (b)

Figure 5.6: Left: Hann window $w(t)$ in the time domain. Right: Hann window $W^2(\nu)$ in the frequency domain.

Convolving the dispersive peak feature with a Hann window has two effects: The peak power is distributed over multiple bins and thus the overall height of the peak is reduced. Figure 5.7a shows the maximum of the convolved dispersive feature as a function of the particle-resonator detuning for typical parameters. By subtracting the resonator noise level at the peak frequency from this maximum, the theoretical SNR can be calculated. Since the resonator background level initially drops faster than the peak noise level, the SNR increases. Once the particle is far-detuned, the resonator background level stays constant and the SNR drops as the peak noise level decreases. Figure 5.7b shows the noise level of the convolved dispersive feature as a function of the particle-resonator detuning for typical parameters. Note that, in case the particle frequency is close to the resonator frequency, the dispersive feature corresponds to one half of the resonator lineshape and thus the definition of the SNR used in Fig. 5.7b is questionable at best.

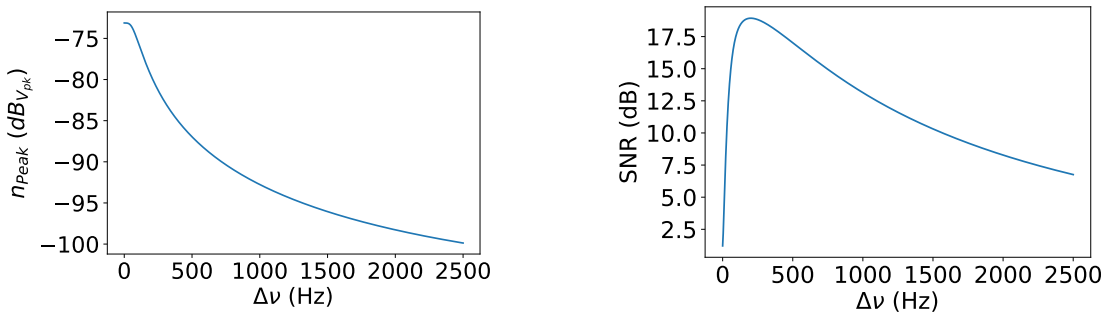

(a) (b)

Figure 5.7: Left: Noise level of the dispersive peak feature. With increasing detuning Δf, the noise level of the convolved dispersive feature decreases. Right: Signal-to-noise ratio of the dispersive peak feature. Initially, the resonator background noise level drops faster than the peak noise level and the SNR increases. Once the particle is far detuned, the resonator noise level is constant and the SNR drops with the peak noise level.

Convolution with the window limits the minimal width of the peak to the width of the window. Figure 5.8 shows the width of the log. lineshape as a function of the particle-resonator detuning for the convolved and unconvolved lineshape. In both cases, the height of the peak feature is defined as the difference between the peak noise level and the resonator noise level at the peak frequency.

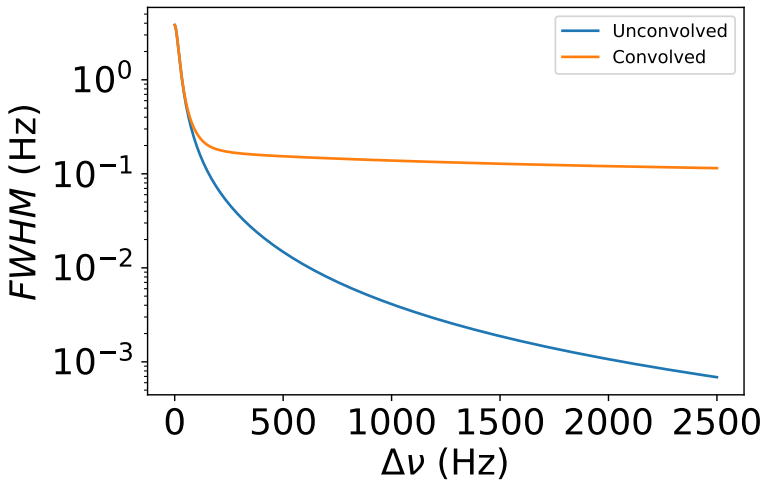

Figure 5.8: Width of the dispersive peak feature as a function of the detuning $\Delta\nu$. Convolution with the window function limits the width of the peak feature to the width of the window, which is given by the acquisition time $t_{Spectrum} = 16\,\mathrm{s}$.

Using the scaling predicted by Cramer-Rao-Bound theory, a figure of merit Fit_{FOM} describing the relative scatter of the fitted peak frequency can be calculated:

$$Fit_{FOM} \propto \frac{SNR}{\sqrt{W}}. \tag{5.12}$$

Figure 5.9 shows the normalized figure of merit for different detunings. The expected fit scatter is minimal for detunings between 250 Hz and 500 Hz as further detuning leads to a reduction in SNR while the width of the peak feature is limited to the width of the window.

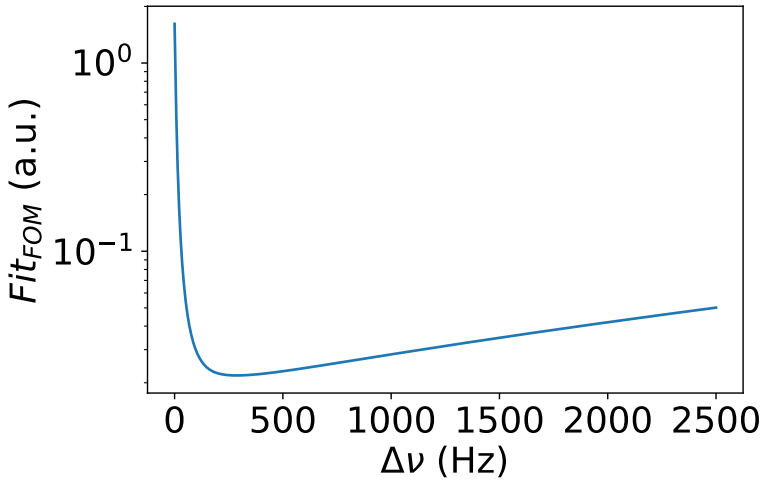

Figure 5.9: Scaled fit scatter as predicted by Cramer-Rao-Bound theory for single spectra acquired at $t_{Spectrum} = 16\,\mathrm{s}$. Initially, the fit scatter drops fast as the peak feature moves off the resonator, which causes an increase in SNR and a decrease in width. Once the particle is far detuned the dispersive feature's width is limited by the width of the Hann window and the decrease in SNR causes the fit scatter to rise.

In order to quantify the expected scatter of the fitted particle frequency, multiple Monte-Carlo simulations were run for different particle-resonator detunings. Using fits to a particle tuned to the resonator frequency, parameters for the noise levels n_1 and n_0 as well as the parameters γ and Q were determined. These parameters were used to calculate the expected linear noise density LSD and samples were created by drawing from a log-Rayleigh distribution [137]. These spectra simulate measurements with an acquisition time $t_{spectrum} = 16\,\mathrm{s}$ and no averaging. Since fitting the convolved lineshape is computationally unfeasible, the unconvolved lineshape given by Eq. (5.3) was fitted to these samples and the scatter of the fitted particle frequency was compared for different detunings. Additionally, a log-Hann peak was fitted to the data, since for large enough detunings the lineshape is determined by the window function. The

initial parameters for the lineshape fit were given by the parameters used to generate the samples while the initial parameters for the Hann peak fit were calculated using the convolved lineshape. The fitted parameters were filtered using a 3σ Grubbs filter [138] and only fits for which all parameters were valid were accepted. Figure 5.10 shows the standard deviation of the filtered fitted particle frequency for 1000 fits at each detuning for both fit functions. For small detunings, the unconvolved lineshape is a good approximation of the experimentally observed lineshape while the Hann peak yields a high fit scatter. At higher detunings, convolution with the window function changes the height and width of the dispersive peak feature. Therefore, the unconvolved lineshape is no longer a suitable description of the observed spectrum and fitting the Hann window to the data yields a more stable result. At the ideal detuning of around 300 Hz - 700 Hz, fitting the Hann window outperforms the fit scatter of a lineshape fit to a particle centered on the resonator i.e. at $\Delta\nu = 0$.

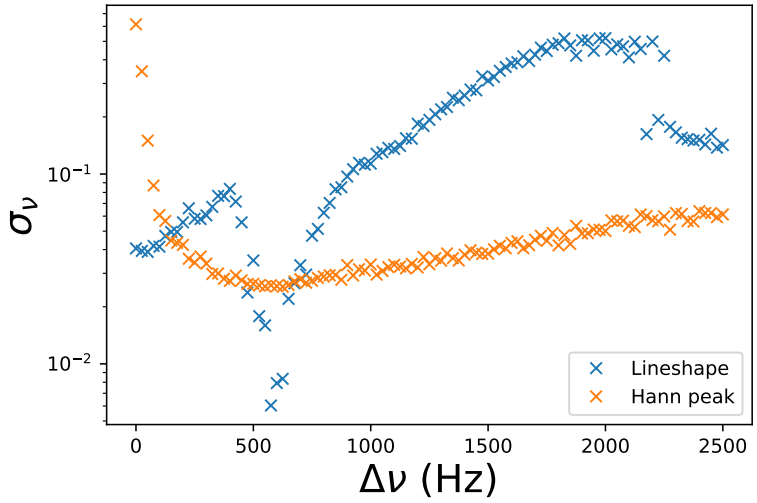

Figure 5.10: Standard deviation of the fitted frequency for different particle-resonator detunings $\Delta\nu$. In the ideal detuning range from 300 Hz - 700 Hz, the fit scatter of the Hann peak fits becomes minimal. The drop in simulated fit scatter for lineshape based fits between 400 Hz and 900 Hz is a result of the increase in rejection rate.

Apart from the fit scatter, the number of failed or rejected fits is important since a high rejection rate increases the measurement time required to achieve statistical significance and indicates, that the fitted lineshape might not describe the observed feature correctly. Figure 5.11 shows the rejection rate as a function of the particle-resonator detuning $\Delta\nu$ for an unconvolved lineshape fit and a Hann peak fit, given that the fits were initiated with ideal parameters derived from the theoretical lineshape. For small detunings the rejection rate of the lineshape based fits increases

sharply as the unconvolved lineshape can not reconcile the decreased peak height with the resonator background.

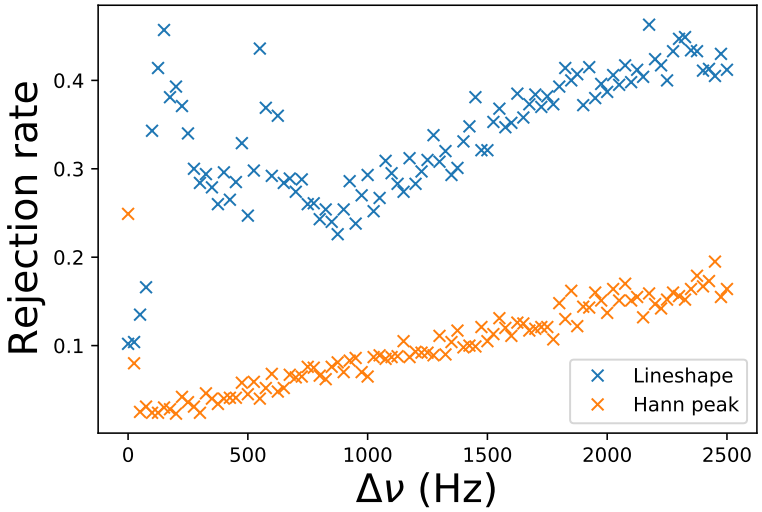

Figure 5.11: Rejection rate of the fitted frequency as a function of the particle-resonator detunings $\Delta\nu$. In the ideal detuning range from 300 Hz - 700 Hz, the rejection rate of fiting the Hann window to the data is around 5 %. Once windowing effects have a strong influence on the observed lineshape, fitting the unconvolved lineshape no longer produces robust estimates of the parameters.

The results from these simulations can be compared to the scaling of the fit scatter predicted by Cramer-Rao-Bound theory. Figure 5.12 shows the filtered standard deviation of the fitted peak frequency together with the fit scatter scaling predicted by Cramer-Rao-Bound theory (see Fig. 5.9). The theoretical values were scaled such that the minimum of the theoretical scaling is equal to the minimum of the observed fit scatter. It is notable, that the observed ideal detuning is higher than the detuning predicted by Cramer-Rao-Bound theory, however, the slope for detunings above 700 Hz is correctly reproduced. One possible explanation for this behaviour might be the fact that samples were not drawn from a Gaussian distribution but a log. Rayleigh distribution. This might cause the width to appear with a power different than in the case of a Gaussian distribution, which results in a different scaling for small detunings where the width is not yet limited by the window function.

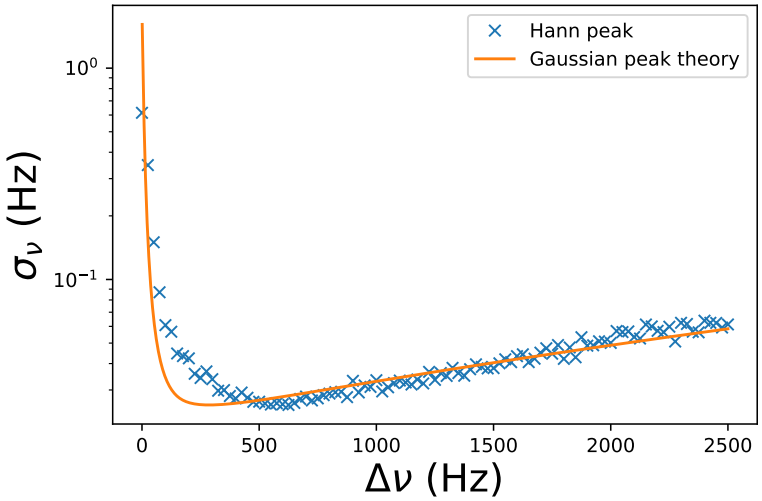

Figure 5.12: Comparison between the fit scatter predicted by Cramer-Rao-Bound theory for gaussian peaks (orange) and the fit scatter observed in non-averaged simulated spectra at $t_{spectrum} = 16\,\mathrm{s}(blue)$. The simulated fit scatter becomes minimal at detunings higher than predicted by Cramer-Rao-Bound theory.

During the commissioning of the upgraded trap system, the determination of the axial frequency with the dispersive detection scheme described above was attempted, however, initial results indicated vastly increased fit scatter compared to the standard dip-based detection scheme and further investigations on the experimental implementation were postponed in favor of faster commissioning of the trap system.

5.2 Cyclotron frequency determination

Both charge-to-mass ratio measurements as well as g-factor measurements require the precise measurement of the trapped particle's free cyclotron frequency ν_c. The invariance theorem [127] provides the possibility to calculate the free cyclotron frequency in case the particles eigenfrequencies ν_+, ν_z and ν_- are known:

$$\nu_c = \sqrt{\nu_+^2 + \nu_z^2 + \nu_-^2}. \tag{5.13}$$

The relative uncertainty of ν_c is given by

$$\frac{\Delta\nu_c}{\nu_c} = \left(\frac{\nu_+}{\nu_c}\right)^2 \frac{\Delta\nu_+}{\nu_+} + \left(\frac{\nu_z}{\nu_c}\right)^2 \frac{\Delta\nu_z}{\nu_z} + \left(\frac{\nu_-}{\nu_c}\right)^2 \frac{\Delta\nu_-}{\nu_-} \tag{5.14}$$

and thus $\frac{\Delta\nu_c}{\nu_c}$ is dominated by the relative uncertainty $\frac{\Delta\nu_+}{\nu_+}$ of the modified cyclotron frequency,

whereas $\frac{\Delta\nu_z}{\nu_z}$ and $\frac{\Delta\nu_-}{\nu_-}$ are suppressed by a factor $\left(\frac{\nu_z}{\nu_c}\right)^2$ and $\left(\frac{\nu_-}{\nu_c}\right)^2$, respectively. Therefore, the modified cyclotron frequency ν_+ needs to be measured with highest precision. The following sections describe different methods for the measurement of ν_+.

5.2.1 Sideband coupling

The simplest method for the measurement of the modified cyclotron frequency ν_+ in the precision trap utilizes a sideband coupling drive that couples the modified cyclotron motion to the axial motion of the particle [82, 109]. By irradiating the particle with a frequency $\nu_{rf} \approx \nu_+ - \nu_z$, energy is continuously exchanged between the axial and modified cyclotron mode of the particle. The rate at which this transfer of energy occurs is called Rabi frequency Ω and depends on the resonant Rabi frequency Ω_{res} as well as the detuning $\delta = \nu_{rf} - \nu_{SB,+}$ between the irradiated radio-frequency ν_{rf} and the true sideband frequency $\nu_{SB,+} = \nu_+ - \nu_z$:

$$\Omega = \sqrt{\Omega_{res}^2 + \delta^2}. \tag{5.15}$$

In the presence of the near-resonant radio-frequency drive, the particle oscillates with the modified frequency $\omega' = \omega_z - \frac{\delta}{2}$ which, in conjunction with the transfer of energy between the axial and cyclotron mode, causes sideband dips to appear in the axial noise spectrum of the particle. The combination of the axial amplitude modulation and frequency shift due to the radio-frequency field leads to an avoided crossing of the sideband frequencies which is displayed in figure 5.13.
The positions ν_R and ν_L of the upper and lower sideband dips are given by:

$$\nu_{R,L} = \nu_z - \frac{\delta}{2} \pm \frac{\Omega}{2}. \tag{5.16}$$

Note that the sum $\nu_R + \nu_L = 2\nu_z - \delta$ does not depend on the Rabi frequency and can thus be used to determine the detuning δ in case the axial frequency ν_z is known. Subsequently, the modified cyclotron frequency ν_+ can be calculated as:

$$\nu_+ = \nu_{SB} + \nu_z = (\nu_{rf} - \delta) + \nu_z = \nu_{rf} + (\nu_L + \nu_R - 2\nu_z) + \nu_z = \nu_{rf} + \nu_L + \nu_R - \nu_z. \tag{5.17}$$

In order to measure the modified cyclotron frequency ν_+, first the axial frequency ν_z is measured. Next, the particle is irradiated with a known radio-frequency ν_{rf} close to the axial-cyclotron sideband frequency ν_{SB} and the position of the sidebands dips ν_L and ν_R in the noise spectrum of the particle on the resonator is measured. Using Eq. (5.17), the modified cyclotron frequency can be calculated. The sideband coupling used in the above described technique causes the

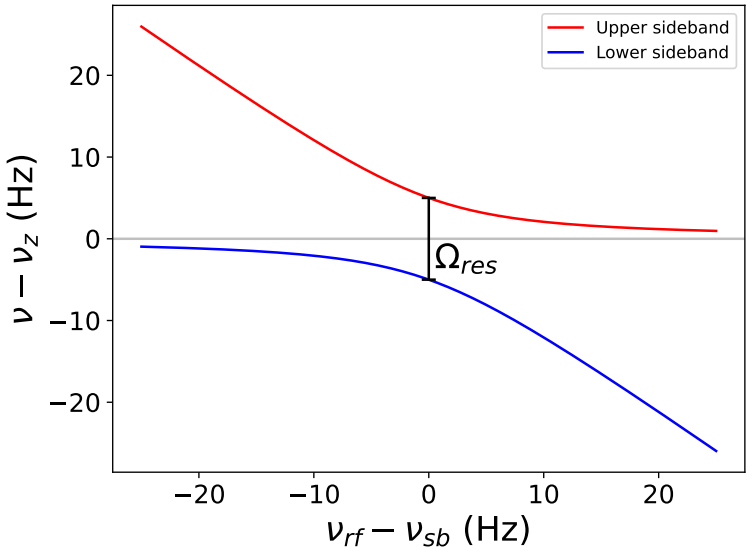

Figure 5.13: Position of the sideband dips as a function of the detuning $\delta = \nu_{rf} - \nu_{SB}$ between the radio-frequency and the axial-cyclotron sideband frequency. The radio-frequency field leads to an avoided crossing. By measuring the position of both sidebands, the detuning between the radio-frequency drive and the sideband frequency can be determined.

sidebands to be measured at an increased temperature $T_+ = \frac{\nu_+}{\nu_z} T_z$ compared to the axial frequency ν_z which results in a systematic shift dominated by the residual magnetic bottle B_2. In case the T_z and B_2 are known, the measured frequency can be corrected using Eqs. (2.45) and (2.50). Additionally, given that the method is based on the measurement of sidebands in the axial spectrum of the particle, the overall achievable precision is limited by the same effects that limit the measurement of the axial frequency, for example the width of the dips in the axial spectrum.

5.2.2 Peak detection

In order to overcome the limitations associated with the sideband method, a technique for the direct measurement of the modified cyclotron mode is implemented in the BASE experiment. A superconducting resonator with a resonance frequency close to the particle's modified cyclotron frequency is connected to the trap. By using a varactor diode, the capacitance of the resonant circuit can be varied and the resonance frequency of the detector can be matched to the particle's modified cyclotron frequency or be detuned on purpose to prevent energy exchange between particle and detector. Given the large effective electrode distance for the pickup of the modified cyclotron motion, the dip created by the particle at the cyclotron motion is to narrow to be detected in the noise spectrum of this detector. In order to detect the particle's modified cyclotron frequency ν_+, its modified cyclotron motion is excited to energies on the order of eV which causes the particle's modified cyclotron radius to increase. The excited particle induces strong image currents in the trap electrodes which are amplified by the high quality detection circuit and result in a peak on the noise spectrum of the resonator. Figure 5.14 shows a typical peak spectrum.

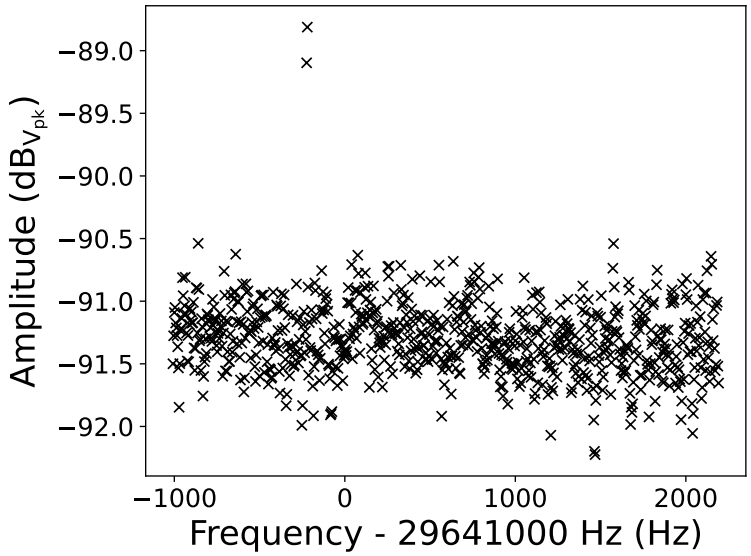

Figure 5.14: After excitation of the modified cyclotron mode, the particle induces image currents in the electrodes which lead to a peak in the spectrum of the cyclotron resonator. The signal to noise ratio of the peak depends on the cyclotron energy of the particle, however, excitation to high energies results in significant shifts of the modified cyclotron frequency $\nu_{+,exc}$.

In order to measure the modified cyclotron frequency using the peak method, first the axial frequency ν_z is measured. Next, the modified cyclotron frequency of the particle is excited by applying a short excitation pulse directly at the particle's modified cyclotron frequency. Depending on the duration and strength of this pulse, the particle's cyclotron energy is increased to $E_{+,exc}$ which results in the appearance of a peak in the noise spectrum of the cyclotron resonator. Typically, $E_{+,exc}$ is chosen in the order of single eV such that the peak is clearly visible while systematic shifts due to relativistic effects and the residual magnetic bottle B_2 are kept small. Next, spectra of the axial dip at $\nu_{z,exc}$ and the cyclotron peak at $\nu_{+,exc}$ are acquired simultaneously. By comparing $\nu_{z,exc}$ and ν_z the excitation energy $E_{+,exc}$ can be determined using Eqs. (2.45) and (2.50) in case B_2 is known. Using the known value of $E_{+,exc}$, the modified cyclotron frequency ν_+ at negligible energy can be determined using the same equations. Since the particle is not oscillating freely, but is damped by the detection circuit, the frequency of oscillation ν'_+ is shifted with respect to the free oscillation frequency ν_+ due to interaction with the resonator. This shift is for example given in [69] and modifies the frequency according to:

$$\nu'_+ = \nu_+ + \frac{1}{4}\frac{1}{2\pi\tau_+}\frac{\Delta\nu_R(\nu_+ - \nu_R)}{(\nu_+ - \nu_R)^2 + (\frac{\Delta\nu_R}{2})^2}. \tag{5.18}$$

The resonator shift thus depends on the cooling time constant τ_+ and width $\Delta\nu_R$ of the resonator as well as the detuning $\nu_+ - \nu_R$ between the modified cyclotron frequency and the resonance frequency of the cyclotron resonator.

5.2.3 Phase sensitive detection methods

In the course of the PhD thesis of Matthias Borchert [99], the first steps towards the implementaion of phase-sensitive detection methods [109, 139] BASE experiment were taken. The following section will give a short overview over the measurement principle and advantages of phase-sensitive measurement techniques. A detailed description of the implementation in BASE is given in [99]. The statistical uncertainty $\Delta\nu_{SNR}$ of the sideband method as well as the peak method described before are limited by the signal to noise ratio which – given the incoherent nature of noise – typically scales as $\Delta\nu_{SNR} \propto \frac{1}{\sqrt{T_{Avg}}}$. Thus a tenfold increase in precision requires the observation time to be increased by a factor of 100. In contrast, the phase $\Delta\phi = 2\pi\nu T_{Avg}$ the particle accumulates during its oscillation increases linearly with the phase evolution time. Thus, if the initial phase ϕ_0 and final phase ϕ_1 after T_{Avg} are known, the particle's frequency can be determined as:

$$\nu_{Phase} = \frac{\phi_1 - \phi_0}{2\pi T_{Avg}}. \tag{5.19}$$

The associated uncertainty consequently scales as:

$$\Delta\nu_{Phase} = \frac{\sqrt{\Delta\phi_1^2 + \Delta\phi_0^2}}{2\pi T_{Avg}}. \tag{5.20}$$

In case the phase scatters $\Delta\phi_1$ and $\Delta\phi_0$ are independent of T_{Avg}, the uncertainty in the measured frequency reduces linearly with the averaging time. In practice, the scatter of the final phase will not be independent for example due to dephasing effects caused by magnetic inhomogeneities.

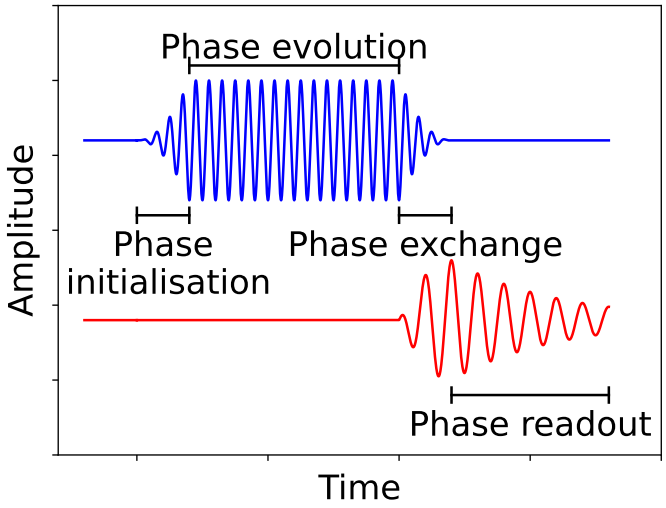

Figure 5.15: Measurement scheme for phase sensitive readout of the modified cyclotron frequency. First, the modified cyclotron motion (blue) is excited and the phase is initialized. Next, the phase evolves freely for the averaging time T_{Avg}. Afterward, the phase of the axial (red) and modified cyclotron motion (blue) are exchanged and the axial phase ϕ_1 is read out. The modified cyclotron frequency can be determined by measuring the final phase for different averaging times T_{Avg}.

Figure 5.15 shows the amplitude of the modified cyclotron and axial motion during a phase measurement sequence. In order to measure the modified cyclotron frequency using phase-sensitive detection methods, the particle's cyclotron mode is excited using an external drive. This imprints a constant phase ϕ_0 determined by the external drive onto the modified cyclotron motion of the particle. Afterward, the drive is switched off and the phase evolves freely for a time T_{Avg}. In order to read out the phase, the cyclotron motion is imprinted onto the axial motion by irradiating the particle on an axial-cyclotron sideband for a time $t = \frac{\pi}{\Omega}$ which corresponds to a complete exchange of cyclotron and axial energy. The duration of this pulse, called π-pulse, depends on the Rabi frequency Ω. Using the fact that these pulses, apart from a constant offset, exchange the phase between the axial and cyclotron motion [109], the phase ϕ_1 can be read out by acquiring an FFT spectrum. Due to the constant offset created by the phase-exchange pulse, the resulting frequency can not be directly calculated using Eq.(5.19), but rather needs to be determined by measuring the slope $\frac{\Delta\phi_1}{\Delta T_{Avg}}$ of the final phase ϕ_1 for different averaging times T_{Avg}:

$$\nu_{Phase} = \frac{1}{2\pi}\frac{\Delta\phi_1}{\Delta T_{Avg}}. \tag{5.21}$$

5.3 Magnetron frequency determination

Given the strong suppression of the magnetron frequency ν_z in the invariance theorem, precise measurements of the magnetron frequency are less important. Typically, the magnetron frequency can be estimated to sufficient precision in case the axial frequency ν_z and the modified cyclotron frequency ν_+ are known:

$$\nu_- = \frac{\nu_z^2}{2\nu_+}. \tag{5.22}$$

This relationship, however, only holds in case the trap is not misaligned with respect to the magnetic field and the trap is perfectly cylindrical. In case the exact magnetron frequency ν_- needs to be known, sideband coupling on the upper axial-magnetron sideband $\nu_{SB} = \nu_z + \nu_-$ can be applied. The measurement scheme is equivalent to the case of sideband coupling between modified cyclotron frequency and axial frequency, however, given that the upper sideband needs to be irradiated, the magnetron frequency is given by:

$$\nu_- = \nu_{rf} + \nu_z - \nu_L - \nu_R. \tag{5.23}$$

Note that since the upper sideband is irradiated, the avoided crossing of the magnetron motion looks mirrored to the one of the modified cyclotron motion shown in figure 5.13. By comparing the magnetron frequency calculated according to Eq. (5.22) with the directly measured magnetron frequency provides the possibility to determine the misalignment of the trap stack with respect to the magnetic field [127].

5.4 Tuning ratio optimization

In order to measure a trapped particles axial frequency in the BASE precision trap, it is brought into contact with an axial detection circuit described in chapter 3.3.1. Non-harmonic contributions to the electrostatic trapping potential cause the particle's axial oscillation frequency to depend on its axial energy E_z. To first order, the dependency of the axial frequency on the axial energy E_z is given by

$$\nu_z(E_z) = \nu_{z,0} \times \left(1 + \frac{3}{4}\frac{1}{qV_0}\frac{C_4}{C_2^2}E_z\right) = \nu_{z,0} \times (1 + \alpha_z E_z) \tag{5.24}$$

as described by Eq. (2.40). The constant α_z depends on the anharmonicity C_4 and describes how strong the axial frequency depends on the axial energy E_z.
As the particle is continuously exchanging energy with the resonator circuit, it's axial frequency

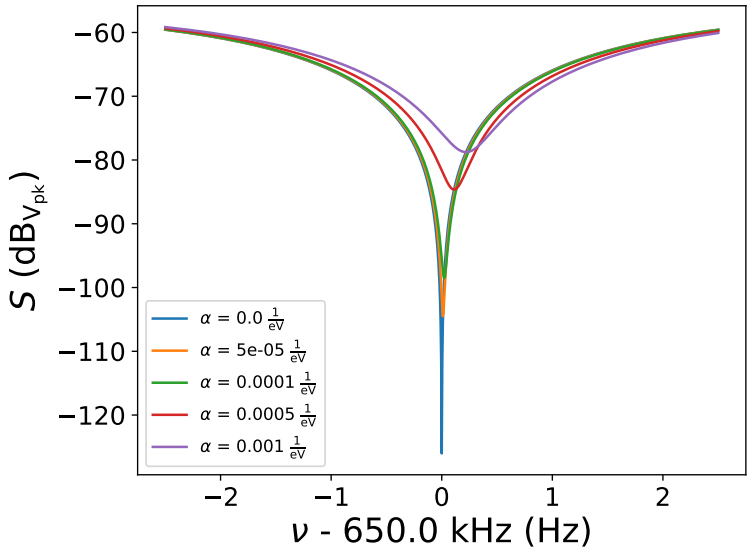

Figure 5.16: Calculated lineshape for different couplings between the axial frequency ν_z and the axial energy E_z. Higher order contributions to the axial trapping potential lead to a dependency of the axial frequency $\nu_z(E_z) = \nu_{z,0} \times (1 + \alpha_z E_z)$ on the axial energy E_z. As the particle is in thermal contact with the axial detection circuit, it's axial energy constantly changes during the acquisition of an axial spectrum. The resulting signal to noise ratio of the dip feature depends on the coupling strength α.

continuously changes. Given that the axial cooling times is typically on the order of $50\,\mathrm{ms}$, the particle's axial energy can not be assumed to be constant during the acquisition of an axial spectrum. The observed spectral power density $S^2_{obs}(\nu)$ is thus given by a convolution of the momentary spectral power density $S^2(\nu, E_z)$ given by Eq. (3.6) and the thermal Boltzman distribution $p(E_z) = \frac{1}{k_B T_{res}} e^{\frac{E_z}{k_B T_{res}}}$:

$$S^2_{obs}(\nu) = \int_0^\infty S^2(\nu, E_z) p(E_z) \mathrm{dE_z}. \tag{5.25}$$

Figure 5.16 shows the convolved spectral noise density $S_{obs}(\nu)$ under typical conditions for a resonator temperature of $T_{res} = 4\,\mathrm{K}$ and different values of α_z.
For high values of α, the particle's random walk through the thermal Boltzmann distribution leads to a significant random walk of the particle's axial frequency during the acquisition of an axial spectrum. Thus, the dip feature moves and the SNR decreases. In order to maximize the signal to noise ratio and suppress these systematic shifts, it is crucial to minimize α by tuning

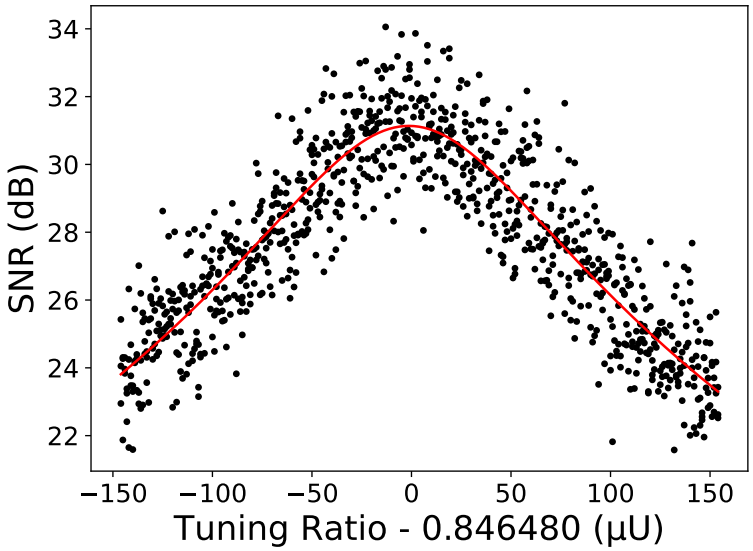

Figure 5.17: Signal-to-noise ratio (SNR) as a function of the applied tuning ratio (TR). At the ideal tuning ratio, the SNR is maximized as the dependency of the particle's axial frequency on it's axial temperature is strongly suppressed. The red line shows a fit of Eq. (5.26) to the data.

C_4 close to 0. Figure 5.17 shows the signal-to-noise ratio (SNR) as a function of the applied tuning ratio (TR).
Typically, an analytic approximation for the dependency of the SNR which is derived by expanding Eq. (5.25) around the minimum, is used to determine the ideal tuning ratio:

$$\mathrm{SNR}(TR) = \mathrm{SNR}_{max} - 10\log_{10}\left(\frac{TR - TR_{ideal}}{A} + 1\right). \tag{5.26}$$

Near the ideal tuning ratio TR_{ideal}, the particle's axial frequency does not depend on it's axial temperature ($\alpha \approx 0$) and the SNR is maximized. The slope A with which the SNR decreases depends on the temperature of the axial resonator.

5.5 Asymmetry compensation

Under ideal conditions, the center of the trapping potential coincides with the geometric center of the trap. However, cooldown of the system and loading of particles can lead to patch potentials located on the surfaces of the electrodes which cause an assymmetry in the potential and shift the particle out of the center in case symmetric voltages are applied to the two correction electrodes. In order to compensate for these patch potentials, an offset voltage V_{Off} is applied

to one of the correction electrodes. Given this asymmetric application of the offset voltage the ideal tuning ratio changes with the chosen offset voltage and the offset ratio used in the experiment is defined as

$$\mathrm{OR} = \frac{V_{Off}}{V_{Ring}}. \tag{5.27}$$

Eq. (2.34) can be modified to include the non-symmetric potential terms Φ_{Off} introduced by the offset voltage:

$$\begin{array}{rrcccccccccc} & \Phi_{\mathrm{R}}(z) & = & (& & E_2 z^2 & + & & E_4 z^4 + & O(z^5)) & V_R \\ + & \Phi_{\mathrm{C}}(z) & = & (& & D_2 z^2 & + & & D_4 z^4 + & O(z^5)) & V_R \cdot \mathrm{TR} \\ + & \Phi_{\mathrm{Off}}(z) & = & (F_1 z & + & F_2 z^2 & + & F_3 z^3 & + F_4 z^4 + & O(z^5)) & V_R \cdot \mathrm{OR} \\ \hline = & \Phi'(z) & = & (C'_1 z & + & C'_2 z^2 & + & C'_3 z^3 & + C'_4 z^4 + & O(z^5)) & V_R. \end{array} \tag{5.28}$$

Given that F_2 is small compared to C_2, the location of the modified axial potential's axial minimum is approximately given by

$$z_{min} \approx -\frac{F_1}{2C_2} \times \mathrm{OR} = 2.81\,\mathrm{mm} \times \mathrm{OR}. \tag{5.29}$$

For typical ring voltages used in the BASE experiment, this corresponds to a transfer function of $z_{min}(V_{Off}) \approx \pm\frac{5.85\,\mu\mathrm{m}}{10\,\mathrm{mV}} \times V_{Off}$. The sign depends on which correction electrode the offset voltage is applied. Note that if the trap is orthogonal ($D_2 \approx 0$), the transfer function does not depend on the tuning ratio.

In order to determine the particle's axial frequency, $\Phi'(z)$ is expanded around z_{min}. Given that $F_4 = \frac{1}{2}D_4$ in a symmetric trap, the tuning ratio needs to be adjusted as well. Requiring $C'_4 = 0$ yields the modified tuning ratio

$$\mathrm{TR}' = -\frac{E_4 + F_4 \times \mathrm{OR}}{D_4} = TR - \frac{F_4}{D_4} \times \mathrm{OR} = TR - \frac{1}{2}\mathrm{OR}. \tag{5.30}$$

Figure 5.18 shows the calculated value of C'_2 as a function of the applied offset voltage ratio in case the tuning ratio is kept static ($\mathrm{TR} = 0.877\,432$) or adjusted according to Eq. (5.27).

Figure 5.19 shows the optimized tuning ratio as a function of the applied offset ratio. For typical offset ratios, the ideal TR can be approximated well by a linear function. Fitting the optimized tuning ratios yields the line of best fit

$$TR_{ideal}(OR) = 0.853\,53(21) - 0.549(12) \times OR. \tag{5.31}$$

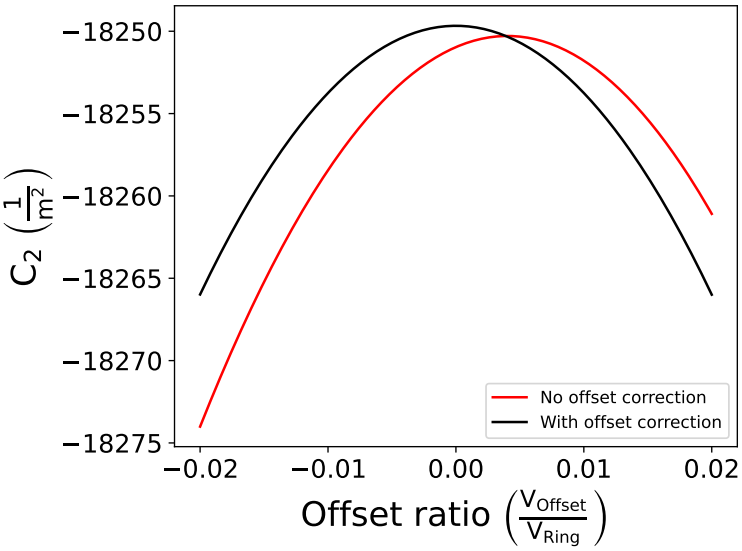

Figure 5.18: Calculated C_2 value for different offset ratios OR applied to one of the correction electrodes. In case of a symmetric trap, the absolute value of C_2 is minimized.

This relationship can be used to determine a starting point for manual tuning ratio optimization in case the particle is shifted along the trap axis.
In order to determine the offset voltage V_{Off} that compensates the patch potentials and symmetrizes the trap, the offset voltage which minimizes the C_2 coefficient after the tuning ratio has been optimized has to be determined. As seen by in the calculations above, this corresponds to the case of a symmetric trapping potential. Figure 5.20 shows the measured C_2 value as a function of the applied offset ratio. A quadratic fit to the data yields the ideal offset ratio of $\mathrm{OR}_{\mathrm{ideal}} = 0.012\,49(3)$ which corresponds to an ideal offset voltage of $V_{Off,ideal} = -0.060\,09(14)\,\mathrm{V}$ at a typical ring voltage of $V_R = -4.810\,140\,\mathrm{V}$.

5.6 Determination of axial temperature

The temperature of the axial detector can be determined by measuring the axial frequency scatter after the cyclotron motion is excited to different energies. If a resonant drive at the modified cyclotron frequency is irradiated on the particle, the particle's cyclotron radius $\rho_+(t)$ increases linearly with time [69]:

$$\rho_+(t) = \rho_{th}\cos(\phi) + \frac{qA_{drive}}{2m\omega_+}t \tag{5.32}$$

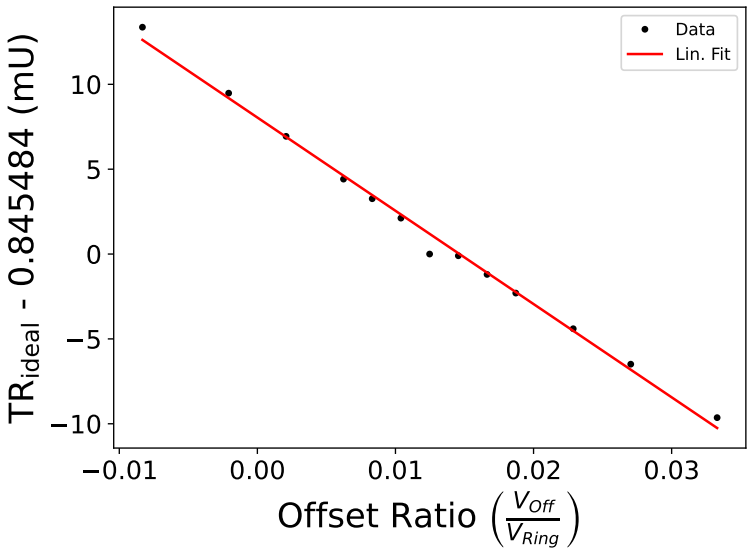

Figure 5.19: Optimized tuning ratio for different offset voltages V_{Off} applied to one of the correction electrodes. A quadratic fit to the data yields the ideal offset voltage $V_{Off,ideal} = -0.060\,09(14)\,\mathrm{V}$.

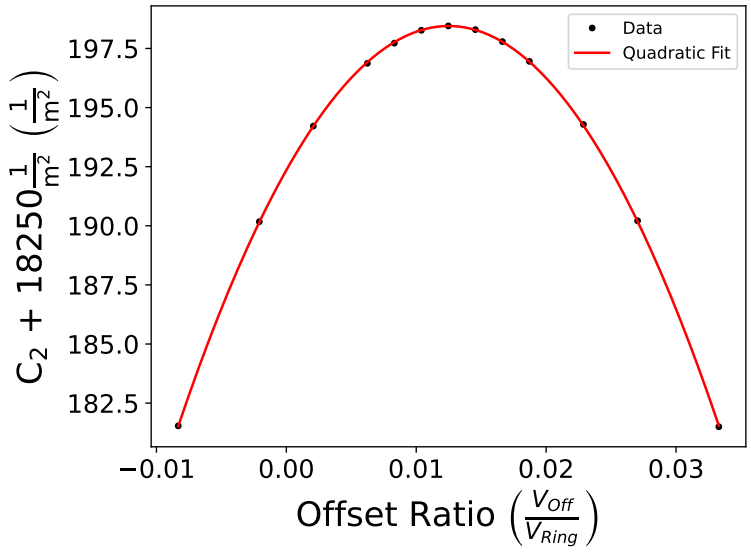

Figure 5.20: Measured C_2 value for different offset ratios OR applied to one of the correction electrodes. A quadratic fit to the data yields the ideal offset voltage $V_{Off,ideal} = -0.060\,09(14)\,\mathrm{V}$.

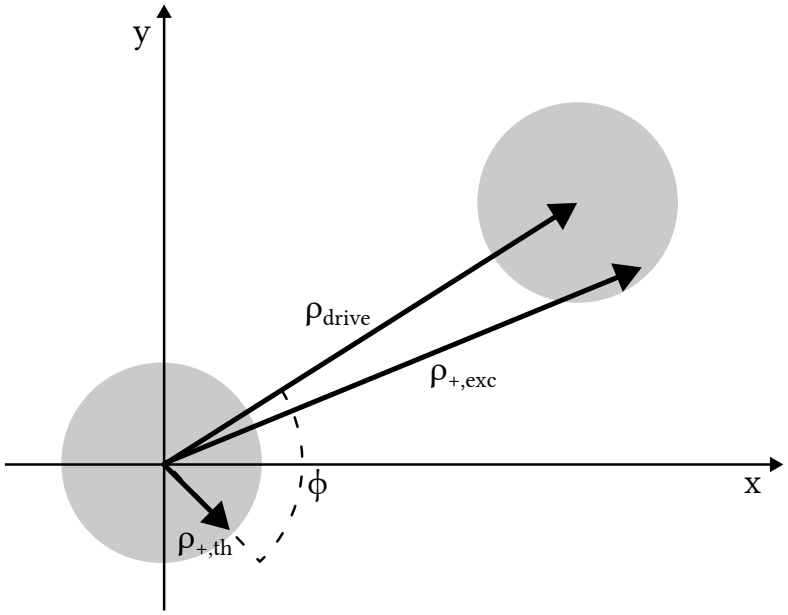

Figure 5.21: Radial position of the particle's mod. cyclotron motion. The initial radius $\rho_{+,th}$ depends on the temperature of the cyclotron mode. Applying a resonant drive shifts the initial distribution by ρ_{drive}. The final radius $\rho_{+,exc}$ depends on the initial radius $\rho_{+,th}$, the shift ρ_{drive} induced by the drive and the phase difference between $\rho_{+,th}$ and ρ_{drive}.

The initial radius ρ_{th} follows a Rayleigh distribution which is determined by the temperature of the cyclotron detector. The finial radius depends on the phase difference ϕ between the initial phase and the drive. The electric field amplitude A_{drive} leads to a linear increase in the radius ρ_{drive} which shifts the initial Rayleigh distribution to higher radii. The final radius $\rho_{+,exc}$ after excitation thus follows a random distribution which causes the particle's modified cyclotron energy $E_{+,exc}$ after excitation to scatter. Figure 5.21 shows a schematic of the radii involved in the excitation scheme.

The residual magnetic bottle present in the precision trap couples the modified cyclotron energy $E_{+,exc}$ after excitation to the axial frequency ν_z. To first order, the scatter $\sigma(\nu_z)$ of the axial frequency is proportional to the scatter $\sigma(E_{+,exc})$ of the modified cyclotron energy after excitation. By integrating the shifted distribution of radial positions over the phase ϕ_0 and initial radii the distribution of final energies $E_{+,exc}$ can be determined. The standard deviation $\sigma(E_{+,exc})$ of the corresponding distribution of radial energies $E_{+,exc}$ depends on the initial thermal energy $E_{+,th} = k_B T_+$ and the energy E_{drive} added by the resonant drive. A detailed derivation is given in [99] and yields:

$$\sigma(E_{+,exc}) = \sqrt{1 + \frac{1}{2}\frac{E_{+,th}}{E_{drive}}} \times \sqrt{E_{+,th}E_{drive}} \approx (1 + \frac{1}{4}\frac{E_{+,th}}{E_{drive}}) \times \sqrt{E_{+,th}E_{drive}}. \quad (5.33)$$

In order to determine the initial temperature T_+, the axial frequency scatter is measured for different excitation energies E_{drive}. First, the particles cyclotron motion is thermalized via sideband coupling to the axial detector. Next, the axial frequency is determined, the particle is excited and the axial frequency after excitation is determined. This sequence is repeated and the excitation strength is varied.
The excitation energy E_{drive} for a given drive setting is determined by comparing the axial frequency before and after excitation. In case the tuning ratio is optimized and $C_4 \approx 0$, the excitation energy E_{drive} can be determined from the observed axial frequency shift $\Delta\nu_z$ using Eq. (2.45).

$$E_{drive} = \frac{\frac{\Delta\nu_z}{\nu_z}}{\frac{1}{4\pi^2 m\nu_z^2}\frac{B_2}{B_0} - \frac{1}{mc^2}}. \quad (5.34)$$

Figure 5.22 shows the axial frequency scatter $\sigma(\nu_z)$ as a function of the average excitation energy $E_{+,exc}$ determined from the observed axial shifts and assuming a background magnetic field $B_2 = 105\,\mathrm{mT}$. By fitting the approximation of Eq.(5.33) to the data, the average initial cyclotron temperature

$$T_+ = \frac{E_+}{k_B} = 622(38)\,\mathrm{K}. \quad (5.35)$$

can be determined. Given that the equilibrium temperature after sideband coupling the axial and cyclotron mode is given by $T_+ = \frac{\nu_+}{\nu_z}T_z$, the temperature of the axial detection system is given by

$$T_z = \frac{\nu_z}{\nu_+}T_z = 13.62(82)\,\mathrm{K}. \quad (5.36)$$

5.7 B_1 measurements

The B_1 coefficient of the magnetic field expansion given by Eq. (2.43) can be measured directly by comparing the trapped particle's cyclotron frequency at different positions along the trap axis. The particle is shifted in z-direction by applying an offset voltage to one of the correction electrodes and adjusting the tuning ratio to locally compensate C_4 and C_6 which maximizes the SNR. Using Eq. 2.32, the location of the potential minimum can be calculated for a given Offset

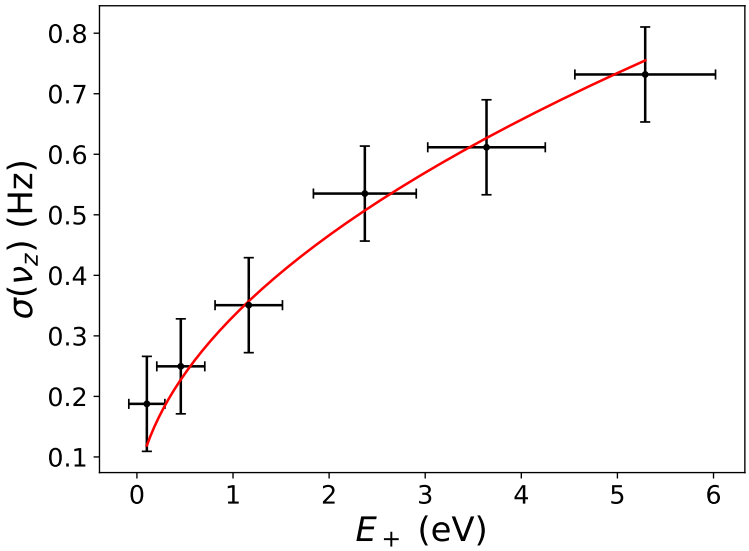

Figure 5.22: Axial frequency scatter $\sigma(\nu_z)$ as a function of the cyclotron energy E_+. By fitting Eq. (5.33) to the measured data, the energy $E_{+,th}$ after thermalization with the axial detector can be determined. This fit yields $T_+ = \frac{E_+}{k_B} = 622(38)\,\mathrm{K}$, which corresponds to an axial temperature of $T_z = \frac{\nu_z}{\nu_+} T_z = 13.62(82)\,\mathrm{K}$.

voltage V_{Off} and tuning ratio TR. Figure 5.23 shows the particle's position along the trap axis for different offset voltages after the SNR has been maximized. Note that for the offset voltages scanned in the dataset shown in Fig. 4 the particle position $z(\Delta V)$ is to first order linear with respect to changes of the offset voltage.

At each position, the axial frequency ν_z and modified cyclotron frequency ν_+ are measured and the free cyclotron frequency ν_c is calculated. Figure 5.24 shows the measured cyclotron frequency for seven different positions along the trap axis.

Fitting a straight line to the data yields for the B_1 background value:

$$B_1 = 2\pi \frac{m}{q} \frac{\Delta \nu_c}{\Delta z} = 25.27(10)\,\frac{\mathrm{mT}}{\mathrm{m}}. \tag{5.37}$$

While shifts of the particles eigenfrequencies caused by B_1 are somewhat suppressed, given that the average field the particle experiences over its oscillation does not change with B_1, knowledge of the B_1 coefficient is still important. On the one hand, the magnetic moment associated with the cyclotron mode creates an additional force in the B_1 gradient which moves the particle along the magnetic field Δz and thus leads to a shift $B = \Delta z \times B_1$ which changes the free cyclotron frequency. On the other hand voltage drifts after particle transport may cause

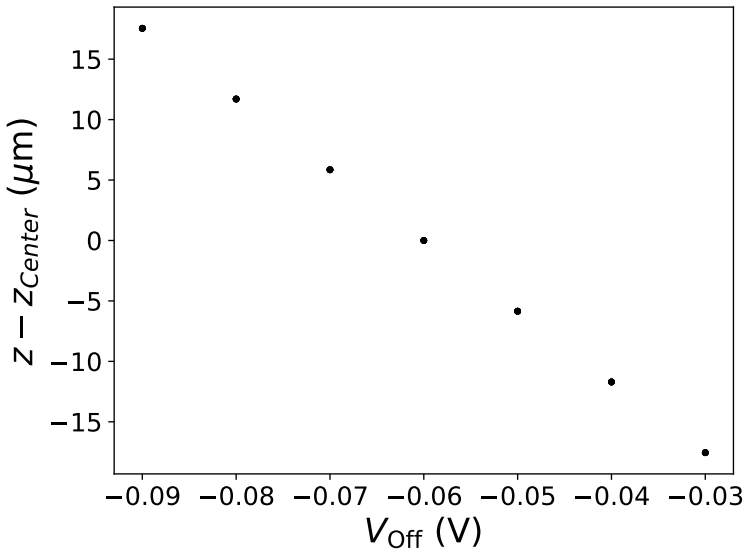

Figure 5.23: Particle position in the precision trap as a function of applied offset voltage. For small deviations from the compensated trap ($V_{\mathrm{Off}} = -60\,\mathrm{mV}$) the change of position along the trap axis is proportional to the change in offset voltage and the particle moves by $\frac{5.85\,\mu\mathrm{m}}{10\,\mathrm{mV}}$.

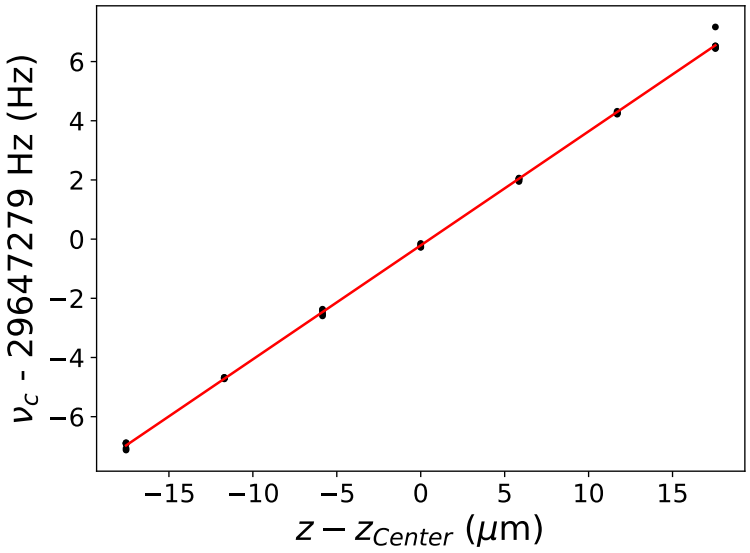

Figure 5.24: Measured free cyclotron frequency ν_c as a function of the particle's position along the trap axis. B_1 changes the magnetic field along the trap axis which leads to a change in free cyclotron frequency. A straight line (red line) fit yields $B_1 = 25.27(10)\,\frac{\mathrm{mT}}{\mathrm{m}}$.

the particles position to change slightly for some time while the electrode voltages settle. In case two particles are moved into the precision trap from different directions and not enough settling time is given after the transport has finished, the particles might be located at different positions along the trap axis and thus might experience slightly different magnetic fields. At the measured background gradient of $B_1 = 25.27(10)\,\frac{\mathrm{mT}}{\mathrm{m}}$ this causes a relative shift of

$$\frac{B_1}{B_0} \approx \frac{25.27\,\frac{\mathrm{mT}}{\mathrm{m}}}{1.944\,\mathrm{T}} = 13.0 \times 10^{-6}\,\frac{1}{\mathrm{m}} = 13\frac{\text{p.p.t.}}{\mu\mathrm{m}}. \tag{5.38}$$

In order to suppress this shift, either great care has to be taken to ensure that enough time is given for all voltages to settle and particle positions are independent of the transport direction and history or B_1 has to be tuned close to 0.

5.8 B_2 measurements

Measurement of the B_1 coefficient show that the magnetic field in the precision trap changes linearly around the trap center and higher field expansion terms do not play a role on length scales that can be probed by shifting the particle along the trap axis. B_2 is therefore measured by exciting the particles cyclotron energy E_+ and measuring the associated shifts of the modified cyclotron frequency ν_+ and the axial frequency ν_z simultaneously. If the trap is well compensated ($C_4 = C_6 = 0$), the shift of the modified cyclotron frequency $\Delta\nu_+$ experienced by protons and antiprotons is dominated by relativistic effects and shifts due to B_1 and B_2:

$$\Delta\nu_+ = \nu_+ \left(-\frac{1}{mc^2} - \frac{1}{4\pi^2 m\nu_z^2}\left(\frac{B_1}{B_0}\right)^2 - \frac{1}{4\pi^2 m\nu_z^2}\left(\frac{\nu_z}{\nu_+}\right)^2 \frac{B_2}{B_0} \right) E_+ \tag{5.39}$$

B_1 can be determined before the measurement using the method outlined above. Solving the shift of the axial frequency

$$\Delta\nu_z = \nu_z \left(-\frac{1}{2mc^2} + \frac{1}{4\pi^2 m\nu_z^2}\frac{B_2}{B_0} \right) E_+ \tag{5.40}$$

for E_+ and inserting the result into Eq. (5.39), results in an equation for B_2 that only depends on the ratio $\frac{\Delta\nu_z}{\Delta\nu_+}$ of the axial and cyclotron frequency shifts:

$$B_2 = \frac{2\pi^2 B_0^2 \nu_z^3 \nu_+ - \frac{\Delta\nu_z}{\Delta\nu_+}\left(c^2\nu_+^2 B_1^2 + 4\pi^2\nu_+^2\nu_z^2 B_0^2\right)}{B_0 c^2 \nu_z \nu_+ + \frac{\Delta\nu_z}{\Delta\nu_+} B_0 c^2 \nu_z^2}. \tag{5.41}$$

For a typical B_2 measurement, the particle is first excited to a reference cyclotron energy of typically $8.5\,\mathrm{eV}$ and $33\,\mathrm{s}$ FFT spectra of the axial dip and the cyclotron peak are acquired. Next,

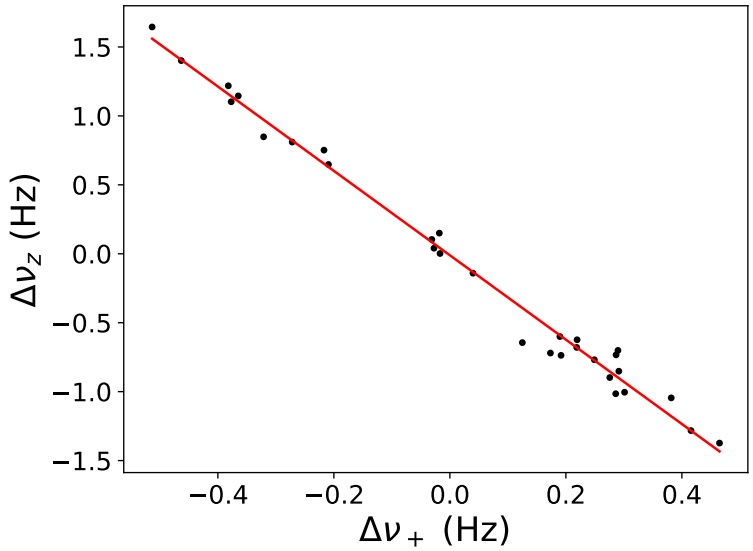

Figure 5.25: Axial and modified cyclotron frequency shifts for 5 different excitation energies. For a known value of B_1, the slope $\frac{\Delta\nu_z}{\Delta\nu_+} = -3.060(64)$ depends on B_2.

the particle is excited to a different excitation energy typically ranging approximately from $4\,\mathrm{eV}$ to $14\,\mathrm{eV}$ and $33\,\mathrm{s}$ FFT spectra of the excited axial dip and the cyclotron peak are taken. By comparing the frequency shifts between the excitation and reference energy, the ratio of shifts $\Delta\nu_z$ and $\Delta\nu_+$ are determined. Typically this measurement scheme is repeated for 5 different excitation energies and measurements are repeated 3 times for each energy. Including cooling and excitation, a typical B_2 measurement takes around $28\,\mathrm{min}$. Figure 5.25 shows the measured shifts of the axial and modified cyclotron frequencies for 6 repetitions at 5 different excitation energies. Due to the initial cyclotron energy of the particle, the energy after burst excitation scatters around the expected values and the datapoints are distributed along the $\frac{\Delta\nu_z}{\Delta\nu_+}$ line. Outliers are cleaned by setting fixed boundaries for the maximum and minimum accepted shifts.

Fitting the slope $\frac{\Delta\nu_z}{\Delta\nu_+} = -3.060(64)$ and using the background value of $B_1 = 25.27(10)\,\frac{\mathrm{mT}}{\mathrm{m}}$ results in a B_2 value of

$$B_2 = 103.50(23)\,\frac{\mathrm{mT}}{\mathrm{m}^2}. \tag{5.42}$$

5.9 B_4 measurements

In addition to the frequency shift's caused by the B_1 and B_2 terms, magnetic inhomogneities of the for $B(z) = B_4 z^4$ cause the ideal tuning ratio to depend on the trapped particle's cyclotron energy E_+. Using the derivation of the magnetic dipole moment $\mu_z \approx -\frac{q}{m}\frac{E_+ - E_-}{\omega_+}$ associated with the radial motion given in [87], the overall axial potential Φ_{total} experienced by the particle no longer depends only on the electrostatic potential described by the C_j term in Eq. (2.34) but also has a contribution due to the magnetic inhomogeneities. The resulting potential Φ_{total} once again can be expanded around $z = 0$ which yields expansion coefficients $\tilde{C}_j$ which depend on the electrostatic expansion coefficients C_j and D_j as well as the magnetic inhomogeneities:

$$\Phi_{total} = \sum\nolimits_{j=0}^{\infty} \left(qV_R C_j - \mu_z B_j\right) z^j = \sum\nolimits_{j=0}^{\infty} \tilde{C}_j z^j. \tag{5.43}$$

In order for Φ_{total} to be harmonic, the $\tilde{C}_j$ need to vanish. In the case of

$$\tilde{C}_4 = C_4 qV_R - \mu_z B_4 = \left(E_4 + \tilde{\mathrm{TR}} D_4\right) qV_R - \mu_z B_4, \tag{5.44}$$

the adjusted tuning ratio $\tilde{\mathrm{TR}}$ can be chosen such that $\tilde{C}_4$ vanishes:

$$\tilde{\mathrm{TR}} = -\frac{E_4}{D_4} + \frac{\mu_z B_4}{qV_R D_4} = \mathrm{TR} - \frac{q}{m}\frac{B_4}{\omega_+ qV_R D_4}\left(E_+ - E_-\right). \tag{5.45}$$

By measuring the dependency of the ideal tuning ratio on the cyclotron energy

$$\frac{\partial \tilde{\mathrm{TR}}}{\partial E_+} = -\frac{q}{m}\frac{B_4}{\omega_+ qV_R D_4}. \tag{5.46}$$

B_4 can be determined as

$$B_4 = -m\omega_+ V_R D_4 \frac{\partial \tilde{\mathrm{TR}}}{\partial E_+} \approx -B_0 qV_R D_4 \frac{\partial \tilde{\mathrm{TR}}}{\partial E_+}. \tag{5.47}$$

In order to resolve $\frac{\partial \tilde{\mathrm{TR}}}{\partial E_+}$ the tuning ratio is optimized as described in 5.4 at different cyclotron energies E_+. The cyclotron energy for each TR optimization is determined by measuring the axial frequency in a known B_2 before and after excitation of the cyclotron mode. Figure 5.26 shows the ideal tuning ratio as a function of the cyclotron energy E_+.
A linear fit to the data yields $\frac{\partial \tilde{\mathrm{TR}}}{\partial E_+} = 5.4(3) \times 10^{-6}\,\frac{1}{\mathrm{eV}}$. Combining this result with the value of $D_4 = -1.30 \times 10^9\,\frac{1}{\mathrm{m}^4}$ obtained from potential theory using Eq. (2.32) and a background magnetic field of $B_0 = 1.945\,\mathrm{T}$ yields a value of

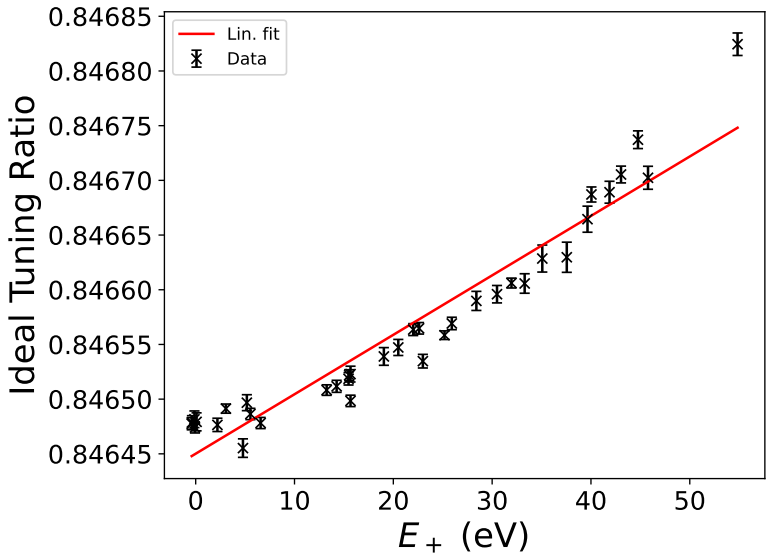

Figure 5.26: Optimized tuning ratio as a function of the radial excitation energy E_+. The quartic magnetic inhomogeneity B_4 causes the ideal tuning ratio to change with the cyclotron energy E_+. A linear fit to the data yields $B_4 = -66(3) \times 10^3 \, \frac{\mathrm{T}}{\mathrm{m}^4}$.

$$B_4 = -66(3) \times 10^3 \, \frac{\mathrm{T}}{\mathrm{m}^4}. \tag{5.48}$$

Given the suppression of cyclotron frequency shifts by additional orders $\Omega = \frac{\nu_z}{\nu_+}$ systematic shifts related to B_4 are of secondary concern for frequency measurements in the precision trap.

6 Characterization of the coil system

6.1 Transfer functions

In order to measure the transfer functions of the individual shimming coils, the respective coil is loaded and B_0, B_1 and B_2 are measured as a function of the loaded current. As long as the loaded current stays below the critical current density of the persistent joint B_0, B_1 and B_2 change proportionally with the current. In case a higher loading current is applied, current in the coil decays until the current density in the persistent joint drops below the critical current density and the change in field therefore plateaus.

6.1.1 B_2 coil

Figures 6.1a - 6.1c show the shift of the B_2, B_1 and B_0 coefficients created by the B_2 coil as a function of the loaded current. Note that for the calculation of the B_2 value the measured B_1 values were used. Fitting a straight line to the data allows the determination of the respective transfer functions. Note that for B_2, only values for loading currents below $150\,\mathrm{mA}$ were used in the fit. Table 6.1d summarizes the measured and theoretical transfer functions of the B_2 coil as well as the adjustment of the theoretical values due to the loading scheme.

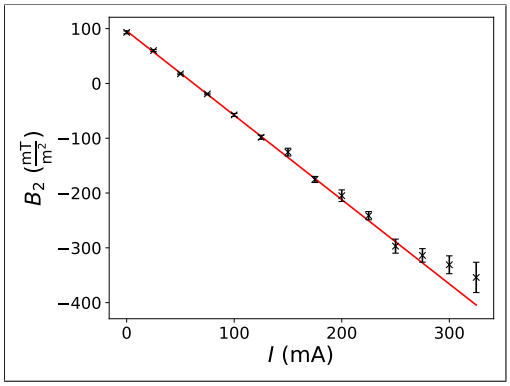

(a)

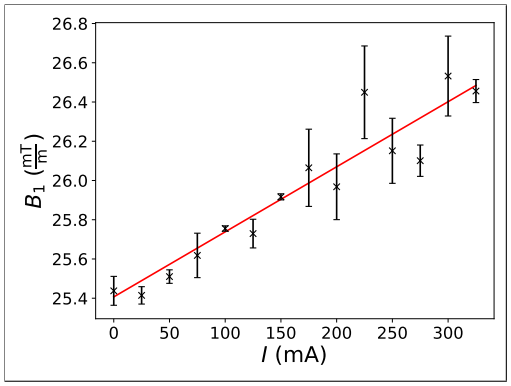

(b)

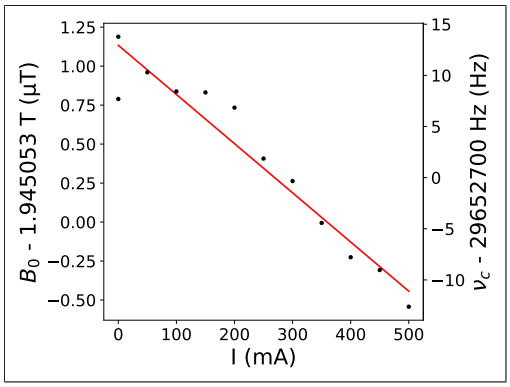

(c)

	$\frac{B_0}{I}$ [$\frac{\mathrm{T}}{\mathrm{A}}$]	$\frac{B_1}{I}$ [$\frac{\mathrm{T}}{\mathrm{mA}}$]	$\frac{B_2}{I}$ [$\frac{\mathrm{T}}{\mathrm{m}^2\,\mathrm{A}}$]
Theory	-359×10^{-9}	0	1.87
Loading scheme adjusted	-346×10^{-9}	0	1.80
Measured	$-223(286) \times 10^{-9}$	$-3.3(2) \times 10^{-3}$	1.538(27)

(d)

Figure 6.1: (a) B_2 transfer function. (b) B_1 transfer function. (c) B_0 transfer function. (d) Summary of the calculated and measured transfer functions of the B_2 coil. The 2nd line indicates the theoretical values adjusted for the losses due to the loading scheme.

Figure 6.1a shows that the B_2 coefficient changes linearly with the applied loading current up to a loading current of approximately 250 mA. For loading currents above 250 mA, the change in B_2 continues to increase, however, heat induced residual resistance leads to a partial decay of the loaded current and the slope decreases. Using the previously measured background value of $B_2 = 103.50(23)\,\frac{\mathrm{mT}}{\mathrm{m}^2}$, the loading current $I_{B_2,comp}$ necessary to tune B_2 to 0 is given by

$$I_{B_2,comp} \approx \frac{B_2}{\frac{\Delta B_2}{\Delta I}} \approx \frac{103.50\,\frac{\mathrm{mT}}{\mathrm{m}^2}}{1.538\,\frac{\mathrm{T}}{\mathrm{m}^2\,\mathrm{A}}} \approx 67.3\,\mathrm{mA}. \tag{6.1}$$

and lies way below the maximum loading current of 250 mA.

6.1.2 B_1 coil

Similarly to the B_2 coil, loading the B_1 coil causes shifts of the B_2, B_1 and B_0 coefficients. Given that it was quickly discovered that the persistent joint of the B_1 coil does not support loading currents above approximately 250 mA and the B_1 transfer function is expected to be small compared to the background B_1, these measurements were done by continuously applying the loading current with all coils quenched. Figures 6.2a - 6.2c show the measured B_2, B_1 and B_0 coefficients as a function of the current applied to the B_1 coil.

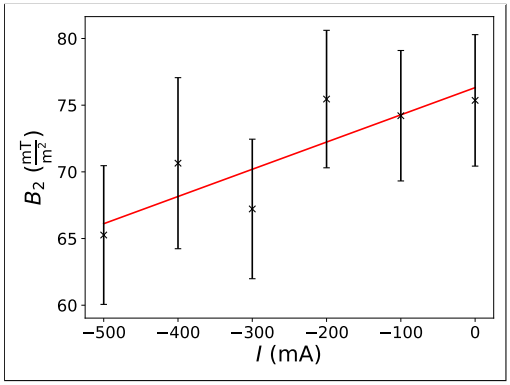

(a)

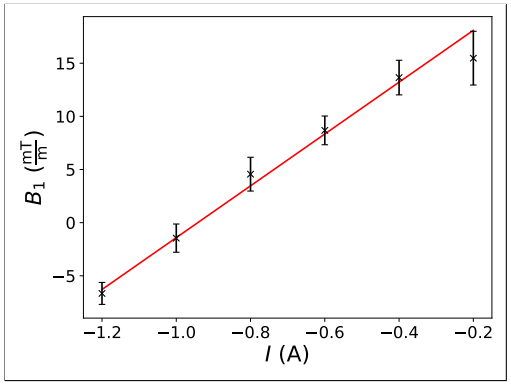

(b)

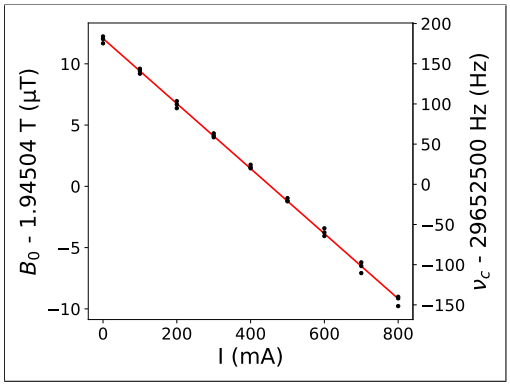

(c)

	$\frac{B_0}{I}$ [$\frac{T}{A}$]	$\frac{B_1}{I}$ [$\frac{T}{mA}$]	$\frac{B_2}{I}$ [$\frac{T}{m^2 A}$]
Calculation	0	26.0	0
Simulation	0.00(2)	26.0(7)	0.00(4)
Measurement	$26.5(2) \times 10^{-6}$	24.4(1)	0.020(6)

(d)

Figure 6.2: (a) B_2 transfer function. (b) B_1 transfer function. (c) B_0 transfer function. (d) Summary of the simulated and measured transfer functions of the B_1 coil.

Table 6.2d summarizes the fitted transfer functions as well as the design values and the results of the Monte-Carlo simulations.

The B_1 transfer function is roughly 94 % of the expected value. This deviation is larger than one would expect given the assumptions on the errors of the coil parameters, however, the Monte-Carlo simulations do not take the additional wire necessary to connect the coil to the

loading joints into account. Given that this wire is located only on one side of the coil, it is reasonable to assume that the parasitic wire has a large influence on the B_1 coefficient.
Given the measured transfer function of the coil, the required current $I_{B_1,Comp}$ to compensate the background B_1 is

$$I_{B_1,comp} \approx \frac{B_1}{\frac{\Delta B_1}{\Delta I}} \approx \frac{25.27\,\frac{\mathrm{mT}}{\mathrm{m}}}{24.4\,\frac{\mathrm{mT}}{\mathrm{m\,A}}} \approx 1.04\,\mathrm{A}. \tag{6.2}$$

With the maximum current $I_{B_1,Max} = 250\,\mathrm{mA}$ that was successfully loaded into the B_1 coil, we expect to be able to tune B_1 to

$$B_{1,Min} \approx B_{1,Background} - \frac{B_1}{I} \times I_{B_1,Max} \approx 25.27\,\frac{\mathrm{mT}}{\mathrm{m}} - 24.4\,\frac{\mathrm{mT}}{\mathrm{m\,A}} \times 250\,\mathrm{mA} \approx 19.17\,\frac{\mathrm{mT}}{\mathrm{m}}. \tag{6.3}$$

Given that shifts due to B_1 are of secondary concern and can be suppressed by carefully excluding voltage drifts on the trap electrodes, we do not expect B_1 to limit the planned antiproton g-factor measurement on the 100 p.p.t level.

6.2 Loading scheme

As described in chapter 4.6, loading the coils requires heating part of the superconducting wire above its critical temperature by dissipating power in a quench resistor. The dissipated energy needs to be high enough to heat the superconducting wire of the associated coil above its critical temperature, but not high enough to quench part of the other coils. In the ideal case, the quench current quenches the associated coil after a short time and once the quench current is removed, the coil quickly becomes superconducting again. At the same time, the current has to be high enough to ensure that the quenching procedure is independent of the history of the applied quench and loading currents, i.e. the quenching behavior should not change between different attempts. In order to ensure good thermal decoupling and minimize crosstalk between the different coils, the quench heaters are spatially separated and isolated from the trapcan by multiple layers of Kapton sheet.
In order to characterize the minimum required quench currents, loading current is run through the coil that is being optimized and the quench current is slowly increased while monitoring the free cyclotron frequency. Once the quench current is high enough to quench the coil, current is forced through the field creating path and the free cyclotron frequency jumps. In case the SSC quench current is optimized, the loading current is applied to the B_0 coil which causes current to be induced in the SSC which partially shields the change of the free cyclotron frequency

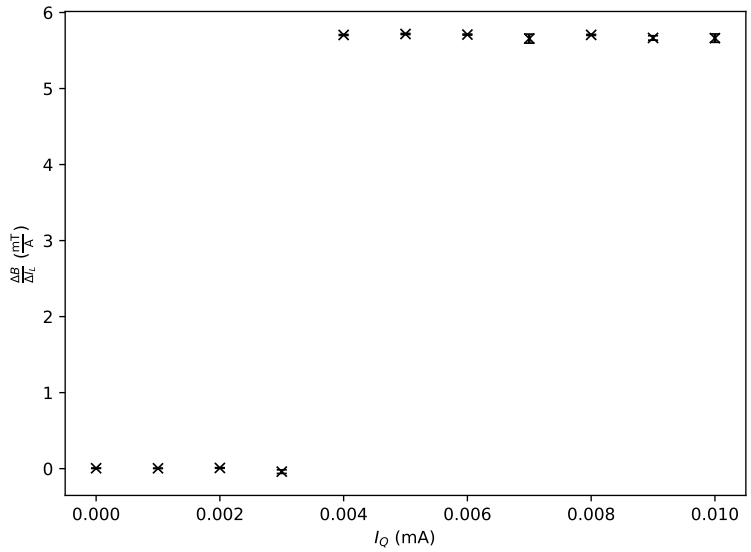

Figure 6.3: B_0 transfer function of the B_0 coil as a function of the B_0 quench current I_Q. For quench currents below $4\,\mathrm{mA}$ the B_0 coil is not quenched and no current can be loaded. Once the quench current is high enough to quench the coil, the transfer function no longer depends on the quench current.

created by the B_0 coil. Increasing the SSC quench current over the minimum amount required to quench the SSC causes the current in the SSC to decay and the shielding vanishes. By plotting the transfer functions of the coils over their respective quench currents, the minimum current required to quench the coil can be determined from the position of the change in the transfer function. Figure 6.3 shows the non-persistent transfer function of the B_0 coil as a function of the applied quench current. Once the quench current is increased to $4\,\mathrm{mA}$, the loading current is forced through the field creating path and the transfer function changes.
During further testing it became apparent that it was not possible to simultaneously quench three of the four coils without quenching the forth coil. Even though the quench heaters were thermally decoupled, the power dissipated by the currents running through the 3 quench heaters heats part of the fourth coil above its critical temperature and all coils become quenched. In general, decreasing the quench currents on the three quenched coils might be possible and settings that leave the fourth coil persistent might exist, however, under such conditions the system would be operated close to the boundary between persistent and quenched state and would therefore be susceptible to external conditions and loading history. In order to reliably load a current into a single coil, the loading scheme described in chapter 4.6 was implemented and the coils were loaded sequentially while the other coils were persistent. Due to the mutual

Coil	B_2 coil	B_1 coil	B_0 coil	SSC
Minimum quench current	5 mA	5 mA	4 mA	5 mA

Table 6.1: Minimum quench current required to quench the individual coils. Note that due to parasitic coupling, it is not possible to quench three coils while keeping the fourth coil persistent if these currents are used.

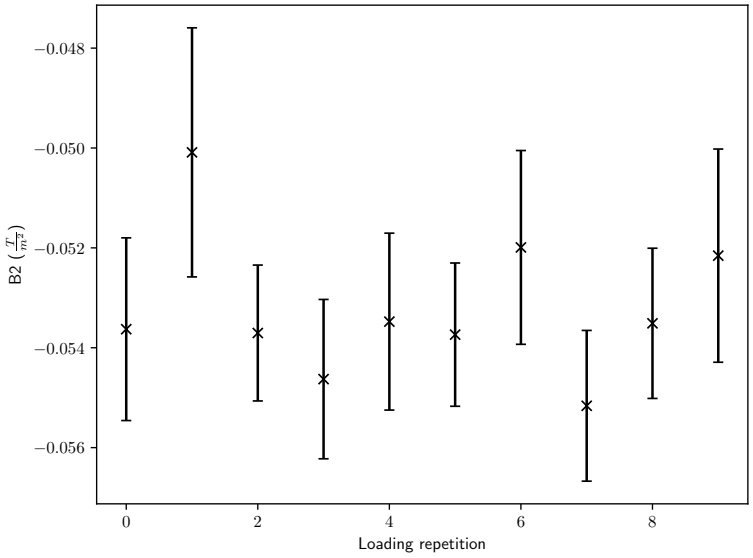

Figure 6.4: Measured B_2 coefficient after each of 10 independent loading attempts. The measured B_2 values after each loading are in good agreement within their errorbars.

inductance between the coils, changing the current in one coil leads to a change in the currents flowing in all coils and an additional quench sequence is necessary after loading in case these induced currents are undesirable. In order to ensure that the loading scheme is independent of the history of applied quench and loading currents, sufficient time has to be given for thermalization. A full sequence consisting of loading and quenching thus takes around 190 s.

6.3 Reproducibility of B_2 loading

In order to reliably tune the B_2 coefficient to zero, it is important to know how much the loaded current varies between individual loadings. To test the reproducibility, the coil is loaded with 100 mA multiple times and the B_2 coefficient is measured as described in chapter 5.8. Figure 6.4 shows the respective measured B_2 coefficient after each of 10 loading attempts.
No trend is visible in the data and calculating the mean and standard deviation yields

$$\bar{B_2} = -53.21(46)\,\frac{\mathrm{mT}}{\mathrm{m}^2} \pm 1.3\,\frac{\mathrm{mT}}{\mathrm{m}^2} \tag{6.4}$$

Given that the standard deviation includes the uncertainties of the loading current supply, the loading process and the B_2 measurement, a conservative estimate of the reproducibility of the loading procedure can be given by assigning the whole uncertainty to the loading process. Subtracting the background value $B_2 = 103.50(23)\,\frac{\mathrm{mT}}{\mathrm{m}^2}$ yields the relative uncertainty σ of the loaded B_2 value:

$$\sigma = \left| \frac{1.3\,\frac{\mathrm{mT}}{\mathrm{m}^2}}{\left(-53.21(46)\,\frac{\mathrm{mT}}{\mathrm{m}^2} - 103.50(23)\,\frac{\mathrm{mT}}{\mathrm{m}^2}\right)} \right| = 9.28(3) \times 10^{-3} \tag{6.5}$$

We therefore expect to be able to tune B_2 to less than $9.28(3) \times 10^{-3} \times 103.50\,\frac{\mathrm{mT}}{\mathrm{m}^2} = 0.96\,\frac{\mathrm{mT}}{\mathrm{m}^2}$ reliably. Compared to the 1.5 p.p.b. measurement of the , this reduces the B_2 coefficient by a factor of approximately 2900 and thus causes the contributions of B_2 to the error budget to become negligible.

6.4 Stability

Additional to being able to reliably tune B_2 to zero it is important to verify that loaded current does not decay with time. In order to constrain the decay time of the current, the B_2 coil is loaded once with $-100\,\mathrm{mA}$ and B_2 is continuously measured. Figure 6.5 shows the measured B_2 value as a function of time.
Over the course of more than $35\,\mathrm{h}$ no change in B_2 could be observed. Thus, we conclude that the current loaded into the B_2 coil does not decay on timescales that correspond to the typical filling cycle of the experiment.

6.5 Shielding factors

In order to measure the shielding factors of the coil system in different configurations, a Helmholtz coil was wound around the outer housing of the BASE superconducting magnet. Figure 6.6a and 6.6b show the position of the Helmholtz coil as well as its measured transfer function at the position of the particle if no shielding coils are active. Note that the bore of the solenoid is not located in the center and thus the symmetry axis of the Helmholtz coil does not coincide with the trap axis.

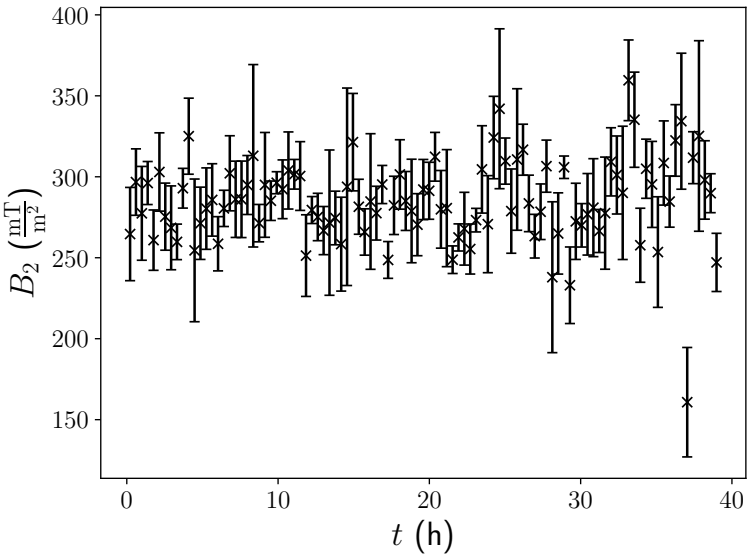

Figure 6.5: Measurement of the B_2 value as a function of time after loading the B_2 coil with $-100\,\mathrm{mA}$. Over the course of more than $35\,\mathrm{h}$ no significant decay of the loaded B_2 value can be observed.

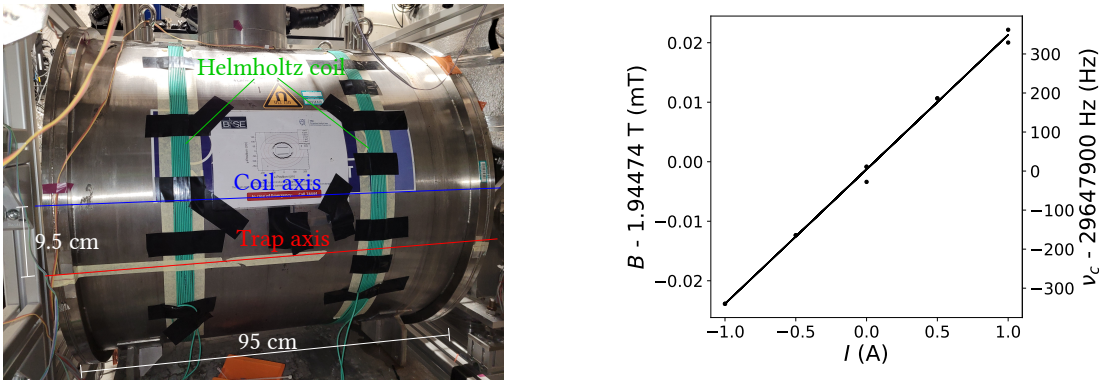

(a) (b)

Figure 6.6: (a) Location of the Helmholtz coil wound on the BASE solenoid. The coil axis and trap axis are parallel, but offset by approximately $9.5\,\mathrm{cm}$. (b) At the location of the particle the Helmholtz coil has a transfer function of $22.5(4)\,\frac{\mu\mathrm{T}}{\mathrm{A}}$.

If one or more superconducting coils are active, changes of the magnetic field created by the Helmholtz coil will be partially shielded and the transfer function will change. The shielding factor S is given by the ratio of the unshielded transfer function and the shielded transfer function. The transfer functions were estimated by measuring the modified cyclotron frequency

Active coils	$\frac{\Delta B}{\Delta I}$	S	S_{theo}
B_2, B_1 and B_0	$23.2\ \frac{\mu T}{A}$	1	1
B_2, B_1 and B_0	$0.61\ \frac{\mu T}{A}$	37.82	4365.29
B_2, B_1 and SSC	$0.61\ \frac{\mu T}{A}$	37.75	86.6822
B_2, B_1, B_0 and SSC	$0.43\ \frac{\mu T}{A}$	54.59	-348.902

Table 6.2: Transfer function of the Helmholtz coil for different shielding coil configurations and their associated shielding factors. If all coils are active, the shielding is most efficient, however, all shielding factors are well below the theoretically calculated ones.

of a trapped particle for different currents in the Helmholtz coil. Table 4.3 summarizes the transfer functions $\frac{\Delta B}{\Delta I}$ of the Helmholtz coil for different shielding coil configurations. The B_2 coil and the B_1 coil are not quenched to reduce the thermal load on the system.
Both the B_0 coil as well as the SSC reduce the shift of the magnetic field created by the Helmholtz coil by a factor of approximately 38. If both the B_0 coil and the SSC are active at the same time, the shielding factor increases to around 55. In all cases, the measured shielding factors are below the values predicted by theory, which is to be expected as the wires used to guide the persistent joints out of the region of strong magnetic field add parasitic resistance to the system and the symmetry axis of the shielding coil system is offset from the symmetry axis of the Helmholtz coil.

6.6 Mutual inductances

In order to make precise predictions of the loaded currents and associated transfer functions for a given loading scheme, knowledge of the mutual inductance matrix is required. In order to measure the mutual inductance between two coils, all other coils are quenched and one coil is loaded with initial current $I_1 = I_{Load}$. If the loaded coil is quenched, magnetic flux conservation causes a current $I_2 = I_{ind}$ to be induced in the second persistent coil. The magnitude of this current can be calculated using Eq. (4.8) and is given by:

$$I_2 = \left| \frac{M_{21}}{M_{22}} I_1 \right| . \tag{6.6}$$

By removing the quench current on the first coil and quenching the second coil, the current can be swapped back to the first coil. As the mutual inductance matrix is symmetrical, the current in the first coil after n swapping cycles is given by:

$$I_1(n) = \left(\frac{M_{21}^2}{M_{11} M_{22}} \right)^n I_{Load} = (k^2)^n I_{Load} \text{ with } k = \frac{M_{21}}{\sqrt{M_{11} M_{22}}}. \tag{6.7}$$

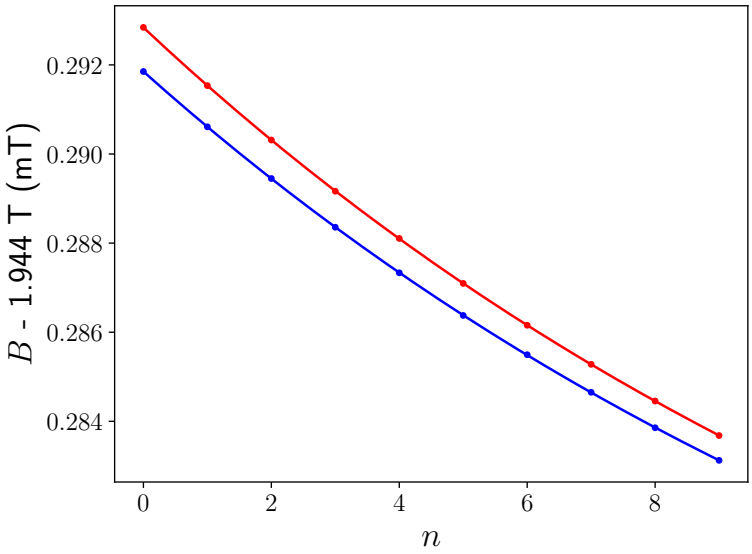

Figure 6.7: Measured magnetic field as a function of current swapping cycles for current in the B_0 coil (red) and the SSC (blue). Each time the current is swapped from one coil to the other, the current is reduced by a factor k. Thus, the shift in magnetic field created by a coil decreases with k^{2n}.

In order to demonstrate this technique, current was swapped between the B_0 coil and the SSC as both coils possess a large B_0 transfer function and thus the loaded current can be determined to sufficient accuracy by measuring the shift in modified cyclotron frequency. During these measurements, the B_2 coil was quenched while the B_1 coil was kept superconducting to limit the heat load on the system. Given the antisymmetric design of the B_1 coil, its mutual inductance with the B_0 coil and the SSC is expected to vanish. By approximating the free cyclotron frequency with the modified cyclotron frequency, the magnetic field at the position of the particle can be approximated as $B = \frac{2\pi m}{q}\nu_+$. Figure 6.7 shows the measured magnetic field as a function of the number of current swaps for current in the B_0 coil and the SSC.
By fitting

$$B(n) = B_0 + \Delta B(k^2)^n \tag{6.8}$$

to the data, the coupling constant k can be determined. Table 6.3 summarizes the best fit parameters for current in the B_0 coil and the SSC. For both fits, the background magnetic field B_0 as well as the coupling constant k are in good agreement within their error bars. The initial shift ΔB depends on the current in the coils and their respective transfer functions and is thus not expected to be the same for both data series.

	B_0	ΔB	k^2	k
B_0 coil	$1.944\,272\,32(7)\,\mathrm{T}$	$0.020\,51(6)\,\mathrm{mT}$	$0.9364(3)$	$0.9676(1)$
SSC	$1.944\,272\,20(10)\,\mathrm{T}$	$0.0196(1)\,\mathrm{mT}$	$0.9368(4)$	$0.9679(2)$

Table 6.3: Best fit parameters for fitting the shift of the magnetic field as a function of swapping cycles between the B_0 coil and the SSC.

Using the calculated mutual inductance matrix given by Eq. (4.25) in chapter 4.3, the coupling constants k between any two coils can be calculated and expressed as a matrix:

$$\mathrm{k} = \begin{pmatrix} 1 & 0 & 0.187 & 0.178 \\ 0 & 1 & 0 & 0 \\ 0.187 & 0 & 1 & 0.981 \\ 0.178 & 0 & 0.981 & 1 \end{pmatrix}. \tag{6.9}$$

The rows correspond to the B_2 coil, B_1 coil, B_0 coil and SSC respectively and thus the matrix element k_{34} describes to the calculated coupling factor between the B_0 coil and the SSC. The measured value reveals that the experimental coupling factor deviates significantly from the theoretical value. As the real coils are wound out of wire with finite thickness, parasitic coupling between the coils might be present and the coils might be rotated or shifted with respect to each other, the deviation of experimental and theoretical value is not surprising. The mutual inductance between different pairs of coils can be measured analogously, however, given that the B_2 coil and the B_1 coil possess a small B_0 transfer function, the current in these coils has to be determined by measuring the shift in B_2 or B_1 respectively.

6.7 Impact on measurements of the cyclotron frequency ratio

The main systematic limitation on past measurements of the antiproton g-factor was caused by a possible difference in axial temperature between the particle used to measure the free cyclotron frequency and the particle used to probe the Larmor frequency. In order to characterize the impact of the coil system on the measurement of the g-factor, the free cyclotron frequency of a particle with high axial temperature is compared to the free cyclotron frequency of a particle with low axial temperature in the same field. The measurement is done by thermalizing the particle on the axial resonator and subsequently measuring its modified cyclotron frequency via sideband coupling. By changing the temperature of the axial resonator via feedback cooling, particles of different temperature can be compared. Figure 6.8 shows the measured cyclotron frequency ratio R between a hot and a cold particle as a function of the B_2 coefficient. The B_2 coefficient causes the average magnetic field that the trapped particle experiences to change with

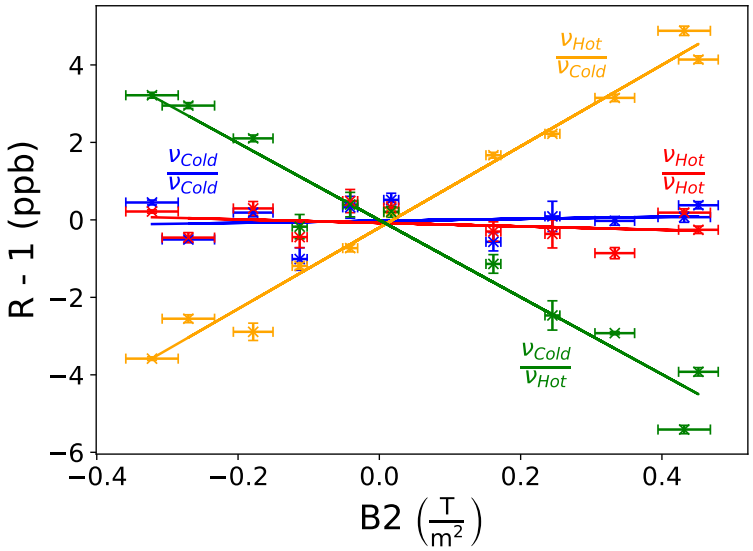

Figure 6.8: Ratio of the free cyclotron frequency of particles at different temperatures as a function of the B_2 coefficient in the precision trap. The B_2 coefficient caused by the residual magnetic bottle causes the ratio to shift if particles of different temperatures are compared. If B_2 is tuned close to 0, free cyclotron frequency shifts due to the axial energy are strongly suppressed and the measured free cyclotron frequency is identical for hot and cold particles.

its axial amplitude. Thus, the modified and free cyclotron frequencies depend on the particles axial temperature. The size of this systematic shift is mainly determined by the B_2 coefficient and is given by Eq. (2.44). Tuning B_2 close to zero causes this shift to vanish and reduces the systematic uncertainty associated with the uncertainty in axial temperature. Therefore, even in case the particles have different axial temperatures, the ratio is not shifted. The good agreement between the measured cyclotron frequencies of two protons at different axial temperatures, demonstrates the possibility to measure

7 Analysis trap measurements

The determination of a particle's g-factor relies in the measurement of the particle's free cyclotron frequency ν_c and its Larmor frequency ν_L in a common magnetic field B_0. The free cyclotron frequency is accessible by measuring the eigenfrequencies of the particle in a Penning trap [82], however, no eigenmotion associated to the Larmor frequency exists. The continuois Stern-Gerlach effect couples the trapped particles spin state to its axial frequency by introducing a strong quadratic inhomogeneity B_2. The shift $\Delta\nu_{z,SF}$ in axial frequency caused by a change in the particles spin state is given by

$$\Delta\nu_{z,SF} = \frac{g}{2}\frac{h\nu_+}{4\pi^2 m_p \nu_z}\frac{B_2}{B_0} \tag{7.1}$$

and depends on the strength ob the magnetic bottle B_2. Under the conditions in the BASE analysis trap ($B_2 \approx 272(22)\,\frac{\mathrm{kT}}{\mathrm{m}^2}$, $B_0 = 1.214\,62(8)\,\mathrm{T}$, $\nu_z \approx 650\,\mathrm{kHz}$) $\Delta\nu_{z,SF}$ is on the order of $172\,\mathrm{mHz}$. At the same time, the strong magnetic bottle leads to significant shifts of the particle's eigenfrequencies as the magnetic field the particle probes during its trajectory strongly depends on the energies E_+, E_z and E_- of the individual modes. The shifts in the observable eigenfrequencies are outlined in chapter 2.3. Given that axial frequency fluctuations on the order of $172\,\mathrm{mHz}$ have to be resolved in order to determine the spin state of the trapped particle, the dependence of the axial frequency on the radial modes is of highest importance.
Under typical conditions, the shift $\Delta\nu_{z,E_+}$ of the axial frequency ν_z caused by the particle's radial energies $E_\pm$ is given by Eq. (2.45):

$$\Delta\nu_{z,E_\pm} = \frac{1}{4\pi^2 m_p \nu_z}\frac{B_2}{B_0}|E_\pm| \approx 800\,\frac{\mathrm{kHz}}{\mathrm{eV}}|E_\pm| = 70\,\frac{\mathrm{Hz}}{\mathrm{K}}T_\pm. \tag{7.2}$$

In order to resolve axial frequency jumps of $\Delta\nu_{z,SF} = 172\,\mathrm{mHz}$, the radial energies have to be constant on a level of approximately $200\,\mathrm{neV}$ which requires excellent shielding of the particle against electronic background noise which could couple to the radial motions. In the following chapter the necessary characterization steps required to achieve the high axial frequency stability required to achieve single spin flip resolution are outlined. After characterization of the trap in the initial cooldown, it was discovered that the radial excitation coils required to drive spin state transitions at high power were broken. After the excitation coils were repaired

during an experiment maintenance cycle, single spin flips were observed at high fidelity paving the way for a (anti)proton g-factor measurement at the 100 p.p.t. level.

7.1 Axial frequency determination

7.1.1 Systematic shifts

The strong magnetic bottle present in the analysis trap causes significant shifts of the axial frequency ν_z with the particle's magnetron and cyclotron energies E_- and E_+. In order to understand the scale of the shifts and the associated difficulty in the determination of the correct trapping parameters it is instructive to calculate the typical range of frequency shifts one has to expect. In case the particle is thermalized by the cyclotron detector of the precision trap which typically has a temperature on the order of 9 K, its cyclotron energy E_+ is sampled from a Boltzmann distribution

$$p(E_+) = \frac{1}{E_{+,typical}} e^{\left(-\frac{E_+}{E_{+,typical}}\right)}. \tag{7.3}$$

with a characteristic width of $E_{+,typical} = k_B T_+ \approx k_B 6\,\mathrm{K}$. During transport from the high magnetic field $B_{0,PT}$ in the precision trap to the comparably lower magnetic field $B_{0,AT}$ of the analysis trap, the effective cyclotron energy of the particle is reduced by a factor of $\frac{B_{0,PT}}{B_{0,AT}} = 1.6$. Therefore, the particle's axial frequency in the analysis trap follows a Boltzmann distribution with a characteristic width of

$$\Delta\nu_{z,E_+,typical} \approx 70\,\frac{\mathrm{Hz}}{\mathrm{K}} \times 6\,\mathrm{K} \times \quad \approx 420\,\mathrm{Hz}. \tag{7.4}$$

In addition to the shift caused by the cyclotron energy, the magnetic moment associated with the magnetron energy E_- is coupled to the axial frequency as well. Given that the magnetron energy can be cooled to temperatures $T_- = \frac{\nu_-}{\nu_z} T_z < 50\,\mathrm{mK}$ by coupling the magnetron motion to the axial detection system at temperature $T_z \approx 5.4\,\mathrm{K}$ in the analysis trap, the typical width due to the Boltzmann distribution of the magnetron energy E_- is given by:

$$\Delta\nu_{z,E_-,typical} \approx 70\,\frac{\mathrm{Hz}}{\mathrm{K}} \times \frac{\nu_-}{\nu_z} 5.4\,\mathrm{K} \approx 7\,\mathrm{Hz}. \tag{7.5}$$

However, transport of the particle between the precision trap and the analysis trap temporarily exposes the particle to conditions where the electrostatic potential is flat ($C_2 \approx 0$). Under these conditions, the magnetron frequency is undefined which can lead to a significant heating and an increase in magnetron radius. This transport heating can cause axial frequency shifts

of multiple hundred Hz which requires extensive cooling in the analysis trap (see Ch. 7.6). Under experimental condition particles are typically found in a frequency range of up to several kHz which, together with the uncertainty of the ideal tuning ratio caused by uncertainties in the manufacturing tolerances, current leaks, calibration offsets and patch potentials, leads to a parameter space that is too large to scan using dip detection techniques in case the trap parameters are initially unknown.

7.1.2 Parametric resonance

The systematic shifts described in section 7.1.1 cause the axial frequency in the analysis trap to depend on the energies E_+ and E_- of the radial motions. Therefore, as long as the particle's cyclotron and magnetron energies are unknown, no straight forward relation between the axial frequency ν_z and the ring voltage V_0 exist. Additionally, the smaller geometry and ring voltage compared to the precision trap causes manufacturing tolerances as well as offset voltages, patch potentials and current leaks to create a larger relative uncertainty on the ideal trapping parameters. Given that the frequency window in which a particle produces a clear dip signal is given by the width of the resonator and typically on the order of $30\,\mathrm{Hz}$ scanning the typical width of possible axial frequencies due to the thermal distribution of the cyclotron mode requires approximately $\frac{1.5\,\mathrm{kHz}}{30\,\mathrm{Hz}} = 300$ spectra. Furthermore, as the magnetic field in the analysis trap has a significant B_4 component, the ideal tuning ratio depends on the radial energies as well. Given the smaller diameter, the axial frequency shows a strong scaling $\left(\frac{\Delta\nu_z}{\Delta\mathrm{TR}}\right)_{PT} = 220\,\frac{\mathrm{mHz}}{\mathrm{mU\,K}} \times T_\pm$ compared to $\left(\frac{\Delta\nu_z}{\Delta\mathrm{TR}}\right)_{PT} = 32\,\frac{\mathrm{mHz}}{\mathrm{mU\,K}} \times T_\pm$ in the precision trap. Thus the tuning ratio typically needs to be optimized up to $500\,\mu\mathrm{U}$ to produce a clear dip. For typical ring voltages on the order of $-0.76\,\mathrm{V}$ and tuning ratios of 0.81 the voltage applied to the correction electrodes is on the order of $-0.62\,\mathrm{V}$. Given that offset voltages of up to $\pm 100\,\mathrm{mV}$ have been observed in the past, optimization of the tuning ratio on a level of $500\,\mu\mathrm{U}$ requires $\frac{200\,\mathrm{mV}}{0.62\,\mathrm{V}}\frac{0.81}{500\mu\mathrm{U}} \approx 500$ spectra at each ring voltage. Scanning the whole parameter space using dip scans thus corresponds to the acquisition of typically $15\,000$ spectra and is not feasible given that the spectrum acquisition time in case of a not optimized dip signal is on the order of tens of seconds. Instead, parametric resonance [140] can be utilized to determine the combination of V_0 and TR that centers the particle on the resonator at maximum SNR. In this measurement scheme, an axial drive at frequency $\nu_D = 2\nu_R$ equal to twice the resonator frequency ν_R is applied, a TR is chosen and V_0 is swept over the region of interest. In case the particle oscillates at an axial frequency $\nu_z \approx \nu_R$, the drive can excite the particle's axial motion parametrically and the particle's axial amplitude increases. The excited particle induces strong image currents in the trap electrodes and becomes visible as a peak signal on the axial detector. This signal is orders of magnitude

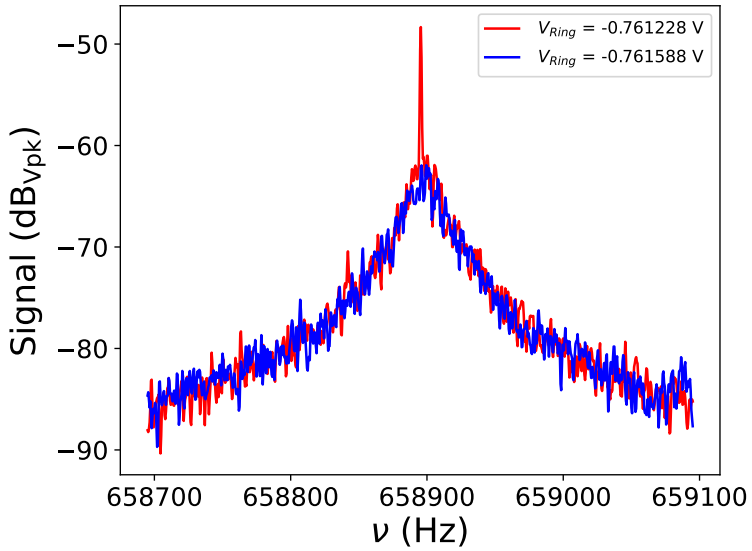

Figure 7.1: Frequency spectrum in case the particle's axial frequency is equal to half of the drive frequency which causes it's axial motion to be excited parametrically (red). In case the particle's axial frequency is not resonant with the parametric drive, the particle is not excited and no peak is visible on the resonator.

above the resonator background and thus can be easily detected even if axial spectra are acquired at a span of 400 Hz, averaged and read out at a rate faster than the 2 s acquisition time corresponding to a full spectrum. Figure 7.1 shows the signal in case the particle is excited parametrically and in case that the particle's axial frequency does not match the condition for parametric resonance.

The range over which the particle is excited depends on the strength of the applied drive. For high drive strengths, the particle can be excited over a wide range of V_0 and TR combinations and little information is gained. By carefully optimizing the drive's power, the window in which the particle is parametrically excited can be narrowed down to values of V_0 and TR close to the ones corresponding to a compensated trap with axial frequency $\nu_z = \nu_R$. Depending on the direction in which the applied TR deviates from the ideal tuning ratio, the sign of C_4 will change. Once excited, the presence of a C_4 term causes the particle to stay excited for a range of different V_0 values. The range over which the particle stays in resonance with the applied drive depends on the drive strength, the sign of C_4 as well as the direction in which V_0 is varied. In case the drive strength has been carefully optimized, the correct tuning ratio can thus be determined by minimizing the range over which parametric resonance can be observed. Figure 7.2 shows the maximum signal as a function of the ring voltage V_0 for different tuning ratios

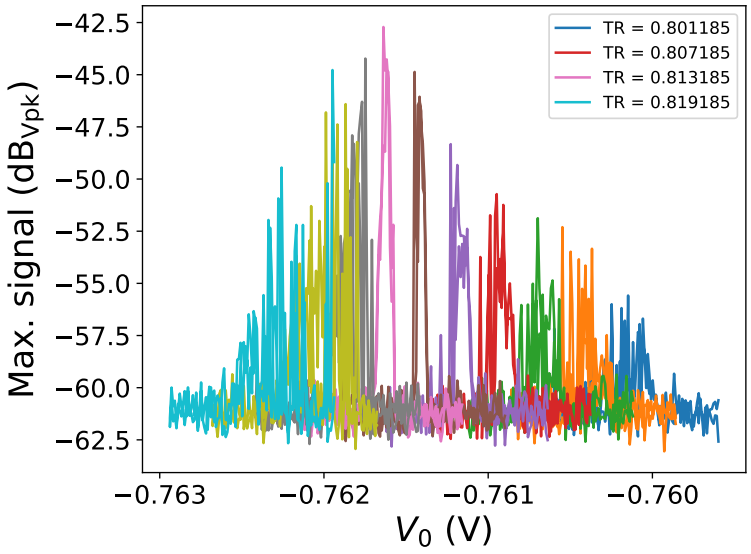

Figure 7.2: Maximum signal as a function of the applied ring voltage for different tuning ratios. For a tuning ratio of $0.809\,185$ (brown) the response to the parametric drive is symmetric and limited to a narrow range of ring voltages indicating that the applied tuning ratio is close to the ideal tuning ratio.

varied from $0.801\,185$ to $0.819\,185$ in steps of 2 mU. The ring voltage is swept in both directions. For a tuning ratio of $0.809\,185$ the response to the parametric drive is symmetric and limited to a narrow range of ring voltages, indicating that the applied tuning ratio is close to the ideal tuning ratio.

By carefully characterizing the response as a function of the applied drive strength a parametric detection scheme can be implemented that allows the quick determination of the required TR and ring voltage after the particle was rethermalized on the PT cyclotron resonator.

7.2 Asymmetry compensation

Similar to the precision trap, an offset compensation measurement is conducted in order to compensate for contact voltages, manufacturing tolerances, calibration offsets, current leaks and patch potentials located on the electrodes. Note that since the analysis trap has a different geometry the shift Δz of the particle position along the trap axis with the offset ratio OR is given by

$$\Delta z_{min} = 1.20\,\mathrm{mm} \times \mathrm{OR} \tag{7.6}$$

which at a typical ring voltage of $-0.762\,58\,\mathrm{V}$ corresponds to a shift of

$$\Delta z_{min} = -1.57\,\frac{\mathrm{mm}}{\mathrm{V}} \times V_{Off}. \tag{7.7}$$

Figures 7.3a and 7.3b show C_2 and the ideal TR as a function of the offset ratio.

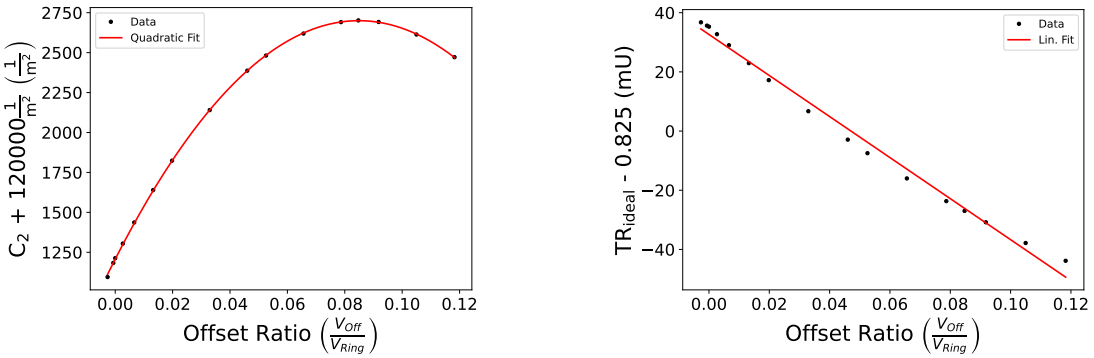

(a) (b)

Figure 7.3: (a) C_2 value as a function of the offset ratio. An offset ratio of $0.0849(6)$ maximizes C_2 and corresponds to a symmetric trap. At a typical ring voltage of $-0.762\,58\,\mathrm{V}$ this corresponds to an offset voltage of $63.9(4)\,\mathrm{mV}$ on the downstream correction electrode. (b) Ideal tuning ratio as a function of the offset ratio. Compared to the measurements in the precision trap the linear approximation of the ideal tuning ratio is worse as higher order terms in the expansion of the potential created by the correction electrode start to play a role.

Initially, the trap is tuned to symmetric conditions and the particle is located in the center of the ring electrode. However, in the final experiment the particle will be shifted to the center of the magnetic bottle in order to suppress systematic shifts.

7.3 Determination of the modified cyclotron frequency

The strong magnetic bottle present in the analysis trap causes a trapped particle's axial ν_z to depend on its cyclotron energy E_+. Therefore, the particle's modified cyclotron frequency ν_+ can not be determined via sideband coupling to the axial detector in the analysis trap as the particle would move through a Boltzmann distribution with a temperature of $T_+ = \frac{\nu_+}{\nu_z} T_z \approx 150\,\mathrm{K}$ which corresponds to a typical frequency width of more then $10\,\mathrm{kHz}$. If the sideband drive was applied, the particle's axial frequency would immediately jump which causes the sideband frequency to change and thus the applied sideband drive would become off-resonant. Instead, the modified cyclotron frequency is driven directly which causes the cyclotron quantum number

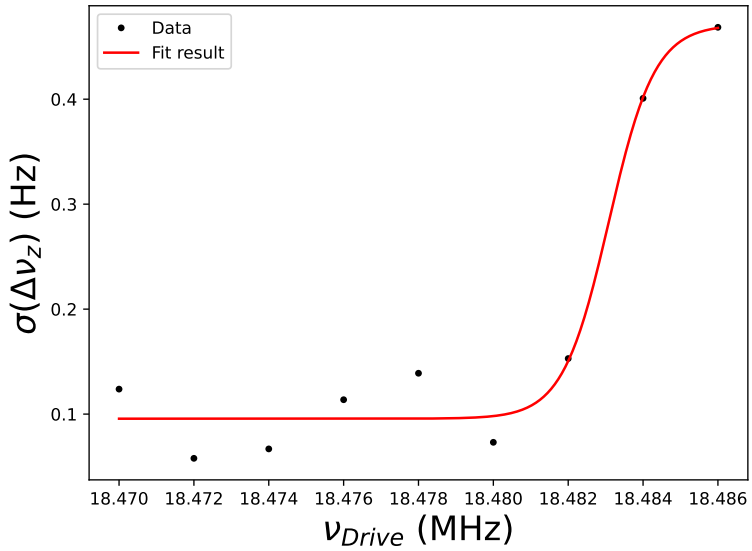

Figure 7.4: Standard deviation of the axial frequency scatter as a function of the drive frequency. The drive is swept over the cyclotron resonance in the analysis trap. The strong magnetic bottle causes the axial frequency ν_z to depend on the cyclotron energy and thus the axial frequency scatter increases in case the sweep window is above the cyclotron frequency cut ν_+ corresponding to a particle with negligible axial energy.

n_+ to change in case the drive frequency is above ν_+. This change in n_+ causes the axial frequency to change. By sweeping the drive frequency over the particle's cyclotron resonance, ν_+ can be determined by resolving an increase in the scatter of the particle's axial frequency. The observed axial frequency scatter is given by

$$\sigma(\Delta\nu_z) = \sqrt{\sigma(\Delta\nu_{z,Background})^2 + \sigma(\Delta\nu_{z,Drive})^2}. \tag{7.8}$$

The scatter introduced by the drive depends on the drive amplitude as well as the lineshape of the cyclotron resonance [127].

Figure 7.4 shows the axial frequency scatter as a function of the drive sweep window center in case the modified cyclotron mode is swept within 10 s over a span of 2000 Hz.

For drive frequencies below the cyclotron frequency cut, the observed axial frequency scatter corresponds to the background scatter $\sigma(\Delta\nu_{z,Background})$ and depends on the particle's cyclotron temperature. Once the sweep window includes frequencies above the cyclotron frequency cut ν_+, the drive can change the trapped particle's cyclotron quantum number n_+, which causes a change in the axial frequency and increases the axial scatter. The uncertainty with which the modified cyclotron frequency can be determined depends on the width of the drive's sweep

window. If only a rough determination is required, a wide sweep span of more than $1\,\mathrm{kHz}$ width can be used whereas usage of a narrow sweep window allows precise resolution of the frequency cut including dynamics caused by the particle's magnetron random walk [88].

7.4 Magnetic field measurement

The magnetic bottle present in the analysis trap is strong enough to be measured directly by measuring the particle's free cyclotron frequency for different positions along the trap axis. Using the parameters obtained during asymmetry compensation, the particle is shifted along the trap axis and the cyclotron frequency is determined as described in section 7.3. Given the strength of the magnetic bottle, ν_+ was measured using a sweep window with a width of $2\,\mathrm{kHz}$, the magnetron frequency was estimated as $\nu_- = \frac{\nu_z^2}{2\nu_+}$ and ν_c was calculated according to the invariance theorem $\nu_c = \sqrt{\nu_+^2 + \nu_z^2 + \nu_-^2}$. The uncertainty of ν_c is determined by the resolution at which ν_+ is measured. Finally, $B(z)$ is calculated using $B(z) = \frac{2\pi m_p}{q}\nu_c(z)$. Figure 7.5 shows the magnetic field as a function of the particle position along the trap axis. Measurements in which the cyclotron frequency could not be clearly resolved or which showed significant deviations from the expected cyclotron frequency were rejected. The presence of these outliers is a topic of future studies, however, the behavior could not be reproduced in subsequent measurements.

By fitting a parabola to the data, the strength and center of the magnetic bottle can be determined as well as the background magnetic field B_0. Given the measured date, the center of the magnetic bottle seems to be shifted by $24(8)\,\mu\mathrm{m}$ towards the upstream direction from the center determined by the asymmetry compensation. By applying an offset voltage of $-48.9\,\mathrm{mV}$ to the downstream correction electrode, the particle is shifted into the center of the magnetic bottle. The fit yields a background magnetic field in the center of the magnetic bottle of

$$B_{0,AT} = 1.214\,62(8)\,\mathrm{T}. \tag{7.9}$$

The strength of the magnetic bottle is given by

$$B_{2,AT} = 272(22)\,\frac{\mathrm{kT}}{\mathrm{m}^2}, \tag{7.10}$$

which is in good agreement with previous values. A more precise value of B_2 can be obtained by determining the axial frequency jump in case of a spin flip (see chapter 7.9.2).

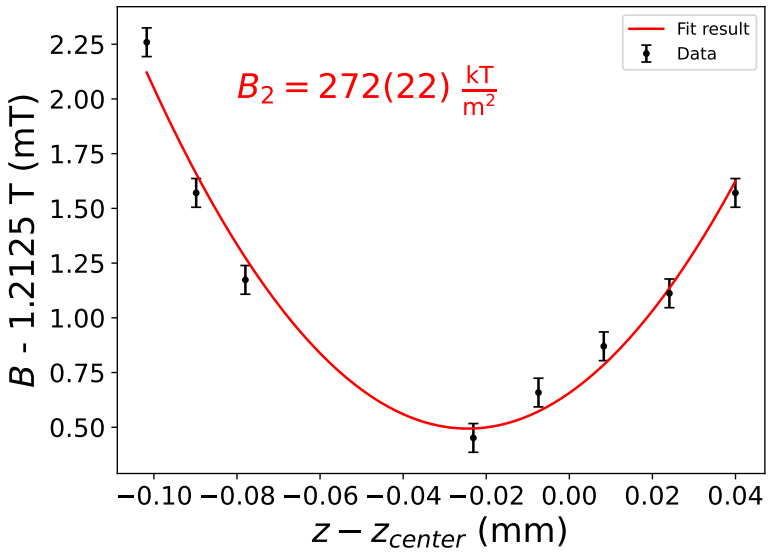

Figure 7.5: Magnetic field as a function of the axial position of the particle. The center of the magnetic bottle is shifted by $24(8)\,\mu\mathrm{m}$ towards the upstream direction from the center determined by the asymmetry compensation. In the center of the magnetic bottle, the background field is $B_{0,AT} = 1.214\,62(8)\,\mathrm{T}$ and the magnetic bottle has a strength of $B_{2,AT} = 272(22)\,\frac{\mathrm{kT}}{\mathrm{m}^2}$.

7.5 B_4 measurement and tuning ratio optimization

The ferromagnetic ring electrode that is used to create the strong magnetic bottle in the analysis trap distorts the magnetic field. Given the symmetry of the ring electrode odd terms in the expansion of the magnetic field around the minimum of the magnetic bottle are suppressed. However, a significant B_4 term is present which causes the ideal tuning ratio $\tilde{\mathrm{TR}}$ to be a function of the radial energies E_+ and E_-. Given that the magnetron mode can be sideband-cooled to low temperatures in the precision trap, $\tilde{\mathrm{TR}}$ mainly depends on the cyclotron energy E_+. As described in Eq. (5.47) B_4 is approximately given by

$$B_4 \approx -B_0 q V_R D_4 \frac{\partial \tilde{\mathrm{TR}}}{\partial E_+} = -B_0 q V_R D_4 \frac{\partial \tilde{\mathrm{TR}}}{\partial \nu_z} \frac{\partial \nu_z}{\partial E_+}. \tag{7.11}$$

Due to the strong magnetic inhomogeneity in the analysis trap, the axial frequency and ideal tuning ratio change with the cyclotron energy E_+ of the particle. Therefore, the combination of the ring voltage V_R and tuning ratio $\tilde{\mathrm{TR}}$ which center the particle on the resonator with high SNR have to be determined after each rethermalization. Once V_R and $\tilde{\mathrm{TR}}$ are known, the particle temperature can be determined. In case the cyclotron temperature is above the cutoff temperature set for the efficient detection of single spin flips, the particle needs to be rethermalized on the cyclotron detector in the PT. This process, called cold particle search (CPS) is repeated until a cold particle is found. Expressing Eq. (7.11) in experimentally relevant quantities yields:

$$B_4 \approx -B_0 q V_R D_4 \frac{\partial \tilde{\mathrm{TR}}}{\partial E_+} = -B_0 q V_R D_4 \frac{\partial \tilde{\mathrm{TR}}}{\partial \nu_z} \frac{\partial \nu_z}{\partial E_+} = -B_0 q V_R D_4 \frac{\partial \tilde{\mathrm{TR}}}{\partial V_R} \frac{\partial V_R}{\partial \nu_z} \frac{\partial \nu_z}{\partial E_+}. \tag{7.12}$$

The dependency of the axial frequency on the ring voltage $\frac{\partial \nu_z}{\partial V_R} = -413(3)\ \frac{\mathrm{Hz}}{\mathrm{mV}}$ in the analysis trap is easy to measure and thus

$$\frac{\partial V_R}{\partial \nu_z} = \frac{1}{\frac{\partial \nu_z}{\partial V_R}} = -2.42(2)\ \frac{\mu\mathrm{V}}{\mathrm{Hz}} \tag{7.13}$$

is well known. Additionally, the values of B_0 and B_2 in the analysis trap are known and thus $\frac{\partial \nu_z}{\partial E_+}$ is given by Eq. (7.14):

$$\frac{\partial \nu_z}{\partial E_+} = \frac{1}{4\pi^2 m_p \nu_{z,0}} \frac{B_2}{B_0}. \tag{7.14}$$

In order to determine the value of $\frac{\partial \tilde{\mathrm{TR}}}{\partial V_R}$, particles at different cyclotron temperatures have to be loaded in the analysis trap and the tuning ratio $\tilde{\mathrm{TR}}$ has to be optimized. Figure 7.6 shows

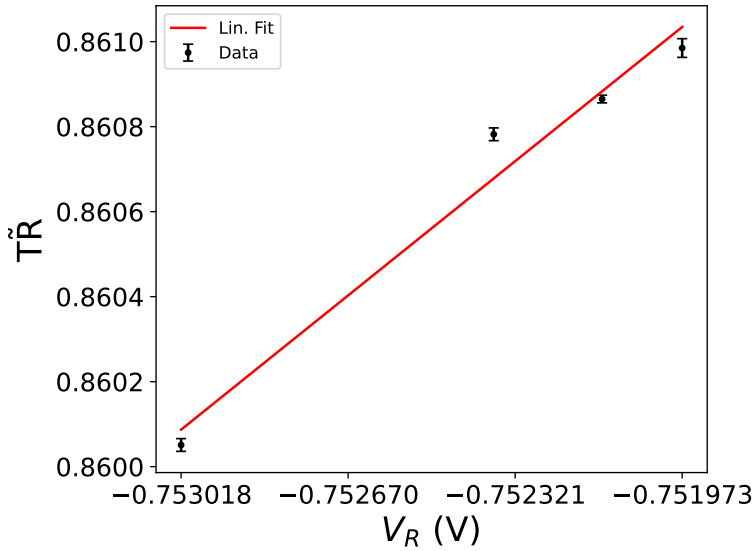

Figure 7.6: Optimal tuning ratio $\tilde{\mathrm{TR}}$ as a function of the ring voltage V_R that centers the particle on the resonator. As the ring voltage V_R and tuning ratio $\tilde{\mathrm{TR}}$ which center the particle on the resonator with high SNR both scale approximately linearly with the particle's cyclotron energy E_+, a linear relationship is expected between V_R and $\tilde{\mathrm{TR}}$. A fit to the data yields a slope of $\frac{\partial \tilde{\mathrm{TR}}}{\partial V_R} = 0.91(11)\,\frac{1}{\mathrm{V}}$.

the optimized tuning ratio $\tilde{\mathrm{TR}}$ as a function of the ring voltage V_R that centers the particle on the axial resonator for the four particles that were used in the initial characterization of the analysis trap.

Under the assumption that both the shifts of the particle's axial frequency ν_z as well as the ideal tuning ratio $\tilde{\mathrm{TR}}$ are dominated by their first order contributions B_2 and B_4 respectively, both shifts scale linearly with E_+. The value of $\frac{\partial \tilde{\mathrm{TR}}}{\partial V_R}$ can thus be determined by a linear fit to the data which yields

$$\frac{\partial \tilde{\mathrm{TR}}}{\partial V_R} = 0.91(11)\,\frac{1}{\mathrm{V}}. \tag{7.15}$$

Inserting the value of $D_4 = -4.81 \times 10^{10}\,\frac{1}{\mathrm{m}^4}$ obtained from potential theory calculations (see chapter 2.2) together with the results of Eqs. (7.13), (7.14) and (7.15) into Eq. (7.12) yields

$$B_4 \approx -\frac{qV_R D_4 B_2}{4\pi^2 m_p \nu_z}\frac{\partial \tilde{\mathrm{TR}}}{\partial V_R}\frac{\partial V_R}{\partial \nu_z} = 81(12)\,\frac{\mathrm{GT}}{\mathrm{m}^4}. \tag{7.16}$$

Note that the uncertainty of this value is currently dominated by the uncertainty in the determination of B_2 and $\frac{\partial \tilde{\mathrm{TR}}}{\partial V_R}$ given that the tuning ratio was only optimized for four cold protons.

Additionally, the measurements were done in the geometric center of the trap which means that the strength of B_2 is slightly different than in the center of the magnetic bottle.
For experimental operation B_4 is of secondary importance compared to the relationship $\frac{\partial \tilde{\mathrm{TR}}}{\partial V_R} = 0.91(11)\,\frac{1}{\mathrm{V}}$ between optimized tuning ratio $\tilde{\mathrm{TR}}$ and centering ring voltage V_R as this line in TR-V_R-space determines how the tuning ratio and the ring voltage have to be varied to find cold particles in the analysis trap. Given the currently known pairs of $\tilde{\mathrm{TR}}$ and V_R, the line along which cold particles can be detected at maximum SNR in the analysis trap is given by:

$$\tilde{TR}(V_R) = 1.54(8) + 0.91(11)\,\frac{1}{\mathrm{V}} \times V_R. \tag{7.17}$$

7.6 Magnetron cooling and determination of the axial temperature

Apart from changes in the cyclotron energy E_+ and the spin state, the magnetron mode changes the axial frequency as well. As described in 7.1.1, the magnetron mode can be sideband-cooled in the precision trap to temperatures below $50\,\mathrm{mK}$ and thus the related axial frequency shifts in the analysis trap are small compared to the shift induced by the cyclotron temperature, however, the magnetron mode can be heated during transport and by background noise. Due to the shift of the axial frequency with the magnetron energy, the sideband cooling scheme used in the precision trap is not applicable in the analysis trap as any significant change in the particle's magnetron energy E_- leads to a shift of the axial frequency ν_z which causes the axial-magnetron sideband to be shifted away cooling drive. Instead the particle is cooled by modulating the sideband drive over the upper magnetron-axial sideband frequency $\nu_{SB} = \nu_z + \nu_-$. Typically the sideband frequency is modulated by $\pm 100\,\mathrm{Hz}$ around the suspected sideband frequency with a modulation period of $2\,\mathrm{s}$ and applied for $10\,\mathrm{s}$. During the modulation, the drive becomes momentarily resonant with the sideband frequency, which causes the magnetron mode to exchange energy with the axial resonator and the axial frequency jumps. After the modulation is finished, the new axial frequency is determined by comparing the axial spectrum of the resonator-particle system with a reference spectrum of the resonator in which the particle is detuned. The particle frequency can be determined by looking for the maximum absolute difference between the axial spectrum and the reference spectrum to account for the cases in which the particle is centered on the resonator and creates a dip as well as the cases in which the particle's axial frequency does not match the resonator frequency and the particle creates a dispersive peak feature in the frequency spectrum. Figure (7.7) shows the reference spectrum as well as the particle spectra at different points in the cooling process.

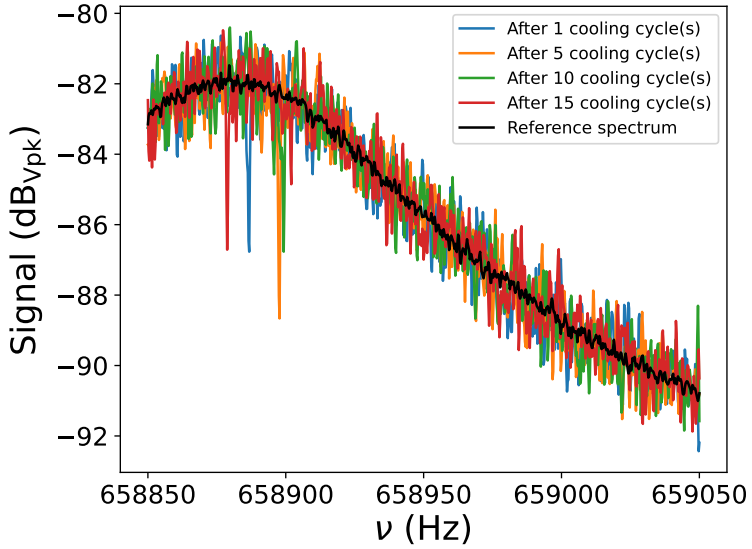

Figure 7.7: Axial spectra during the magnetron cooling process in the analysis trap. After each sweep of the cooling drive over the upper axial-magnetron sideband the magnetron exchanges energy with the axial detector and the particle's axial frequency jumps. The cooling drive frequency is readjusted by comparing the particle spectrum with a reference spectrum.

In order to determine when the magnetron mode of the particle is cold, the axial frequency is monitored during the cooling scheme. The drive thermalizes the particle on the axial detector and thus the magnetron energy follows a Boltzmann distribution with temperature $T_- = \frac{\nu_-}{\nu_z} T_z$. In case the magnetron mode is cold, $|E_-|$ is minimal and thus ν_z is minimized as well. During one cooling cycle the minimum frequency $\nu_{z,cut}$ corresponding to a cold particle is determined by acquiring typically 15 axial spectra. Fitting the cumulative distribution function of the thermal Boltzmann distribution

$$F_{\nu_z} = \Theta(\nu_z - \nu_{z,cut}) \times (1 - e^{\left(-\frac{|E_-|}{k_B T_-}\right)}) = \Theta(\nu_z - \nu_{z,cut}) \times (1 - e^{\left(-\frac{\nu_z - \nu_{z,cut}}{\Delta\nu_z}\right)}) \tag{7.18}$$

yields the characteristic width

$$\Delta\nu_z = \frac{1}{4\pi^2 m_p \nu_z} \frac{B_2}{B_0} k_B T_- \tag{7.19}$$

which can be solved for the magnetron temperature

$$T_- = \frac{4\pi^2 m_p \nu_z B_0}{k_B B_2 \Delta\nu_z}. \tag{7.20}$$

Figure 7.8 shows the cumulative distribution function of 200 axial frequencies acquired during a magnetron cooling sequence in the analysis trap with strong negative feedback on the axial resonator. The blue line indicates the best fit of Eq. (7.18) to the data and yields $\nu_{z,cut} = 658\,878.98(2)\,\mathrm{Hz}$ and $\Delta\nu_z = 6.83(4)\,\mathrm{Hz}$.
Inserting $\Delta\nu_z$ together with the known values of B_0 and B_2 into Eq. (7.20) results in a magnetron temperature of

$$T_{-,AT} = 95.8(76)\,\mathrm{mK} \tag{7.21}$$

which corresponds to a temperature

$$T_{z,AT} = \frac{\nu_z}{\nu_-} T_- = 5.38(43)\,\mathrm{K} \tag{7.22}$$

of the feedback-cooled axial detection system.

7.7 Determination of the cyclotron detector temperature

Determination of the PT cyclotron detector uses the same principle as described in the previous chapter. Instead of thermalizing the cyclotron mode using a sideband drive, the particles

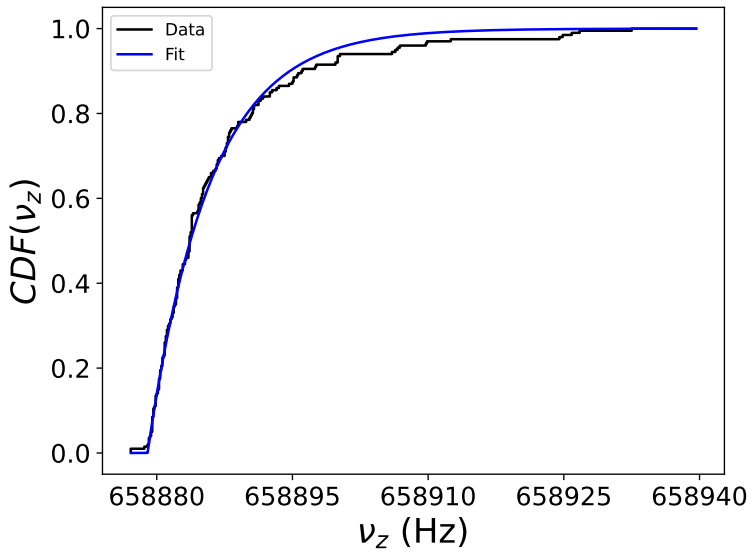

Figure 7.8: Cumulative distribution function of 200 axial frequency samples acquired during a magnetron cooling sequence in the analysis trap with strong axial feedback. Fitting Eq. (7.18) to the data yields $\nu_{z,cut} = 658\,878.98(2)$ Hz and $\Delta\nu_z = 6.83(4)$ Hz. The scale $\Delta\nu_z$ of the distribution depends on the temperature of the axial detection system and thus $T_z = 5.38(43)$ K can be determined from the fit.

modified. cyclotron mode is thermalized directly by shuttling the particle to the precision trap and tuning the cyclotron detectors frequency to the particles modified cyclotron frequency ν_+. After the particle has been in contact for multiple cooling time constants $\tau_{+,PT} \approx 90\,\mathrm{s}$, it is shuttled to the analysis trap where the strong magnetic bottle couples the cyclotron energy E_+ to the axial frequency. Once again, the observed axial frequency ν_z is given by

$$\nu_z = \nu_{z,cut} + \frac{1}{4\pi^2 m_p \nu_z}\frac{B_2}{B_0}E_+ \tag{7.23}$$

where $\nu_{z,cut}$ corresponds to a particle with negligible cyclotron energy E_+. Inserting the Boltzmann distribution of E_+ into Eq. (7.23) yields the probability density $p(\nu_z)$ to observe an axial frequency ν_z

$$p(\nu_z) = \Theta(\nu_z - \nu_{z,cut}) \times \frac{1}{\Delta\nu_z} e^{\left(-\frac{\nu_z - \nu_{z,cut}}{\Delta\nu_z}\right)} \tag{7.24}$$

with the characteristic width

$$\Delta\nu_z = \frac{1}{4\pi^2 m_p \nu_z}\frac{B_2}{B_0}k_B T_+. \tag{7.25}$$

The scaling of the characteristic width $\Delta\nu_z$ is the same for the magnetron and the modified cyclotron temperature, however, given that the temperature T_- of the modified cyclotron mode after sideband coupling is suppressed by a factor of $\frac{\nu_-}{\nu_z} \approx \frac{1}{50}$ assuming that the axial and cyclotron detector have similar temperatures, the axial frequency shifts after cooling on the PT cyclotron detector are expected to be larger by approximately a factor of 50 compared to what is observed during magnetron cooling in the analysis trap. In order to find the particle, the ring voltage V_R and tuning ratio TR are varied along the V_R-TR line as described in chapter 7.5. Particles are detected by comparing axial spectra for different V_R-TR combinations with a reference spectrum of the axial resonator. Given that the particle's axial frequency ν_z depends on the ring voltage and the tuning ratio, all observed frequencies are referenced to a common ring voltage of $V_{R,ref} = -0.755\,\mathrm{V}$ and a reference tuning ratio of $\mathrm{TR_{ref}} = 0.852\,950$ according to

$$\nu_{z,ref} = \nu_z - (V_R - V_{R,ref}) \times \frac{\Delta\nu_z}{\Delta V_R} - (\mathrm{TR} - \mathrm{TR_{ref}}) \times \frac{\Delta\nu_z}{\Delta \mathrm{TR}} \tag{7.26}$$

using the measured values of $\frac{\Delta\nu_z}{\Delta V_R} = -402\,\frac{\mathrm{Hz}}{\mathrm{mV}}$ and $\frac{\Delta\nu_z}{\mathrm{TR_{ref}}} = -52\frac{\mathrm{Hz}}{\mathrm{mU}}$.
Figure 7.9 shows the cumulative distribution function of observed frequencies $\nu_{z,ref}$ for 34 particles that were detected at a residual of at least $4\mathrm{dB_{V_{pk}}}$.
In order to determine the temperature of the feedback cooled cyclotron detector in the precision

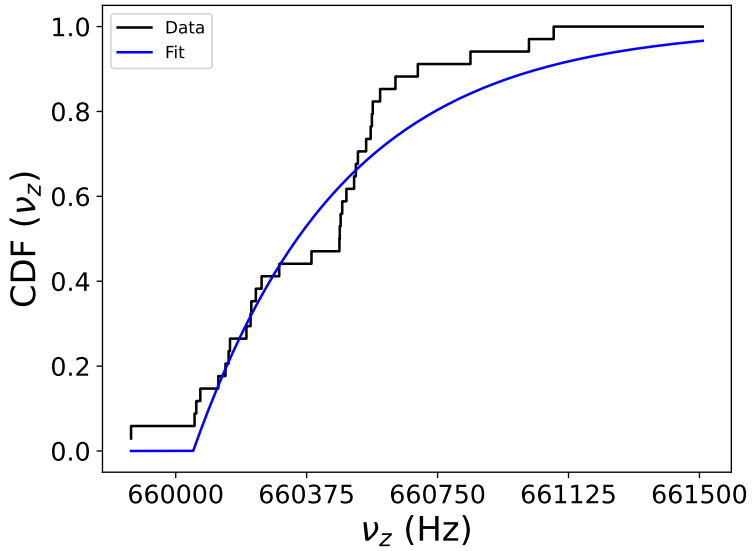

Figure 7.9: Cumulative distribution function of the observed axial frequencies in the analysis trap after cooling the particle repeatedly on the cyclotron detector of the precision trap. The blue line indicates the best fit of Eq. (7.27) to the data and yields the characteristic width $\Delta\nu_z = 430(24)$ Hz which corresponds to a temperature $T_+ = 6.04(59)$ K of the cyclotron temperature in the analysis trap.

trap, the cumulative distribution function of Eq. (7.24) which is given by

$$F_{\nu_z} = \Theta(\nu_{z,ref} - \nu_{z,cut}) \times (1 - e^{(-\frac{\nu_{z,ref} - \nu_{z,cut}}{\Delta\nu_z})}) \tag{7.27}$$

is fit to the data and $\Delta\nu_z = 430(24)\,\mathrm{Hz}$ is extracted. Inserting this value together with the known values of B_0 and B_2 into Eq. (7.25) yields

$$T_{+,AT} = 6.0(6)\,\mathrm{K}. \tag{7.28}$$

Note, however, that the effective cyclotron temperature changes when the proton is transported from the background field $B_{0,PT} = 1.944\,\mathrm{T}$ present in the precision trap to $B_{0,AT} = 1.21\,\mathrm{T}$. Thus the observed cyclotron temperature in the analysis trap is underestimated by a factor $\frac{B_{0,PT}}{B_{0,AT}}$ and the temperature of the PT cyclotron detector is given by:

$$T_{+,PT} = T_{+,AT} \times \frac{B_{0,PT}}{B_{0,AT}} = 9.6(9)\,\mathrm{K}. \tag{7.29}$$

The cyclotron detector is located within the trap can which is cooled to approximately $4.2\,\mathrm{K}$ by the liquid helium cryostats. However, the "electronic temperature" of the detection circuit can be above the ambient temperature in case external noise – as for example the input noise of the amplifier circuits – couples to the detector. Feedback cooling provides the possibility to reduce the "electronic temperature" up to a certain degree and can help to increase the probability of extracting a cold particle from the thermal distribution.

7.8 Determination of the ideal averaging time

In order to resolve spin state transitions, the axial background frequency scatter Ξ_{BG} has to be minimized. The BASE Allan deviation, which is defined as the standard deviation of the difference between subsequent frequency measurements, provides a good measure of Ξ_{BG} as a function of the utilized averaging time t_{avg}.
By averaging for longer durations, the scatter Ξ_{Fit} introduced by the uncertainty of the fit is expected to decrease with the square root of the averaging time t_{avg}:

$$\Xi(t_{avg})_{Fit} \propto \frac{1}{\sqrt{t_{avg}}}. \tag{7.30}$$

In addition to the fit scatter contribution outlined above, the particle's axial frequency in the analysis trap changes as the cyclotron mode undergoes a random walk driven by electrical background noise. Given that the mean change in cyclotron energy is proportional to the square root of the averaging time, the random walk contributes to the background scatter as:

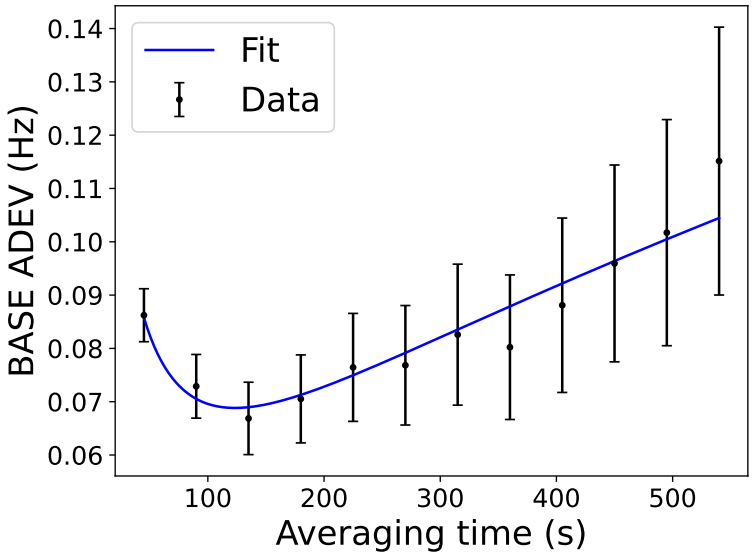

Figure 7.10

$$\Xi(t_{avg})_{RW} \propto \sqrt{t_{avg}}. \tag{7.31}$$

Finally, the finite stability of the voltage supplies contributes to the observed fit scatter. Typically, the Allan deviation of the voltage stability is constant for timescales relevant to the experiment and thus Ξ_V is constant.

$$\Xi(t_{avg})_V = const. \tag{7.32}$$

The final observed axial frequency scatter $\Xi_{BG}(t_avg)$ thus is a function of the averaging time can be modeled as:

$$\Xi_{BG}(t_{avg}) = \sqrt{\left(\frac{\Xi_{Fit}}{\sqrt{t_{avg}}}\right)^2 + (\Xi_{RW}\sqrt{t_{avg}})^2 + \Xi_V^2}. \tag{7.33}$$

The parameters Ξ_{Fit}, Ξ_{RW} and Ξ_V determine the strength of the individual contributions outlined above. Figure 7.10 shows the axial Allan deviation for a particle trapped in the Analysis trap.

A fit of Eq. (7.33) to the data yields $\Xi_{Fit} = 540(30)\,\mathrm{mHz\,s^{0.5}}$, $\Xi_{RW} = 4.4(2)\,\frac{\mathrm{mHz}}{\mathrm{s^{0.5}}}$ and $\Xi_V = 0(22)\,\mathrm{Hz}$. At the given fit- and random walk scatter contributions, Ξ_V is negligible and can not be determined from the BASE Allen deviation.

The ideal averaging time $t_{avg,opt}$ which minimizes the axial frequency scatter is given by

$$t_{avg,opt} = \frac{\Xi_{Fit}}{\Xi_{RW}} = 123(8)\,\mathrm{s}. \tag{7.34}$$

Note that the strength of the particles random walk depends on it's cyclotron temperature T_+. In case a hot particle with a high random walk contribution Ξ_{RW} is used, the optimal averaging time decreases.

7.9 Detection of spin flips

7.9.1 Statistical spin-flip detection

After the characterization steps outlined above, it was attempted to drive spin flips in the analysis trap. During these measurements it became apparent that the connections to the spin flip coils were broken. Thus, after the magnetic shimming and shielding system had been characterized, the experiment was opened and the spin flip lines were successfully repaired. Given the strong magnetic bottle present in the Analysis trap, the particle's motion through the axial Boltzmann distribution causes it's momentary cyclotron and Larmor frequency to continuously change. Thus, spin flips can be driven as soon as the particle is irradiated at a frequency $\nu_{rf} \geq \nu_{L,cut} = \frac{g}{2}\nu_{c,cut}$. The frequencies $\nu_{L,cut}$ and $\nu_{c,cut}$ indicate the Larmor- and free cyclotron frequency at vanishing axial energy. In order to drive and detect spin flips in the analysis trap, a radiofrequency drive at a frequency ν_{rf} is applied and the scatter Ξ_z of the particle's axial frequency is observed. In case the radiofrequency drive flips the particle's spin orientation, the axial frequency jump is given by

$$\Delta\nu_{z,SF} = \frac{g}{2}\frac{h\nu_+}{4\pi^2 m_p \nu_z}\frac{B_2}{B_0} = 172(13)\,\mathrm{mHz} \tag{7.35}$$

using the current values of B_0 and B_2. This jump of the axial frequency increases the scatter Ξ_z of subsequent axial frequency measurements. In case the probability to flip the spin between two axial frequency measurements in given by p_{SF}, the observed axial frequency scatter Ξ_z is given by Eq. (7.35):

$$\Xi_z = \sqrt{\Xi_{BG}^2 + \Xi_{SF}^2} = \sqrt{\Xi_{BG}^2 + p_{SF}\Delta\nu_{z,SF}^2}. \tag{7.36}$$

The background scatter Ξ_{BG} is determined by measuring the axial frequency scatter in case the drive frequency ν_{rf} is tuned far from the Larmor frequency cut $\nu_{L,cut}$. The resulting background scatter Ξ_{BG} includes contributions from fitting, finite stability of the voltage sources and the particle's cyclotron random walk as well as possible scatter that is induced by the drive but not related to spin flips. Figure (7.11) shows the axial frequency scatter for a sequence of axial

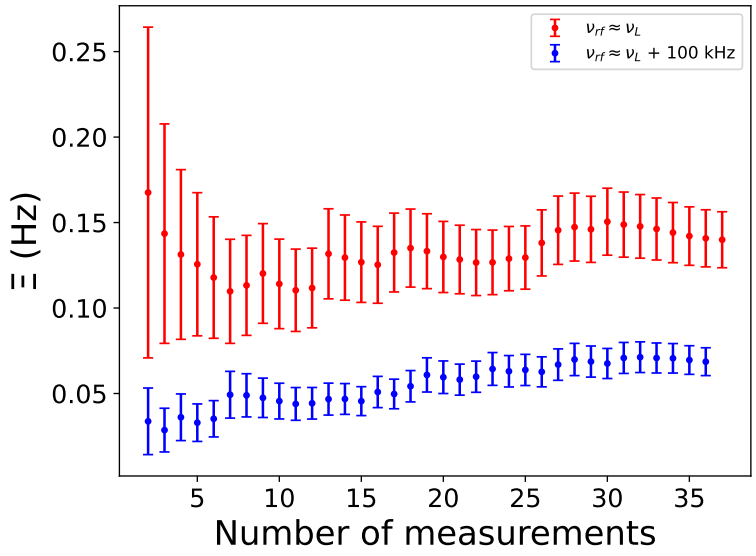

Figure 7.11: Axial frequency scatter in case the radiofrquency drive is detuned from the Larmor frequency (blue) or resonant with the Larmor frequency (red). In case the drive is close to the Larmor frequency, spin flips are driven and the axial frequency scatter increses significantly above the background. Evaluating the scatter yields $\Xi_{SF} = 140(16)\,\mathrm{mHz}$ and $\Xi_{BG} = 47.7(6)\,\mathrm{mHz}$ which corresponds to a spin flip probability of $p_{SF} = 58(18)\,\%$.

frequency measurements in case the drive frequency is tuned away from the Larmor frequency cut (blue) and in case spin flips are driven (red).
Using the full amount of available data, the background scatter Ξ_{BG} in case the radiofrequency drive is detuned from the Larmor resonance is given by

$$\Xi_{BG} = 47.7(6)\,\mathrm{mHz} \tag{7.37}$$

and the axial scatter Ξ_{SF} in case the drive is resonant with the Larmor frequency is

$$\Xi_{SF} = 140(16)\,\mathrm{mHz}. \tag{7.38}$$

Using Eqs. (7.35) and (7.36) finally yields the spin flip probability

$$p_{SF} = \frac{\Xi_{SF}^2 - \Xi_{BG}^2}{\Delta\nu_{z,SF}^2} = 58(18)\,\%. \tag{7.39}$$

The uncertainty of the spin flip probability is dominated by the uncertainty of the magnetic inhomogeneity B_2, which during the initial characterization of the trap had a relative uncertainty

of $8\,\%$ and has since been measured more precisely. Nevertheless the significant increase in axial frequency scatter clearly indicates that spin flips were driven.

7.9.2 Single spin flip detection

Instead of resolving spin flips by an increase of the axial frequency scatter, individual jumps of the axial frequency can be resolved. Compared to statistical spin flip detection, the resolution of individual spin flips requires a low axial background scatter as a frequency jump of $\Delta_{z,SF} = 172\,\mathrm{mHz}$ has to be resolved from a single measurement. In order to resolve single spin flips, the axial frequency $\nu_{z,1}$ is measured, the spin flip drive is applied and the axial frequency $\nu_{z,2}$ after application of the drive is measured. If no spin flip occurred, the frequency shifts $\Delta\nu_z = \nu_{z,2} - \nu_{z,1}$ follow a Gaussian distribution centered around $0\,\mathrm{Hz}$ with a standard deviation Ξ_{BG}. However, in the case that the spin state of the particle was flipped, the resulting frequency differences are drawn from Gaussian distribution centered around $\pm\Delta_{z,SF}$, depending on the initial spin state. The probability density $p(\Delta\nu_z)$ to observe a frequency shift of $\Delta\nu_z$ depends on the spin flip probability p_{SF}, the background scatter Ξ_{BG} and the initial spin state. In case many spin flips are observed, the probabilities $p_\uparrow$ to find a particle in the spin up state and $p_\downarrow$ to find the particle in the spin down state are equal and $p(\Delta\nu_z)$ given by Eq. (3.35) becomes:

$$\begin{aligned} p(\Delta\nu_z) =& (1 - p_{SF})\,\mathcal{N}(0, \Xi_{BG}) \\ &+ 0.5\,p_{SF}\,\mathcal{N}(-\Delta\nu_{z,SF}, \Xi_{BG}) \\ &+ 0.5\,p_{SF}\,\mathcal{N}(\Delta\nu_{z,SF}, \Xi_{BG}). \end{aligned} \tag{7.40}$$

Figure 7.12 shows the probability density of the observed frequency shifts $\Delta\nu_z$ during a single spin-flip measurement sequence in the analysis trap using a proton with a cyclotron temperature of approximately $80\,\mathrm{mK}$. Each axial spectrum is acquired at an averaging time of $t_{avg} = 105\,\mathrm{s}$, corresponding to an averaging time close to the minimum of the BASE ADEV. The blue line indicates the fitted probability density obtained from a fit to the cumulative distribution function. The three sub distributions are visible, however, the whole probability density seems to be shifted towards negative values. The axial frequency shows no strong drift which indicates that the frequency relaxes back to the equilibrium value while no spin flip drive is applied. In case this shift proves to be persistent, asymmetric thresholds have to be applied in the single spin flip detection scheme outlined in chapter 3.5.2, however, the cause shift has yet to be understood and warrants further investigation regarding its impact on the final spin state identification procedure.

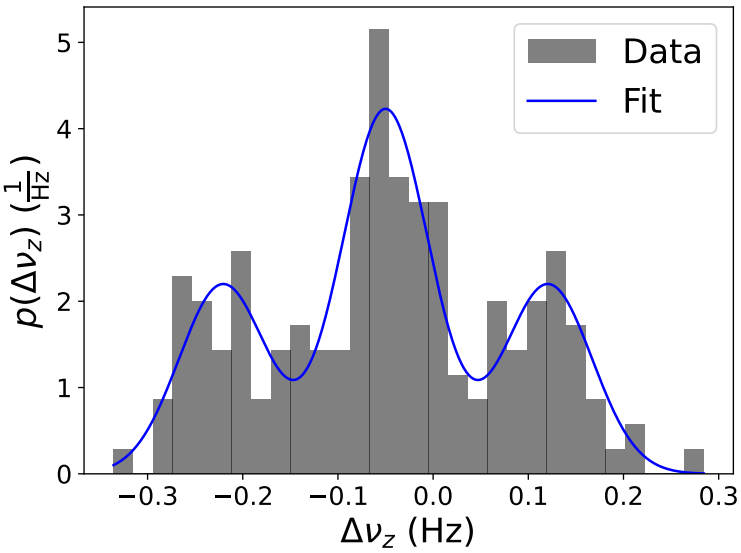

Figure 7.12: Histogram of the observed frequency differences $\Delta\nu_z$ in case a resonant spin flip drive is applied between the frequency measurements. In case the spin is flipped, the axial frequency jumps by $\pm\Delta_{z,SF} = \pm 170.8(8)\,\mathrm{mHz}$ which leads to the two side distributions next to the central distribution corresponding to the axial frequency scatter in case no spin is flipped. The blue line shows the fitted probability density obtained from a fit to the cumulative distribution function of the observed frequency shifts. The whole distribution is shifted by $50.0(2)\,\mathrm{mHz}$ towards negative shifts, however no strong drift is visible in the axial frequency data, indicating that the shift is caused by the spin flip drive. The exact mechanism leading to the shift has yet to be understood and is topic of further investigations.

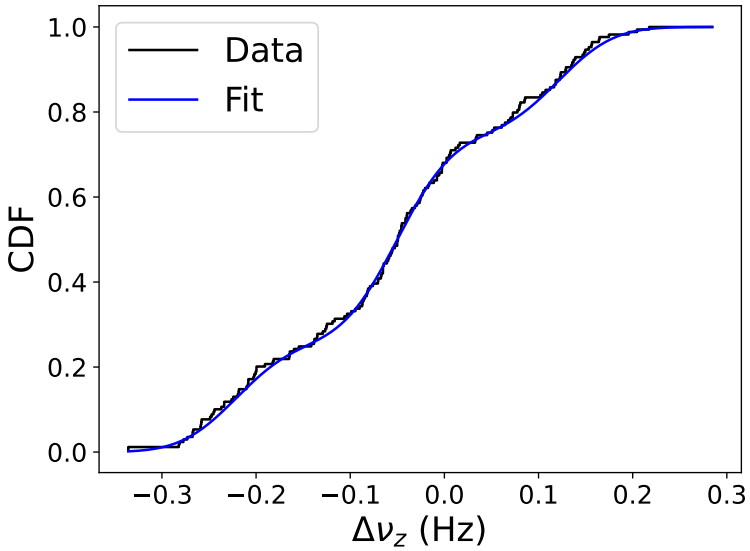

Figure 7.13: Cumulative distribution function of the observed axial frequency differences in case a resonant spin flip drive is applied between the frequency measurements. The CDF increases fastest at the location of the sub distributions corresponding to no spin flip, a flip from the spin down state to the spin up state and vice versa. The blue line shows the best fit of the cumulative distribution function of Eq. (7.40) – expanded by a parameter $\Delta\nu_{z,center}$ accounting for the observed bias towards negative shifts – to the data and yields $\Delta\nu_{z,center} = -50.0(2)\,\mathrm{mHz}$, $\Delta_{z,SF} = 170.8(8)\,\mathrm{mHz}$, $\Xi_{BG} = 46.3(6)\,\mathrm{mHz}$ and$p_{SF} = 51.0(4)\,\%$.

In order to determine the parameters $\Delta\nu_{z,SF}$, Ξ_{BG} and p_{SF} the cumulative distribution function of Eq. (7.40) is fit to the data. An additional parameter $\Delta\nu_{z,center}$ which shifts the whole distribution is introduced to account for the bias in the observed data. Figure 7.13 shows the cumulative distribution function as well as the line of best fit.

The fit yields a shift of the whole distribution by $\Delta\nu_{z,center} = -50.0(2)\,\mathrm{mHz}$ towards negative frequency shifts. The fitted frequency jump $\Delta_{z,SF} = 170.8(8)\,\mathrm{mHz}$ associated with a spin flip is in good agreement with the predicted value based on measurements of B_2 and B_0. The fitted background scatter $\Xi_{BG} = 46.3(6)\,\mathrm{mHz}$ is comparable to the previous values observed during statistical spin flip observation and the spin flip probability $p_{SF} = 51.0(4)\,\%$ indicates that the spin flip transition was driven at high enough power to be saturated.

By proving the observation of single spin flips at a fidelity comparable to the best conditions during the 2016 g-factor measurement campaign [102] all prerequisites for a g-factor measurement at significantly improved magnetic field homogeneity in the precision trap have been demonstrated, paving the way for a (anti)proton g-factor measurement at the 100 p.p.t. level.

8 Impact on future measurements

The successful demonstration of the ability to tune the magnetic field in the center of the precision trap enables comparisons of the charge-to-mass ratios and the g-factors of the proton and antiproton at unpreceded precision. In addition, the ability to cancel the inhomogeneities of the magnetic field provides the possibility to utilize novel measurement techniques, which will be discussed in the following.

8.1 Impact on charge-to-mass ratio comparisons

The comparison of the charge-to-mass ratio of the proton and the antiproton relies on the comparison of the individual particle's free cyclotron frequencies in a common, homogeneous magnetic field B_0. The ratio R of charge-to-mass ratios is given by:

$$R = \frac{\nu_{c,\bar{p}}}{\nu_{c,p}} = \frac{\left(\frac{q}{m}\right)_{\bar{p}} B_0}{\left(\frac{q}{m}\right)_{p} B_0} = \frac{\left(\frac{q}{m}\right)_{\bar{p}}}{\left(\frac{q}{m}\right)_{p}}. \tag{8.1}$$

In case both particles' free cyclotron frequencies are measured in the same field, R is independent of B_0. In order to suppress shifts of the particle position when the polarity is inverted to change between a negatively charged antiproton and a positive proton, the antiproton is compared to a negatively charged H^--ion and the final ratio is corrected by the proton-to-H^- mass ratio (see sec. 3.4).

In the presence of magnetic inhomogeneities, the average magnetic field the particles experience during the measurement depends on the eigenenergies of the particles. Given the ratio of eigenfrequencies, the dominant shift of the free cyclotron frequency depends on the shift of the modified cyclotron frequency which is given by Eq. (2.45). Since the particles are measured in the same potential, they both experience the same shift and R is only shifted by the difference ΔE in particle energies rather than the absolute value of the eigenenergies. Using Eq. (2.45), the shift of R with the residual magnetic bottle B_2 present in the precision trap and the temperature difference ΔE_z is given by:

$$\frac{\Delta R}{R} = \frac{1}{m\omega_z^2}\frac{1}{B_0} \times B_2 \times \Delta E_z = \frac{26.2 \times 10^{-9}}{\frac{\mathrm{T}}{\mathrm{m}^2}\mathrm{K}} \times B_2 \times \Delta E_z. \tag{8.2}$$

Since B_2 and the axial temperature of the particles are continuously observed during a charge-to-mass ratio measurement campaign, R can be corrected for the shift related to the residual magnetic bottle described by Eq. (8.2). The uncertainty $\sigma(\frac{\Delta R}{R})$ of this correction is given by the uncertainties $\sigma(B_2)$ and $\sigma(\Delta E_z)$ of the residual magnetic bottle and the temperature difference:

$$\sigma(\frac{\Delta R}{R}) = \frac{1}{m\omega_z^2}\frac{1}{B_0} \times \sqrt{\left(\Delta E_z \sigma(B_2)\right)^2 + \left(B_2 \sigma(\Delta E_z)\right)^2}. \tag{8.3}$$

During the last charge-to-mass measurement campaign [69] $B_{2,SB} = -0.267(2)\,\frac{\mathrm{T}}{\mathrm{m}^2}$ and $B_{2,Peak} = -0.0894(6)\,\frac{\mathrm{T}}{\mathrm{m}^2}$ were measured for the sideband and peak measurements respectively. In chapter 6.3 the ability to reproducibly change B_2 by loading the B_2-coil was demonstrated and it was demonstrated experimentally, that this shift can be suppressed by more than a factor 100.

8.2 g-factor measurements

Measurements of the magnetic moment rely on a comparison of the trapped particle's free cyclotron frequency $\nu_c = \frac{1}{2\pi}\frac{q}{m}B_0$ and its Larmor frequency $\nu_L = \frac{1}{2\pi}\frac{g}{2}\frac{q}{m}B_0$ such that $\frac{g}{2}$ can be determined via:

$$\frac{g}{2} = \frac{\nu_L}{\nu_c}. \tag{8.4}$$

A correct measurement of $\frac{g}{2}$ thus requires ν_c and ν_L to be measured in the same magnetic field. While ν_c can be determined via the sideband or peak method outlined in 5.2, determination of the Larmor frequency requires the resolution of single spin flips in the analysis trap. The spin state of the particle, however, can only be resolved in case the particle's cyclotron energy E_+ is small. Given that measurements of the free cyclotron frequency heat the particle's cyclotron energy to temperatures of $E_+ \approx 300\,\mathrm{K}$, a novel measurement scheme using two particles is typically applied (see 3.5.3). While this method reduces the requirement to cool the particle after each cyclotron frequency measurement, it has the disadvantage, that ν_c and ν_L are no longer measured simultaneously. In particular, it can not be excluded that the radio-frequency drive irradiating the particle with the Larmor frequency excites the axial resonator which leads to a temperature difference $\Delta T_z = T_{z,L} - T_{z,c}$ between the axial temperature $T_{z,L}$ of the particle used to probe the Larmor frequency and the temperature $T_{z,c}$ of the particle used to measure the free cyclotron frequency. Given that ν_+ and ν_L have the same scaling with the particle's

eigenenergies, the systematic shift of g due to a difference in axial energy E_z is equivalent to the case of charge-to-mass ratio measurements:

$$\frac{\Delta g}{g} = \frac{1}{m\omega_z^2}\frac{1}{B_0} \times B_2 \times \Delta E_z = \frac{26.2d - 9}{\frac{\mathrm{T}}{\mathrm{m}^2}\mathrm{K}} \times B_2 \times \Delta E_z. \tag{8.5}$$

Once again, the related uncertainty of the systematic shift is given by a combination the uncertainties $\sigma(B_2)$ and $\sigma(\Delta E_z)$:

$$\sigma(\frac{\Delta g}{g}) = \frac{1}{m\omega_z^2}\frac{1}{B_0} \times \sqrt{\left(\Delta E_z \sigma(B_2)\right)^2 + \left(B_2 \sigma(\Delta E_z)\right)^2}. \tag{8.6}$$

In 2017 the antiproton g-factor was determined with a fractional precision of 1.5 p.p.t. ($95\,\%$ confidence) [68] using the two particle measurement scheme outlined in 3.5.3. During this measurement it was observed, that application the Larmor drive lead to saturation of the axial resonator in the precision trap. Thus it could not be excluded, that the Larmor particle's axial temperature $T_{z,L}$ was up to $0.68(7)$ K higher than the axial temperature $T_{z,c}$ of the particle used to measure the cyclotron frequency. Given the strong magnetic bottle of $B_{2,PT} = 2.74(22)\ \frac{\mathrm{T}}{\mathrm{m}^2}$ present in the precision trap, this uncertainty in temperature introduced by the Larmor drive lead to the dominant systematic uncertainty of 970 p.p.b. Thanks to the redesign of the trap stack in the course of the thesis, the residual magnetic bottle in the precision trap was reduced to $B_2 = 103.50(23)\ \frac{\mathrm{mT}}{\mathrm{m}^2}$. With the help of the implemented superconducting magnetic shimming and shielding system, the residual magnetic bottle can be further reduced to values close to $B_2 = 0$ which eliminates the main systematic uncertainty present in the last measurement. Alternatively, the successful implementation of a dedicated cooling trap into the experiment [100] provides the possibility to rapidly cool particles and thus enables single particle measurement schemes in which the cyclotron frequency is measured during irradiation with the Larmor drive. In this measurement scheme, ν_c and ν_L are probed simultaneously and therefore are measured at the same axial temperature by design.

8.3 Coherent spin flip techniques

The increased homogeneity provided by the magnetic shimming and shielding system provides the possibility to apply novel coherent techniques for the determination of the Larmor frequency. In case the magnetic field in the precision trap is not homogeneous, the particle experiences magnetic fields of different strength during its axial oscillation. As a result, the particles oscillates in and out of resonance and its spin state can change, even if the applied radio-frequency does not correspond to the Larmor frequency at the background field B_0. This causes the Larmor

resonance to be broadened. A detailed derivation of the shape of the Larmor resonance is given in [127]. In the presence of a magnetic inhomogeneity, the spin flip probability as thus limited to $50\,\%$ and significant power broadening is present in case the spin flip drive is applied for long times.
By tuning the gradient B_1 and the magnetic bottle B_2 to values close zeros, the strength of the magnetic field stays constant during the oscillation of the particle. As a consequence, the particle's Larmor frequency does not change with its position and in case a resonant drive is applied, the particle stays in resonance. The increased homogeneity thus allows for longer excitation times which reduces the width of the frequency spectrum of the Larmor drive and leads to a narrower g-factor resonance.
In addition to reduced power broadening, the homogeneous field provides the possibility to drive spin flips coherently. As soon as the Larmor drive is applied, the two spin states are coupled and the probability to find the particle in one or the other state changes with the (modified) Rabi frequency Ω (see 5.2.1):

$$\Omega = \sqrt{\Omega_{res}^2 + \delta^2}. \tag{8.7}$$

As in case of the sideband coupling between eigenmotions of the particle, Ω_{res} describes the resonant Rabi frequency which depends on the strength of the drive whereas δ describes the detuning of the applied drive from the true Larmor frequency. The probability to flip the trapped particle's spin state thus becomes a function of time and it is in theory possible to achieve full inversion of the spin state, thus increasing the contrast in the g-factor resonance. The possibility to extend the time in which the Larmor drive is applied depends on the leftover inhomogeneities of the magnetic field as any excitation in the presence of magnetic inhomogeneities leads to a dephasing which reduces the achievable contrast. In order to minimize the time during which the drive is applied Ramsey methods can be implemented [141]. In this measurement scheme, the excitation is limited to two short pulses before and after a time of free evolution.

8.4 Determination of measurement systematics

Characterization of the systematic shifts caused by magnetic and electrostatic inhomogeneities requires the measurement of frequency shifts as a function of the particle's eigenenergies. The strength of these shifts depends on the magnitude of the inhomogeneity, typically parametrized by the coefficients B_n and C_n as well as the energies E_+, E_z and E_-. The magnetic shimming and shielding system improves the determination of systematic effects in multiple ways.
First, the possibility to change B_1 and B_2 in situ provides the possibility to study the effects

magnetic inhomogeneities have on measurements directly (see 6.7). Second, the measurement of the particle's eigenenergies E_+ and E_- relies on the observation of frequency shifts in the presence of magnetic inhomogeneities. By purposely increasing the strength of B_1 and B_2, the observed frequency shifts at a certain energy difference can be increased which leads to a lower uncertainty in the calibration of the energy a drive imparts on the particle.

9 Conclusion and Outlook

9.1 Summary

The BASE experiment tests CPT-symmetry by comparing the fundamental properties of protons and antiprotons. The comparison of the charge-to-mass ratio as well as the g-factor of the proton and antiproton require the measurement of the free cyclotron frequency ν_c and the Larmor frequency ν_L in the common magnetic field B_0 of a Penning trap. In order to ensure high precision, the magnetic field has to be shielded against fluctuations induced from external sources present in the environment of the experiment. In addition, higher order coefficients of the magnetic field lead to systematic shifts of the measured frequencies with the particles eigenenergies. The goal of this thesis was the design, successful implementation and characterization of a superconducting magnetic shimming and shielding system which prevents fluctuations of B_0 due to external sources and provides the possibility to tune the linear and quadratic inhomogeneities B_1 and B_2 of the magnetic field. The main results of the thesis are outlined below:

- The penning trap stack was redesigned to increase spacial separation between the precision trap and the analysis trap. By decreasing the size of the high-voltage catching electrodes, the distance between the center of the precision trap and the analysis trap was increased by $2.5\,\mathrm{cm}$. The increased distance between the traps reduces the strength of the residual magnetic bottle $B_{2,PT}$ in the precision trap which is caused by the ferromagnetic ring electrode of the analysis trap. Compared to the last g-factor measurement campaign, the residual B_2 in the center of the precision trap is reduced from $2.74(22)\ \frac{\mathrm{T}}{\mathrm{m}^2}$ to $103.50(23)\ \frac{\mathrm{mT}}{\mathrm{m}^2}$.
- A superconducting shimming and shielding system was successfully designed, implemented and characterized. This system suppresses external fluctuation of the magnetic field by approximately a factor 50 and provides the possibility to conduct frequency measurements during operation of the antiproton decelerator. In addition, the shimming system can be charged using an external current which provides the possibility to change the linear and quadratic inhomogeneities B_1 and B_2. A loading scheme that allows

reliable loading was developed and the ability of the system to hold current without detectable loss for multiple days was demonstrated. By charging the system, B_2 can be tuned to 0 which eliminates the dominant systematic uncertainty of past g-factor measurements and paves the way for a comparison of the proton and antiproton g-factor at the 100 p.p.t. level.

- In the course of this thesis, the Penning trap system was recharacterized after the implementation of the magnetic shimming and shielding system. Protons were successfully trapped in both the precision trap and the analysis trap, the traps were characterized and loss-less transport between the traps was established. These measurements paved the way for the detection of single spin flips which demonstrates the possibility to successfully measure the (anti)proton g-factor with the upgraded system.

After the successful demonstration of single spin flip detection using protons, the experiment was connected to the Antiproton decelerator in order to load antiprotons into the reservoir trap. However, due to the reduced beam energy provided by ELENA, the steering parameters required to guide the beam into the trap apparatus changed and a novel degrader had to be implemented. After catching of antiprotons initially was not successful during the 2022 beamtime, the upgraded system was used to measure the proton g-factor in order to prepare the experiement for the implementation of phase-sensitive measurement methods and characterize long-term performance of the newly implemented coil system and cooling trap. After the successful conclusion of the proton g-factor measurement in 2023, antiprotons were successfully loaded for the first time using the novel degrader system [95]. As of December 2023, the system is being prepared for a measurement of the antiproton g-factor.

9.2 Outlook

9.2.1 Current measurement campaign

Operation of all critical components was demonstrated during the characterization outlined in this thesis and the proton g-factor was successfully measured using the upgraded apparatus. After the successful loading of antiprotons in late 2023 the experiment is prepared to measure the antiproton g-factor at improved precision in 2023/2024.

9.2.2 Development of persistent joints

In parallel to the g-factor campaign, novel manufacturing techniques for the production persistent joints using superconducting solder as outlined in [135] are tested. The goal of these

tests is to find a simple yet reliable manufacturing process for superconducting joints with high critical currents in the presence of strong magnetic fields which would provide the possibility to further increase the critical current of the B_1-coil which could provide the possibility to compensate the residual B_1 in the precision trap completely.

9.2.3 Feasibility studies of a 7-pole trap

In order to tackle electrostatic asymmetries created by manufacturing errors and patch potentials on the electrodes, feasibility studies on the construction of a 7-pole trap are being conducted. By using 2 independent sets of correction electrodes and two tuning ratios, C_4 and C_6 can be tuned to 0 simultaneously, even in case of voltage offsets or mismatch of the electrode dimensions. This additional degree of freedom helps to suppress the systematic shifts due to higher order terms in the expansion of the electrostatic potential (see Eq. (2.40)) which could lead to an increase in the signal-to-noise ratio of the particle signature in the analysis trap, which corresponds to a higher spin flip detection fidelity at comparable averaging time.

9.2.4 Design of an analysis trap with inverted magnetic bottle

The resolution of single spin flips in the analysis trap requires the preparation of a particle with low cyclotron energy E_+ as the cyclotron transition rate ζ_+ given by Eq. (3.30) is proportional to the cyclotron quantum number n_+. In the typical configuration, the ring electrode is manufactured out of a ferromagnetic alloy, which reduces the magnetic field in the center of the analysis trap and creates the superimposed magnetic bottle B_2 which is required to resolve spin state transitions. Note, however, that ζ_+ depends on modified cyclotron frequency ν_+ and thus can be reduced by increasing the modified cyclotron frequency in the center of the trap. In order to accomplish this goal, a novel analysis trap using two ferromagnetic correction electrodes was designed. In this configuration, the magnetic field in the center of the analysis trap is maximized and a magnetic bottle with $B_2 < 0$ is superimposed.

9.2.5 Stabilization of the experimental apparatus

In order to further stabilize the frequency stability of the experimental apparatus, an active pressure stabilization system is currently developed. During previous measurement campaigns it was observed that pressure fluctuations can lead to an increased scatter of the particle's eigenfrequencies. This system will monitor the pressure in the helium exhaust line and use a flow controller to actively keep the pressure in the helium exhaust line at a constant pressure. In addition to the pressure, the temperature near the top of the cryostats is known to have an

effect of the frequency stability of the experiment. While currently not an active area of work, active stabilization of the temperature might be implemented in the future.

9.2.6 Implementation of novel measurement methods

In preparation of future charge-to-mass ratio measurement campaigns, the implementation of phase-sensitive detection methods into the experiment which was in large parts developed in the PhD thesis of Matthias Borchert [99] is advanced. On long-term timescales, the feasibility of a direct comparison of g-factors using coupled ions as described in [142] will be studied.

9.2.7 Implementation of a transportable penning trap

Currently, research on baryonic antimatter systems is limited by the required access to a particle accelerator. However, the operation of said accelerator creates a noisy environment which complicates high-precision measurements. In order to overcome these limitations, a transportable trap [71] is currently being commissioned. This project – called BASE-STEP – will provide the possibility to load antiprotons at the antiproton decelerator. The trapped antiprotons will be transported out of the accelerator hall and transferred into a high-precision penning trap system located at an offline laboratory at CERN. Once loss-less transport is established over short distances, BASE-STEP could deliver antiprotons to experiments located outside of CERN.

Acknowledgments

I would like to use the opportunity to thank several people who were crucial for the success of the work presented in this thesis:
First of all, I would like to thank my doctoral supervisor Klaus Blaum. Whenever problems arose, be it missing electrodes or problems during writing, you always found encouraging words and quick solutions. Your continuous support made this work possible.

Next, I want to thank Stefan Ulmer, who is the mastermind behind BASE and supervised the development, integration and characterization of the superconducting shimming and shielding system at CERN. I appreciate that I always had the opportunity to spontaneously enter your office and trap you in fruitful discussions about anything. Your passion is infectious and I will remember the shared shifts fondly. I am absolutely certain that you will continue to produce excellent research both at CERN and in Düsseldorf, and I hope that the bureaucratic obligations that are inherent with your new position still allow you to spend ample time at your experiments. Thank you for your patience, continued support and the opportunity to learn from you.

Furthermore, I would like to thank my current and former colleagues, who always were available for discussions and support. I always enjoyed working with you, no matter if you were a new students challenging my knowledge of the experiment by asking questions or long-term colleagues available for the discussion of minute details. I am thankful for the time I was able to spend with you and the friendships we formed.
I would like to thank the following people in particular:
Barbara Latacz, for being an unstoppable force of nature which continuously pushes towards the resolution of the problems at hand. It was almost impossible to stop you from working on the experiment and I am convinced that you and BASE will continue to be successful with you in your new role.
Markus Fleck, who I shared countless hours with characterizing the experiment. You made sure that long shifts were never boring but fun. I thoroughly enjoyed picking your brain about programming paradigms and wish you the best no matter if your future lies in Europe or Asia.
Elise Wursten, who helped me getting an overview over the intricacies of the Standard Model and provided invaluable help during the characterization of the coil system. You were always a calming force and open to help if any problem, be it scientific or personal, arose.

Outside of work, I would like to thank my circle of friends from school, university and shared hobbies who I kept in contact with online. You always provided an environment to relax after long shifts and I am thankful that you always had an open ear for my grievances no matter if

work related or personal. In particular, I am thankful for the close friendships I formed with Lisa, Margun and Kevin over the last five years and I hope that we will have more opportunities to see each other in person in the future.

In addition to the friendships formed in person at CERN and online, I would like to thank my friends at home in Esslingen. Whenever I visit, you treat me as if I had never been gone and I am looking forward to many more shared memories.

Finally, I would like to thank my family. You always supported me and gave me a place to come home to whenever I needed a change of scenery. Without your love and support, I would never have been able to finish this work and I am looking forward to spending more time with you again.

Part of this work has been sponsored by the Wolfgang Gentner Programme of the German Federal Ministry of Education and Research (grant no. 13E18CHA).

List of publications

1. Devlin, Jack A., et al. ”Superconducting solenoid system with adjustable shielding factor for precision measurements of the properties of the antiproton.” Physical Review Applied 12.4 (2019): 044012.

2. Smorra, C., et al. ”Direct limits on the interaction of antiprotons with axion-like dark matter.” Nature 575.7782 (2019): 310-314.

3. Devlin, Jack A., et al. ”Constraints on the coupling between axionlike dark matter and photons using an antiproton superconducting tuned detection circuit in a cryogenic penning trap.” Physical Review Letters 126.4 (2021): 041301.

4. Bohman, M., et al. ”Sympathetic cooling of a trapped proton mediated by an LC circuit.” Nature 596.7873 (2021): 514-518.

5. Borchert, M. J., et al. ”A 16-parts-per-trillion measurement of the antiproton-to-proton charge–mass ratio.” Nature 601.7891 (2022): 53-57. (Parts used in this thesis)

6. Will, Christian, et al. ”Sympathetic cooling schemes for separately trapped ions coupled via image currents.” New Journal of Physics 24.3 (2022): 033021.

7. Völksen, F., et al. ”A high-Q superconducting toroidal medium frequency detection system with a capacitively adjustable frequency range $>$ 180 kHz.” Review of Scientific Instruments 93.9 (2022).

8. Latacz, Barbara M., et al. ”BASE—high-precision comparisons of the fundamental properties of protons and antiprotons.” The European Physical Journal D 77.6 (2023): 94.

9. Latacz, Barbara M., et al. ”Ultra-thin polymer foil cryogenic window for antiproton deceleration and storage.” Review of Scientific Instruments 94.10 (2023).

Bibliography

[1] Particle Data Group. “Review of Particle Physics”. In: *Progress of Theoretical and Experimental Physics* 2022.8 (Aug. 2022), p. 083C01.

[2] G Arnison et al. “Experimental observation of isolated large transverse energy electrons with associated missing energy at s= 540 GeV”. In: *Physics Letters B* 122.1 (1983), pp. 103–116.

[3] Marcel Banner et al. “Observation of single isolated electrons of high transverse momentum in events with missing transverse energy at the CERN pp collider”. In: *Physics Letters B* 122.5-6 (1983), pp. 476–485.

[4] Fumio Abe et al. “Observation of top quark production in $p\bar{p}$ collisions with the collider detector at fermilab”. In: *Physical review letters* 74.14 (1995), p. 2626.

[5] S Abachi et al. “Search for high mass top quark production in $p\bar{p}$ collisions at s= 1.8 TeV”. In: *Physical review letters* 74.13 (1995), p. 2422.

[6] R Brandelik et al. “Evidence for planar events in e+ e- annihilation at high energies”. In: *Physics Letters B* 86.2 (1979), pp. 243–249.

[7] DP Barber et al. “Discovery of three-jet events and a test of quantum chromodynamics at PETRA”. In: *Physical Review Letters* 43.12 (1979), p. 830.

[8] Ch Berger et al. “Evidence for gluon bremsstrahlung in e+ e- annihilations at high energies”. In: *Physics Letters B* 86.3-4 (1979), pp. 418–425.

[9] Wulfrin Bartel et al. “Observation of planar three-jet events in e+ e- annihilation and evidence for gluon bremsstrahlung”. In: *Physics Letters B* 91.1 (1980), pp. 142–147.

[10] Steven Weinberg. “A model of leptons”. In: *Physical review letters* 19.21 (1967), p. 1264.

[11] Georges Aad et al. “Observation of a new particle in the search for the Standard Model Higgs boson with the ATLAS detector at the LHC”. In: *Physics Letters B* 716.1 (2012), pp. 1–29.

[12] CMS collaboration et al. “Observation of a new boson with mass near 125 GeV in pp collisions at sqrt (s)= 7 and 8 TeV”. In: *arXiv preprint arXiv:1303.4571* (2013).

[13] François Englert and Robert Brout. “Broken symmetry and the mass of gauge vector mesons”. In: *Physical review letters* 13.9 (1964), p. 321.

[14] Peter Ware Higgs. “Broken symmetries, massless particles and gauge fields”. In: *Phys. Lett.* 12 (1964), pp. 132–133.

[15] V Gribov and B Pontecorvo. “Neutrino astronomy and lepton charge”. In: *Physics Letters B* 28.7 (1969), pp. 493–496.

[16] Yoshiyuki Fukuda et al. “Evidence for oscillation of atmospheric neutrinos”. In: *Physical review letters* 81.8 (1998), p. 1562.

[17] Werner Rodejohann. “Neutrino-less double beta decay and particle physics”. In: *International Journal of Modern Physics E* 20.09 (2011), pp. 1833–1930.

[18] Gerhart Lüders. “On the equivalence of invariance under time reversal and under particle-antiparticle conjugation for relativistic field theories”. In: *Dan. Mat. Fys. Medd.* 28 (1954), pp. 1–17.

[19] Wolfgang Pauli, Léon Rosenfeld, and Victor Weisskopf. “Niels Bohr and the development of physics”. In: *British Journal for the Philosophy of Science* 7.28 (1957).

[20] Laurent Canetti, Marco Drewes, and Mikhail Shaposhnikov. “Matter and Antimatter in the Universe”. In: *New Journal of Physics* 14.9 (2012), p. 095012.

[21] Richard H Cyburt. “Primordial nucleosynthesis for the new cosmology: Determining uncertainties and examining concordance”. In: *Physical Review D* 70.2 (2004), p. 023505.

[22] George R Blumenthal et al. “Formation of galaxies and large-scale structure with cold dark matter”. In: *Nature* 311.5986 (1984), pp. 517–525.

[23] P James E Peebles and Bharat Ratra. “The cosmological constant and dark energy”. In: *Reviews of modern physics* 75.2 (2003), p. 559.

[24] Nabila Aghanim et al. “Planck 2018 results-VI. Cosmological parameters”. In: *Astronomy & Astrophysics* 641 (2020), A6.

[25] Andrei D Sakharov. “Violation of CP-invariance, C-asymmetry, and baryon asymmetry of the Universe”. In: *In The Intermissions… Collected Works on Research into the Essentials of Theoretical Physics in Russian Federal Nuclear Center, Arzamas-16*. World Scientific, 1998, pp. 84–87.

[26] Gerard t Hooft. “Symmetry breaking through Bell-Jackiw anomalies”. In: *Physical Review Letters* 37.1 (1976), pp. 8–11.

[27] J. H. Christenson et al. “Evidence for the 2π Decay of the K_2^0 Meson”. In: *Phys. Rev. Lett.* 13 (4 July 1964), pp. 138–140.

[28] A. Alavi-Harati et al. “Observation of Direct CP Violation in $K_{S,L} \to \pi\pi$ Decays”. In: *Phys. Rev. Lett.* 83 (1 July 1999), pp. 22–27.

[29] V. Fanti et al. “A new measurement of direct CP violation in two pion decays of the neutral kaon”. In: *Physics Letters B* 465.1 (1999), pp. 335–348.

[30] AD Dolgov and Ya B Zeldovich. “Cosmology and elementary particles”. In: *Reviews of Modern Physics* 53.1 (1981), p. 1.

[31] Orfeu Bertolami et al. “CPT violation and baryogenesis”. In: *Physics Letters B* 395.3-4 (1997), pp. 178–183.

[32] V Alan Kostelecký and Stuart Samuel. “Spontaneous breaking of Lorentz symmetry in string theory”. In: *Physical Review D* 39.2 (1989), p. 683.

[33] Don Colladay and V Alan Kostelecký. “Lorentz-violating extension of the standard model”. In: *Physical Review D* 58.11 (1998), p. 116002.

[34] Don Colladay and V Alan Kostelecký. “CPT violation and the standard model”. In: *Physical Review D* 55.11 (1997), p. 6760.

[35] V. Alan Kostelecký and Neil Russell. “Data tables for Lorentz and CPT violation”. In: *Reviews of Modern Physics* 83.1 (Mar. 2011), pp. 11–31.

[36] Paul Adrien Maurice Dirac. “The quantum theory of the electron”. In: *Proceedings of the Royal Society of London. Series A, Containing Papers of a Mathematical and Physical Character* 117.778 (1928), pp. 610–624.

[37] Paul Adrien Maurice Dirac. “Quantised singularities in the electromagnetic field”. In: *Proceedings of the Royal Society of London. Series A, Containing Papers of a Mathematical and Physical Character* 133.821 (1931), pp. 60–72.

[38] Carl D Anderson. “The positive electron”. In: *Physical Review* 43.6 (1933), p. 491.

[39] Chien-Shiung Wu et al. “Experimental test of parity conservation in beta decay”. In: *Physical review* 105.4 (1957), p. 1413.

[40] Owen Chamberlain et al. “Observation of antiprotons”. In: *Physical Review* 100.3 (1955), p. 947.

[41] Bruce Cork et al. “Antineutrons produced from antiprotons in charge-exchange collisions”. In: *Physical Review* 104.4 (1956), p. 1193.

[42] Thomas Massam et al. “Experimental observation of antideuteron production”. In: *Il Nuovo Cimento A* 63 (1965), pp. 10–14.

[43] Günther Plass. *Design study of a facility for experiments with low energy antiprotons (LEAR)*. Tech. rep. CERN, 1980.

[44] G Gabrielse et al. "Barkas effect with use of antiprotons and protons". In: *Physical Review A* 40.1 (1989), p. 481.

[45] G Gabrielse et al. "First capture of antiprotons in a Penning trap: a kiloelectronvolt source". In: *Physical review letters* 57.20 (1986), p. 2504.

[46] Gerald Gabrielse et al. "Cooling and slowing of trapped antiprotons below 100 meV". In: *Physical review letters* 63.13 (1989), p. 1360.

[47] Gerald Gabrielse et al. "Thousandfold improvement in the measured antiproton mass". In: *Physical review letters* 65.11 (1990), p. 1317.

[48] G Gabrielse et al. "Special relativity and the single antiproton: Fortyfold improved comparison of p and p charge-to-mass ratios". In: *Physical review letters* 74.18 (1995), p. 3544.

[49] G Gabrielse et al. "Precision mass spectroscopy of the antiproton and proton using simultaneously trapped particles". In: *Physical Review Letters* 82.16 (1999), p. 3198.

[50] G ai Baur et al. "Production of antihydrogen". In: *Physics Letters B* 368.3 (1996), pp. 251–258.

[51] M Iwasaki et al. "Discovery of antiproton trapping by long-lived metastable states in liquid helium". In: *Physical review letters* 67.10 (1991), p. 1246.

[52] SA Baird et al. *Design study of the antiproton decelerator: AD*. Tech. rep. 1996.

[53] MEA Amoretti et al. "Production and detection of cold antihydrogen atoms". In: *Nature* 419.6906 (2002), pp. 456–459.

[54] Gerry Gabrielse et al. "Background-free observation of cold antihydrogen with field-ionization analysis of its states". In: *Physical Review Letters* 89.21 (2002), p. 213401.

[55] G Gabrielse et al. "Antihydrogen production using trapped plasmas". In: *Physics Letters A* 129.1 (1988), pp. 38–42.

[56] Lars V Jørgensen. "The AEgIS antihydrogen gravity experiment". In: *Hyperfine Interactions* 212.1 (2012), pp. 41–49.

[57] Claude Amsler et al. "Pulsed production of antihydrogen". In: *Communications Physics* 4.1 (2021), p. 19.

[58] "Confinement of antihydrogen for 1,000 seconds". In: *Nature Physics* 7.7 (2011), pp. 558–564.

[59] M Ahmadi et al. “Characterization of the 1S–2S transition in antihydrogen”. In: *Nature* 557.7703 (2018), pp. 71–75.

[60] M Ahmadi et al. “Observation of the 1S–2P Lyman-α transition in antihydrogen”. In: *Nature* 561.7722 (2018), pp. 211–215.

[61] CJ Baker et al. “Laser cooling of antihydrogen atoms”. In: *Nature* 592.7852 (2021), pp. 35–42.

[62] AE Charman. “Description and first application of a new technique to measure the gravitational mass of antihydrogen”. In: *Nature communications* 4.1 (2013), p. 1785.

[63] EK Anderson et al. “Observation of the effect of gravity on the motion of antimatter”. In: *Nature* 621.7980 (2023), pp. 716–722.

[64] Patrice Perez et al. “The GBAR antimatter gravity experiment”. In: *Hyperfine Interactions* 233.1 (2015), pp. 21–27.

[65] Masaki Hori et al. “Buffer-gas cooling of antiprotonic helium to 1.5 to 1.7 K, and antiproton-to–electron mass ratio”. In: *Science* 354.6312 (2016), pp. 610–614.

[66] A Mooser et al. “Resolution of single spin flips of a single proton”. In: *Physical review letters* 110.14 (2013), p. 140405.

[67] J DiSciacca et al. “One-particle measurement of the antiproton magnetic moment”. In: *Physical review letters* 110.13 (2013), p. 130801.

[68] Ch Smorra et al. “A parts-per-billion measurement of the antiproton magnetic moment”. In: *Nature* 550.7676 (2017), pp. 371–374.

[69] MJ Borchert et al. “A 16-parts-per-trillion measurement of the antiproton-to-proton charge–mass ratio”. In: *Nature* 601.7891 (2022), pp. 53–57.

[70] T Aumann et al. *PUMA: antiprotons and radioactive nuclei*. Tech. rep. 2019.

[71] Christian Smorra et al. *Technical Design Report of BASE-STEP*. Tech. rep. 2021.

[72] Erich Kugler. “The ISOLDE facility”. In: *Hyperfine interactions* 129.1-4 (2000), pp. 23–42.

[73] Isao Tanihata. “Neutron halo nuclei”. In: *Journal of Physics G: Nuclear and Particle Physics* 22.2 (1996), p. 157.

[74] M Aguilar et al. “The Alpha Magnetic Spectrometer (AMS) on the International Space Station: Part I–results from the test flight on the space shuttle”. In: *Physics Reports* 366.6 (2002), pp. 331–405.

[75] M Aguilar et al. “The Alpha Magnetic Spectrometer (AMS) on the international space station: Part II—Results from the first seven years”. In: *Physics reports* 894 (2021), pp. 1–116.

[76] H Dehmelt et al. “Past electron-positron g- 2 experiments yielded sharpest bound on CPT violation for point particles”. In: *Physical Review Letters* 83.23 (1999), p. 4694.

[77] GWea Bennett et al. “Search for Lorentz and C P T Violation Effects in Muon Spin Precession”. In: *Physical review letters* 100.9 (2008), p. 091602.

[78] Samuel Earnshaw. “On the nature of the molecular forces which regulate the constitution of the luminiferous ether”. In: *Transactions of the Cambridge Philosophical Society* 7 (1848), p. 97.

[79] Wolfgang Paul and Helmut Steinwedel. “Ein neues massenspektrometer ohne magnetfeld”. In: *Zeitschrift für Naturforschung A* 8.7 (1953), pp. 448–450.

[80] Colin D Bruzewicz et al. “Trapped-ion quantum computing: Progress and challenges”. In: *Applied Physics Reviews* 6.2 (2019), p. 021314.

[81] P Micke et al. “Coherent laser spectroscopy of highly charged ions using quantum logic”. In: *Nature* 578.7793 (2020), pp. 60–65.

[82] Lowell S Brown and Gerald Gabrielse. “Geonium theory: Physics of a single electron or ion in a Penning trap”. In: *Reviews of Modern Physics* 58.1 (1986), p. 233.

[83] Fouad G Major et al. *Charged particle traps: physics and techniques of charged particle field confinement*. Vol. 37. Springer Science & Business Media, 2005.

[84] Sven Sturm et al. “The ALPHATRAP experiment”. In: *The European Physical Journal Special Topics* 227 (2019), pp. 1425–1491.

[85] Christian Roux et al. “The trap design of PENTATRAP”. In: *Applied Physics B* 107 (2012), pp. 997–1005.

[86] Jochen Ketter et al. “First-order perturbative calculation of the frequency-shifts caused by static cylindrically-symmetric electric and magnetic imperfections of a Penning trap”. In: *International Journal of Mass Spectrometry* 358 (2014), pp. 1–16.

[87] JL Verdu Galiana. “Ultrapräzise Messung des elektronischen g-Faktors in wasserstoffähnlichem Sauerstoff”. In: *Doktorarbeit, Johannes Gutenberg-Universität Mainz* (2003).

[88] H Nagahama et al. “Sixfold improved single particle measurement of the magnetic moment of the antiproton”. In: *Nature Communications* 8.1 (2017), pp. 1–7.

[89] James Karl Thompson. “Two-ion control and polarization forces for precise mass comparisons”. PhD thesis. Massachusetts Institute of Technology, 2003.

[90] Sascha Rau. “High-precision measurement of the deuteron’s atomic mass”. PhD thesis. Ruprecht-Karls-Universität Heidelberg, 2020.

[91] Masaki Hori. “The ASACUSA experiment at CERN’s antiproton decelerator”. In: *Nuclear physics. A, Nuclear and hadronic physics* 692.1-2 (2001), pp. 119–128.

[92] Jeffrey S Hangst and Paul Bowe. *The ALPHA Collaboration Antihydrogen Laser PHysics Apparatus*. Tech. rep. 2004.

[93] Christian Smorra et al. “BASE–the baryon antibaryon symmetry experiment”. In: *The European Physical Journal Special Topics* 224.16 (2015), pp. 3055–3108.

[94] L. Ponce et al. “ELENA - From Commissioning to Operation”. In: *Proc. IPAC’22* (Bangkok, Thailand). International Particle Accelerator Conference 13. JACoW Publishing, Geneva, Switzerland, July 2022, THOXGD1, pp. 2391–2394.

[95] Barbara M Latacz et al. “Ultra-thin polymer foil cryogenic window for antiproton deceleration and storage”. In: *Review of Scientific Instruments* 94.10 (2023).

[96] H Nagahama et al. “Highly sensitive superconducting circuits at 700 kHz with tunable quality factors for image-current detection of single trapped antiprotons”. In: *Review of Scientific Instruments* 87.11 (2016), p. 113305.

[97] S Sellner et al. “Improved limit on the directly measured antiproton lifetime”. In: *New Journal of Physics* 19.8 (2017), p. 083023.

[98] Christian Smorra et al. “A reservoir trap for antiprotons”. In: *International Journal of Mass Spectrometry* 389 (2015), pp. 10–13.

[99] Matthias Joachim Borchert. “Challenging the Standard Model by high precision comparisons of the fundamental properties of antiprotons and protons”. PhD thesis. Hannover: Institutionelles Repositorium der Leibniz Universität Hannover, 2021.

[100] Markus Fleck. “Towards a Tenfold Improvement on the Measurement of the Antiproton Magnetic Moment”. PhD thesis. University of Tokyo, 2022.

[101] Stefan Ulmer et al. “Observation of spin flips with a single trapped proton”. In: *Physical review letters* 106.25 (2011), p. 253001.

[102] Christian Smorra et al. “Observation of individual spin quantum transitions of a single antiproton”. In: *Physics Letters B* 769 (2017), pp. 1–6.

[103] *SOFT MAGNETIC COBALT-IRON ALLOYS*. VACUUMSCHMELZE GmbH & Co. KG, 2021.

[104] MJ Borchert et al. “Measurement of ultralow heating rates of a single antiproton in a cryogenic Penning trap”. In: *Physical review letters* 122.4 (2019), p. 043201.

[105] Frederik Völksen. “Development of a precisely tuneable cryogenic low-loss capacitor for axion-like particle detection and precision measurements in Penning traps”. Justus-Liebig-Universität Giessen, 2021.

[106] DJ Wineland and HG Dehmelt. “Principles of the stored ion calorimeter”. In: *Journal of Applied Physics* 46.2 (1975), pp. 919–930.

[107] Stefan Ulmer. “First Observation of Spin Flips with a Single Proton Stored in a Cryogenic Penning Trap”. PhD thesis. July 2011.

[108] Harry Nyquist. “Thermal agitation of electric charge in conductors”. In: *Physical review* 32.1 (1928), p. 110.

[109] Eric A Cornell et al. “Mode coupling in a Penning trap: π pulses and a classical avoided crossing”. In: *Physical Review A* 41.1 (1990), p. 312.

[110] Robert Mark Weisskoff. “Detecting single, trapped ions”. PhD thesis. Massachusetts Institute of Technology, 1988.

[111] B d’Urso, B Odom, and G Gabrielse. “Feedback cooling of a one-electron oscillator”. In: *Physical review letters* 90.4 (2003), p. 043001.

[112] Jost Herkenhoff et al. “A digital feedback system for advanced ion manipulation techniques in Penning traps”. In: *Review of Scientific Instruments* 92.10 (2021).

[113] *UM-Series, Multichannel Precision Voltage Source*. stahl-electronics, 2021.

[114] *UM-Series, Multichannel Precision Voltage Source*. stahl-electronics, 2021.

[115] Fabian Heiße et al. “High-precision measurement of the proton’s atomic mass”. In: *Physical Review Letters* 119.3 (2017), p. 033001.

[116] Sascha Rau et al. “Penning trap mass measurements of the deuteron and the HD+ molecular ion”. In: *Nature* 585.7823 (2020), pp. 43–47.

[117] James K Thompson, Simon Rainville, and David E Pritchard. “Cyclotron frequency shifts arising from polarization forces”. In: *Nature* 430.6995 (2004), pp. 58–61.

[118] IV Kortunov et al. “Proton–electron mass ratio by high-resolution optical spectroscopy of ion ensembles in the resolved-carrier regime”. In: *Nature physics* 17.5 (2021), pp. 569–573.

[119] KR Lykke, KK Murray, and WC Lineberger. “Threshold photodetachment of H-”. In: *Physical Review A* 43.11 (1991), p. 6104.

[120] A. Kramida et al. NIST Atomic Spectra Database (ver. 5.9), [Online]. Available: https://physics.nist.gov/asd [2022, October 6]. National Institute of Standards and Technology, Gaithersburg, MD. 2021.

[121] S Ulmer et al. “High-precision comparison of the antiproton-to-proton charge-to-mass ratio”. In: *Nature* 524.7564 (2015), pp. 196–199.

[122] Jack A Devlin et al. “Superconducting solenoid system with adjustable shielding factor for precision measurements of the properties of the antiproton”. In: *Physical Review Applied* 12.4 (2019), p. 044012.

[123] Stefano Laporta. “High-precision calculation of the 4-loop contribution to the electron g-2 in QED1”. In: *Journal of Physics: Conference Series*. Vol. 1085. 5. IOP Publishing. 2018, p. 052008.

[124] Tatsumi Aoyama, Toichiro Kinoshita, and Makiko Nio. “Revised and improved value of the QED tenth-order electron anomalous magnetic moment”. In: *Physical Review D* 97.3 (2018), p. 036001.

[125] Alexandre Deur, Stanley J Brodsky, and Guy F De Téramond. “The spin structure of the nucleon”. In: *Reports on Progress in Physics* 82.7 (2019), p. 076201.

[126] S Ulmer et al. *Future Program of the BASE Experiment at the Antiproton Decelerator of CERN*. Tech. rep. 2019.

[127] Lowell S Brown. “Geonium lineshape”. In: *Annals of Physics* 159.1 (1985), pp. 62–98.

[128] H Häffner et al. “Double Penning trap technique for precise g factor determinations in highly charged ions”. In: *The European Physical Journal D-Atomic, Molecular, Optical and Plasma Physics* 22 (2003), pp. 163–182.

[129] A Mooser et al. “Direct high-precision measurement of the magnetic moment of the proton”. In: *Nature* 509.7502 (2014), pp. 596–599.

[130] Georg Schneider et al. “Double-trap measurement of the proton magnetic moment at 0.3 parts per billion precision”. In: *Science* 358.6366 (2017), pp. 1081–1084.

[131] G Gabrielse and J Tan. “Self-shielding superconducting solenoid systems”. In: *Journal of Applied Physics* 63.10 (1988), pp. 5143–5148.

[132] Edmund E Callaghan and Stephen H Maslen. *The magnetic field of a finite solenoid*. Vol. 465. National Aeronautics and Space Administration, 1960.

[133] Jannek Hansen. “Active stabilization of magnetic field fluctuations in the BASE antiproton-experiment at CERN”. 2019.

[134] Louis Cohen. *An exact formula for the mutual inductance of coaxial solenoids*. 58. US Government Printing Office, 1907.

[135] GD Brittles et al. “Persistent current joints between technological superconductors”. In: *Superconductor Science and Technology* 28.9 (2015), p. 093001.

[136] Gerhard Heinzel, Albrecht Rüdiger, and Roland Schilling. “Spectrum and spectral density estimation by the Discrete Fourier transform (DFT), including a comprehensive list of window functions and some new at-top windows”. In: (2002).

[137] Bertrand Rivet, Laurent Girin, and Christian Jutten. “Log-rayleigh distribution: A simple and efficient statistical representation of log-spectral coefficients”. In: *IEEE transactions on audio, speech, and language processing* 15.3 (2007), pp. 796–802.

[138] Frank E Grubbs. “Sample criteria for testing outlying observations”. In: *The Annals of Mathematical Statistics* (1950), pp. 27–58.

[139] Sven Sturm et al. “Phase-sensitive cyclotron frequency measurements at ultralow energies”. In: *Physical review letters* 107.14 (2011), p. 143003.

[140] CH Tseng et al. “1-bit memory using one electron: Parametric oscillations in a Penning trap”. In: *Physical Review A* 59.3 (1999), p. 2094.

[141] Norman F Ramsey. “The method of successive oscillatory fields”. In: *Physics Today* 66.1 (2013), pp. 36–41.

[142] Tim Sailer et al. “Measurement of the bound-electron g-factor difference in coupled ions”. In: *Nature* 606.7914 (2022), pp. 479–483.